Measurements of Turbulence Parameters and Observations of Multipath Arrivals in Two Contrasting Coastal Environments Using Acoustical Scintillation Analysis

by

Daniela Di Iorio
B.Sc., University of Victoria, 1988

A Dissertation submitted in Partial Fulfillment of the
Requirements for the Degree of
DOCTOR OF PHILOSOPHY
in the Department of Physics and Astronomy

We accept this thesis as conforming to the required standard

Dr. David M. Farmer, supervisor (Dept. of Physics)

Dr. Arthur Watton, supervisor (Dept. of Physics)

Dr. Robert W. Stewart, member (SEOS, Dept. of Physics)

Dr. Chris J. R. Garrett, member (Dept. of Physics, SEOS)

Dr. Adam Zielinski, outside member (Dept. Elec. Eng.)

Dr. Valerian I. Tatarskii, external (NOAA/ETL, Boulder Co.)

Supervisor: Dr. David M. Farmer

Abstract

The purpose of this research is to explore the potential of acoustical propagation as a probe of oceanographic processes in the coastal ocean. This is done by examining acoustical scintillation in two contrasting regimes: a turbulent tidal flow, and a quiescent, weakly stratified environment.

In one experiment, two-dimensional arrays of acoustic projectors and receivers are used to examine the refractive index variability in a high Reynolds number, low Richardson number tidal flow through a channel. Our acoustic data are compared with predictions of the weak scattering theory of Tatarskii assuming a Kolmogorov turbulence model, and interpreted in terms of available oceanographic data. Using the acoustic propagation and turbulence models we are able to measure some of the oceanographic processes characteristic of a turbulent channel flow.

It is found that the dominant component of the observed acoustical scintillations is due to turbulent velocity fluctuations, leading to estimates of the path averaged turbulent kinetic energy dissipation (ϵ) which rises and falls with the tidal current ($\epsilon \sim 10^{-7}$ to $10^{-5}\ m^2 s^{-3}$). Analysis of the low frequency variability in the two dimensional angle of arrival shows that advection of the acoustic waveform by current and refraction by stratification can be modelled by a ray approach. The two-dimensional angle of arrival distribution for rapidly fluctuating acoustic signals is correlated during strongly sheared flow. Both these characteristics confirm that the turbulence is anisotropic over scales less than 32 m. This anisotropy is discussed in terms of the horizontal (x) and vertical (z) cross channel velocity (v) gradients: $\partial v/\partial x$ and $\partial v/\partial z$. Based on the dissipation measurement the root mean square velocity gradient, calculated over the turbulent wavenumber scales, does explain the total mean square arrival angle fluctuations within a factor of 3. An attempt to model the anisotropy in terms of the refractivity spectrum and the Reynolds stress both proved to be impracticable. These measurements provide motivation for further studies comparing

our observations to *in situ* measurements of the turbulent parameters.

Acoustical scintillation measurements are also made in a completely different coastal oceanographic site in order to provide a direct comparison with Cordova Channel. Since currents are minimal, stable stratification is maintained. Because of this stratification acoustic multipaths occur which are separated such that the amplitude and phase for a particular wholly refracted path may be analyzed. A maximum likelihood estimation technique is used to fit a sum of three paths to the received signal such that the error between the received signal and the modelled signal is minimized. The intensity fluctuations are large ($S_I^2 \sim 1$) and are approximately exponentially distributed implying that the multiple scatter acoustic propagation theory is applicable. Refractive index fluctuations due to internal waves and fine structure may explain the large acoustic intensity variations observed in the data.

Examiners:

Dr. David M. Farmer, supervisor (Dept. of Physics)

Dr. Arthur Watton, supervisor (Dept. of Physics)

Dr. Robert W. Stewart, member (SEOS, Dept. of Physics)

Dr. Chris J. R. Garrett, member (Dept. of Physics, SEOS)

Dr. Adam Zielinski, outside member (Dept. Elec. Eng.)

Dr. Valerian I. Tatarskii, external (NOAA/ETL, Boulder Co.)

Contents

List of Tables

List of Figures

Glossary of Notation

Acoustic parameters

f_a, $\omega_a = 2\pi f_a$	acoustic frequency $[Hz]$, and angular frequency $[rad\ s^{-1}]$,
λ, $k = 2\pi/\lambda$	acoustic wavelength $[m]$ and wavenumber $[rad\ m^{-1}]$,
ρ, τ	spatial $[m]$ and temporal $[s]$ separations,
L	acoustic path length $[m]$,
$\sqrt{\lambda L}$	Fresnel radius $[m]$,
$\mathcal{I}$, $\mathcal{Q}$	in-phase and quadrature components,
A	amplitude,
$I = A^2$	intensity,
$\chi = \ln(A/ < A >)$	log-amplitude,
T, ϕ	time of arrival $[s]$ and phase $[rad]$,
$\delta\phi$	phase difference $[rad]$,
θ_{a_x}, θ_{a_z}	horizontal and vertical acoustic arrival angle $[rad]$,
$R_I(\tau)$	intensity auto covariance,
$S_I^2 = R_I(0)/ < I >^2$	scintillation index,
$C_\chi(\rho, \tau)$	two dimensional space – time log-amplitude cross covariance function,

$\sigma_\chi^2 = C_\chi(0,0)$	log-amplitude variance,
$D(\rho,\tau) = D_\chi(\rho,\tau) + D_\phi(\rho,\tau)$	wave structure function defined as a sum of log-amplitude and phase structure functions,
$W_{\chi,\phi,\delta\phi}(f)$	frequency spectrum for log-amplitude $[Hz^{-1}]$, phase $[rad^2\ Hz^{-1}]$, or phase difference $[rad^2\ Hz^{-1}]$,
$f_0 = U/\sqrt{\lambda L}$	characteristic frequency induced by Fresnel scale sizes advected by the mean flow $[Hz]$,
$f_1 = U/\rho$	characteristic frequency induced by receiver separation scale sizes advected by the mean flow $[Hz]$,
$\Gamma,\ X$	scattering strength of the refractive index fluctuations, and normalized propagation range.

Medium parameters

$x,\ y,\ z$	along stream, cross stream and vertical cartesian coordinates,
$c_o,\ \frac{dc}{dz}$	mean sound speed $[m\ s^{-1}]$ and sound speed gradient $[s^{-1}]$ at the depth of acoustic propagation,
$\rho_o,\ \frac{d\rho}{dz}$	mean density $[kg\ m^{-3}]$ and density gradient $[kg\ m^{-4}]$ at the depth of acoustic propagation,
$N(z)$	Brunt-Vaisala angular frequency $[rad\ s^{-1}]$,
$n = n_o + \eta$	refractive index in terms of a mean and fluctuating component,
$\mathbf{K},\ \kappa = \lvert\mathbf{K}\rvert = \frac{2\pi}{\ell}$	3D refractive index wave number and the magnitude of the refractive index wavenumber vector $[rad\ m^{-1}]$,
$\ell_o,\ L_o$	inner (dissipating) and outer (energy containing) scale of turbulence $[m]$,
C_D	drag coefficient at the depth of the acoustic paths,
$\mathcal{K}$	von Karman's constant,
ν	kinematic viscosity $[m^2 s^{-1}]$,

$\overline{z}$	path averaged distance from the boundary to the acoustic propagation depth $[m]$,
D	average depth of channel or inlet $[m]$,
$U,\ \overline{U}$	point and path averaged measurement of the current perpendicular to the acoustic propagation direction $[m\ s^{-1}]$,
$\frac{dU}{dz}$	vertical along channel mean velocity gradient $[s^{-1}]$,
$u,\ v,\ w$	velocity fluctuations along the x, y, and z directions $[m\ s^{-1}]$,
$\frac{\partial u}{\partial x}$	turbulent velocity gradient $[s^{-1}]$,
$\left\langle \frac{\partial v}{\partial x}\frac{\partial v}{\partial z} \right\rangle$	correlation of horizontal and vertical cross channel velocity gradient $[s^{-1}]$,
$\delta\theta_x \approx U/c_o$	horizontal arrival angle due to advection of the acoustic waveform $[rad]$,
$\theta_z \approx \frac{L}{2c_o}\frac{dc}{dz}$	vertical arrival angle due to refraction $[rad]$,
$\epsilon,\ \overline{\epsilon}$	point and path averaged measurement of the turbulent kinetic energy dissipation $[m^2 s^{-3}]$,
$\mathcal{D}_{n_s}(r) = C_{n_s}^2 r^{2/3}$	refractive index structure function for scalar variables,
$\Phi_{1n_s}(\kappa) \propto C_{n_s}^2 \kappa_1^{-5/3}$	one dimensional spectral density for isotropic and homogeneous refractive index fluctuations due to scalars $[m]$,
$C_n^2 = C_{n_s}^2 + 11/6 C_{n_v}^2$	refractive index structure parameter in terms of scalar and vector properties $[m^{-2/3}]$,
$\Phi_n(\kappa) \propto C_n^2 \kappa^{-11/3}$	three dimensional spectral density for isotropic and homogeneous refractive index fluctuations $[m^3]$,
$\mathcal{U}_n(\mathbf{K}, w)$	three dimensional space - time spectral density for refractive index fluctuations $[m^3 s]$,
$E(\kappa) \propto \epsilon^{2/3}\kappa^{-5/3}$	three dimensional spectral density for isotropic and homogeneous velocity fluctuations $[m^3 s^{-2}]$.

Dimensionless parameters

$\mathrm{Re} = \frac{UD}{\nu}$	Reynolds number,
$\mathrm{Ri} = -g\frac{\Delta\rho}{\rho_o}h/\Delta U^2$	bulk Richardson number.

Acknowledgements

I would like to thank Dr. David Farmer for giving me the opportunity to work on an extremely challenging and interesting research project. I am grateful for his enthusiasm, guidance, support and encouragement at every stage of my research. I would also like to thank Dr. Stewart for many helpful and stimulating discussions on turbulence and channel flow properties. I thank Dr. Garrett for questioning the basic physics of acoustic propagation and for careful analysis of the thesis. I thank Dr. Watton for his support as a university supervisor and also for his detailed analysis of the theoretical write up. Finally, I would like to thank Dr. Zielinski for his interest in the instrumentation and serving as a committee member.

Thanks are due to David Lemon and Rene Chave and their colleagues at ASL Environmental Sciences for designing, building and deploying the acoustical scintillation system. I thank them for providing continuous support in analysing the raw data. Thanks are due to Tom Juhasz, Reg Bigham, John Love, Les Spearing, Andrew Lee and the crew of the CSS VECTOR and PARIZEAU for designing, deploying and recovering all the oceanographic instrumentation. Thanks are also due to Mike Dempsey and David Spear for their support in servicing the oceanographic instruments.

I am very grateful to Grace Kamitakahara-King for her continuous computer support and to Ron Teichrob for his technical support. I would like to also thank my Ocean Acoustic friends and colleagues for stimulating discussions and support through the years, making my life at the Institute of Ocean Sciences interesting and enjoyable. In particular, I thank Grace Kamitakahara and David King for their wonderful din-

ner parties, Len and Liz Zedel for many wonderful hikes, Yunbo Xie for all the music lessons and duets, Dimitris Menemenlis for the wonderful philosophical arguments on politics and science and for organising IOS soccer, Li Ding for stimulating discussions on time series analysis, Craig McNiel for all the laughs and the pub nights, Mark Trevorrow for the soccer games ending at the pub, Willi Weichselbaumer for his help on computer system debugging, Zhen Ye for his ideas on two-dimensional structure functions, Anna-Lea Rantalainan and Al Adrian for the bike rides, Donald Booth for his outspoken and entertaining views, Peter Hallschmid for processing the Saanich Inlet data, and Terry Russell for her CEOR administrative help.

Last, but not least, I would like to thank Raymond Clary for giving me the love and support during my undergraduate years and encouragement for starting the Ph.D. Also, I thank Don Newman for giving me love and support during the final stages of the Ph.D. and for his helpful ideas on the design of the frontispiece. Finally, I thank my mother, Livia Di Iorio and sister, Mafalda Di Iorio for their continued patience and dedicate this thesis to my nephew, Nicholas Edward Benn and to my parents.

This work received support from the Canadian Panel on Energy Research and Development, and the U.S. Office of Naval Research. The author was funded by scholarships from the Natural Sciences and Engineering Research Council of Canada and the Science Council of British Columbia.

I dedicate this thesis to my nephew,

Nicholas Edward Benn,

and to my parents,

Matthew and Livia Di Iorio

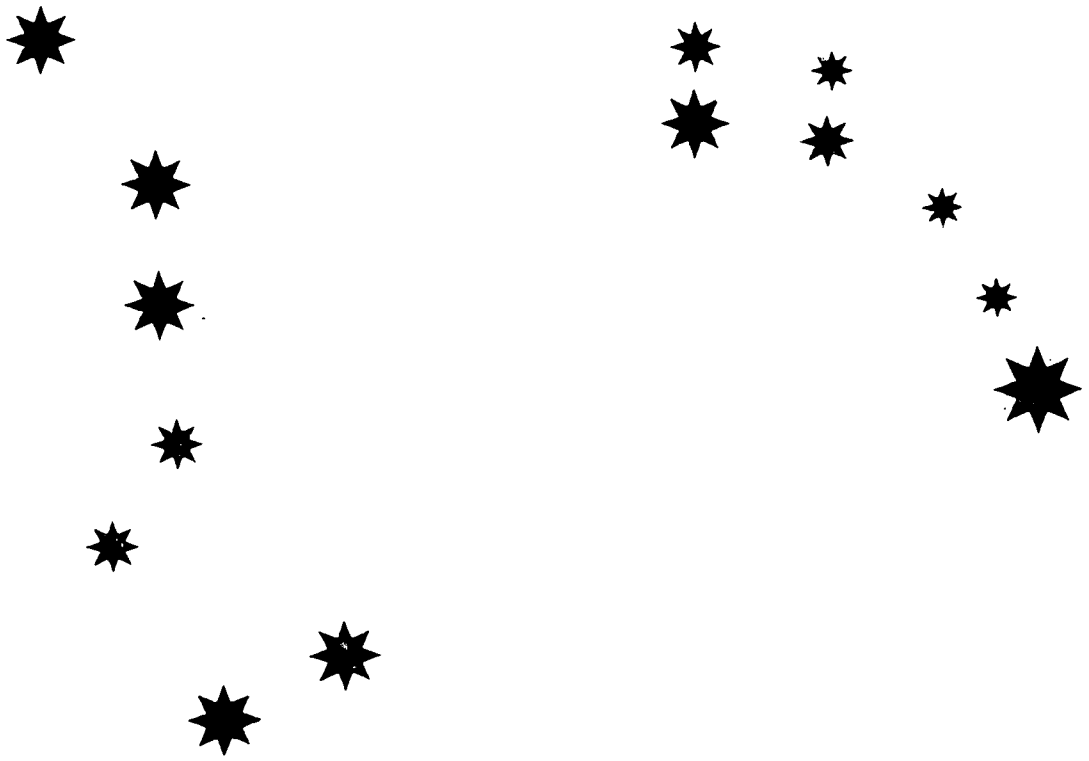

Twinkle, twinkle little star, how I wonder what you are.
Up above the world so high, like a diamond in the sky.
Twinkle, twinkle little star, how I wonder what you are.

Ann Taylor (1849-1892) and Jane Taylor (1842-1920).

Chapter 1

Introduction

Much work has been done on the propagation of waves through media containing both spatial and temporal fluctuations in the refractive index. This type of wave propagation occurs in many branches of experimental physics including radio propagation in the ionosphere, light propagation in the atmosphere, and acoustic propagation in the ocean (see Tatarskii, Ishimaru, and Zavorotny [54]). The intensity and phase of the signal at the receiving station show variations that evolve with time defining a scintillation pattern. This scintillation pattern contains information about the intervening medium.

The theory of wave propagation through random media (WPRM) provides the basis for inferring path averaged properties of the propagation medium from the measured signal. A theory for wave propagation through a medium characterized by Kolmogorov's model of homogeneous, isotropic turbulence, which results in the characteristic '-5/3' power-law spectrum for velocity and scalar properties of the fluid, has been developed for the case of weak fluctuations, primarily by Soviet scientists. This work is summarized by Tatarskii [52], and atmospheric experiments show good agreement with the theory. In many coastal waters, the interaction of tidal flow with bottom topography results in turbulence and hence this theory was used by Farmer *et.al.* [24] as a tool to measure current and turbulent structure in a coastal

environment.

In the open ocean, and in more quiescent coastal inlets, however, the assumption of homogeneous, isotropic turbulence and weak acoustic fluctuations cannot be made. Most ocean acoustic experiments are complicated by internal waves as the source of randomness, or the path length and refractive index variability are such that Tatarskii's weak scattering theory, based on Rytov's approximation, is no longer applicable. Recent theoretical work by Uscinski [57] describes both large and small acoustic intensity fluctuations. In 1977 Ewart and Reynolds [22] made simultaneous measurements of acoustic and refractive index fluctuations. The physical processes responsible for the refractive index fluctuations are tides, internal waves and fine structure. Their acoustic measurements reveal these effects.

We apply these techniques to active and quiet coastal ocean environments by first giving motivation for studying the coastal waters and then describing the experimental approach.

1.1 Motivation

The coastal ocean is very diverse. The circulation is set by the local bathymetry, meteorological forcing and the interaction with river run off and deeper oceanic waters. In order for numerical models of the circulation to be accurate, parameterization of the turbulent processes is required. To do this, data describing the structure of turbulence are needed.

Turbulence and mixing plays a strong role in the active coastal environment. Since the currents are strong and the water is shallow compared to the deep ocean, energy must be dissipated in less volume and so the dissipation rate and thus the level of the turbulence is generally higher. This is because the interaction of the tidal current with channel boundaries results in turbulence which occupies a large part and sometimes all of the water column. The turbulence in a channel flow contains structures over a broad range of scales. The most important source of mixing in the coastal ocean is

often turbulence generated by tidally driven currents. Moreover, mixing in a channel flow is a complex and intermittent process.

In deep coastal inlets and fjords, currents are small and stratification changes s· · nally. The circulation in a fjord is complicated because of a *sill* that exists at the entrance of the fjord. This sill cuts off most of the deeper water from interacting with the adjacent coastal ocean and so circulation is primarily controlled by density differences. In order to study mixing in this environment it is necessary to identify the source of turbulent energy. Is it driven by wind stress, internal waves, directly by current shear or is it driven by bottom stress? Answering this question provides the necessary background for interpreting and modelling data in this kind of environment.

A better understanding of turbulence, mixing and circulation is vital to progress in coastal oceanography. This is because the coastal ocean is home to most food fish and shell fish relying on a nutrient rich environment. The coastal ocean is also subject to the dilution and dispersion of a great variety of wastes, both liquid and solid. Contamination from waste chemicals, paper mill wastes and sewage wastes are often discharged in the coastal ocean and concentrations are diluted through mixing with large volumes of ocean waters. The coastal circulation then disperses the water masses.

Measurement of the turbulence parameters have traditionally been carried out using *in situ* sensors of temperature, conductivity and three orthogonal components of current velocity, or using high-resolution vertical profilers. The drawback of these measurements is that they are essentially local in character and may not reflect the average properties of the turbulence. Path averaged measurements of the coastal ocean can be a desirable way to obtain parameterization of turbulence properties in a channel flow for numerical modellers. For many purposes such as transport calculations, a path averaged result is more useful than a point measurement. Path averaging has an additional benefit: the effect of smaller scale processes is filtered and the scale of greatest sensitivity is controlled by the path length and the acoustic wavelength. Our experimental approach describes a novel way of obtaining path

averaged measurements of current and turbulent structure.

1.2 Experimental approach

Acoustical scintillation experiments described in this thesis were carried out in two completely different coastal environments (Cordova Channel (1986) and Saanich Inlet (1989)) in order to examine and contrast the corresponding acoustic characteristics and where possible relate these to the oceanographic environments. The primary study was carried out in Cordova Channel, and the analysis explores some of the ways in which mean and turbulent properties can be measured acoustically, making detailed comparisons with available oceanographic data. The contrasting scintillation data from Saanich Inlet are much less completely supported by oceanographic data, but nevertheless provides an opportunity to examine the analytical procedures, in particular multipath separation, that must be used to derive an interpretable signal.

For Cordova Channel we first test the applicability of the models within the limitations of our experiment, and then use the results to derive path averaged turbulence characteristics of the flow. One quite surprising result of this work is that acoustic propagation in a turbulent coastal environment leads to a signal dominated by velocity fluctuations rather than temperature fluctuations, as will be shown. This allows us to evaluate directly the turbulent kinetic energy dissipation. Path averaged dissipation measurements have been carried out by Menemenlis [41] using reciprocal acoustic transmission in the boundary layer under Arctic ice to directly measure the turbulent kinetic energy spectrum. Our measurements of path averaged dissipation described in this thesis make use of the forward scattered signal together with the isotropic turbulence model.

Oceanographic measurements from time series and profiles together with acoustic measurements from square transmitting and receiving arrays provide a better understanding of the two dimensional deterministic and turbulent effects. The deterministic effects are explained in terms of the ray approach which shows advection and

refraction of the acoustic waveform. The turbulent effects are discussed by analysing correlated vertical and horizontal (along-channel) components of the acoustic angle of arrival fluctuations. These observed correlations imply anisotropic turbulence which is then discussed in terms of the turbulent velocity fluctuations and gradients. An attempt to model the anisotropy is then done.

Propagation of sound over greater path lengths tends to increase the opportunity for multipath effects. When there is a strong dominant path the coherence is high; when there are many multipaths the coherence is low (Urick [56]). Thus, application of propagation techniques for probing oceanographic processes will invariably confront the multipath problem and separation of multipaths remains one of the outstanding challenges for this approach. Ehrenberg *et.al.* [20] and Ewart *et.al.* [21] developed a maximum likelihood algorithm for separating FM slide and pulsed-tone signals. The Saanich Inlet data show multipath arrivals and we use the maximum likelihood estimation algorithm for separating signals processed with a matched filter.

The oceanographic variability in Saanich Inlet was not measured as completely as in Cordova Channel, where temperature and salinity time series measurements in the tidal flow allowed estimates of the spatial variability over the inertial subrange. It does however, show an interesting contrast to the turbulent environment in Cordova Channel. The analysis of data from Saanich Inlet, which is in some ways a more complex environment, is limited to a comparison of (1) characteristic oceanographic and acoustic variability and (2) the deterministic aspects of propagation with measured sound speed profiles. Some potential explanations for the former are provided. Although the deterministic propagation is very well described, the random components are not, and present a very challenging analysis problem.

This thesis gives further insights into the way in which turbulent and other fluctuations in the ocean contribute to the received signal, and these in turn contribute to our ability to tackle the inverse problem of using the propagation characteristics to resolve oceanic structure. There are several important features of these experiments that distinguish it from many other acoustic experiments. These include, the use of

a high acoustic frequency, the use of two-dimensional rigid transmitter and receiver arrays, the use of a coherent scheme allowing precise phase measurements and high enough sampling rate and signal-to-noise ratio to allow resolution of phase ambiguity in the phase time series.

An understanding of acoustic propagation and the scintillation pattern is essential in attempting to use the acoustics for measuring oceanographic variables, as well as for other applications such as underwater communication systems, positioning devices and fish stock assessment. ASL Environmental Sciences Ltd., have made scintillation flow measurements in the Fraser River (see Lemon [37]) and in hydroelectric dams for efficiency calculations (see Birch and Lemon [2]). The understanding that results from this work provides the necessary scientific basis for commercial application of the scintillation technique.

1.3 Thesis outline

An overview of statistical functions and their notation is given in Chapter 2. Chapter 3 provides some of the background theory for acoustic propagation in random media. Following is a description of the random medium in terms of isotropic and homogeneous turbulence. Finally, a description of the acoustic propagation models for weak and multiple scattering is presented. This chapter is a review chapter and the only original contribution to acoustical oceanography is the discussion of the refractive index structure parameter in terms of both velocity and scalar contributions.

Chapter 4 describes the novel acoustic instrumentation used to study the turbulence in Cordova Channel (1986) and the multipath acoustic signals in Saanich Inlet (1989). The acoustic system was developed by ASL Environmental Sciences under contract to the Institute of Ocean Sciences. I had the opportunity to participate in the Cordova Channel experiment as a co-op student and for the Saanich Inlet experiment I helped organize and collect all the data.

Chapter 5 describes the measurements of the turbulent kinetic energy parameters

obtained in Cordova Channel. An overview of the *in situ* oceanographic measurements are described and the channel is quantified in terms of the Reynolds and Richardson numbers as a first step in defining the turbulence. Acoustic measurements of amplitude and phase are described together with a comparison with the weak scattering theory. Since the acoustic scintillations can be modelled, we can use our observations to obtain path averaged oceanographic measurements. A new technique for the acoustical remote sensing of the turbulence outer scale, current, mean shear, refractive index structure parameter and the turbulent kinetic energy dissipation is the most significant original contribution of the thesis. We compare our acoustic propagation experiment to other experiments and show that this is the first time acoustical scintillation measurements have been reported in a coastal environment characterized by fully developed turbulence.

The two dimensional angle of arrival distribution is analyzed to reveal both deterministic and turbulent effects. The deterministic effects are described in terms of refraction and advection of the acoustic waveform and the turbulent effects show a degree of anisotropy. For this reason an anisotropic model for the refractivity spectrum is examined. Also, the angle of arrival correlations are discussed in terms of the cross channel velocity gradients. This section of the thesis is also a significant original contribution.

Chapter 6 describes the acoustic multipath propagation characteristics observed in Saanich Inlet. The most original contribution in this chapter is primarily the multipath separation technique developed for match filtered signals. The results from this analysis together with the oceanographic analysis formulates the "forward" problem of acoustic propagation. This kind of environment demonstrates the difficulty in using acoustical scintillation analysis to solve the "inverse" problem, that is, to measure the oceanographic characteristics.

Chapter 7 is the conclusions of the thesis and outlines all the oceanographic measurements that can be made with a relatively simple square and linear acoustic array. Some recommendations for future work is also suggested.

Chapter 2

Statistical Definitions

A review of the statistical functions measured and described throughout the thesis will be summarized in this chapter. Although the notation varies from author to author, I have tried to use the same notation as Tatarskii [52].

2.1 Covariance functions

Random processes can be described by statistical quantities. The simplest statistical quantity of a random function $g(\mathbf{r},t)$ is its mean $< g(\mathbf{r},t) >$, where the angle brackets $< >$ denote an average over time at the location $\mathbf{r}$. The next statistical quantity of importance is the space-time cross covariance function,

$$C_g(\mathbf{r}_1,t_1,\mathbf{r}_2,t_2) =< g'(\mathbf{r}_1,t_1)g'(\mathbf{r}_2,t_2)^* >, \tag{2.1}$$

where $g'(\mathbf{r},t) = g(\mathbf{r},t) - < g(\mathbf{r},t) >$ is a zero mean process and $*$ denotes complex conjugate in cases where the function g represents propagating wave fields. If the random process is a stationary random variable, then the statistical moments remain constant with time and space, and the covariance function depends only on the spatial and temporal separation ($\boldsymbol{\rho} = \mathbf{r}_1 - \mathbf{r}_2$ and $\tau = t_1 - t_2$ respectively). That is,

$$\begin{aligned} < g(\mathbf{r}_1,t_1)^n > &= < g(\mathbf{r}_2,t_2)^n > \quad n = 1,2,3,... \\ \text{and} \quad C_g(\mathbf{r}_1,t_1,\mathbf{r}_2,t_2) &= C_g(\boldsymbol{\rho},\tau). \end{aligned} \tag{2.2}$$

Stationarity in space, defines homogeneity. Statistical isotropy implies that $C_g(\boldsymbol{\rho}, \tau)$ depends only on the magnitude, $\rho = |\boldsymbol{\rho}|$ and not on direction. The spatial covariance and temporal covariance function can be recovered by the space-time covariance function using the following notation,

$$B_g(\boldsymbol{\rho}) = C_g(\boldsymbol{\rho}, \tau = 0), \tag{2.3}$$

$$R_g(\tau) = C_g(\boldsymbol{\rho} = 0, \tau). \tag{2.4}$$

2.2 Structure functions

In oceanographic (or meteorological) conditions, random processes cannot be regarded as stationary since mean values change with both space and time. To avoid this difficulty, the difference function,

$$G(\mathbf{r}_1, t_1) = g'(\mathbf{r}_1 + \mathbf{r}, t_1 + t) - g'(\mathbf{r}_1, t_1), \tag{2.5}$$

is considered, where $'$ denotes zero mean processes. This function removes the effects of large scale inhomogeneities that are common to both $g(\mathbf{r}_1 + \mathbf{r}, t_1 + t)$ and $g(\mathbf{r}_1, t_1)$. For values of $\mathbf{r}$ and t which are not too large, the function G can be considered stationary.

Following Tatarskii [52], the covariance for the function G can be written as the sum,

$$\begin{aligned} C_G(\mathbf{r}_1, t_1, \mathbf{r}_2, t_2) =& < G(\mathbf{r}_1, t_1) G(\mathbf{r}_2, t_2) > = \\ & \tfrac{1}{2} \left(< [g'(\mathbf{r}_1 + \mathbf{r}, t_1 + t) - g'(\mathbf{r}_2, t_2)]^2 > + < [g'(\mathbf{r}_1, t_1) - g'(\mathbf{r}_2 + \mathbf{r}, t_2 + t)]^2 > \right. \\ & \left. - < [g'(\mathbf{r}_1 + \mathbf{r}, t_1 + t) - g'(\mathbf{r}_2 + \mathbf{r}, t_2 + t)]^2 > - < [g'(\mathbf{r}_1, t_1) - g'(\mathbf{r}_2, t_2)]^2 > \right), \end{aligned} \tag{2.6}$$

by making use of the identity, $(a-b)(c-d) = 1/2[(a-d)^2 + (b-c)^2 - (a-c)^2 - (b-d)^2]$. Thus the covariance of a stationary random process is expressed as a sum of structure functions,

$$\begin{aligned} C_G(\mathbf{r}_1, t_1, \mathbf{r}_2, t_2) = \frac{1}{2} \quad & (D_g(\mathbf{r}_1 + \mathbf{r}, t_1 + t, \mathbf{r}_2, t_2) + D_g(\mathbf{r}_1, t_1, \mathbf{r}_2 + \mathbf{r}, t_2 + t) \\ & - D_g(\mathbf{r}_1 + \mathbf{r}, t_1 + t, \mathbf{r}_2 + \mathbf{r}, t_2 + t) - D_g(\mathbf{r}_1, t_1, \mathbf{r}_2, t_2)) . \end{aligned} \tag{2.7}$$

The structure function can be used for stationary and non-stationary random processes. In order for $C_G(\mathbf{r}_1, t_1, \mathbf{r}_2, t_2)$ to depend on the differences $\boldsymbol{\rho} = \mathbf{r}_1 - \mathbf{r}_2$ and $\tau = t_1 - t_2$ it is necessary that each structure function depend on the differences in space and time. That is,

$$C_G(\boldsymbol{\rho}, \tau) = \frac{1}{2} D_g(\boldsymbol{\rho} + r, \tau + t) + \frac{1}{2} D_g(\boldsymbol{\rho} - r, \tau - t) - 2D_g(\boldsymbol{\rho}, \tau) \tag{2.8}$$

Thus the structure function characterizes the intensity of those inhomogeneities having periods of order τ or smaller and having scale sizes of order $\boldsymbol{\rho}$ or less. Essentially the structure function acts as a high pass filter. The spatial structure function is recovered from the space-time structure function by,

$$\mathcal{D}_g(\boldsymbol{\rho}) = D_g(\boldsymbol{\rho}, \tau = 0). \tag{2.9}$$

If $g'(\mathbf{r}, t)$ is a stationary isotropic random field, then the structure function can be expressed in terms of the covariance function,

$$D_g(\boldsymbol{\rho}, \tau) = 2C_g(0, 0) - 2C_g(\boldsymbol{\rho}, \tau). \tag{2.10}$$

2.3 Spectral functions

The three dimensional spatial spectral density, $\Phi_g(\mathbf{K})$ of a random process g is defined as the Fourier transform of its spatial covariance function (Arfken [1]),

$$\Phi_g(\mathbf{K}) = \frac{1}{(2\pi)^3} \int\int\int e^{-i\mathbf{K}\cdot\boldsymbol{\rho}} B_g(\boldsymbol{\rho}) d\boldsymbol{\rho}, \tag{2.11}$$

where $B_g(\boldsymbol{\rho})$ characterizes the statistical dependence between fluctuations spatially separated by $\boldsymbol{\rho}$. The spatial covariance function B_g and the spatial spectral density Φ_g are Fourier transform pairs so,

$$B_g(\boldsymbol{\rho}) = \int\int\int e^{i\mathbf{K}\cdot\boldsymbol{\rho}} \Phi_g(\mathbf{K}) d\mathbf{K}. \tag{2.12}$$

Assuming isotropy ($\Phi_g(\mathbf{K}) = \Phi_g(\kappa)$ and $B_g(\boldsymbol{\rho}) = B_g(\rho)$) and integrating both (2.11) and (2.12) over spherical coordinates ($d\boldsymbol{\rho} = \rho^2 \sin\theta d\rho d\theta d\phi$ and

$d\mathbf{K} = \kappa^2 \sin\theta d\kappa d\theta d\phi$) gives,

$$\Phi_g(\kappa) = \frac{1}{2\pi^2}\int_0^\infty \rho^2 B_g(\rho)\frac{\sin\kappa\rho}{\kappa\rho}d\rho, \tag{2.13}$$

and,

$$B_g(\rho) = 4\pi\int_0^\infty \kappa^2\Phi_g(\kappa)\frac{\sin\kappa\rho}{\kappa\rho}d\kappa. \tag{2.14}$$

These results are obtained by taking into account the even property of both the covariance function and the spectral density. The variance of the function g (σ_g^2) is then defined as,

$$B_g(0) = 4\pi\int_0^\infty \kappa^2\Phi_g(\kappa)d\kappa, \tag{2.15}$$

$$= 2\int_0^\infty \Phi_{3g}(\kappa)d\kappa, \tag{2.16}$$

where $\Phi_{3g}(\kappa) = 2\pi\kappa^2\Phi_g(\kappa)$ is an extension of the three-dimensional spectral density $\Phi_g(\kappa)$. The spatial structure function can also be expressed in terms of the spectral density,

$$\mathcal{D}_g(\rho) = 8\pi\int_0^\infty \kappa^2\Phi_g(\kappa)\left(1-\frac{\sin\kappa\rho}{\kappa\rho}\right)d\kappa. \tag{2.17}$$

In space, these spectrum functions will have a three-dimensional character. However, what can be measured is the one-dimensional spectrum (see Hinze [31]),

$$\Phi_{1g}(\kappa_1) = \frac{1}{2\pi}\int e^{-i\kappa_1 x}B_g(x)dx, \tag{2.18}$$

where the covariance function,

$$B_g(x) = \int e^{i\kappa_1 x}\Phi_{1g}(\kappa_1)d\kappa_1, \tag{2.19}$$

is measured along some straight line x in space. The Fourier transform relations are written in this way so that the definition of the variance,

$$2\int_0^\infty \Phi_{1g}(\kappa_1)d\kappa_1 = 2\int_0^\infty \Phi_{3g}(\kappa)d\kappa, \tag{2.20}$$

is consistent. Differentiating (2.18) with respect to κ_1 and using (2.13) together with the isotropy assumption gives,

$$\frac{\partial\Phi_{1g}(\kappa_1)}{\partial\kappa_1} = -2\pi\kappa_1\Phi_g(\kappa_1). \tag{2.21}$$

The angular frequency spectrum, $W_g(\omega)$ of a random process g is defined as the Fourier transform of its temporal covariance function (Arfken [1]),

$$W_g(\omega) = \frac{1}{2\pi} \int e^{-i\omega\tau} R_g(\tau) d\tau, \tag{2.22}$$

where $R_g(\tau)$ characterizes the statistical dependence between fluctuations temporally separated by τ. The temporal covariance function R_g and the temporal spectrum W_g are Fourier transform pairs so,

$$R_g(\tau) = \int e^{i\omega\tau} W_g(\omega) d\omega. \tag{2.23}$$

The variance is then defined as

$$R_g(0) = 2 \int_0^\infty W_g(\omega) d\omega. \tag{2.24}$$

The frequency spectrum is recovered from the angular frequency spectrum by

$$W_g(f) = 2\pi W_g(\omega = 2\pi f). \tag{2.25}$$

For three dimensional space and time varying random fields, the spectral density is,

$$\mathcal{U}_g(\mathbf{K}, \omega) = \frac{1}{(2\pi)^4} \int \int \int d\mathbf{r} \int d\tau \; C_g(\mathbf{r}, \tau) e^{-i(\mathbf{K}\cdot\mathbf{r} + \omega\tau)}. \tag{2.26}$$

The spatial (temporal) spectral density is recovered by integrating the 4D spectral density over all frequencies (wavenumbers). The three dimensional space-time cross covariance is then defined as the inverse Fourier transform,

$$C_g(\mathbf{r}, \tau) = \int \int \int d\mathbf{K} \int d\omega \; \mathcal{U}_g(\mathbf{K}, \omega) e^{i(\mathbf{K}\cdot\mathbf{r} + \omega\tau)}. \tag{2.27}$$

Chapter 3

Acoustic Propagation Through Random Media

The theory of wave propagation through random media (WPRM) is coupled closely to a detailed knowledge of the random medium. A statistical description of the refractive index fluctuations and the acoustic fluctuations is essential. The acoustic fluctuations considered are those that result from random inhomogeneities in the medium's refractive index. These inhomogeneities are produced when the medium characteristics (e.g. temperature, salinity or current velocity) deviate from their mean values. The term 'turbulence' is defined as this random process and can be caused by mixing, strong tidal flow or internal waves.

The refractive index fluctuations due to Kolmogorov's isotropic and homogeneous turbulence is described in terms of some of the statistical parameters described previously. Also included in this chapter is a discussion of the weak scattering theory of Tatarskii [51], [52] and the multiple scattering techniques of Uscinski [57] and Dashen [11] in describing acoustic fluctuations. The acoustic fluctuations are then described by statistical functions.

3.1 Turbulent Random Media

In classical turbulence theory, Kolmogorov hypothesized that for sufficiently high Reynolds number there exists an equilibrium range where the statistical properties for turbulent velocity fluctuations are determined by the turbulent kinetic energy dissipation ϵ and wavenumber κ. The energy enters the turbulence at large scales (the outer scale) and cascades to smaller and smaller scales until the velocity gradients become large enough for viscosity to dissipate the energy (the inner scale). The structure function of the velocity fluctuations is determined mainly by turbulent structures having sizes $r \simeq |\mathbf{r}_1 - \mathbf{r}_2|$. If these sizes are within the Kolmogorov inertial subrange bounded by the inner (ℓ_o) and outer (L_o) scale of turbulence (i.e. $\ell_o \ll r \ll L_o$) then the structure function becomes dependent on r and ϵ (see Tatarskii [52]). Dimensional analysis techniques lead to the following formula,

$$\left.\begin{array}{rcl} \mathcal{D}_{v_r}(r) & \propto & \epsilon^{2/3} r^{2/3} \\ & = & C_v^2 r^{2/3} \end{array}\right\} \qquad \ell_o \ll r \ll L_o, \tag{3.1}$$

where $\mathcal{D}_{v_r}(r) = < [v_r(\mathbf{r}_1+\mathbf{r}) - v_r(\mathbf{r}_1)]^2 >$ is the longitudinal component of the structure function tensor, the velocity v_r is the projection of the velocity $\mathbf{v}$ along the direction r and C_v^2 is called the structure constant for velocity fluctuations and represents the intensity of the turbulence. The longitudinal form is used since the transverse structure function $\mathcal{D}_{v_t}$ and the tensor can be determined by this function (see Tatarskii [51]).

The fluctuations of a passive scalar s (for example temperature and salinity) have statistical properties dependent on ϵ and $\mathcal{N}_s$ which is the rate of dissipation of $\frac{<s^2>}{2}$ taking into account diffusion. The structure function of scalar fluctuations is also determined mainly by structures having sizes $r \simeq |\mathbf{r}_1 - \mathbf{r}_2|$ and if these sizes are within the Kolmogorov inertial subrange ($\ell_o \ll r \ll L_o$) then the structure function becomes dependent on r, ϵ and $\mathcal{N}_s$ (see Tatarskii [52]). Dimensional analysis techniques lead

to the following formula,

$$\left.\begin{aligned} \mathcal{D}_s(r) &\propto \mathcal{N}_s \epsilon^{-1/3} r^{2/3} \\ &= C_s^2 r^{2/3} \end{aligned}\right\} \qquad \ell_o \ll r \ll L_o, \tag{3.2}$$

where C_s^2 is called the structure constant for scalar fluctuations and is a measure of the intensity of the fluctuations.

The refractive index (n) fluctuations are dependent on both scalar and velocity fluctuations. Following the development of Tatarskii [52] which assumes zero scattering angle between incident and scattered energy, the refractive index structure function can be written as,

$$\mathcal{D}_n(r) = \frac{\mathcal{D}_{v_r}(r)}{c_o^2} + \mathcal{D}_{n_s}(r), \tag{3.3}$$

where c_o is the wave speed and converts velocity fluctuations to refractive index fluctuations. The structure function for velocity fluctuations is dependent on ϵ and the structure function for scalar fluctuations is dependent on both ϵ and $\mathcal{N}_{n_s}$. Therefore,

$$\left.\begin{aligned} \mathcal{D}_n(r) &= (A\epsilon^{2/3} c_o^{-2} + B\mathcal{N}_{n_s}\epsilon^{-1/3}) r^{2/3} \\ &= (C_{n_v}^2 + C_{n_s}^2) r^{2/3} \\ &= C_n^2 r^{2/3} \end{aligned}\right\} \qquad \ell_o \ll r \ll L_o. \tag{3.4}$$

where the constants A and B are dimensionless proportionality constants. For electromagnetic wave propagation through the atmosphere, scalar fluctuations dominate over velocity fluctuations in producing refractive index fluctuations since the wave speeds are very much greater than the wind speeds (Ishimaru [32]). For acoustic propagation, however, both scalar and velocity fluctuations may affect the refractive index (Di Iorio and Farmer [18]).

The three-dimensional spectral density of the refractive index fluctuations, $\Phi_n(\kappa)$ can be expressed in terms of the refractive index structure function, $\mathcal{D}_n(r)$. Equation (2.17) must be inverted in order to obtain $\Phi_n(\kappa)$ in terms of $\mathcal{D}_n(r)$ (see Clifford [7]). The mathematical steps have been eliminated, but it is easy to show that,

$$\Phi_n(\kappa) = \frac{1}{4\pi^2\kappa^2} \int_0^\infty \frac{\sin \kappa r}{\kappa r} \frac{d}{dr}\left[r^2 \frac{d}{dr}\mathcal{D}_n(r)\right] dr. \tag{3.5}$$

Inserting the structure function formula (3.4) and carrying out the indicated operations, one obtains,

$$\Phi_n(\kappa) = \frac{5}{18\pi^2} C_n^2 \kappa^{-3} \int_{\ell_o}^{L_o} r^{-1/3} \sin(\kappa r) dr. \tag{3.6}$$

At scale sizes ℓ_o and smaller (typical sizes less than 1 cm in coastal waters), viscosity and diffusion effects dominate to dissipate the turbulent kinetic energy and the refractive index inhomogeneities respectively. Thus, it can be assumed that the contribution to the spectral density, at these scales, is negligible. At scale sizes L_o and larger the energy is presumed to be introduced into the turbulence. Both the channel dimensions and the stratification are expected to put bounds on the outer scale limit. For scales beyond L_o, statistical isotropy and homogeneity cannot be assumed. To obtain an analytical expression for the spectral density we let the limits on the integral go from 0 to ∞ giving,

$$\Phi_n(\kappa) = 0.033 C_n^2 \kappa^{-11/3}, \tag{3.7}$$

where the constant 0.033 takes into account factors of π and the constant of integration. The wavenumber κ theoretically ranges from 0 to ∞ but physically,
$2\pi/L_o \ll \kappa \ll 2\pi/\ell_o$.

The mean current $\mathbf{U}$ produces time changes by transporting spatial variations of the refractive index past the point of observation. Under Taylor's hypothesis these spatial variations are frozen as they are advected past the observation area, that is, the translation is not accompanied by any mixing. This assumption implies that the three dimensional wavenumber - frequency spectrum for refractive index fluctuations is (see Tatarskii [52]),

$$\mathcal{U}_n(\mathbf{K}, \omega) = \Phi_n(\mathbf{K}) \delta(\omega + \mathbf{K} \cdot \mathbf{U}). \tag{3.8}$$

3.2 Acoustic Propagation

3.2.1 Acoustic fluctuations

When waves propagate through random media they are distorted by a number of mechanisms. Three such mechanisms are absorption, refraction and diffraction. Absorption attenuates the signal and will be ignored since it is the fluctuations due to the random medium that are of interest. Refraction causes phase fluctuations since sound velocity changes as a ray passes through regions of different refractive index variations. Refractive index inhomogeneities due to turbulence act as lenses and so because of refraction, lenses will focus or defocus incident rays thus causing amplitude fluctuations. Diffraction (scattering) takes into account the Huygens-Fresnel principle which states that every point on the wavefront becomes a source of spherical secondary wavelets. Random scattering due to random fluctuations in the refractive index causes amplitude (and phase) fluctuations because the received signal is a superposition of all the wavelets (see Chernov [5]).

If diffraction effects are negligible, then Chernov [5] and Tatarskii [51] used pure ray theory to find expressions for the phase and amplitude fluctuations. However, if diffraction effects are important, then random scattering of acoustic signals plays a role in the observed amplitude (and phase) fluctuations. Strohbehn [50] makes an excellent comparison between the approximations used for ray theory and scattering theory, some of which will be described below.

Consider Figure 3.1, where a turbulent lens of refractive index (S) with size ℓ (having any distribution) is centrally located between a transmitter (T) and receiver (R). According to optical theory, the scattered path TSR should differ from the ray path TR by integral multiples of one-half wavelength in order for there to be destructive interference at R. Using the simple geometry, it is easy to show that

$$\ell = \sqrt{\lambda L}, \tag{3.9}$$

where λ is the acoustic wavelength and L is the separation between the transmitter

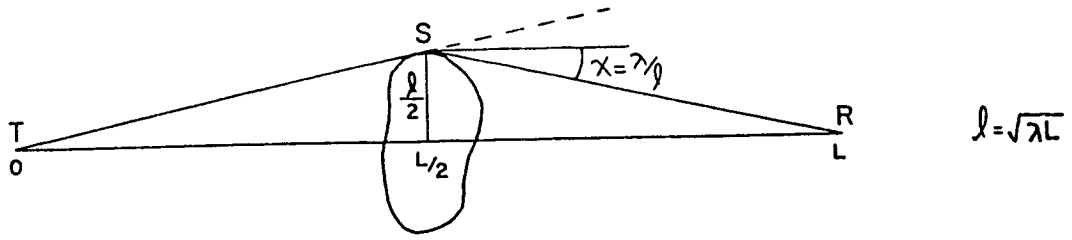

Figure 3.1: Diagram to show the scale size which produces destructive interference at the receiving plane (L). This size is known as the radius of the first Fresnel zone.

and the receiver. This equation defines the radius of the first Fresnel zone and the radius of the m^{th} zone is $\sqrt{m\lambda L}$.

The conditions for geometrical optics are (1) $\lambda \ll \ell_o$ and (2) $\sqrt{\lambda L} \ll \ell_o$ where ℓ_o is the scale of smallest inhomogeneities. The first condition is well known and is described by the *geometrical optics* regime. The second condition is explained by Tatarskii [53] and arises by considering the following. The shadow of some body at the receiving plane will be similar to the object if its diffractional spreading is small in comparison with the scale of the body ($\ell \gg \sqrt{\lambda L}$). Hence focusing or defocusing of the lenses is important. If the scale of the body is much less than the diffractional spreading scale ($\ell \ll \sqrt{\lambda L}$), then diffraction becomes more important than focussing or defocussing. This means that lenses with a diameter less than the Fresnel scale cannot focus or defocus the beam. Thus, the smallest lenses that can do this are lenses with a scale size $\sqrt{\lambda L}$.

For our experiment in Cordova Channel where turbulent structures exists, the Fresnel scale $\sqrt{\lambda L} = 3.8\ m$. For this environment, it cannot be assumed that ℓ_o is greater than $\sqrt{\lambda L}$. Thus, diffractional spreading from scale sizes smaller than the Fresnel scale must be taken into account. The inner scale of turbulence for Cordova Channel is expected to be less than 1 cm.

Another important parameter to consider in the theory of wave propagation through random media is the focal point of the turbulent lens. The focal point is defined as $F = R/\Delta n$ where $R = \ell/2$ is the radius of the turbulent lens and Δn is

the change in the refractive index between the surrounding medium and the lens. For example, in coastal waters $\Delta n \sim 5 \times 10^{-5}$ and $R \sim 2\ m$ (for Fresnel scale structures) thus defining the focal length to be $\sim 40\ km$. Therefore, the receiving plane is always much less than the focal length of the turbulent eddy ($L \ll F$).

Γ and X parameters

Acoustic propagation experiments are often described in terms of two parameters (see, for example, Uscinski *et.al.* [59] and Ewart *et.al.* [21]),

$$\Gamma = k^3 < \eta^2 > L_V^2 L_p, \tag{3.10}$$

and

$$X = \frac{L}{kL_V^2} = \frac{1}{2\pi}\left(\frac{\sqrt{\lambda L}}{L_V}\right)^2. \tag{3.11}$$

These parameters serve to characterize the acoustic scattering regime. The scattering strength of the medium is denoted by Γ (high values indicate that multiple scattering will occur and hence cause large intensity fluctuations). It takes into account the variance of the refractive index fluctuations $< \eta^2 >$, a vertical correlation length scale L_V, and the integral correlation length,

$$L_p = \int_0^L B_\eta(y)dy \tag{3.12}$$

defined as the integral of the refractive index auto covariance function taken along the propagation path. Uscinski *et.al.* [59] defines kL_V^2 as the 'Fresnel length' and the propagation range L scaled by this length gives the parameter X. The product,

$$\Gamma X = k^2 < \eta^2 > L_p L =< \phi^2 >, \tag{3.13}$$

is the variance of the phase fluctuations due to the random medium and provides a way to obtain measurements of L_p.

3.2.2 Weak scattering theory

The Helmholtz equation for the sound pressure $p(\mathbf{r})$ is,

$$\nabla^2 p(\mathbf{r}) + k^2 n(\mathbf{r})^2 p(\mathbf{r}) = 0, \tag{3.14}$$

where k is the acoustic wavenumber and $n(\mathbf{r}) = c_o/c(\mathbf{r})$ is the refractive index of the medium. There are two methods described by Chernov [5] and Tatarskii [51], [52] for solving this equation. Both these methods include the effect of diffraction. The first method, called the Born approximation (the method of small perturbations) assumes that the logarithmic amplitude and phase fluctuations are small (i.e. χ and $\phi \ll 1$). Rytov's method (the method of smooth perturbations) relaxed this restriction by assuming that the gradients of the log-amplitude and phase fluctuations are small (i.e. $\nabla\chi$ and $\nabla\phi \ll 1$) in the transformed equation,

$$\nabla^2 \Psi(\mathbf{r}) + \nabla\Psi(\mathbf{r}) \cdot \nabla\Psi(\mathbf{r}) + k^2 n(\mathbf{r})^2 = 0, \tag{3.15}$$

where $\Psi = \ln p$. Since the refractive index is a random function of space (and time), (3.15) can only be solved by approximate methods.

If it is assumed that the fluctuations in the parameters are small then perturbation techniques can be applied,

$$\begin{aligned} n(\mathbf{r}) &= n_o + \nu\eta(\mathbf{r}) \\ \Psi(\mathbf{r}) &= \Psi_o(\mathbf{r}) + \nu\Psi_1(\mathbf{r}) + \nu^2\Psi_2(\mathbf{r}) + ..., \end{aligned} \tag{3.16}$$

where ν is a dummy variable which shows the order of smallness for the various terms. Substituting equations (3.16) into (3.15) and then equating equal powers of ν gives the following set of equations,

$$\begin{aligned} \nabla^2\Psi_o + \nabla\Psi_o \cdot \nabla\Psi_o &= -k^2 n_o^2, \\ \nabla^2\Psi_1 + 2(\nabla\Psi_o \cdot \nabla\Psi_1) &= -2k^2 n_o \eta, \\ \nabla^2\Psi_2 + 2(\nabla\Psi_o \cdot \nabla\Psi_2) &= -\nabla\Psi_1 \cdot \nabla\Psi_1 - k^2\eta^2. \end{aligned} \tag{3.17}$$

The first equation of (3.17) can be solved exactly since it corresponds to wave propagation in a medium without any fluctuations (for spherical waves and $n_o = 1$, $\Psi_o = \ln Q/r + ikr$ where Q is constant). The second equation in this set has the solution (see Tatarskii [52]) for forward scattered waves,

$$\Psi_1(\mathbf{r}) = \frac{1}{4\pi}\int_{V'} \frac{e^{ik|\mathbf{r}-\mathbf{r}'|}}{|\mathbf{r}-\mathbf{r}'|} e^{\Psi_o(\mathbf{r}')-\Psi_o(\mathbf{r})} 2k^2 n_o \eta(\mathbf{r}')d\mathbf{r}', \tag{3.18}$$

where integration is over the scattering volume V'. Recall $\Psi_o = \ln p_o$ and for spherical waves $p_o(r) = Qe^{ikr}/r$, thus (3.18) becomes,

$$\Psi_1(\mathbf{r}) = \frac{k^2}{2\pi}\int_{V'} \frac{e^{ik|\mathbf{r}-\mathbf{r}'|}}{|\mathbf{r}-\mathbf{r}'|} \frac{re^{-ik(r-r')}}{r'} \eta(\mathbf{r}')d\mathbf{r}', \tag{3.19}$$

where $r = |\mathbf{r}|$, $r' = |\mathbf{r}'|$ and we have made the assumption that $n_o = 1$. The single scattering theory neglects the higher order terms (Ψ_2 etc.) so that the third and higher equations in the set (3.17) are neglected provided that $\nabla\Psi_1 \ll \nabla\Psi_0$.

It is the amplitude and phase fluctuations that are of interest, so if $p = Ae^{iS}$ then $\Psi = \ln A + iS = \Psi_o + \Psi_1$. Thus, $\Psi_1 = \ln \frac{A}{A_o} + i(S - S_o) = \chi + i\phi$. The logarithmic amplitude and phase fluctuations at the location $\mathbf{r}$ are given by the real and imaginary parts of (3.19).

Covariance functions

The space-time cross covariance of log-amplitude and phase in the two dimensional receiving plane $\boldsymbol{\rho} = (x, z)$ for spherically spreading waves is (see Farmer and Clifford [23]),

$$C_{\substack{\chi \\ \phi}}(\boldsymbol{\rho},\tau) = \left\langle \begin{array}{c} \chi'(\mathbf{r},t)\chi'(\mathbf{r}+\boldsymbol{\rho},t+\tau) \\ \phi'(\mathbf{r},t)\phi'(\mathbf{r}+\boldsymbol{\rho},t+\tau) \end{array} \right\rangle, \tag{3.20}$$

$$= \int d\mathbf{K}\int d\omega\, \mathcal{U}_2 \begin{matrix}\chi \\ \phi\end{matrix}(\mathbf{K},\omega) e^{i(\mathbf{K}\cdot\boldsymbol{\varrho}+\omega\tau)} \tag{3.21}$$

$$= \int d\mathbf{K}\int d\omega\, 2\pi k^2 \int_0^L dy\, \mathcal{U}_n(\mathbf{K},\omega) \begin{matrix}\sin^2 \\ \cos^2\end{matrix}\left(\frac{K^2 y(L-y)}{2kL}\right), \tag{3.22}$$

$$e^{i(\mathbf{K}\cdot\boldsymbol{\varrho}+\omega\tau)}$$

where $\chi' = \chi - <\chi>$, $\phi' = \phi - <\phi>$, $\boldsymbol{\varrho} = \boldsymbol{\rho}$ for two sources and two receivers (parallel paths), $\boldsymbol{\varrho} = \boldsymbol{\rho} y/L$ for a single source and two receivers (diverging paths), k is the acoustic wavenumber and $\mathcal{U}_2$ is the two dimensional space-time spectral density for log-amplitude or phase. Integration is over the acoustic path y, over the two-dimensional wavenumber space $\mathbf{K} = (K_x, 0, K_z)$ and over frequency space ω.

Lee and Harp [36] describe each of the terms as follows: $\mathcal{U}_n(\mathbf{K}, \omega)$ defined by (3.8) is the three dimensional space-time spectral density for refractive index fluctuations evaluated at $K_y = 0$ and is the input to the scattering process; the $\sin^2$ or $\cos^2$ term takes into account diffraction effects, and hence measures the scattering efficiency of the refractive index perturbation having wavenumber $\mathbf{K}$ at a given position y along the path; the exponential function relates the perturbations present at one point and time in the receiving plane to those at another point and time.

Integration of (3.22) over frequency for the case of advection of refractive index variations by the mean flow gives,

$$C \begin{matrix} \chi \\ \phi \end{matrix} (\boldsymbol{\rho}, \tau) = 2\pi k^2 \int_0^L dy \int d\mathbf{K} \Phi_n(\mathbf{K}) e^{i\mathbf{K}\cdot(\boldsymbol{\varrho} - \mathbf{U}(y)\tau)} \begin{matrix} \sin^2 \\ \cos^2 \end{matrix} \left(\frac{K^2 y(L-y)}{2kL} \right). \quad (3.23)$$

Assuming the current flow is uniform across the channel, and the refractive index fluctuations are isotropic in the plane perpendicular to the direction of acoustic propagation, integration of this function over the two dimensional wave-number space ($d\mathbf{K} = dK_x dK_z = \kappa d\kappa d\theta$) gives,

$$C \begin{matrix} \chi \\ \phi \end{matrix} (\boldsymbol{\rho}, \tau) = 4\pi^2 k^2 \int_0^L dy \int_0^\infty d\kappa \kappa \Phi_n(\kappa) J_o(\kappa A) \begin{matrix} \sin^2 \\ \cos^2 \end{matrix} \left(\frac{\kappa^2 y(L-y)}{2kL} \right), \quad (3.24)$$

where $J_o(\kappa A)$ is the zero order Bessel function, with

$$A = \begin{cases} |\boldsymbol{\varrho}_x - \mathbf{U}\tau| & \text{horizontally spaced receivers} \\ \sqrt{\varrho_z^2 + (U\tau)^2} & \text{vertically spaced receivers} \\ \sqrt{(\varrho_x - U\tau)^2 + \varrho_z^2} & \text{diagonally spaced receivers} \end{cases} . \quad (3.25)$$

The log-amplitude χ excludes contributions from larger scale variability since the $\sin^2$ term $\rightarrow \kappa^4$ as $\kappa \rightarrow 0$, whereas observations of the phase ϕ include contributions

from the largest scales since the $\cos^2$ term $\rightarrow 1$ as $\kappa \rightarrow 0$. The spectral density Φ_n behaves as $\kappa^{-11/3}$ in the inertial subrange so this means the log-amplitude cross covariance integrand $\rightarrow \kappa^{4/3}$ which remains finite as $\kappa \rightarrow 0$ and the integral exists; the phase cross covariance integrand $\rightarrow \kappa^{-8/3}$ which becomes infinite as $\kappa \rightarrow 0$ and the integral does not exist without defining an outer scale limit.

Since the phase measurement has temporal variability associated with large scale changes in the temperature and current velocity field, the phase difference between two receivers is taken so as to eliminate the effects from large scale inhomogeneities that are common to each measurement. Thus the temporal auto covariance for the phase difference ($\delta\phi'(\boldsymbol{\rho},t) = \phi'(\mathbf{r},t) - \phi'(\mathbf{r}+\boldsymbol{\rho},t)$) is defined as (see Clifford [6]),

$$\begin{aligned} R_{\delta\phi}(\tau) &= <\delta\phi'(\boldsymbol{\rho},t)\delta\phi'(\boldsymbol{\rho},t+\tau)>, & (3.26)\\ &= 2R_\phi(\tau) - C_\phi(\boldsymbol{\rho},\tau) - C_\phi(-\boldsymbol{\rho},\tau), & (3.27)\\ &= 4\pi^2k^2\int_0^L dy\int_0^\infty d\kappa\kappa\Phi_n(\kappa)\cos^2\left(\frac{\kappa^2 y(L-y)}{2kL}\right) \\ &\qquad [2J_0(\kappa U\tau) - J_0(\kappa A(\boldsymbol{\rho})) - J_0(\kappa A(-\boldsymbol{\rho}))], & (3.28) \end{aligned}$$

where $\phi' = \phi - <\phi>$ denotes a zero mean random variable. As $\kappa \rightarrow 0$ the Bessel function term $\rightarrow \kappa^2$ and thus the integrand $\rightarrow \kappa^{-2/3}$. Even though the integrand is not defined at the origin the integral still exists.

Structure functions

In addition to the cross covariance functions defined by (3.24), the structure function, defined by (2.10), can be used,

$$\begin{aligned} D_{\phi}^{\chi}(\boldsymbol{\rho},\tau) &= \left\langle \begin{array}{c} (\chi'(\mathbf{r},t) - \chi'(\mathbf{r}+\boldsymbol{\rho},t+\tau))^2 \\ (\phi'(\mathbf{r},t) - \phi'(\mathbf{r}+\boldsymbol{\rho},t+\tau))^2 \end{array} \right\rangle, \\ &= 8\pi^2k^2\int_0^L dy\int_0^\infty d\kappa\kappa\Phi_n(\kappa)(1-J_o(\kappa A)) \begin{matrix}\sin^2\\ \cos^2\end{matrix}\left(\frac{\kappa^2 y(L-y)}{2kL}\right) \quad (3.29) \end{aligned}$$

where all parameters and $'$ notation are described previously. As $\kappa \rightarrow 0$ the integrand for the log-amplitude structure function $\rightarrow \kappa^{10/3}$ and hence the function exists. The

phase structure function $\rightarrow \kappa^{-2/3}$ and thus the integral also exists. Hence, there is no need to specify an outer scale limit like there is for the phase cross covariance. For this reason the phase structure function is often used in turbulence study.

The wave structure function is given as,

$$\begin{aligned} D(\boldsymbol{\rho},\tau) &= D_\chi(\boldsymbol{\rho},\tau) + D_\phi(\boldsymbol{\rho},\tau) && (3.30)\\ &= 8\pi^2 k^2 \int_0^L dy \int_0^\infty d\kappa \kappa \Phi_n(\kappa)(1 - J_o(\kappa A)). && (3.31) \end{aligned}$$

This function is independent of the Fresnel scale $\sqrt{\lambda L}$ which arises in the $\sin^2$ and $\cos^2$ terms. This function also $\rightarrow \kappa^{-2/3}$ as $\kappa \rightarrow 0$ and hence the integral exists.

For Gaussian log-amplitude and phase difference statistics the mutual coherence function (MCF) of the fluctuating acoustic wave field ($p_1 = e^{\Psi_1} = \frac{A}{<A>} e^{i\phi}$) is expressed in terms of the wave structure function,

$$\begin{aligned} MCF(\boldsymbol{\rho},\tau) &= \frac{< p_1(\mathbf{r},t) p_1^*(\mathbf{r}+\boldsymbol{\rho}, t+\tau) >}{\sqrt{< p_1^2(\mathbf{r},t) >< p_1^2(\mathbf{r}+\boldsymbol{\rho}, t+\tau) >}} \\ &= \exp\left(-\frac{1}{2} D(\boldsymbol{\rho},\tau)\right). && (3.32) \end{aligned}$$

The mutual coherence function is also defined by Uscinski [57] as the second moment (m^{II}). Dashen *et.al.* [12] have shown that (3.32) is also true in the multiple scattering regime provided that the wave structure function is stationary in the receiving plane.

Spectral functions

The temporal frequency spectrum (2.22) for log-amplitude and phase is shown to be (see Clifford [6]),

$$W \begin{matrix} \chi \\ \phi \end{matrix} (f) = 8\pi^2 k^2 \int_0^L dy \int_{\kappa > \frac{2\pi f}{U}}^\infty d\kappa \frac{\kappa \Phi_n(\kappa)}{((\kappa U)^2 - (2\pi f)^2)^{1/2}} \begin{matrix} \sin^2 \\ \cos^2 \end{matrix} \left(\frac{\kappa^2 y(L-y)}{2kL}\right), \quad (3.33)$$

since

$$\int_{-\infty}^\infty e^{-i2\pi f\tau} J_0(\kappa U \tau) d\tau = \begin{cases} \frac{2}{((\kappa U)^2 - (2\pi f)^2)^{1/2}} & \kappa > \frac{2\pi f}{U} \\ 0 & \text{otherwise} \end{cases}. \quad (3.34)$$

Following the method of Clifford [6], the temporal frequency spectrum for the phase difference using horizontally spaced receivers (i.e. for ϱ_x parallel to U) is,

$$W_{\delta\phi_x}(f) = 32\pi^2 k^2 \int_0^L dy \int_{\kappa > \frac{2\pi f}{U}}^{\infty} d\kappa \frac{\kappa \Phi_n(\kappa)}{((\kappa U)^2 - (2\pi f)^2)^{1/2}} \sin^2\left(\frac{\varrho_x}{2U} 2\pi f\right) \cos^2\left(\frac{\kappa^2 y(L-y)}{2kL}\right), \tag{3.35}$$

since,

$$\int_{-\infty}^{\infty} e^{-i2\pi f\tau} \left[2J_0(\kappa U\tau) - J_0(\kappa|\boldsymbol{\varrho}_x - \mathbf{U}\tau|) - J_0(\kappa|\boldsymbol{\varrho}_x + \mathbf{U}\tau|)\right] d\tau = \begin{cases} \frac{8}{((\kappa U)^2 - (2\pi f)^2)^{1/2}} \sin^2\left(\frac{\pi f \varrho_x}{U}\right) & \kappa > \frac{2\pi f}{U} \\ 0 & \text{otherwise} \end{cases}. \tag{3.36}$$

Appendix A lists some of the relevant Bessel identities which are used to derive this result.

For parallel paths $\varrho_x = \rho_x$ and there are nulls in the spectrum corresponding to the zeros of the $\sin^2$ term since it is independent of the variables of integration. These zeros occur at frequencies $f = nU/\rho_x$ for $n = 0, 1, 2....$ Experimentally, these zeros will not be observed because of the fluctuations in U. For diverging paths $\varrho_x = \rho_x y/L$ and there are no zeros since the $\sin^2$ term is dependent on the variable of integration along the path.

Using vertically spaced receivers we can proceed in a similar way by making use of some Bessel identities described by Watson [61] and summarized in Appendix A. The resulting phase difference spectrum for vertically spaced receivers (i.e. for ϱ_z perpendicular to U) is then,

$$W_{\delta\phi_z}(f) = 32\pi^2 k^2 \int_0^L dy \int_{\kappa > \frac{2\pi f}{U}}^{\infty} d\kappa \frac{\kappa \Phi_n(\kappa)}{((\kappa U)^2 - (2\pi f)^2)^{1/2}} \sin^2\left(\frac{\varrho_z}{2U}((\kappa U)^2 - (2\pi f)^2)^{1/2}\right) \cos^2\left(\frac{\kappa^2 y(L-y)}{2kL}\right), \tag{3.37}$$

since,

$$\int_{-\infty}^{\infty} e^{-i2\pi f\tau}\left[2J_0(\kappa U\tau) - 2J_0(\kappa\sqrt{\varrho_z^2 + (U\tau)^2})\right] d\tau$$

$$= \begin{cases} \frac{8}{((\kappa U)^2-(2\pi f)^2)^{1/2}} \sin^2\left(\frac{\varrho_z}{2U}((\kappa U)^2 - (2\pi f)^2)^{1/2}\right) & \kappa > \frac{2\pi f}{U} \\ 0 & \text{otherwise} \end{cases} . \qquad (3.38)$$

Appendix A gives a short derivation of this result. The difference between (3.35) and (3.37) lies in the $\sin^2$ term.

3.2.3 Multiple scattering theory

For strong amplitude fluctuations, Rytov's method breaks down. For this reason a number of other techniques have been developed. Uscinski [57] developed a technique where he derives a propagation equation for the mutual coherence function, m^{II} (3.32) from the Helmholtz equation. Since this technique does not give amplitude and phase cross covariances he developed a propagation equation for the normalized cross correlation of intensity. He called this the fourth moment (m^{IV}) approach. Full solutions to these equations were then found.

Another technique for dealing with multiple scatter was developed by Dashen [11]. He solves the parabolic wave equation,

$$\left(2ik\frac{\partial}{\partial y} + \frac{\partial^2}{\partial x^2} + \frac{\partial^2}{\partial z^2} + k^2(n^2(\mathbf{r},t) - 1)\right) A(\mathbf{r},t) = 0, \qquad (3.39)$$

using Feynman's path integral technique, which is widely used in quantum mechanics and statistical mechanics. This equation originates from the Helmholtz equation where the pressure field p is expressed in terms of an envelope function A and in terms of the propagation direction y. That is $p(\mathbf{r},t) = A(\mathbf{r},t)\exp(iky)$. The time dependence is due to the refractive index fluctuations in the medium. From this solution, Dashen [11] then determines the second and fourth moments.

Chapter 4

Acoustic Instrumentation

The first generation (1982) acoustic scintillation system is described by Clifford and Farmer [8]. A 215 kHz source and two receivers were suspended by rigid masts mounted on opposite sides of a barge such that the axis of propagation was perpendicular to the direction of travel, and the flow rate was equal to the barge velocity. The second generation (1984) system is described by Farmer *et.al.* [24] where measurements were made in Cordova Channel with one 86 kHz source and two receivers. The third generation (1986) is described in this chapter.

4.1 Cordova Channel

The acoustic system is divided into two sections: a transmitting side (remote) and a receiving side (base). Figure 4.1 shows the geometrical configuration for both the square and linear array scintillation system used in Cordova Channel. The linear array had 0.61 m separation between transducers and the square array had 1.0 m separation. Communication between the base and the remote is via UHF radio. To define operation of the transmitter, parameters such as carrier frequency, pulse length, coded/uncoded operation, cycling mode and power level are sent from the base to the remote over the radio.

The acoustic signal for scintillation analysis must travel over wholly refracted

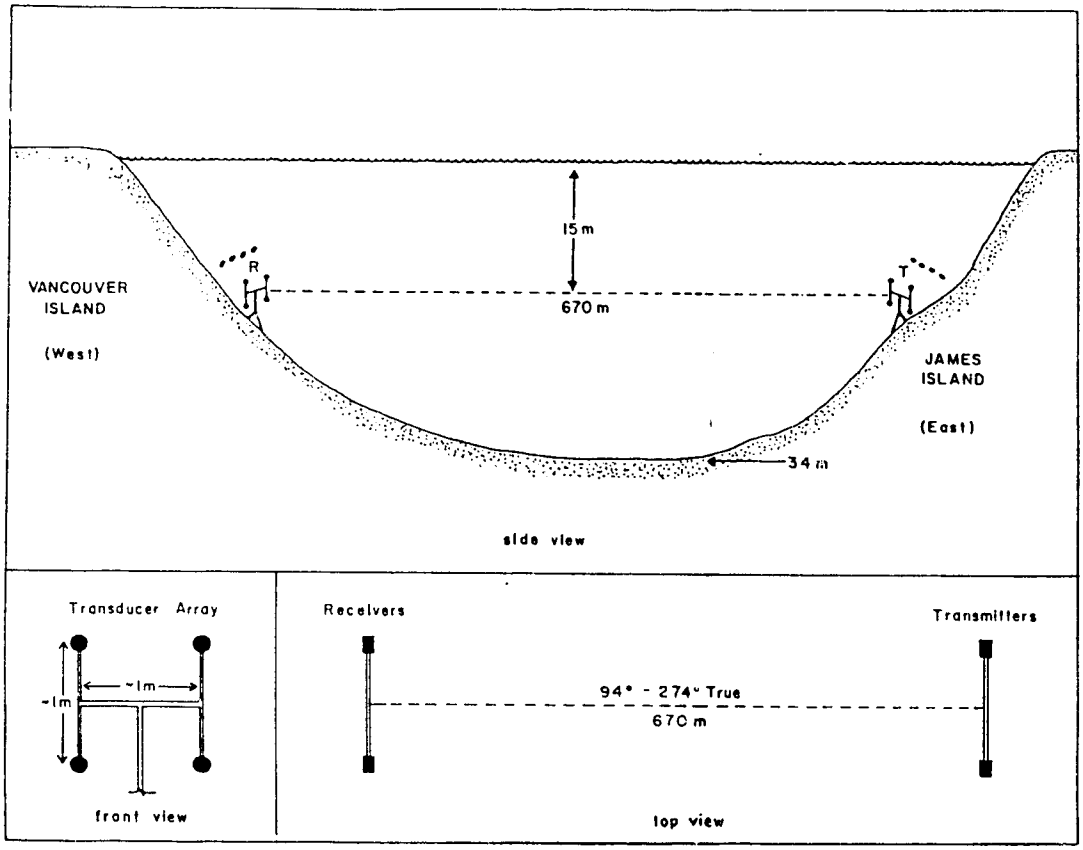

Figure 4.1: Deployment scheme for the square and linear acoustic array in Cordova Channel. Linear array has 0.61 m separation between transducers.

paths without reflection from the surface or bottom. In Cordova Channel the time difference between a surface or a bottom reflected path and a direct path is at least $500\mu s$. Separation of the direct path signal requires an effective pulse width of less than $250\mu s$ imposing a bandwidth requirement of at least 4 kHz. This is a severe constraint to impose on the pulse width. In order to maintain a good signal to noise ratio (SNR), phase modulated pseudo-random noise (PRN) coding was applied to an acoustic carrier frequency (see Farmer and Clifford [23] and Lemon *et.al.* [38]) having center frequency 67 kHz and bandwidth 6.8 kHz at -3 dB. The bit width was chosen to be less than 222 μs. Coded signals have the advantage of increasing the system's signal-to-noise ratio (SNR) and improving the phase measurement. Table 4.1 lists the relevant acoustic parameters for the scintillation system during the linear

Parameter	Linear Array	Square Array	
Array depth (m)	15	15	
Path length L (m)	670	670	
Receiver separation (m)	$\rho_x = 0.61, 1.22, 1.83$	$\rho_x = 1.18$, $\rho_z = 1.03$	
Cycling mode	continuous	block	continuous
Observation period	21/10/86 18:00	23/10/86 12:00	24/10/86 00:00
(PDT)	23/10/86 10:00	24/10/86 00:00	24/10/86/12:30

Parameter	continuous mode	block mode
Acoustic frequency f_a (Hz)	67567	69444
Acoustic wavenumber k (m^{-1})	285.89	293.82
Fresnel radius $\sqrt{\lambda L}$ (m)	3.87	3.79
Code length ($bits$ (ms))	63 (14)	63 (11)
Bit width ($cycles/bit$ (μs))	15 (222)	12 (173)
Phase shift for coding (deg)	180	180
Digitization rate ($samples/bit$ (kHz))	3 (13.5)	3 (17.4)
Window size ($samples$ (ms))	11 (0.814)	21 (1.211)
Repetition rate (Hz)	17.875	5.251

Table 4.1: Acoustic parameters for Cordova Channel scintillation experiment.

and square array deployments.

A 63 bit code is generated using a 6-bit shift register and then the transmitters are fired consecutively (defining a transmission) either in continuous or block mode (block mode gives a time break between the fourth and the first transmitter whereas continuous mode has no time break). In block mode the T1/R1 pair is easily obtained because of this break, whereas in continuous mode the last cycle of the code on alternating transmissions was dropped in order to determine the T1/R1 pair. This produced a time of arrival difference of 0.2 samples (14.8 μs) on alternating trans-

missions.

Incoming signals were filtered with bandpass 20.5 kHz at -3 dB, amplified and then separated into in-phase ($\mathcal{I}$) and quadrature ($\mathcal{Q}$) components. Each were then low passed filtered to remove the carrier so that the components were reduced to the PRN code. The in-phase and quadrature components were then digitized and correlated with a template of the transmitted code. The correlator output is linearly related to the signal voltage. Data flow through the system is limited by the real-time correlator. This in turn imposes constraints on the combinations of repetition (or transmission) rate, bit width and digitization rate which are allowed.

The correlation score shows a series of peaks with each peak corresponding to a different signal path. The width of the peak at the base is 2 bits (6 samples) and the height of the peak for a 6-bit shift register is proportional to $2^6 - 1$ (63 bits). The direct path signal is the first arrival and any peaks following are the surface or bottom reflected paths. Figure 4.2 shows the in-phase and quadrature components, and the amplitude and phase calculated as a function of arrival time (21 samples = 1.211 ms) for a given receiver listening to all four transmitters. Windowing of the data minimized data storage.

In order to increase the SNR, guard sequences are used to suppress the side lobes of the correlation. Side lobes occur for a duration of $2^6 - 2$ bits and have peak amplitudes less than $\sqrt{2^6 - 1}$ (see Menemenlis [40]). In continuous mode operation the side lobes of the correlation peak for a particular transmitter (T_i) and receiver (R_j) are suppressed since the T_{i-1}/R_j and the T_{i+1}/R_j transmission act as guard sequences. In block mode, however, the transmission cycles as T_1, T_1, T_2, T_3, T_4, T_4.

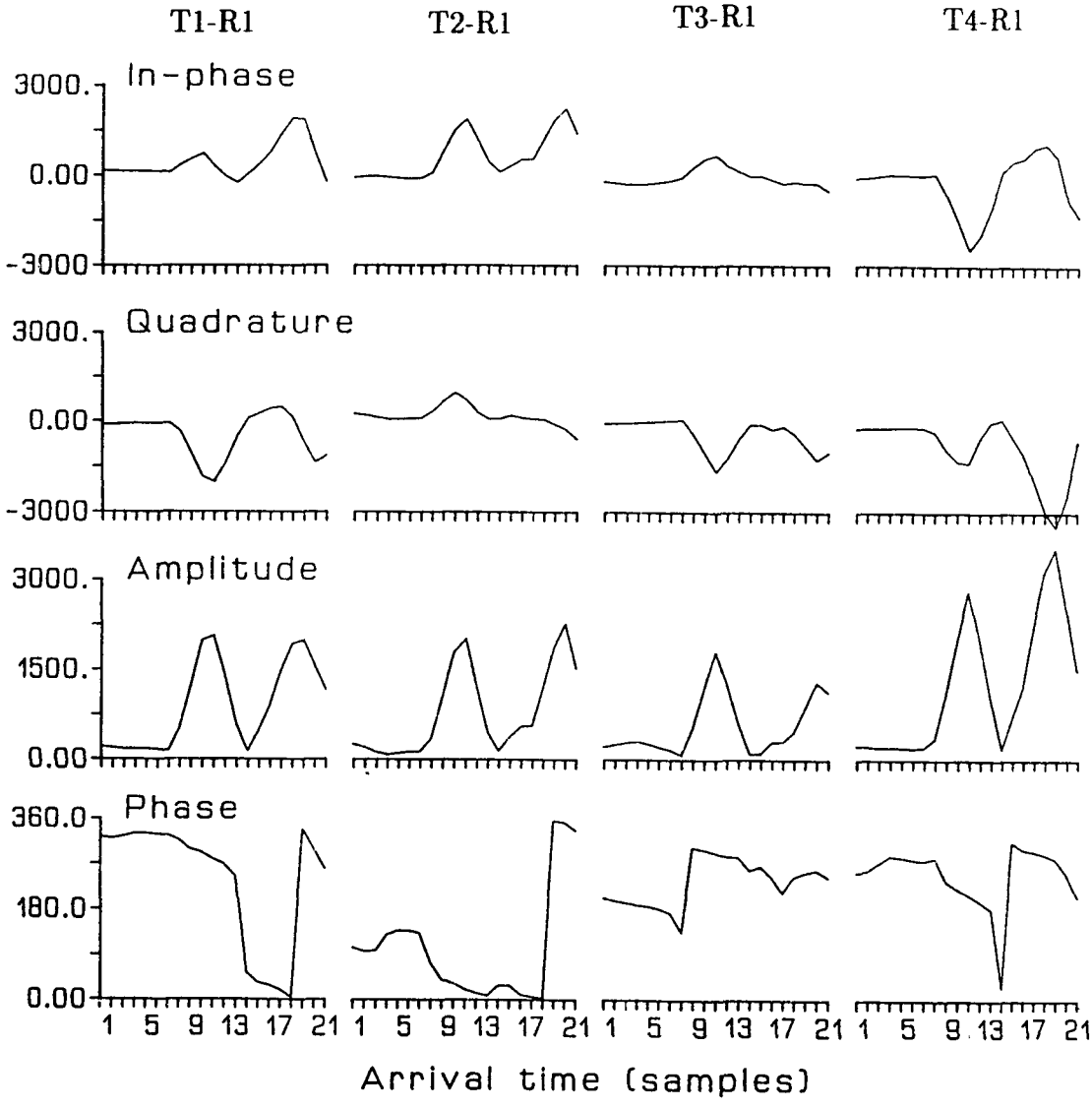

Figure 4.2: The in-phase and quadrature components giving the amplitude and phase as a function of arrival time (in samples) for a given receiver listening to four transmitters (21 samples = 1.211 ms).

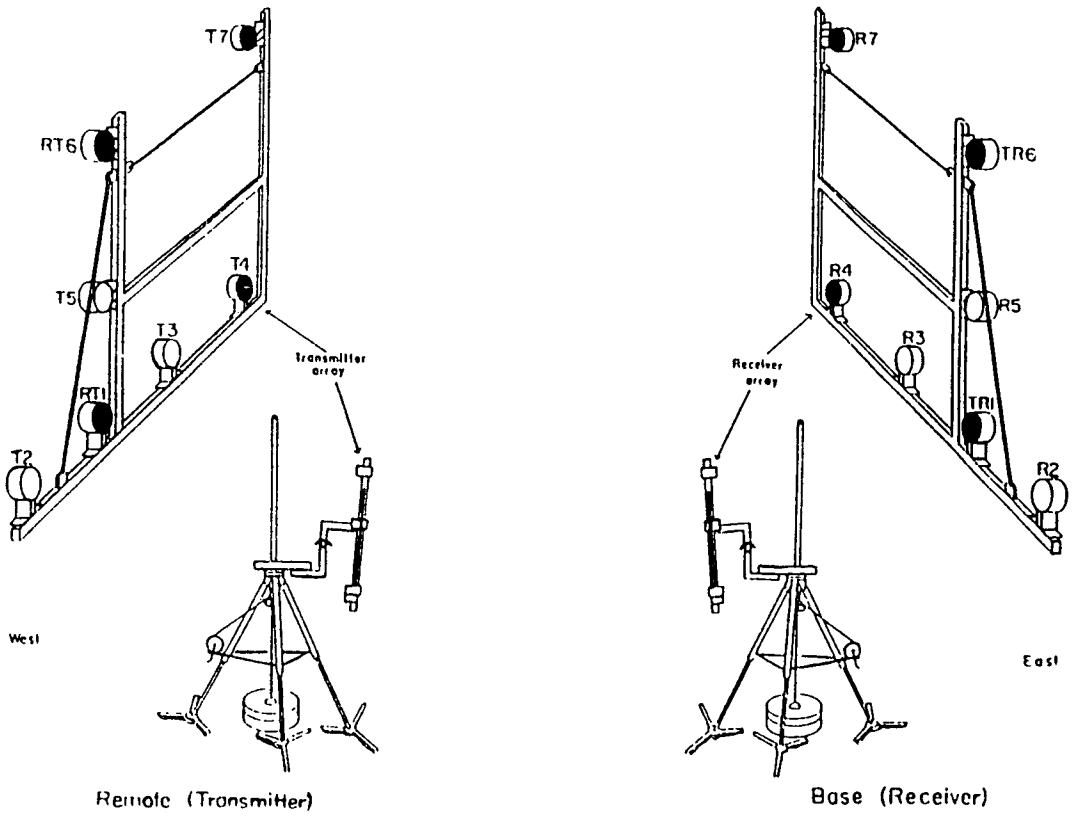

Figure 4.3: Transmitter and receiver array configurations for Saanich Inlet. Linear array (−): T/R 1,2,3,4; Square array (X): T/R 1,4,6,7; L-shaped array (L): T/R 1,4,5,6.

4.2 Saanich Inlet

The transmitted and received signals as well as the communications used in the separate experiment in Saanich Inlet follow the same method as that used in Cordova Channel. The acoustic array configuration used in Saanich Inlet was either linear (−), square (X) or L-shaped and was programmed via the radio link. For the analysis described in this thesis, only data from the square array will be used. Figure 4.3 shows the moored acoustic array and coloured transducers form the square array.

The code length was increased to 127 bits so as to increase the signal to noise ratio and operation was done in block mode with transmitted guard sequences. The bit width was decreased to 9 cycles/bit so that multipaths separated by 130 μs could be

Parameter	Deployment 1
Transducer array depth (m)	35
Path length L (m)	2350
Hydrophone separation (m)	$\rho_{x,z} = 2.0$
Cycling mode	block
Observation period (X array)	19/04/89 17:15 to
(PDT)	20/04/89 02:15
Acoustic frequency f_a (Hz)	67567
Acoustic wavenumber k (m^{-1})	287.82
Fresnel radius $\sqrt{\lambda L}$ (m)	7.16
Code length ($bits$ (ms))	127 (17)
Bit width ($cycles/bit$ (μs))	9 (133)
Phase shift for coding (deg)	180
Digitization rate ($samples/bit$ (kHz))	3 (22.5)
Window size ($samples$ (ms))	73 (3.24)
Repetition rate (Hz)	5.0

Table 4.2: Acoustic parameters for Saanich Inlet scintillation system for deployment 1.

analyzed. This imposed an effective bandwidth of 7.7 kHz. Since there were many undefined multipaths a large window was used. The bit width, digitization rate and the window size limited the repetition rate to 5 Hz. The experimental and acoustic parameters are summarized in Table 4.2.

Figure 4.4 shows sample in-phase and quadrature components giving amplitude and phase as a function of arrival time (in samples) for a given transmitter and receiver. The amplitude clearly shows multipath propagation. The need for guard sequences in this experiment is very important because the correlation side lobes of closely space multipaths can interfere with the main correlation peak. Data were

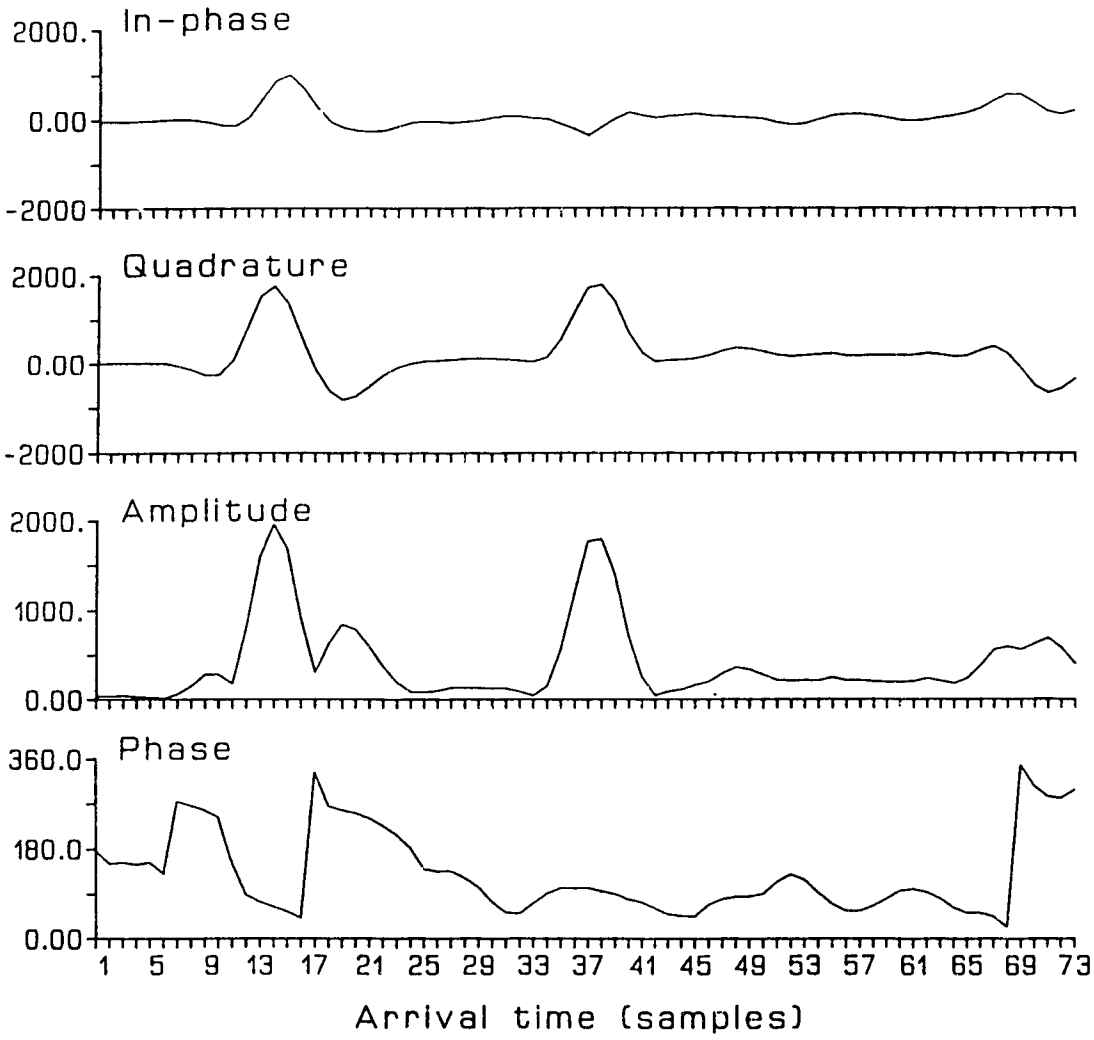

Figure 4.4: The in-phase and quadrature components giving amplitude and phase as a function of arrival time (in samples) for T1/R7 (73 samples = 3.24 ms).

windowed so that no signals occur before the start of the window and after the end of the window.

Chapter 5

Measurements of Turbulence Parameters in Cordova Channel

5.1 Introduction

In 1984 Farmer *et.al.* [24] carried out an acoustic experiment where Tatarskii's weak scattering theory together with Kolmogorov's turbulence model was used to probe the intervening medium. The oceanographic site (Cordova Channel) was chosen specifically with this in mind. The primary focus was to test the concept of along channel flow speed measurements using a single source and two receivers. Acoustical and *in situ* current measurements compare very well and hence demonstrates the technique. Based on that experiment, a second experiment in October, 1986 was carried out to study path averaged turbulence quantities from acoustic signals transmitted 670 m across Cordova Channel, British Columbia (Figure 5.1).

Acoustic transmitter and receiver arrays, as well as oceanographic instruments were deployed as shown in Figure 5.1. Acoustical measurements were made with 4-transmitter and 4-receiver arrays. A linear array was used to study the technique of spatial filtering (see Crawford *et.al.* [10] and Farmer and Crawford [25]), and a square array was specifically designed to shed light on some 2-dimensional features

of the turbulent environment in Cordova Channel.

This chapter will describe the oceanographic instrumentation and give an overview of the data collected during the experiment. The technique used to obtain measurements of amplitude and phase will be described and characteristics of the data will be shown. A check on the validity of the Tatarskii model together with the turbulence model invoking the Taylor hypothesis will also be made. Path averaged oceanographic measurements assuming isotropic turbulence include: turbulent outer scale estimates, measurements of current speed, measurements of the refractive index structure parameter and finally measurements of the turbulent kinetic energy dissipation. Estimates of the scattering parameters (Γ, X) provide a comparison with other acoustic experiments. Both the deterministic and rapid fluctuations in the acoustic arrival angles are examined and an anisotropic description of the random medium is described.

Some merits of using a scintillation system to measure the above parameters include the ability to carry out real time oceanographic analysis, the capability of permanent deployment and the ability to look at fine structure, since the sampling rate is high and the wavelength is small. Also, the results are path averaged which give a different and complementary measurement compared to point measurements.

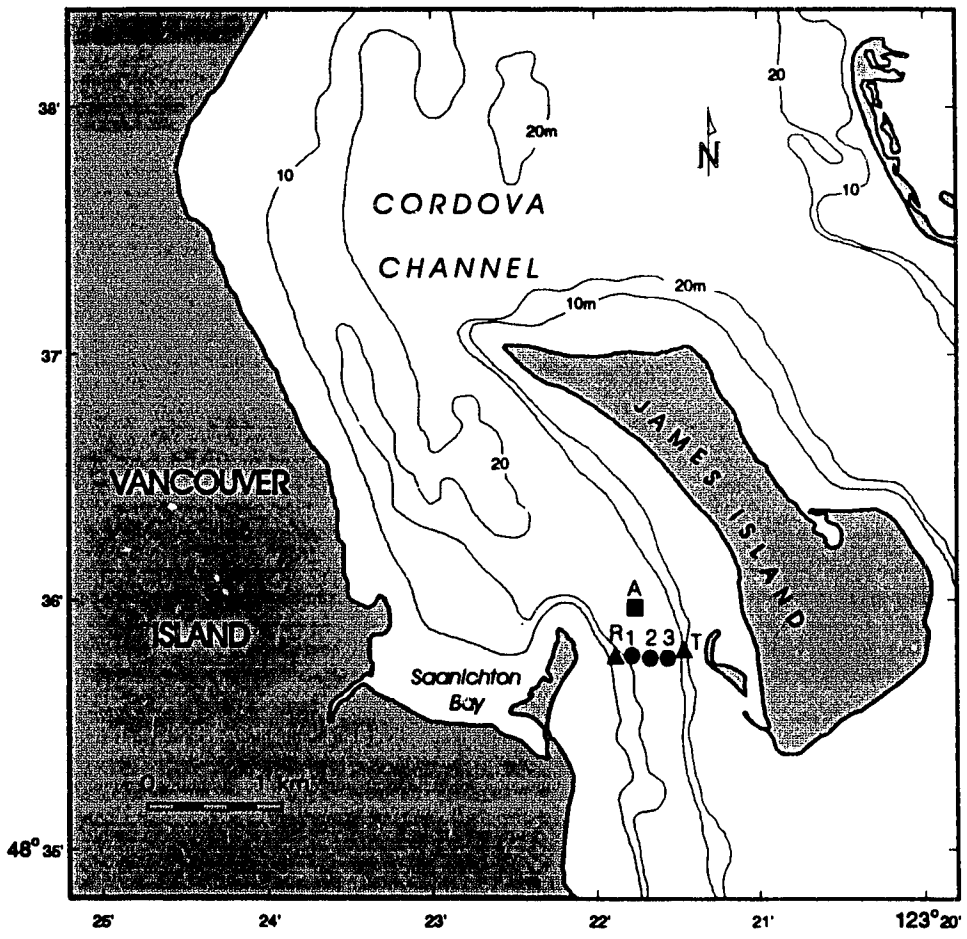

Figure 5.1: Cordova Channel showing instrument locations, together with the transmitter array (T) and hydrophone array (R). Recording current meters were moored at stations 1, 2 and 3 (•); CTD profiles and time series were obtained at station **A** (■).

5.2 Oceanographic Characteristics

This section will describe the flow characteristics of Cordova Channel during a period of 2.75 days. The oceanographic data will show that strong tidal currents ($\sim 1\ m\ s^{-1}$) through this relatively shallow ($32\ m$) channel ensure that the water is almost always turbulent and the stratification is weak as a result of turbulent mixing.

5.2.1 Current meter observations

Each current meter mooring shown in Figure 5.1 has Aanderaa current meters at 15 and 16 metres depth. Each instrument records the temperature, salinity, current speed and direction with a sampling interval of 2 minutes. The current meter data at the two depths are used to give some indication of shear. The current meters placed across the channel provide a basis for determining the distribution of current flow along the propagation path. Farmer and Crawford [25] have used the technique of spatial aperture filtering to measure the distribution of current across the channel.

Figure 5.2 shows 2.75 days of data obtained from a 15 m current meter at station 2 (o). The current velocity is described by two components: a component perpendicular ($\perp\ 4^{o}\ True$) to the acoustic ray path and the other one parallel ($\parallel\ 94^{o}\ True$), but opposite to the direction of acoustic propagation. Positive values indicate flow toward the North and East. The effect that the perpendicular component has is to advect the acoustic waveform in the direction of flow resulting in slightly longer path lengths (see section 5.6.1); the parallel component will either increase or decrease the total acoustic travel time. A parallel current speed of 0.2 $m\ s^{-1}$ with an average sound speed of 1485 $m\ s^{-1}$, yields a travel time difference (with and without cross channel flow) of $60.7\mu s$ (1478 deg). This difference is equivalent to a change in temperature of 0.16 $deg\ C$. Hence the available resolution of 3^{o} ($123\ ns$) implies a resolution of $\pm 0.41 mm\ s^{-1}$ or equivalently $\pm 0.32 mdegC$.

The current velocity across the channel is less along the sides of the channel compared to the center. Since the difference is small (differences of 0.15 $m\ s^{-1}$ at

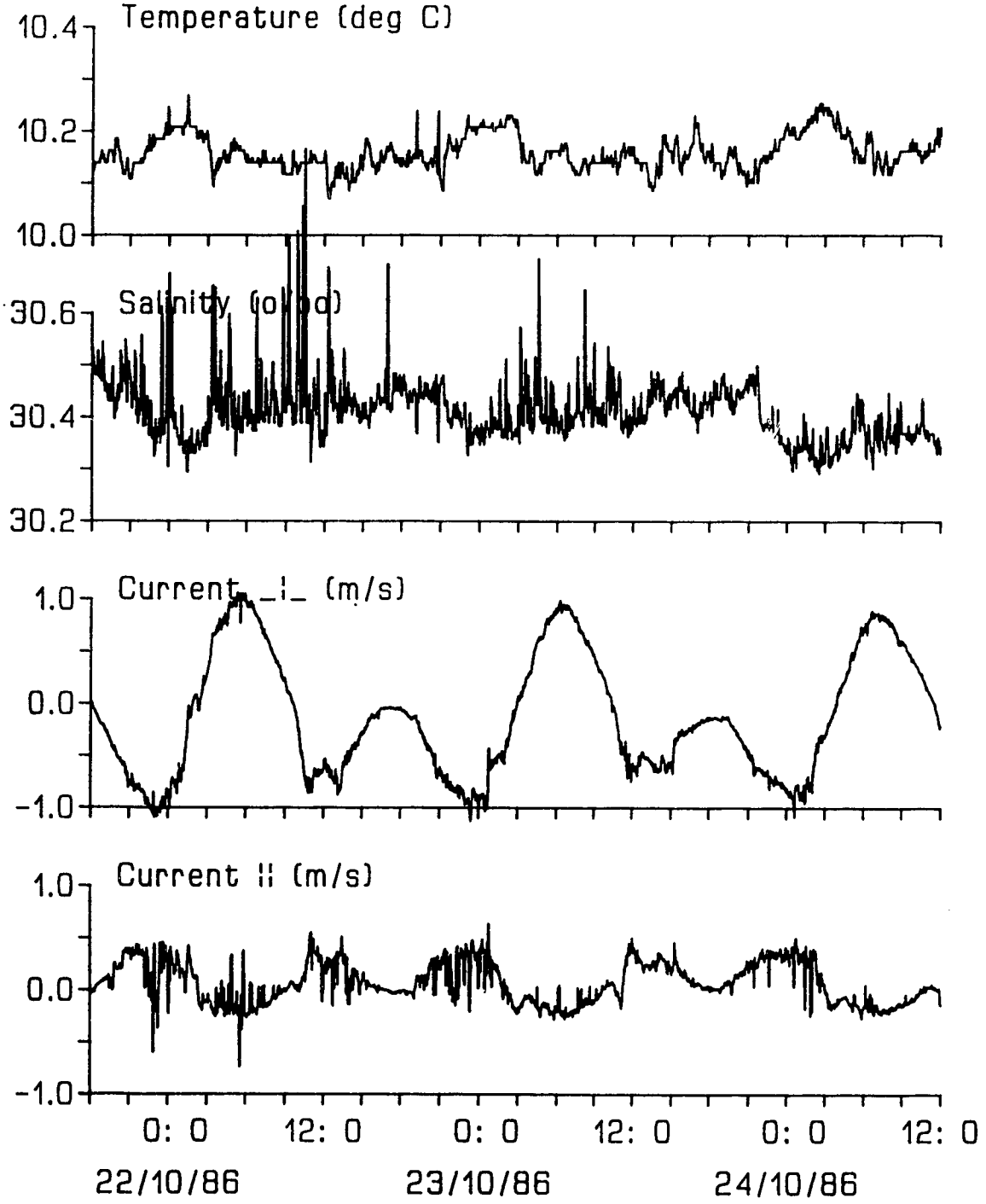

Figure 5.2: Observed current meter data (15 metre) at station 2 (•) for 2.75 days. The current velocity is shown as two components: along channel current component ($\perp$) at 4° True, and the cross channel current component ($\parallel$) at 94° True.

maximum flow) we can make the assumption that the distribution across the channel is approximately uniform. Farmer and Crawford's [25] measurement of the transverse shear is in agreement with the inferred shear based on the spatial aperture filter. They obtain velocity differences ranging from $-0.3m\ s^{-1}$ to $0.3m\ s^{-1}$.

The current meter data also show tidal variations in the temperature and salinity. Although the salinity measurement is noisy the tidal variations can still be observed. The tidal variations occur because fresh water of higher temperature and less salinity, primarily from the Fraser River, is mixed with water of lower temperature and higher salinity from oceanic origin.

As a first step in defining turbulence in this tidal channel we need to quantify the Reynolds number,

$$\mathrm{Re} = \frac{UD}{\nu}, \tag{5.1}$$

where U is the mean stream velocity, D is the average depth of the channel ($28\ m$) and $\nu = 1 \times 10^{-6}\ m^2\ s^{-1}$ is the kinematic viscosity. For strong tidal flow ($U = 0.8\ m\ s^{-1}$), the Reynolds number is 2.2×10^7 and for weaker flows ($U = 0.2\ m\ s^{-1}$) the Reynolds number is 5.6×10^6. These Reynolds numbers can be difficult to achieve in laboratory experiments.

5.2.2 CTD observations

A conductivity, temperature and depth (CTD) survey was conducted at station **A** (□) in Figure 5.1. Profiles were acquired every 15 minutes and time series were taken for 12 minutes after each profile at 15 m depth. The lowering rate for the CTD meter was approximately 1 $m\ s^{-1}$ and the sampling rate was 4 Hz. The time series were acquired by suspending the instrument at a fixed depth while the vessel maintained its position in the tidal current, in the neighborhood of the acoustic path. Since the temperature and salinity measurements from the current meters lack the sampling rate required for analysis of turbulent fluctuations, the CTD time series are used to measure the intensity of the refractive index fluctuations due to temperature and

salinity; the profiles show the vertical mixing characteristics for the channel as well as give measurements of the sound speed gradients.

Typical temperature time series and profiles from the CTD data, during a 24 hour tidal cycle, are shown in Figure 5.3. The time for each time series and profile is indicated on each plot and shown on the tidal cycle in Figure 5.3(a) as T and P respectively. Only temperature data are shown in Figure 5.3(b) and (c), but the temperature - salinity relationship remained linear with an average equation,

$$S - < S > = \left\langle \frac{dS}{dT} \right\rangle (T - < T >), \tag{5.2}$$

$$S - 30.4 = -0.89\ (T - 10.1). \tag{5.3}$$

The corresponding sound speed (c in $m\ s^{-1}$) dependence on temperature (T in $degC$), salinity (S in $^{o}/_{oo}$) and depth (z in m) is (see Brekhovskikh and Lysanov [4]),

$$c(T,S,z) = 1449.2 + 4.6T - 0.055T^2 + .00029T^3 + (1.34 - .01T)(S - 35.0) + .016z. \tag{5.4}$$

The channel flow is characterized by well mixed water properties, except during slack water. The time series show that during strong tidal flow the water column is being intensively mixed. However, there are brief periods when imperfectly mixed water passes through the measurement area. These occur more typically during weaker tidal flows when the mixing is less intense and there is more stratification.

Shear provides a source of energy for the turbulence and buoyancy provides either a source or a sink of energy depending on the sign of the density gradient. If the density increases upwards, then buoyancy forces provide a source of energy for the turbulence; if the density decreases upwards, then turbulence must do work against the buoyancy forces. Hence, a dimensionless parameter (in one form or another) in terms of the two gradients can by defined by the bulk Richardson number,

$$\mathrm{Ri} = -\frac{g\frac{\Delta\rho}{\rho_o}h}{\Delta U^2}, \tag{5.5}$$

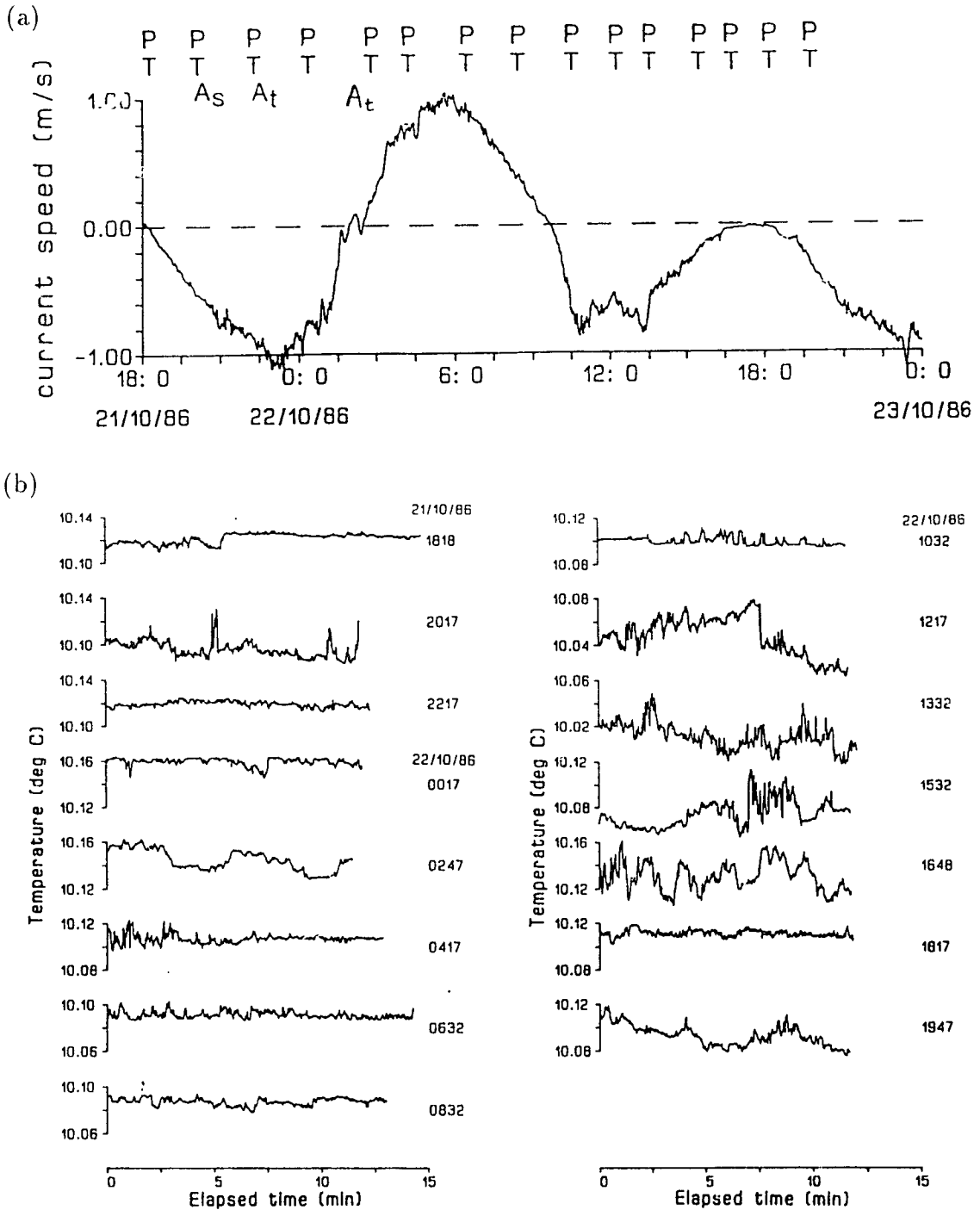

Figure 5.3: (a) Current speed perpendicular to the acoustic path. Sample profiles and time series of temperature taken through the tidal cycle are shown as P and T respectively. Sample acoustic time series (Figure 5.6) are taken at A_t. A sample phase difference spectrum (Figure 5.18) and one-dimensional spectrum for refractive index fluctuations due to scalars (Figure 5.23) are taken at A_s. (b) Time series and (c) profiles of temperature during the tidal cycle.

(c)

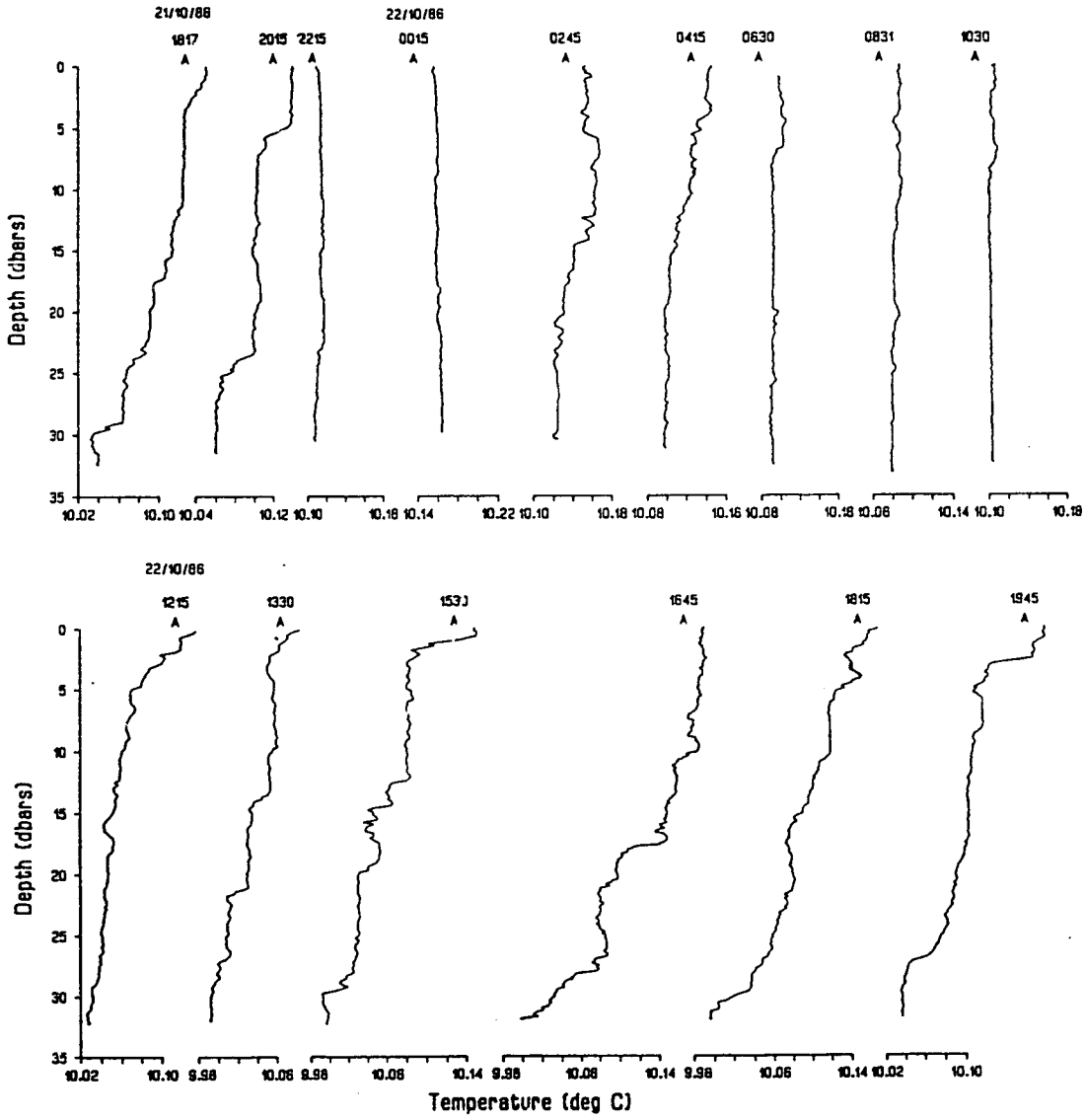

Figure 4.3 continued.

where g is gravitational acceleration, $\Delta\rho/\rho_o$ is the relative density difference across the active layer of depth h and ΔU is the corresponding flow speed difference across h. The potential for instability and hence mixing is given by this Richardson number. If Ri is negative then both shear and buoyancy generate turbulence; if Ri is positive then density gradients stabilize the flow and turbulence is generated by shear. If Ri is large ($> 1/4$), the turbulence may not be strong enough to overcome the stratification and hence mixing is weak. If Ri is small ($< 1/4$) then the shear provides energy to the turbulence and so the flow is easily mixed (see Pond and Pickard [45]). For representative values during the experiment Ri $\sim$ 0.026 confirming that buoyancy effects are small relative to inertial effects and density stratification cannot stabilize the flow.

There is much fine structure in the flow at all phases of the tide. At slack water the temperature and salinity are stratified. For the most part, Cordova Channel can be characterized as a channel flow where the full depth has turbulent characteristics. For this reason we can assume that the refractive index fluctuations can be approximated as statistically isotropic and homogeneous within an inertial subrange.

5.3 Acoustic Characteristics

In this section the acoustic data collected in Cordova Channel for 2.75 days will be discussed in terms of the observed oceanography. The acoustic data for diverging and parallel paths, using the linear and square array will show tidal variations and define the spatial and temporal correlation scales. Structure function characteristics are also shown. In addition, a check on the validity of the Tatarskii and Kolmogorov model is made by comparing spectral densities for log-amplitude, phase and phase difference with the theory.

5.3.1 Amplitude and phase calculations

Since the received signals are correlated with a template of the transmitted code, the correlation peak is defined, theoretically, as a triangle function. For this reason the time of arrival (T) and the amplitude,

$$A(T) = \sqrt{\mathcal{I}(T)^2 + \mathcal{Q}(T)^2}, \tag{5.6}$$

where $\mathcal{I}(T)$ is the in-phase and $\mathcal{Q}(T)$ is the quadrature component, are calculated by a triangle fit to five points representing the amplitude correlation peak. At times when the signal falls below a cutoff threshold a quadratic function is fitted to three points representing the amplitude correlation peak. From the measured signal amplitude and noise level, an average SNR of 25 dB was obtained. The root-mean-square (rms) phase noise is ± 3.2 degrees based on the equation $< \phi_n^2 >= 10^{-SNR/10}$ assuming independent amplitude and phase random signals. This noise can be reduced by averaging over long time periods.

Triangular or quadratic interpolation on the in-phase and quadrature components defines $\mathcal{I}(T)$ and $\mathcal{Q}(T)$. The phase is then calculated by,

$$\phi = \arctan\left(\frac{\mathcal{Q}(T)}{\mathcal{I}(T)}\right), \tag{5.7}$$

(see Figure 4.2). The phase measurement is very sensitive since it is nearly constant over the peak of the arrival. However, it is subject to a 2π ambiguity. For this reason

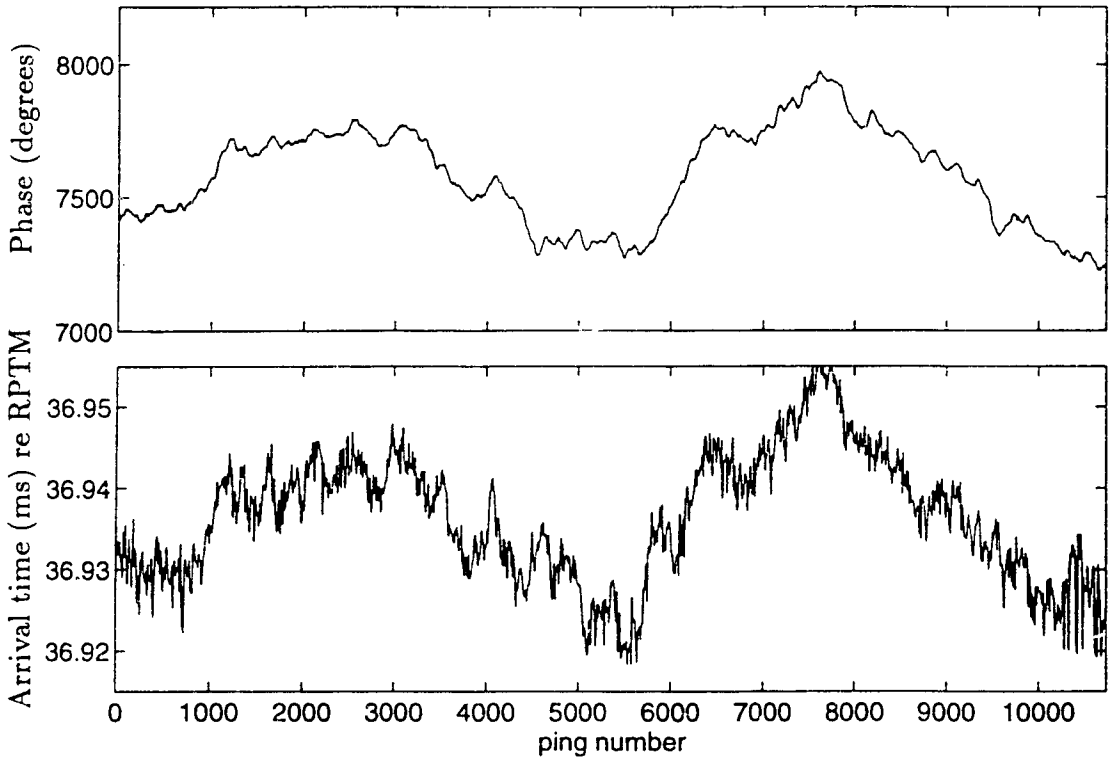

Figure 5.4: Example of phase (ϕ) and time of arrival (T) plotted to the same scale. All times are relative to the receiver ping timing mark (RPTM).

it is used as a vernier scale for the time of arrival, which is a noisy measurement but which can be used to resolve the phase ambiguity. Figure 5.4 shows the phase (ϕ) calculated from (5.7) and the time of arrival (T) calculated from the peak fit. Both are plotted to the same scale for 10 minutes of data. The time of arrival is used only to resolve the 360° phase ambiguity inherent in the calculation defined by (5.7). That is, $\phi' = \phi + 360N$, where $N = \text{int}(Tf_a)$. All times are relative to the receiver ping timing mark (RPTM) and do not represent total travel time across the channel. That is, the time of arrival (and hence the phase) is referenced to the receiver system's transmission timing signals so that the window of arrivals remains locked to the transmission timing to within the relative accuracy of the two master oscillators. The relative time of arrival remains continuous so long as neither the transmitter nor the receiver transmission timing mark stops.

Since the acoustic amplitude remained strong and separated from the surface and bottom reflected path, peak detection and tracking was simple. For future experiments a maximum likelihood estimation algorithm described in Appendix D can be used to calculate the amplitude, phase and time of arrival. This algorithm was discovered when multipaths in Saanich Inlet had to be separated and will work well when there is a single path. It has been successfully tested on some of the Cordova Channel data and has also been successfully used in a recent acoustical scintillation experiment in Hood Canal (1993).

Figure 5.5 shows a 12-hour period on October 24 of amplitude (A) and phase (ϕ). Data are heavily averaged over 10 seconds (180 transmissions). The phase clearly shows the temporal variability associated with large scale changes in both the temperature and velocity field. For example, from 0000h to 0300h the change in temperature is 0.05 *deg C* and the change in the parallel current component is $-0.25\ m \cdot s^{-1}$ (see Figure 5.2). This results in a change of arrival time of $-130\ \mu s$ consistent with that observed in the phase measurement. Also, from 0300h to 0600h the temperature change is -0.1 *deg C* and the parallel current change is $-.125\ m \cdot s^{-1}$ corresponding to a phase change of 71 μs consistent with the observations. These results are summarized in Table 5.1. It should be emphasized that the change in phase taking into account only temperature variations does not describe the observed phase variations.

The amplitude is dominated by high frequency variability where, according to diffraction theory, the smallest scale size that can focus the acoustic rays is of the order the Fresnel scale ($\sqrt{\lambda L} = 3.8\ m$). Focussing from smaller scale inhomogeneities is essentially removed by diffraction effects. The scintillation index, S_I^2 (the normalized variance of the intensity fluctuations), which is defined as

$$S_I^2 = \frac{< I^2 > - < I >^2}{< I >^2}, \tag{5.8}$$

where $I = A^2$ is the intensity, is of order 0.06. This indicates that the weak scattering theory ($S_I^2 \ll 1$) is appropriate, as required for Rytov's method (see Ewart *et.al.* [21]).

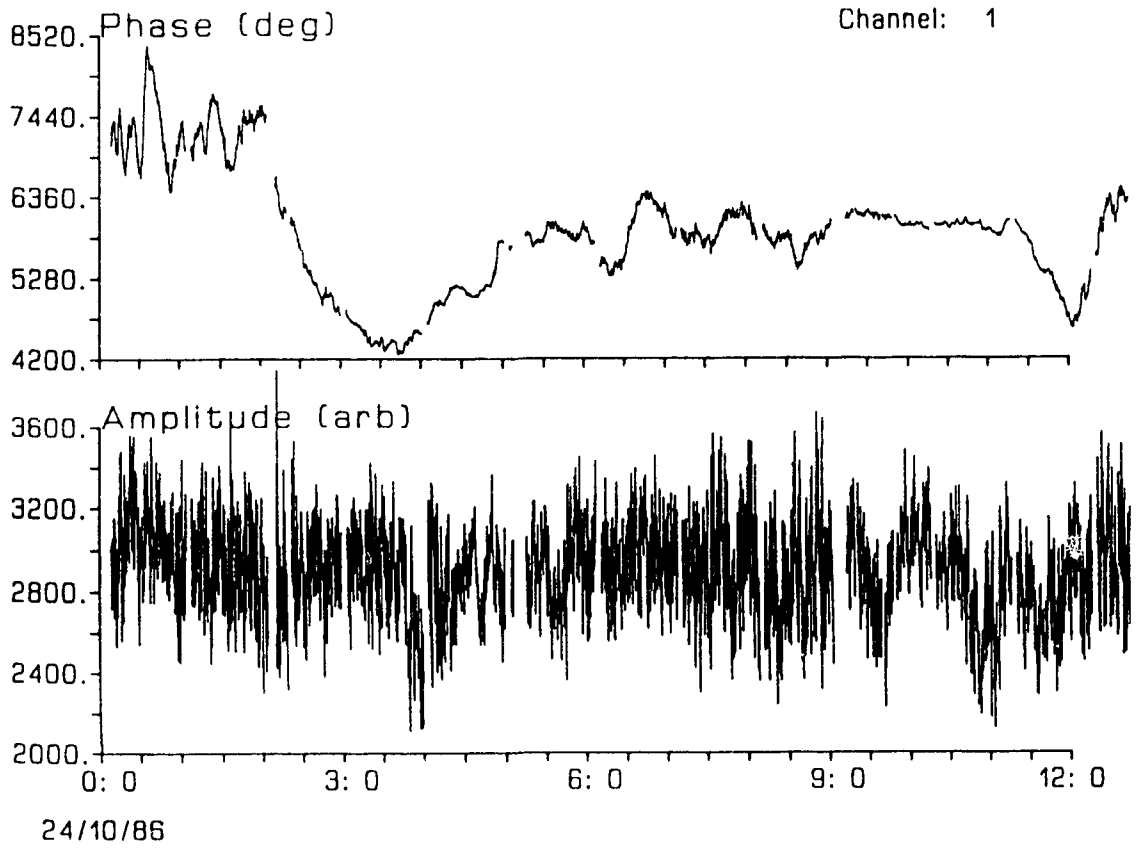

Figure 5.5: Example of amplitude and phase time series recorded during a 12 hour period on October 24. Data were averaged for 10 seconds ($S_I^2 = 0.06$).

24/10/86	0000h	0300h	0600h
Temperature (deg C)	10.2	10.25	10.15
Salinity ($^o/_{oo}$)	30.35	30.35	30.35
Sound speed ($m\ s^{-1}$)	1485.189	1485.369	1485.008
Phase difference (μs)	-54.7		109.7
Parallel current ($m\ s^{-1}$)	0.25	0.0	-0.12
Phase difference (μs)	-130.0		71.0

Table 5.1: Observed phase difference resulting from changes in temperature alone and changes in both temperature and parallel current component.

Greater variability and more rapid fluctuations in the log-amplitude ($\chi = \ln(\frac{A}{<A>})$), phase ($\phi$) and phase difference ($\delta\phi$) occur during periods of strong tidal flow. In computing the log-amplitude, the amplitude was averaged over one hour giving $< A >$. This average approximates the signal level in a medium without any random variabilities. Figure 5.6(a) is a 12 minute section during a period of strong ebb ($S_I^2 = 0.11$) and Figure 5.6(b) is a section during slack water ($S_I^2 = 0.05$). These times are shown in Figure 5.3(a) and can be compared respectively with the 2217h and 0247h CTD time series in Figure 5.3(b). The probability distribution for both the log-amplitude and the phase difference follow Gaussian statistics as predicted by the weak scattering theory.

Noise analysis

Measurement related noise provides a limit to the useful resolution of both log-amplitude and phase at the highest sampling frequencies. Figure 5.7(a) and (b) shows the log-amplitude and phase spectra respectively. These plots represent twelve 15 minute two-sided periodograms taken during a 12 hour measurement period. The vertical spread in the spectral levels correspond to increased levels of refractive index variability. Horizontal spread also exists because the frequency is dependent on the mean flow U arising from the Taylor hypothesis. The data clearly show noise at the highest frequencies. Based on these spectral plots, a 3rd order low-pass Butterworth filter was carried out at a cutoff frequency of $f_c = 6.3\ Hz$ for log-amplitude and $f_c = 4.5\ Hz$ for phase. Filtering was done both forwards and backwards in order to eliminate phase shifts.

Most of this measurement noise occurs from the peak fit algorithm. For example, at the Nyquist frequency ($f_N = 17.875/2$) a calculated rms phase noise of 5.8 degrees exists because of the 0.2 sample (one cycle) peak shift that occurs on alternating transmissions for continuous mode data. Even though the phase and the time of arrival were corrected for this time shift some noise remains. This is also true for the amplitude.

(a)

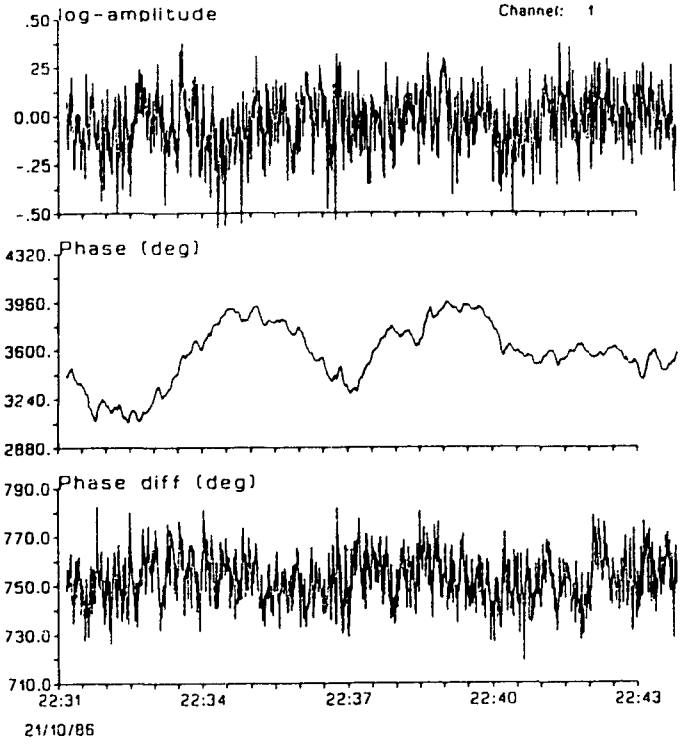

(b)

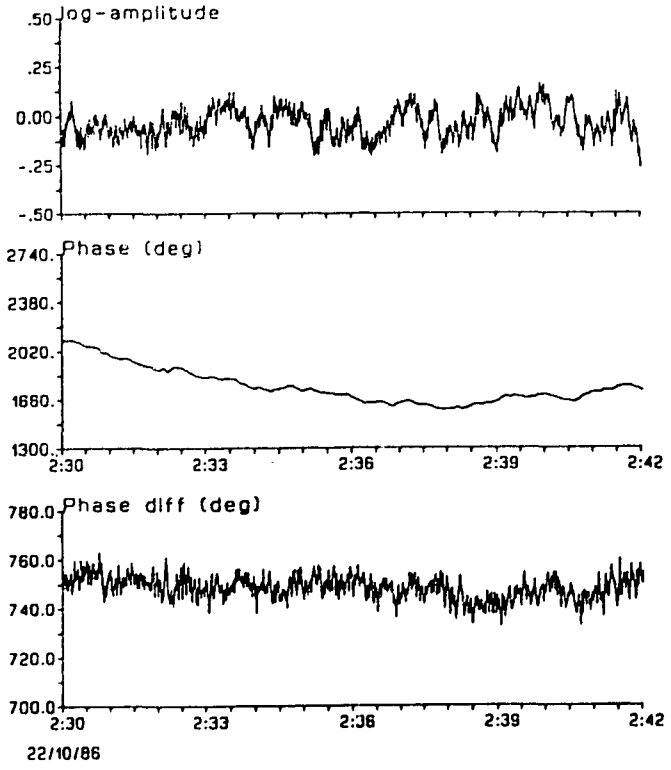

Figure 5.6: Example of log-amplitude (χ), phase (ϕ) and phase difference ($\delta\phi$) time series during (a) strong ebb flow ($S_I^2 = 0.11$) and (b) slack water. ($S_I^2 = 0.05$). These times correspond to A_t in Figure 5.3(a).

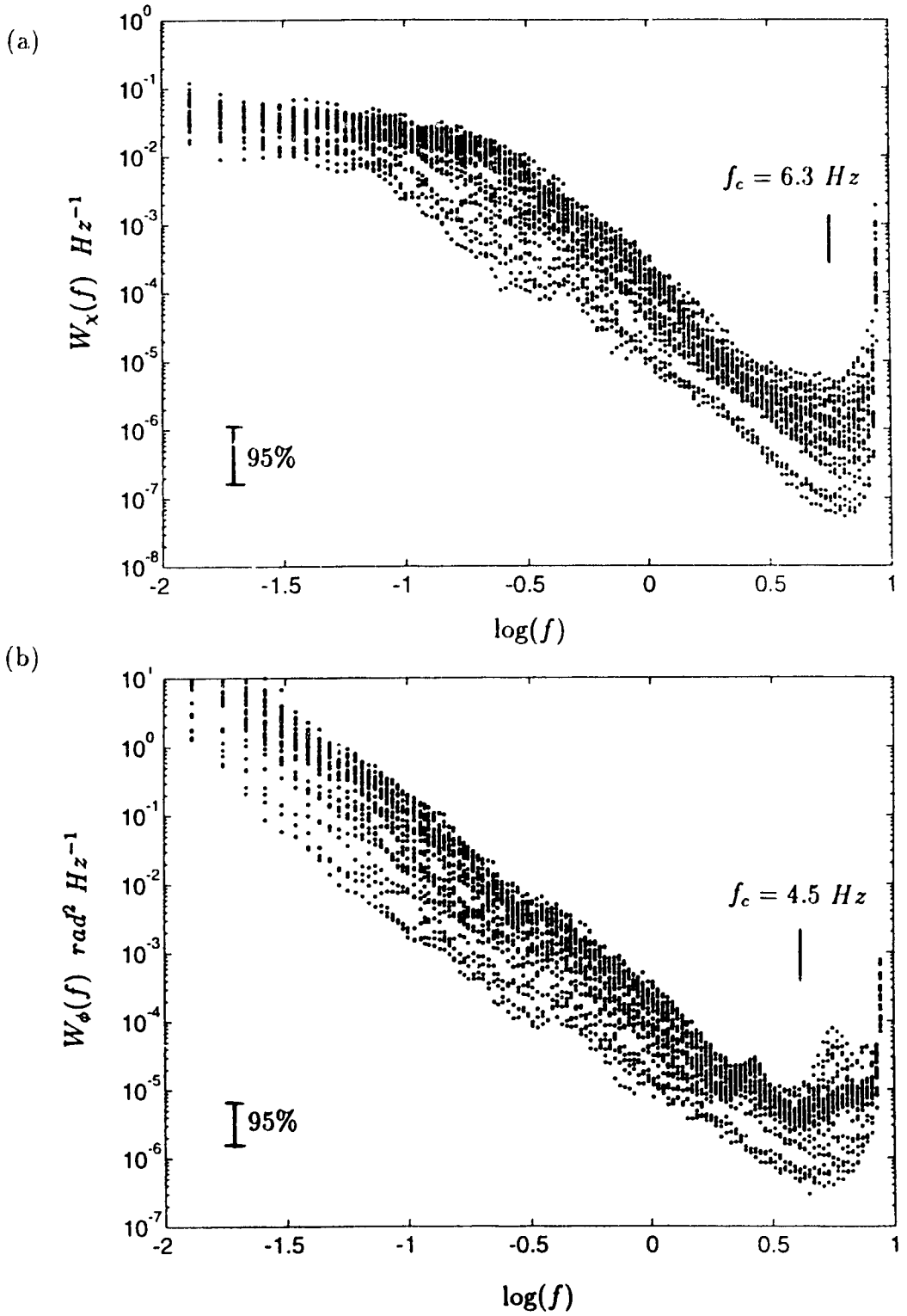

Figure 5.7: Twelve (a) log-amplitude and (b) phase spectra taken during a 12 hour measurement period in order to show measurement related noise at the highest frequencies. The low pass filter cutoff point is shown as $f_c = 6.3\ Hz$ for log-amplitude and $f_c = 4.5\ Hz$ for phase.

The high frequency fluctuations are observed using high pass filtered data. Since the theory is valid for $f > U/L_o$ (see section 5.3.4), where L_o is the outer scale of turbulence and U is the mean current speed, an appropriate high frequency cutoff depends on the outer scale.

5.3.2 Covariance scales

The covariance scale for the log-amplitude fluctuations can be examined using the spatial log-amplitude cross covariance function, defined by (3.24), at zero time lag ($C_\chi(\rho, 0)$). If this function is normalized by the log-amplitude variance $C_\chi(0,0)$ then variations due to the refractive index fluctuations can be removed. Figure 5.8 is a plot of the normalized spatial cross covariance function for parallel and diverging paths. The theoretical curves are obtained by numerical evaluation of the integrals in (3.24) given the experimental parameters. Superimposed are the experimental measurements taken for all different spatial separations from the linear and square array. The error bars, indicating the standard deviation, show that the experimental measurements are within the theoretical predictions. The log-amplitude covariance scale for parallel paths is of the order $\sqrt{\lambda L}/3 = 1.2\ m$ whereas for diverging paths it is of the order the Fresnel scale $\sqrt{\lambda L} = 3.8\ m$.

The temporal length scale for the log-amplitude fluctuations can be examined using the temporal log-amplitude cross covariance function, defined by (3.24), taken at a constant horizontal separation ($C_\chi(\rho_x = 1.18, \tau)$). This function is also normalized by the log-amplitude variance $C_\chi(0,0)$ in order to remove the effects of the random medium. Figure 5.9 is a plot of the normalized temporal cross covariance function for parallel and diverging paths taken at a time when the current is at maximum ebb and when the current is close to slack water. For parallel paths the correlation time scale for maximum flow is of the order $\rho_x/U = 2$ seconds and for flow close to slack water it is of the order 10 seconds. For diverging paths the time scales are halved. The width of the covariance function is also dependent on the current speed.

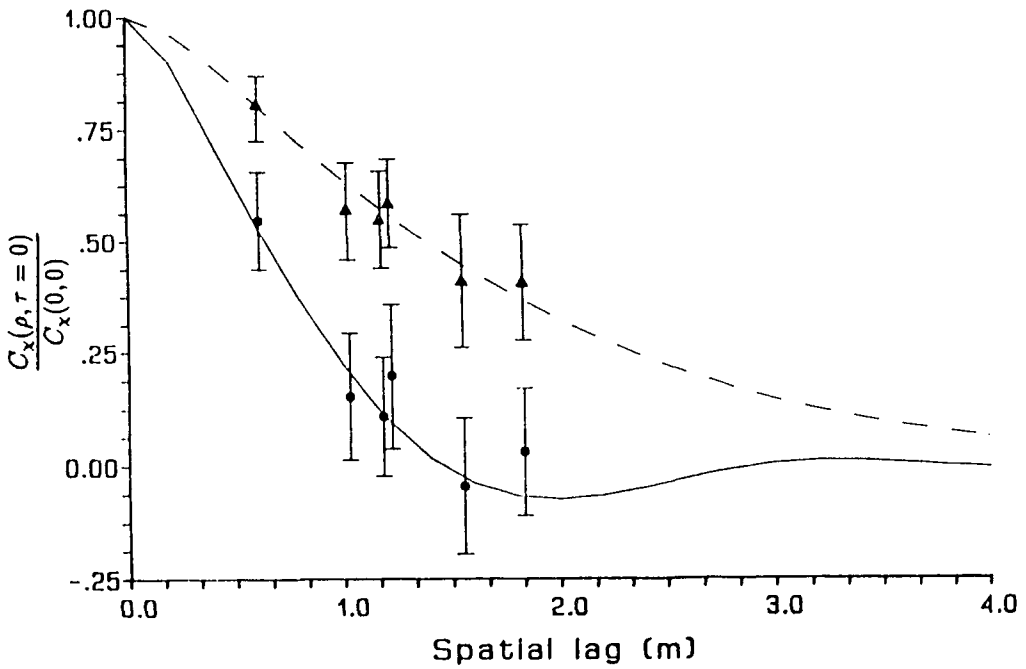

Figure 5.8: The normalized spatial cross covariance function for log-amplitude fluctuations for parallel paths (solid curve) and diverging paths (dashed curve). Experimental measurements are shown as • (parallel paths) and ▲ (diverging paths).

The peak value of the covariance function provides a measure of the validity of the Taylor hypothesis. Figure 5.10 is a plot of the normalized temporal log-amplitude cross covariance function for different receiver spacings. Parallel paths are shown; diverging paths give similar characteristics except the delay to the peak is halved. We can assume that the structures are essentially frozen during their passage across the receiver array since the correlation remains relatively high ($C_{N_\chi}(\rho_x = 1.83, \tau) = 0.7$) at the maximum spacing. Wernik *et.al.* [62] describe several processes that might be responsible for the violation of the Taylor hypothesis, namely, temporal and spatial variations of the drift velocity, dispersive nature of the motion, fluctuations of the drift velocity and the decay of irregularities due to diffusion.

5.3.3 Structure functions

The temporal structure functions for log-amplitude and phase are shown in Figure 5.11 for horizontal diverging paths during a time of strong ebb flow. The wave

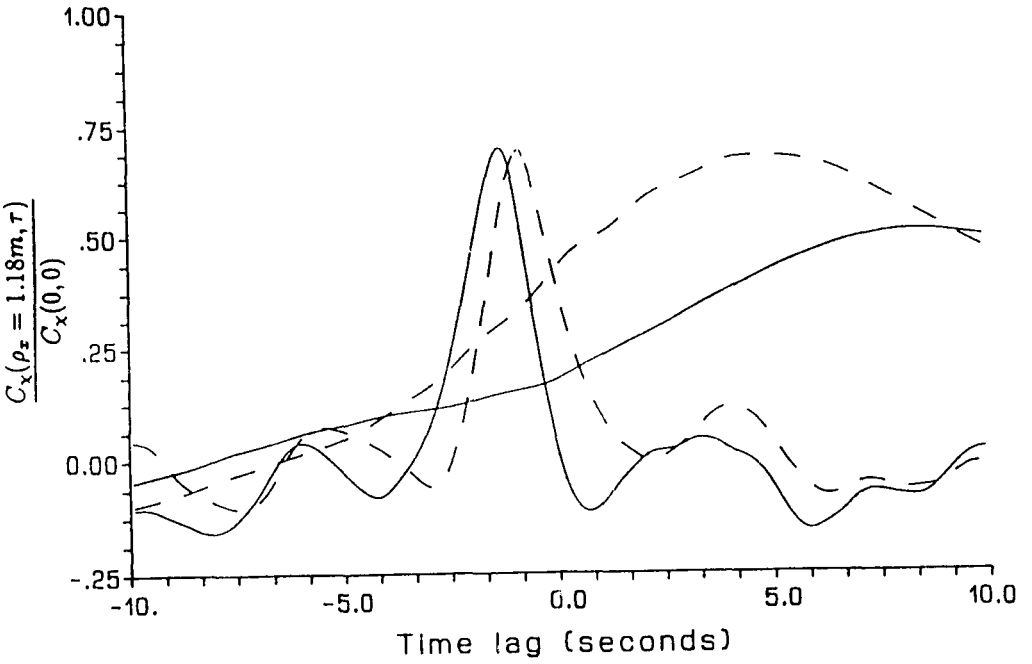

Figure 5.9: The normalized temporal cross covariance function for log-amplitude fluctuations for parallel (solid curve) and diverging (dashed curve) paths taken at a time of strong ebb and close to slack water.

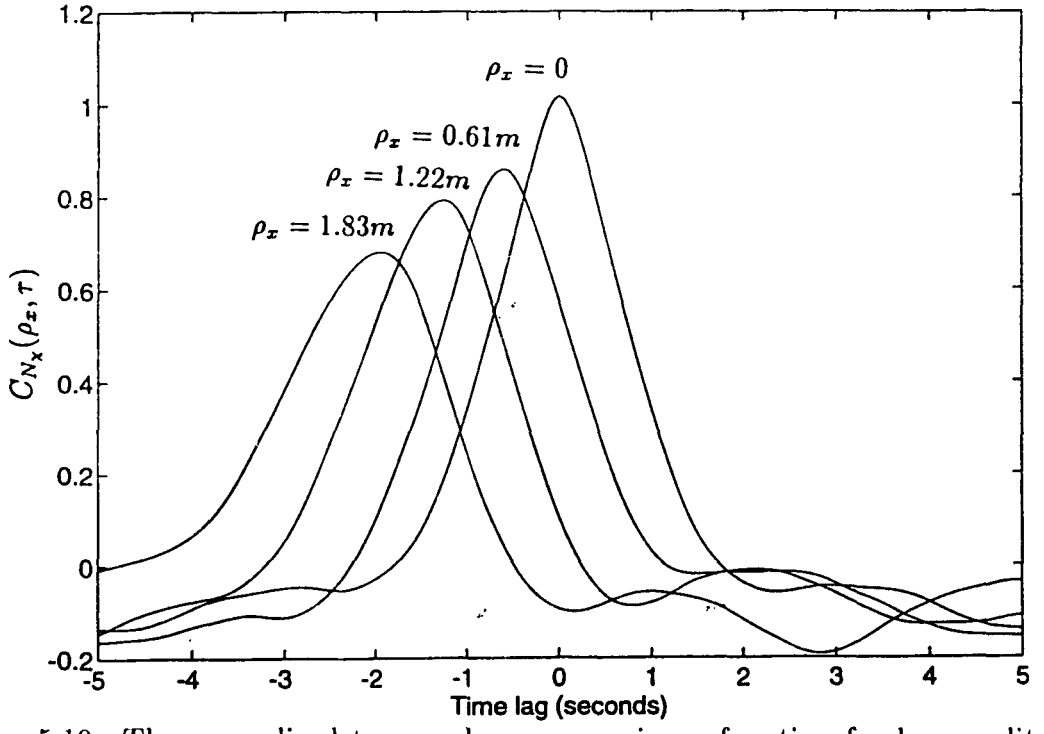

Figure 5.10: The normalized temporal cross covariance function for log-amplitude computed for different receiver spacings using parallel paths. Data are taken during strong ebb flow.

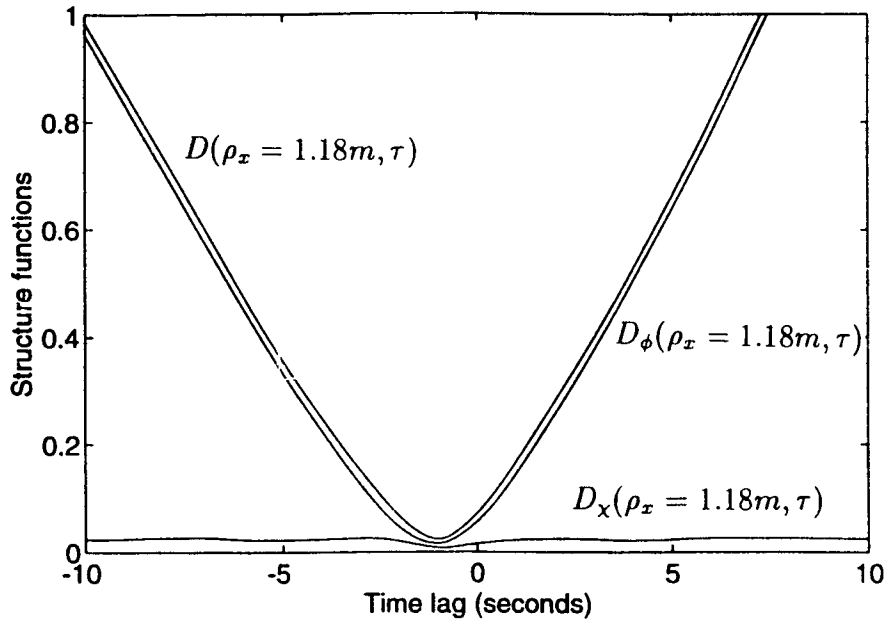

Figure 5.11: The log - amplitude, phase and wave temporal structure functions ($D_\chi(\rho_x = 1.18m, \tau)$, $D_\phi(\rho_x = 1.18m, \tau)$ and $D(\rho_x = 1.18m, \tau)$ respectively) computed for diverging paths. Data were taken during strong ebb flow.

structure function defined by $D = D_\chi + D_\phi$ is dominated by the phase as seen in the figure and for the most part the phase structure function is greater than the log-amplitude structure function for all time lags. Horizontal parallel paths are similar in shape except the delay to the minimum is doubled. During weaker flows the phase structure function becomes flattened and has the same order of magnitude as the log-amplitude structure function for all time lags.

5.3.4 Spectral densities

The frequency spectra for spherically spreading waves for log-amplitude (3.33), phase (3.33) and phase difference from horizontally spaced receivers (3.35) have been derived by Clifford [6]. In order to provide the framework for comparisons with the data, these results are presented below; some differences occur in the normalization parameters and we include aperture averaging effects since the finite size of the transducers effectively average the smaller scales and hence suppress the high frequency

fluctuations. We also derive the theoretical form for the frequency spectrum of intensity ($I = A^2$) fluctuations. In addition, we give the phase difference spectrum for vertically spaced receivers (3.37) but we discuss its difference to the horizontally spaced receivers in section 5.6

In order to take into account aperture averaging effects, Lee and Harp [36] show that for finite transmitter (T) and receiver (R) apertures, the factor
$\mid F_T(\kappa(L-y)/L) \mid^2 \mid F_R(\kappa y/L) \mid^2$ is included in the log-amplitude and phase cross covariance equation, defined by (3.24), as a product term in the integrand. The function F is defined as the normalized Fourier transform of the transmission and reception function. That is,

$$F_j(\mathbf{\Lambda}) = \frac{\int\int d\mathbf{r} e^{-i\mathbf{\Lambda}\cdot\mathbf{r}} f_j(\mathbf{r})}{\int\int d\mathbf{r} f_j(\mathbf{r})}, \tag{5.9}$$

where the integral is over $\mathbf{r} = (x, z)$ the plane of the receiver and $f_j(\mathbf{r})$ is the transmitter ($j = T$) or receiver ($j = R$) aperture function. A Gaussian form is assumed for both intensity and phase,

$$f_j(r) = \frac{1}{2\pi R_j^2} \exp(-r^2/2R_j^2), \tag{5.10}$$

where R_j is the standard deviation of the aperture radius ($j = T, R$) . Thus, the term,

$$\mid F_T(\kappa(L-y)/L) \mid^2 \mid F_R(\kappa y/L) \mid^2 = \exp\left(\frac{-\kappa^2(L-y)^2 R_T^2}{L^2}\right) \exp\left(\frac{-\kappa^2 y^2 R_R^2}{L^2}\right), \tag{5.11}$$

is included in the log-amplitude and phase cross covariance function defined by (3.24). If the inner and outer scale of turbulence is denoted by ℓ_o and L_o respectively, then scale sizes, $\ell_0 \ll \ell < R_{T,R}$ are suppressed and scale sizes $R_{T,R} < \ell \ll L_0$ are virtually unaffected. An irregularity of size $\ell = 2\pi/\kappa$ induces a frequency $f = U/\ell$. Therefore, frequencies, $f > U/R_{T,R}$ are suppressed.

Log-amplitude and phase spectra

The temporal power spectrum for log-amplitude and phase (3.33) taking into account aperture averaging effects is,

$$W_\phi^\chi(f) = 8\pi^2 k^2 \int_0^L dy \int_{\kappa > \frac{2\pi f}{U}}^\infty d\kappa \frac{\kappa \Phi_n(\kappa)}{((\kappa U)^2 - (2\pi f)^2)^{1/2}}$$
$$\begin{matrix}\sin^2 \\ \cos^2\end{matrix} \left(\frac{\kappa^2 y(L-y)}{2kL}\right) \exp\left(\frac{-\kappa^2 R^2}{L^2}(y^2 + (L-y)^2)\right), \tag{5.12}$$

where $R = R_T = R_R$ is the transducer aperture radius. The log-amplitude variance is then,

$$\sigma_\chi^2 = 2\int_0^\infty W_\chi(f) df. \tag{5.13}$$

The key assumption underlying our comparison is that within the scales of interest the flow field is adequately described by the Kolmogorov similarity theory, and the three dimensional refractive index spectrum is defined by (3.7). Analysis of the two-dimensional angle of arrival distribution in section 5.6.2 reveals some anisotropy in the turbulence but to a first approximation in comparing theory with experiment it is not unwise to assume the isotropic form. The isotropic spectrum holds over the inertial subrange $2\pi/L_o \ll \kappa \ll 2\pi/\ell_o$ where ℓ_o and L_o are the inner and outer scales respectively. This restriction together with the requirement $\kappa > 2\pi f/U$ in (3.34) limits the frequency range over which the spectra may be used. Specifically, the theory is only valid for frequencies $f > U/L_o$.

Insertion of the refractive index fluctuations spectrum, (3.7) into (5.12), setting $s = y/L$ and $\gamma^2 = (\kappa U/2\pi f)^2 - 1$ and defining a characteristic frequency scaling $f_0 = U/\sqrt{\lambda L}$ gives,

$$W_\phi^\chi(f) = a_1 C_n^2 k^{2/3} L^{7/3} U^{-1} \left(\frac{f}{f_0}\right)^{-8/3} \int_0^1 ds$$
$$\int_{\gamma>0}^\infty \frac{d\gamma}{(\gamma^2+1)^{11/6}} \begin{matrix}\sin^2 \\ \cos^2\end{matrix} \left(\pi \left(\frac{f}{f_0}\right)^2 (\gamma^2+1)s(1-s)\right)$$
$$\exp\left(-4\pi^2 \left(\frac{R}{\sqrt{\lambda L}}\frac{f}{f_0}\right)^2 (\gamma^2+1)(s^2+(1-s)^2)\right), \tag{5.14}$$

where the coefficient $a_1 = 2(0.033)(2\pi)^{2/3} = 0.2247$. The $-11/3$ Kolmogorov wavenumber dependence appears in the $(\gamma^2+1)^{11/6}$ term, diffraction is included in the $\sin^2$ and

$\cos^2$ terms for log-amplitude and phase respectively and finally aperture averaging is represented by the exponential term.

The level of the spectrum is thus determined by the structure parameter C_n^2. The current speed U is a function of the characteristic frequency, f_0. The log-amplitude variance (σ_χ^2) defined in (C.10) together with the frequency scaling, f_0 is used to normalize the log-amplitude and phase power spectra giving,

$$\frac{fW_\phi^\chi(f)}{\sigma_\chi^2} = a_2 \left(\frac{f}{f_0}\right)^{-5/3} \int_0^1 ds$$
$$\int_{\gamma>0}^{\infty} \frac{d\gamma}{(\gamma^2+1)^{11/6}} \begin{matrix}\sin^2 \\ \cos^2\end{matrix} \left(\pi \left(\frac{f}{f_0}\right)^2 (\gamma^2+1)s(1-s)\right)$$
$$\exp\left(-4\pi^2 \left(\frac{R}{\sqrt{\lambda L}}\frac{f}{f_0}\right)^2 (\gamma^2+1)(s^2+(1-s)^2)\right), \qquad (5.15)$$

where the coefficient $a_2 = 2(0.033)(2\pi)^{1/6}/0.124 = 0.723$. In normalizing this spectrum we have made the assumption that the current U is independent of path position.

The log-amplitude fluctuations are sensitive to the Fresnel scale length $\sqrt{\lambda L}$ which is assumed to lie between the inner and outer scales of turbulence. (This assumption is supported by estimates of L_o, discussed in section 5.4.1). They are also insensitive to the large scale variability and hence also to the outer scale provided $L_o \gg \sqrt{\lambda L} = 3.8\ m$. The solid lines shown in Figure 5.12 are the theoretical normalized log-amplitude spectra evaluated from (5.15) with ($R = 4.5\ cm$) and without ($R = 0\ cm$) aperture averaging, as a function of $\log(f/f_0)$. The spectrum is decreased at higher frequencies by aperture averaging effects. Superimposed on this plot are twenty 26 minute two-sided periodograms taken through the tidal cycle shown in Figure 5.22. Data during current speeds less than 0.2 $m\ s^{-1}$ are eliminated.

Each periodogram is obtained by separating the 26 minute run into eleven overlapping segments containing 4096 data values, detrending, windowing and fast Fourier transforming (FFT) each segment, averaging the resulting spectra to form a single spectrum, and then finally averaging this spectrum in logarithmically spaced frequency bins. The final spectrum is then normalized by the averaged log-amplitude

variance in the 26 minute time series. The normalizing frequency, f_0 is based on the current speed measured from the current meter. Theory predicts a peak at the characteristic frequency $f = f_0$. The aperture averaged model fit the data closely for $\log(f/f_0) > -0.5$ except where frequency dependent noise exists at the highest frequencies ($\log(f/f_0) > 1.25$). At lower frequencies the observations imply somewhat greater variability than the model. The Fresnel scale of 3.8 m is ~ 0.12 of the water depth and thus well within the expected inertial subrange for a fully developed turbulent flow. However, at scales greater than $10-20$ m the influence of the boundaries will be felt and the Kolmogorov model cannot be expected to be applicable.

In order to see that the Fresnel scale size contributes most to the log-amplitude variance the spectra are plotted on a linear scale (see Figure 5.13). This variance preserving plot is such that equal areas under the curves represent equal contribution to the log-amplitude variance.

Unlike the present study most acoustic experiments are such that they cannot assume weak scattering and so have to employ Uscinski's [58] moment approach. The fourth moment solution (m^{IV}) gives the normalized intensity auto correlation function. The normalized temporal auto covariance function for intensity ($I = A^2$) fluctuations is then defined as,

$$\frac{R_I(\tau)}{< I(t) >< I(t+\tau) >} = m^{IV} - 1, \tag{5.16}$$

$$= \frac{< (I(t) - < I(t) >)(I(t+\tau) - < I(t+\tau) >) >}{< I(t) >< I(t+\tau) >} \tag{5.17}$$

$$= \exp(4R_\chi(\tau)) - 1, \tag{5.18}$$

for Gaussian log-amplitude distribution. The scintillation index
$S_I^2 = R_I(0)/ < I >^2$. For the weak scattering regime $R_\chi(\tau) \ll 0.25$ (or $R_I(\tau) \ll 1.0$) so that $R_I(\tau) \approx 4R_\chi(\tau)$ and hence $W_I(f) \approx 4W_\chi(f)$. Normalizing by the variance of intensity fluctuations σ_I^2 gives

$$\frac{fW_I(f)}{\sigma_I^2} = \frac{fW_\chi(f)}{\sigma_\chi^2}. \tag{5.19}$$

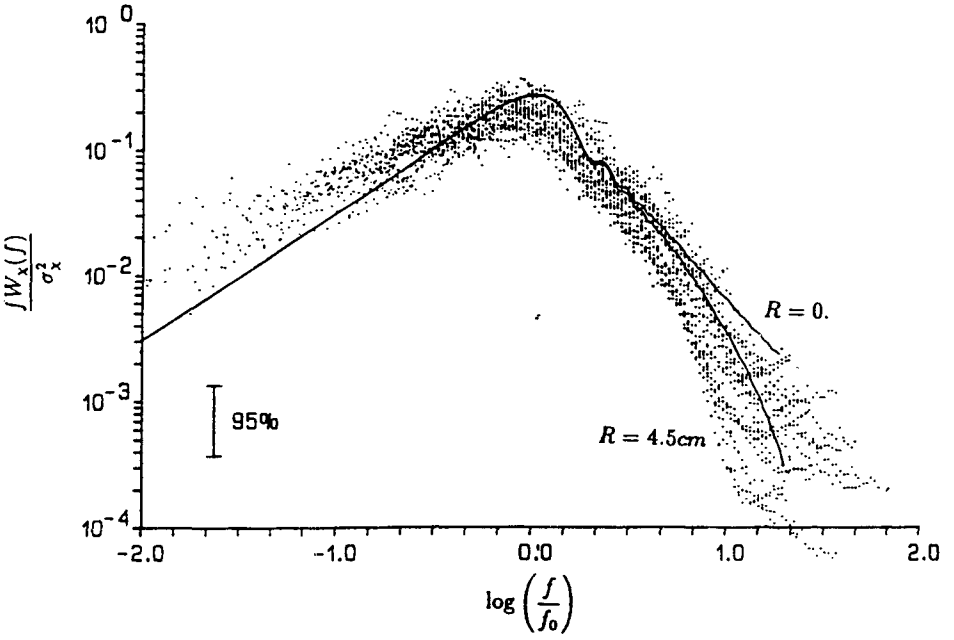

Figure 5.12: Theoretical (solid curves) log-amplitude spectra showing the effects of aperture averaging and twenty experimental (dots) log-amplitude spectra taken through a tidal cycle superimposed. Normalizing frequency is defined as $f_0 = U/(\lambda L)^{1/2}$.

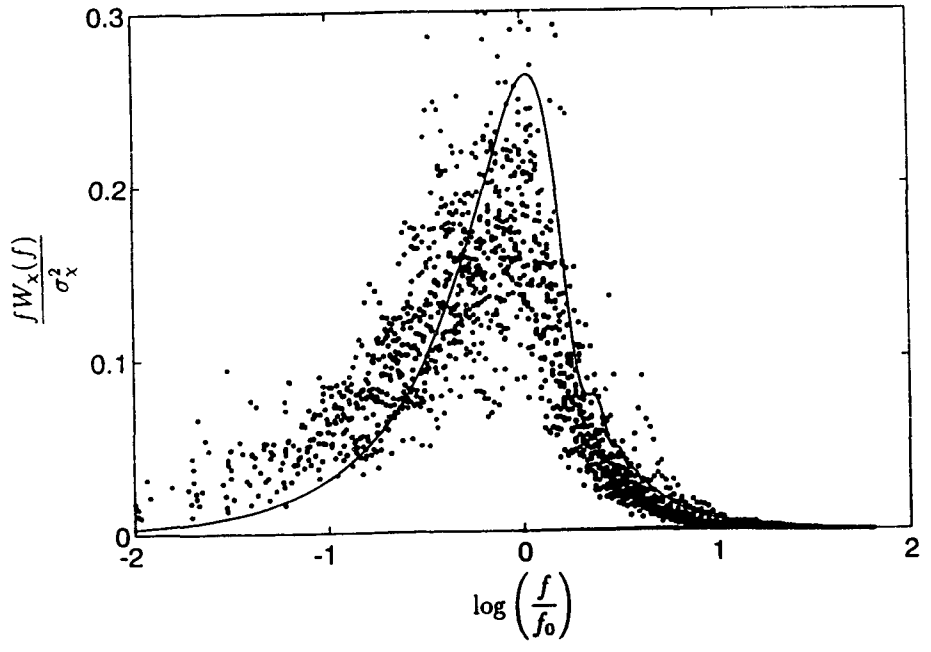

Figure 5.13: Variance preserving plot of the theoretical (solid curve) log-amplitude spectra and twenty experimental (dots) spectra taken through a tidal cycle superimposed. Normalizing frequency is defined as $f_0 = U/(\lambda L)^{1/2}$ for $(\lambda L)^{1/2} = 3.8m$.

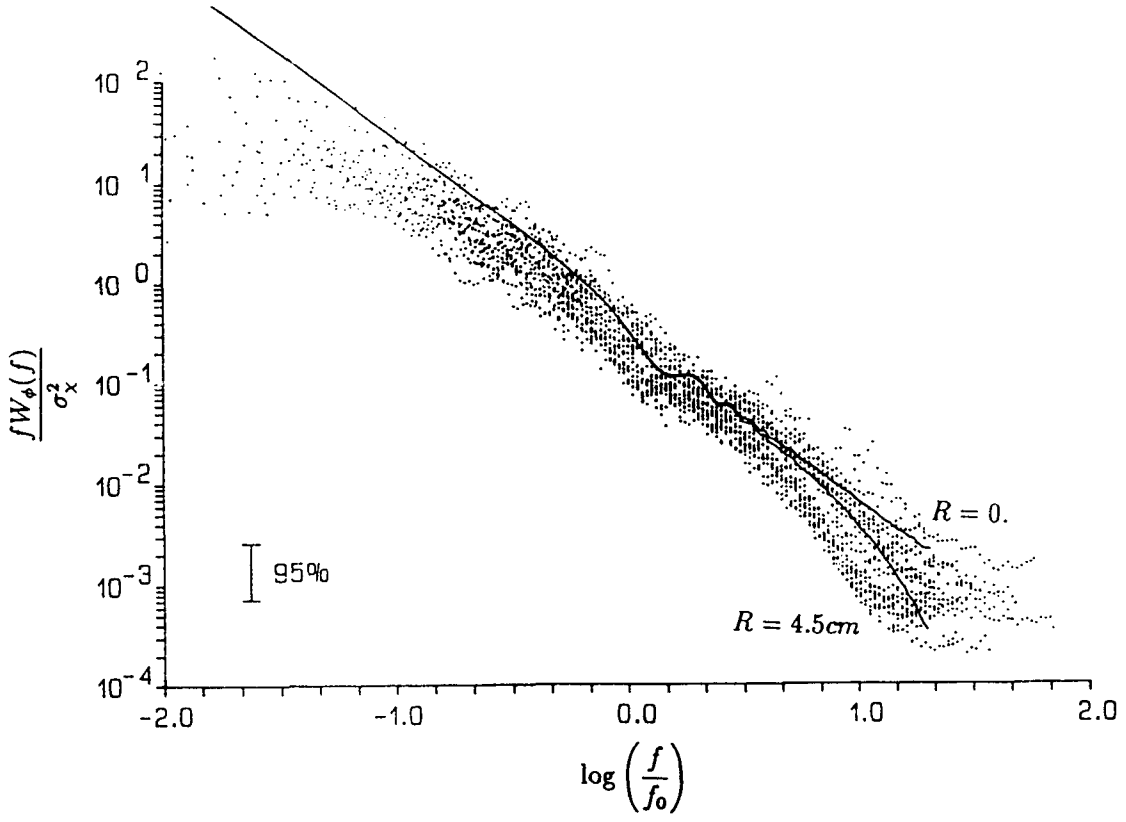

Figure 5.14: Theoretical (solid curves) phase spectra showing the effects of aperture averaging and twenty experimental (dots) phase spectra taken through a tidal cycle superimposed. Normalizing frequency is defined as $f_0 = U/(\lambda L)^{1/2}$.

This result is presented in order to show the connection with results given in other studies (Ewart *et.al.* [21]).

Phase perturbations accumulate throughout the path and include contributions from the largest scales. The solid curves of Figure 5.14 are the theoretical phase spectra showing aperture averaging effects. Experimental data processed in the same way as the log-amplitude time series are superimposed. The log-amplitude variance is used as the normalization for the phase because it is impossible to define the variance of the phase fluctuations without introducing other parameters such as the outer scale. Inclusion of the aperture averaging provides a better fit at high frequencies except at the highest frequencies where noise exists. The predicted modulation of the spectrum by the diffraction is reproduced in the observed spectra.

Phase difference spectrum

The temporal power spectrum for the phase difference from horizontal diverging acoustic paths defined by (3.35), taking into account aperture averaging effects, is,

$$W_{\delta\phi_x}(f) = 32\pi^2 k^2 \int_0^L dy \int_{\kappa > \frac{2\pi f}{U}}^{\infty} d\kappa \frac{\kappa \Phi_n(\kappa)}{((\kappa U)^2 - (2\pi f)^2)^{1/2}} \sin^2\left(\pi \frac{f\rho_x}{U}\frac{y}{L}\right) \cos^2\left(\frac{\kappa^2 y(L-y)}{2kL}\right) \exp\left(\frac{-\kappa^2 R^2}{L^2}(y^2 + (L-y)^2)\right). \quad (5.20)$$

The phase structure function evaluated at zero time lag is then defined as the phase difference variance which is defined by,

$$D_\phi(\rho_x, \tau = 0) = \sigma^2_{\delta\phi_x} = 2\int_0^\infty W_{\delta\phi_x}(f) df. \quad (5.21)$$

The $\sin^2$ term in (5.20) suggests a frequency scaling ($f_{1_x} = U/\rho_x$) for this measurement. Inserting the Kolmogorov spectrum defined by (3.7) and making the substitutions, $s = y/L$ and $\gamma^2 = (\kappa U/2\pi f)^2 - 1$ gives,

$$W_{\delta\phi_x}(f) = a_3 C_n^2 k^2 L \rho_x^{8/3} U^{-1} \left(\frac{f}{f_{1_x}}\right)^{-8/3} \int_0^1 ds \int_{\gamma>0}^\infty \frac{d\gamma}{(\gamma^2+1)^{11/6}} \sin^2\left(\pi \frac{f}{f_{1_x}} s\right) \cos^2\left(\pi \left(\frac{f}{f_{1_x}}\right)^2 \frac{\lambda L}{\rho_x^2}(\gamma^2+1)s(1-s)\right) \exp\left(-4\pi^2 \left(\frac{R}{\rho_x}\frac{f}{f_{1_x}}\right)^2 (\gamma^2+1)(s^2 + (1-s)^2)\right), \quad (5.22)$$

where the coefficient $a_3 = 8(0.033)(2\pi)^{-2/3} = 0.0775$. The Kolmogorov $-11/3$ power law is in the $(\gamma^2+1)^{11/6}$ term, the diffraction is included in the $\cos^2$ term and aperture averaging is the exponential term.

A proper normalization to apply to the phase difference spectrum is the wave structure function for diverging acoustic paths defined by (C.15). The wave structure function is dominated by the phase measurement so that $D(\rho, \tau = 0) \sim D_\phi(\rho, \tau = 0)$. Taking into account the frequency scaling, f_1 and the wave structure function (C.15), we normalize the phase difference spectrum. Thus, for horizontally spaced receivers,

$$\frac{fW_{\delta\phi_x}(f)}{D(\rho_x,\tau=0)} = a_4\left(\frac{f}{f_{1_x}}\right)^{-5/3}\int_0^1 ds\int_{\gamma>0}^{\infty}\frac{d\gamma}{(\gamma^2+1)^{11/6}}$$
$$\sin^2\left(\pi\frac{f}{f_{1_x}}s\right)\cos^2\left(\pi\left(\frac{f}{f_{1_x}}\right)^2\frac{\lambda L}{\rho_x^2}(\gamma^2+1)s(1-s)\right)$$
$$\exp\left(-4\pi^2\left(\frac{R}{\rho_x}\frac{f}{f_{1_x}}\right)^2(\gamma^2+1)(s^2+(1-s)^2)\right), \tag{5.23}$$

where the coefficient $a_4 = 8(0.033)(2\pi)^{-2/3}/1.0889 = 0.0712$.

A similar expression exists for the phase difference spectrum using vertically spaced receivers. Using (3.37) with aperture averaging effects and applying similar substitutions and normalizations gives,

$$\frac{fW_{\delta\phi_z}(f)}{D(\rho_z,\tau=0)} = a_4\left(\frac{f}{f_{1_z}}\right)^{-5/3}\int_0^1 ds\int_{\gamma>0}^{\infty}\frac{d\gamma}{(\gamma^2+1)^{11/6}}$$
$$\sin^2\left(\pi\frac{f}{f_{1_z}}s\gamma\right)\cos^2\left(\pi\left(\frac{f}{f_{1_z}}\right)^2\frac{\lambda L}{\rho_z^2}(\gamma^2+1)s(1-s)\right)$$
$$\exp\left(-4\pi^2\left(\frac{R}{\rho_z}\frac{f}{f_{1_z}}\right)^2(\gamma^2+1)(s^2+(1-s)^2)\right), \tag{5.24}$$

Figure 5.15 shows the theoretical (based on Kolmogorov's spectrum) and experimental phase difference spectra for horizontally spaced receivers as a function of $\log(f/f_{1_x})$ which are calculated by the same procedure as the log-amplitude and phase spectra. This time, however each spectrum is normalized by the wave structure function. The data fit very well to the aperture averaging theory at high frequencies. At low frequencies the phase difference is more sensitive to the outer scale, L_o than the phase or log-amplitude. This is because the log-amplitude is most sensitive to scales of the order $\sqrt{\lambda L} \ll L_o$ and the phase is most sensitive to large scales even those greater than L_o.

Measurement shows that the spectral peak in Figure 5.15 occurs at $f = 0.22 f_{1_x}$ consistent with the theory (see Tatarskii [52]). This spectral peak corresponds to scales sizes $\ell \approx 4.5\rho_x$. The peak, however, is very broad in comparison to the log-amplitude spectra. This implies that the phase difference measurement is sensitive

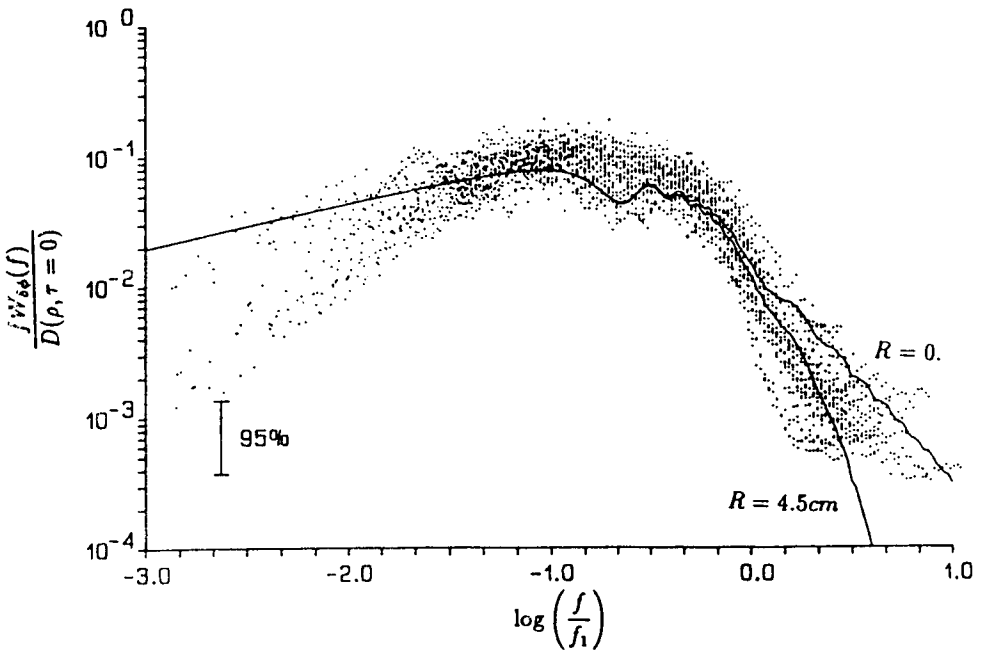

Figure 5.15: Theoretical (solid curve) phase difference spectra for horizontally spaced receivers showing the effects of aperture averaging and twenty experimental (dots) phase difference spectra taken through a tidal cycle superimposed. Normalizing frequency is defined as $f_{1_x} = U/\rho_x$ where $\rho_x = 0.61m$.

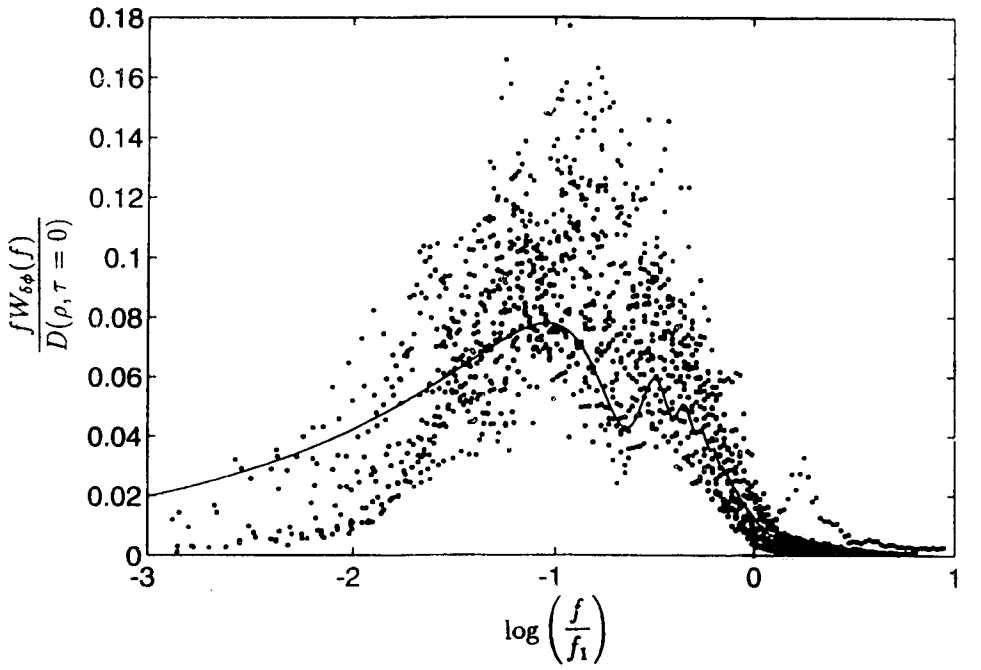

Figure 5.16: Variance preserving plot of the theoretical (solid curve) phase difference spectrum for horizontally spaced receivers and twenty experimental (dots) spectra taken through a tidal cycle superimposed. Normalizing frequency is defined as $f_{1_x} = U/\rho_x$ for $\rho_x = 0.61m$.

to scale sizes ranging from the receiver separation to ten times the separation. The modulation to the spectrum by diffraction can also be seen in the data. It should be mentioned that since these results are normalized by the measured flow speed, corresponding spectra are not found at slack water.

In order to see that scale size $\ell = 4.5\rho_x$ contributes most to the phase difference variance the spectra are plotted on a linear scale (see Figure 5.16). Again, equal areas under the curves represent equal contribution to the phase difference variance. Spectra for vertically spaced receivers show a peak corresponding to scale size $\ell = 16.6\rho_z$. They are shown in section 5.6 for comparison with the spectra for horizontally spaced receivers.

Thus, experimental log-amplitude, phase and phase difference temporal spectra agree quite well with the theory including aperture averaging effects. These results indicate that during times of current flow, Cordova Channel can be characterized as having fully developed turbulence within which the Kolmogorov scaling laws apply. These results also indicate that the weak scattering theory is appropriate in describing the log-amplitude, phase and phase difference measurements.

5.4 Path Averaged Oceanographic Measurements Assuming Isotropic Turbulence

5.4.1 Turbulent outer scale (L_o) estimate

Clifford *et.al.* [9] and Lataitis *et.al.* [34] arbitrarily introduce an outer scale, L_o as a variable through the von Karman spectrum (Hinze [31]) for the refractive index fluctuations,

$$\Phi_n(\kappa) = \frac{0.033 C_n^2}{(\kappa^2 + \kappa_o^2)^{11/6}}, \tag{5.25}$$

where $\kappa_o = 2\pi/L_o$. Insertion of (5.25) into the phase difference spectrum for horizontally spaced receivers defined by (5.20) and introducing the normalizations, $f_{1_x} = U/\rho_x$, $f_m = \frac{\kappa_o U}{2\pi} = U/L_o = f_{1_x}\rho_x/L_o$, $\gamma^2 = (\kappa U/2\pi f)^2 - 1$, and $s = y/L$ gives,

$$W_{\delta\phi_x}(f) = a_3 C_n^2 k^2 L \rho_x^{8/3} U^{-1} \left(\frac{f}{f_{1_x}}\right)^{-8/3} \int_0^1 ds \int_{\gamma>0}^{\infty} \frac{d\gamma}{(\gamma^2 + 1 + (f_m/f)^2)^{11/6}} \sin^2\left(\pi \frac{f}{f_{1_x}} s\right) \cos^2\left(\pi \left(\frac{f}{f_{1_x}}\right)^2 \frac{\lambda L}{\rho_x^2}(\gamma^2+1)s(1-s)\right) \exp\left(-4\pi^2 \left(\frac{R}{\rho_x}\frac{f}{f_{1_x}}\right)^2 (\gamma^2+1)(s^2+(1-s)^2)\right). \tag{5.26}$$

Using the wave structure function defined by (C.15) as a normalization finally gives,

$$\frac{f W_{\delta\phi_x}(f)}{D(\rho_x, \tau=0)} = a_4 \left(\frac{f}{f_{1_x}}\right)^{-5/3} \int_0^1 ds \int_{\gamma>0}^{\infty} \frac{d\gamma}{(\gamma^2 + 1 + (f_m/f)^2)^{11/6}} \sin^2\left(\pi \frac{f}{f_{1_x}} s\right) \cos^2\left(\pi \left(\frac{f}{f_{1_x}}\right)^2 \frac{\lambda L}{\rho_x^2}(\gamma^2+1)s(1-s)\right) \exp\left(-4\pi^2 \left(\frac{R}{\rho_x}\frac{f}{f_{1_x}}\right)^2 (\gamma^2+1)(s^2+(1-s)^2)\right). \tag{5.27}$$

It should be noted that the wave structure function used as a normalization is evaluated for $l_o = \infty$.

The phase difference is used to measure L_o because it is more sensitive to the outer scale than the log-amplitude or phase. This is because the log-amplitude is primarily

sensitive to $\sqrt{\lambda L} \ll L_o$ and the phase is sensitive to larger scales including those scales $> L_o$. Also, horizontally instead of vertically spaced receivers are used since the depth of the channel imposes a bound on the vertical eddy scale. The theoretical curves for the normalized phase difference spectrum as a function of $\log(f/f_{1_x})$ and as a function of the outer scale L_o are shown in Figure 5.17 taking into account aperture averaging. We can use these curves as a template to estimate an outer scale L_o that best fits the measured phase difference spectra at low frequencies under the assumption implicit in (5.25). However, it is important to emphasize that the resulting comparison is one-dimensional.

Comparison of Figure 5.15 with Figure 5.17 shows that the minimum outer scale that can be inferred by this comparison is 16 m. Most of the time the data are consistent with $L_o \geq 32$ m. The implication is that the horizontal properties of the flow can exhibit the same spectral properties outside the inertial subrange as predicted for isotropic turbulence, even though the channel depth provides a 32 m bound on the vertical eddy scale. This result is not inconsistent with reported observations of a -5/3 spectral slope extending beyond the inertial subrange in the one dimensional turbulent kinetic energy spectrum (see Gargett *et.al.* [26]).

The normalized phase difference spectrum shown in Figure 5.18 was acquired when there was slight stratification (see temperature profile in Figure 5.3(b) 21/10/86 2015h) and a current velocity of -0.55 m s^{-1} (see A_s in Figure 5.3(a)). The theoretical spectrum for an outer scale of $L_o = 16$ m and magnitude adjusted by a factor of two, is superimposed with the measured spectrum of the phase difference. This factor of two is introduced because of the decrease in spectral level for decreasing L_o shown in Figure 5.17. In order to maintain the same spectral level the wave structure function $D(\rho, 0)$ and hence C_n^2 would have to decrease with decreasing L_o and then this should be used as an appropriate normalization. Hence, our measurement of the wave structure function at $L_o = 16m$ is approximately half that at $L_o = \infty$.

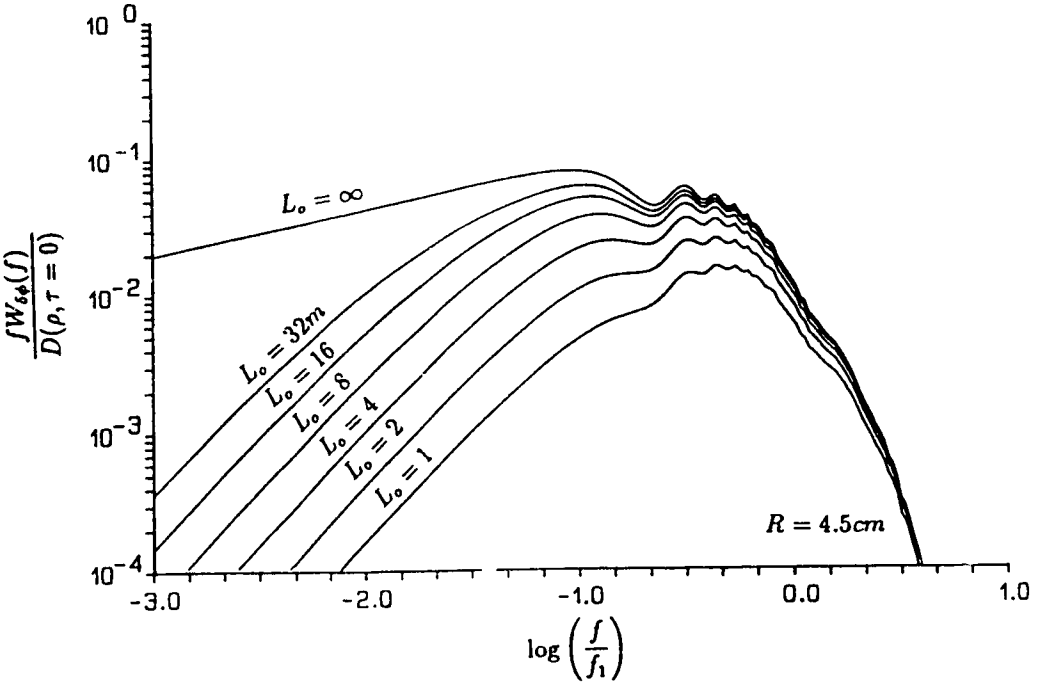

Figure 5.17: Theoretical curves for the phase difference spectra with aperture averaging ($R = 4.5\ cm$) as a function of L_o. The Kolmogorov spectrum is identified as $L_o = \infty$ and the receiver spacing is $\rho_x = 0.61m$.

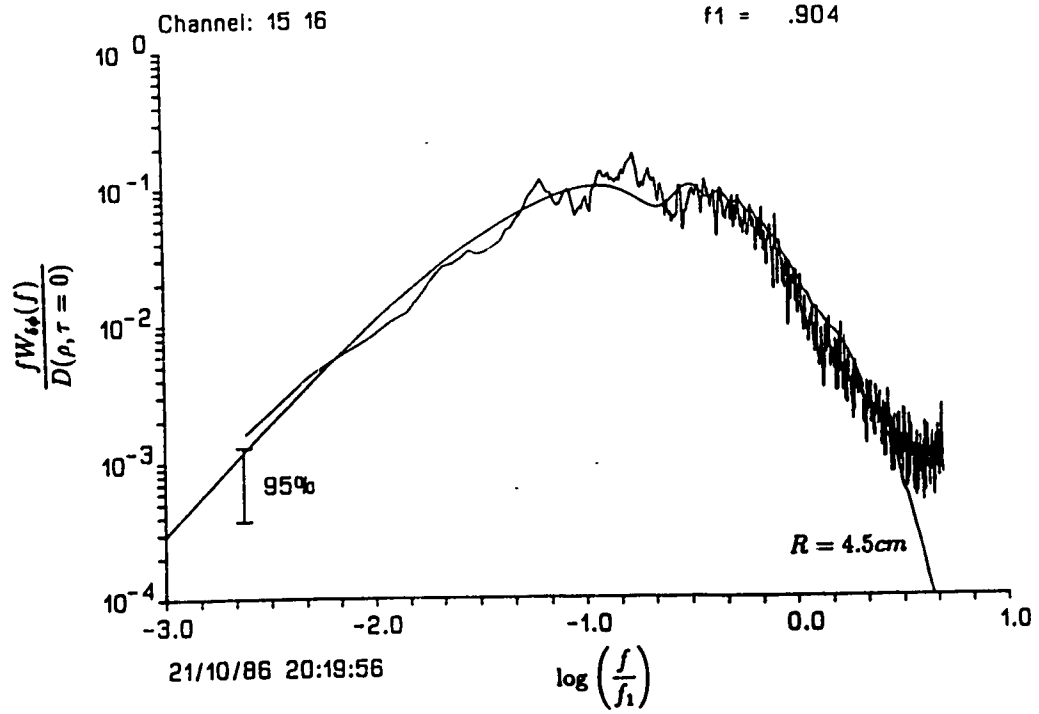

Figure 5.18: Phase difference spectrum during a time of stratification when an outer scale of 16 metres is inferred (see A_s on Figure 5.3(a)). The level of the theoretical spectrum is adjusted by a factor of two and the receiver spacing is $\rho_x = 0.61m$.

5.4.2 Current speed

The application of acoustical scintillation theory using spherical acoustic waves diverging from one acoustic source has been successfully demonstrated by Farmer *et.al.* [24] for the remote sensing of current flow. In addition, Farmer and Crawford [25] measured the cross-channel current distribution using the dominant frequency of a spatial aperture filter, obtainable from the linear array. In this section the current is calculated using parallel acoustic signals (two horizontally spaced transmitters and receivers) in order to test the concept of along channel flow speed measurements. The motivation for using acoustic scintillation techniques for measuring current is that it gives a path averaged measurement and it is this measurement that will be used in subsequent analysis whenever U is required. Also, these measurements can be made in real time and the system can be deployed for long periods of time (longer than any conventional current meter).

There are three different ways that the current perpendicular to the acoustic path can be determined. This section will compare all of them since some methods work better than others (refer to Appendix B for a complete derivation of the following equations and the assumptions made to obtain them). The slope at zero time lag of the normalized log-amplitude cross covariance function and the normalized wave structure function provide two methods to determine current speed. The third method takes into account the time delay to the peak of the normalized log-amplitude cross covariance function. These equations are as follows (see (B.6), (B.13) and (B.16) respectively),

$$\overline{U} = R_p \frac{\partial C_{N_X}(\rho_x, \tau)}{\partial \tau}\bigg|_{\tau=0}, \tag{5.28}$$

$$\overline{U} = -\frac{3}{5}\rho_x \frac{\partial D_N(\rho_x, \tau)}{\partial \tau}\bigg|_{\tau=0}, \tag{5.29}$$

$$\overline{U} = \frac{\rho_x}{\tau_p}, \tag{5.30}$$

where the overbar indicates a path averaged quantity and the calibrating factor R_p is listed in Table 5.2. The significance of the parameter $\beta = \rho_x/\sqrt{\lambda L}$ is described in

f_a (Hz)	ρ_x (m)	β	R_d	R_p
67567	0.61	0.1589	1.2703	1.1263
67567	1.22	0.3179	1.2747	2.0565
67567	1.18	0.3075	1.2661	1.9294
69444	1.18	0.3118	1.2520	1.9530

Table 5.2: Calibrating factor R for current speed determination based on diverging acoustic paths (d) and parallel acoustic paths (p).

Appendix B.1. Also, the relative weight to the current measurement from different parts along the channel is described in Appendix B.1 and B.2. The current speed measured from the slope of the log-amplitude cross covariance is weighted towards the center of the channel whereas the current speed measured from the slope of the wave structure function for parallel paths is uniform.

Calculation of current is based on bandpass filtered log-amplitude ($U/32 < f < 6.3\ Hz$) and phase ($U/32 < f < 4.5\ Hz$) data (see Figure 5.7). The absence of high-pass filtering allows larger scale features, which cannot be presumed to satisfy Taylor's hypothesis, to influence the observations and thus render the weak scattering theory invalid (see Farmer and Clifford [23]). Figure 5.19 compares the acoustic measurements of current flow using the normalized log-amplitude cross covariance function (5.28), the normalized wave structure function (5.29) and the delay to peak (5.30) with that obtained from a 16 m current meter at station 2o. It should be emphasized that our acoustic measurements are path averaged with specific weighting across the channel and the current meter gives a point measurement.

Poor results from the log-amplitude cross covariance technique (5.28) can be explained for the case of $\rho_x = 1.18\ m$ during the square array deployment period. Figure 5.9 shows an example of the cross covariance function $C_{N_\chi}(\rho_x, \tau)$ during strong ebb and close to slack water. The slope at zero time lag during strong ebb for parallel paths is calculated at low correlation. The low correlation is a consequence of the

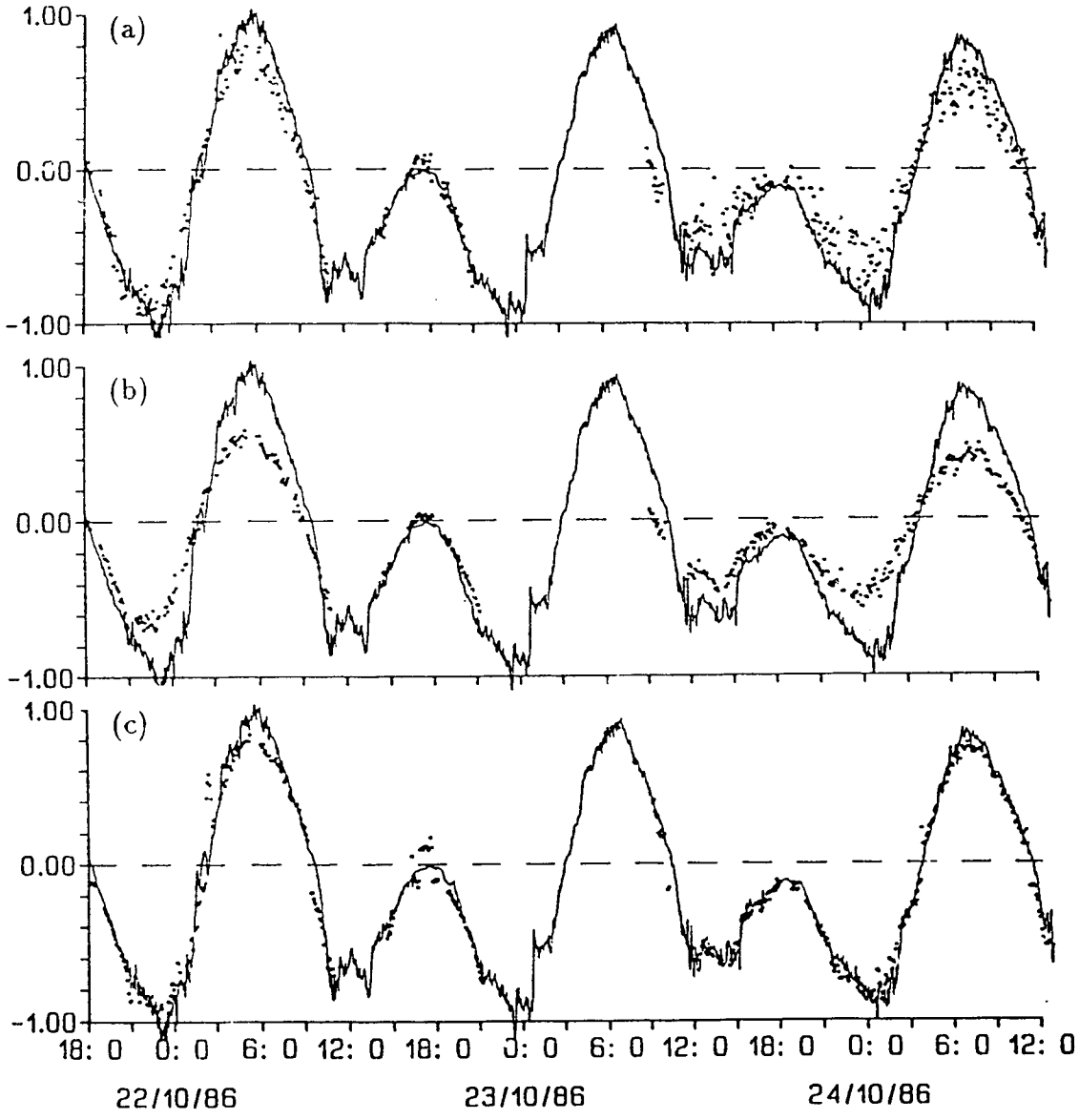

Figure 5.19: Comparison of the along channel current component observed by a 16 m current meter at station 2 (solid curve) with acoustical scintillation techniques (dots) using (a) the slope of the normalized log-amplitude cross covariance function (5.28), (b) the slope of the normalized wave structure function (5.29) and (c) the delay to peak (5.30) using 5 minute averages.

fact that the receiver spacing ($\rho_x = 1.18\ m$) is much greater than the correlation scale. Ideally, the receiver spacing should be chosen such that at maximum flow, zero time lag occurs at half the height of the correlation function. Mathematically, the conditions are (see Appendix B.1),

$$\beta_p = \frac{\rho_x}{\sqrt{\lambda L}} = 0.15 \qquad \text{parallel paths,} \tag{5.31}$$

and,

$$\beta_d = \frac{\rho_x}{\sqrt{\lambda L}} = 0.33 \qquad \text{diverging paths.} \tag{5.32}$$

From Figure 5.8 and Figure 5.10, the spacing 0.61 m during the linear array deployment works well for parallel paths. This explains why the first half of the current time series follows the current meter better than the second half.

The wave structure function technique (5.29) underestimates the current flow by a factor of 1.5–2 throughout the time series. In addition, the current speed determined from diverging paths and this same method also underestimates the flow by the same amount. This is rather peculiar since the experiment described by Farmer *et.al.* [24] is virtually identical to this experiment and their results show excellent agreement for diverging paths although the location of the current meter in their experiment was somewhat different.

Figure 5.20 shows the theoretical and the measured wave structure function during strong ebb flow ($-0.85\ m\ s^{-1}$). The measured wave structure function is calculated for both low pass filtered and band pass filtered data. The theoretical function is determined from the current speed calculated by the delay to peak method. The measured structure function for both data types (low pass filtered and band pass filtered) is flattened compared to the theoretical structure function hence reducing the slope at zero time lag. Regardless of whether the data are low pass filtered or band pass filtered the calculated current speed gives essentially the same result.

The delay to peak method works very well except close to slack water. The breakdown at slack water results from the fact that the time lag is not defined for zero flow. Computationally, it is only practical to have maximum time lags of $\pm 10.0s$

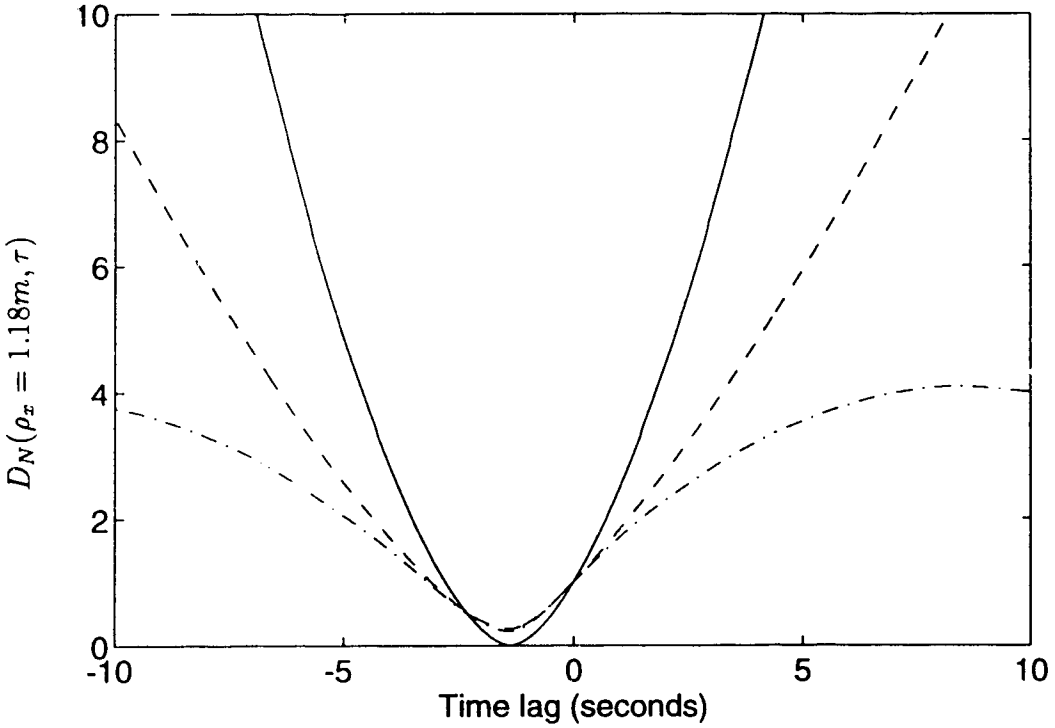

Figure 5.20: Theoretical (solid curve) and measured wave structure function during a strong ebb of $-0.85\ m\ s^{-1}$ on 24/10/86 0000h. Low pass filtered data are shown as a dashed curve and band pass filtered data are shown as a dash-dot curve.

for parallel paths (see Figure 5.9). This means that the smaliest current flow that can be measured by the peak delay method is $\pm 0.12\ m\ s^{-1}$. The slope technique, however, successfully measures very slow current speeds and computationally is very simple since only one point on each side of zero time lag is needed.

Using the square receiving array and the moored current meters at two depths we can calculate the mean shear in the along channel direction. First, the shear is evaluated using current meters at 15 and 16 metres depth. Second, the shear is calculated based on acoustic measurements of the current using top and bottom horizontal receivers and the delay to peak method using parallel paths. The acoustic method is desirable since it gives a path averaged measurement. The results are shown in Figure 5.21(b) and (c) respectively. The current speed from the current meter (solid curve) and from the acoustic technique (dots) are shown for comparison in Figure 5.21(a).

The current meter shear is calculated by applying a moving average filter to the

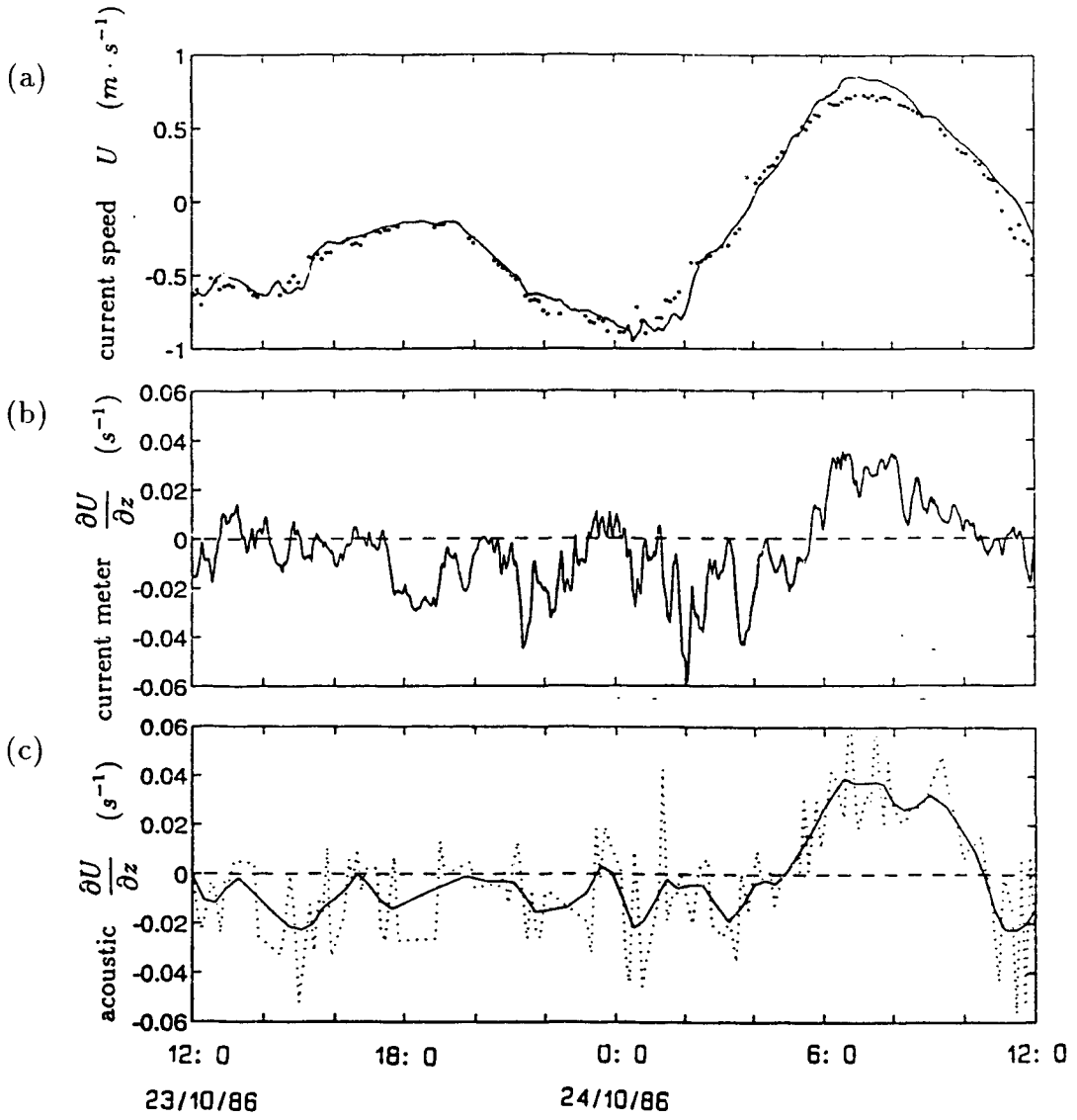

Figure 5.21: (a)The current speed obtained from a 15 m current meter at station 2 (solid curve) and from acoustic delay to peak method for parallel paths (dots). The mean vertical shear $\partial U/\partial z$ determined by (b) two vertically spaced current meters and by (c) the acoustic data. Dotted line represents 7.5 minute averages and solid line represents 15 minute averages obtained from a moving average filter over 30 minutes.

current time series from each depth and then taking the difference. The acoustic shear is evaluated by obtaining 7.5 minute averages of current speed from each depth, applying a moving average filter over 30 minutes of data and then finally subsampling to obtain 15 minute averages of current speed. The resulting difference is then computed. The dotted line shows the difference from 7.5 minute averages and the solid curve represents the difference from the filtered time series. Comparing the shear from the current meter and the shear from the acoustic technique reveals a close agreement. The only time any significant shear exists ($0.04s^{-1}$) is during the flood. This corresponds to a time when anisotropy in the turbulence is observed (see section 5.6.2).

Based on the above analysis, subsequent discussions make use of either the log-amplitude cross covariance slope or peak delay method for calculating U. That is, data from the linear array make use of the slope technique and data from the square array make use of the delay technique.

5.4.3 C_n^2 variability

Rapid fluctuations in the refractive index are due to temperature, salinity and current velocity fluctuations. These small scale variations in the water properties are advected through the acoustical path. For a fully developed and uniform turbulent flow this variability is expressed in terms of the structure constant C_n^2 of the refractive index structure function. From section 3.1, the refractive index structure constant defines the level of the refractive index fluctuations. It can be determined using the acoustic information. The CTD time series together with the current measurement provides a way to determine $C_{n_s}^2$ — the level of the refractive index fluctuations due to scalar fluctuations.

The structure constant C_n^2 can be determined in two ways (see Appendix C for a full derivation) using the acoustic information. One method uses the log-amplitude variance σ_χ^2 and the other takes into account the wave structure function at zero time lag, $D(\rho, \tau = 0)$ for parallel acoustic paths. These equations are as follows (refer to (C.10) and (C.14) respectively),

$$C_n^2 = 8.091 k^{-7/6} L^{-11/6} \sigma_\chi^2, \tag{5.33}$$

$$C_n^2 = 0.344 k^{-2} L^{-1} \rho^{-5/3} D(\rho, \tau = 0), \tag{5.34}$$

where k is the acoustic wavenumber and L is the path length. These equations are derived on the basis of the assumptions of homogeneous and isotropic turbulence (see Tatarskii [52]). The relative weight to the C_n^2 measurement from different parts along the channel is described in Appendix C.1 and C.2. The structure parameter measured from the log-amplitude variance is weighted towards the center of the channel whereas the structure parameter measured from the wave structure function for parallel paths is uniform assuming C_n^2 is not strongly path dependent.

Figure 5.22(a) shows measurements of C_n^2, based on the log-amplitude variance, σ_χ^2 defined by (5.33) through the tidal cycle shown at the top of the figure. The variance is calculated from inhomogeneities having scale sizes less than 32 m. These

small scale variations in the water properties are advected through the acoustical path. Very low values of C_n^2 occur near slack water. These low values represent times at which well mixed water is moving relatively slowly through the channel. At strong tidal flows ($\sim \pm 1\ m\ s^{-1}$), C_n^2 is maximal.

The wave structure function is dominated by the phase properties so that $D(\rho, \tau = 0) \sim D_\phi(\rho, \tau = 0)$. Figure 5.22(b) shows measurements of C_n^2 based on the wave structure function method defined by (5.34) through the tidal cycle. These measurements are consistent with the log-amplitude variance method for obtaining C_n^2. The difference in the levels corresponds to the different scale sizes to which the functions are sensitive. Log-amplitude fluctuations are primarily sensitive to the Fresnel length (3.8 m) whereas the wave structure function is sensitive to a broad range of scale sizes: from the receiver separation (0.61m and 1.18m) to approximately ten times the separation (see spectral characteristics discussion in section 5.3.4). Also, differences may occur because of the different weighting on C_n^2 from different parts of the channel.

The scalar refractive index fluctuations $C_{n_s}^2$ can be calculated from the one-dimensional spectral density using conductivity, temperature and depth (CTD) time series data acquired at the depth of the acoustic paths. This spectrum represents the scalar contribution to the refractive index fluctuations. The spectrum is obtained from the *in situ* time series by computing the sound speed time series $c(t)$ from (5.4) based on temperature (see Figure 5.3(c)) and salinity measurements, converting to refractive index fluctuations $\eta(t) = \frac{<c>}{c(t)} - n_o$, generating 8 overlapping segments of 1024 data points, fast Fourier transforming (FFT), and then finally averaging the 8 spectra to obtain the one-dimensional spectrum. Detrending and windowing preceded each FFT. Frequency space is transformed to wavenumber space ($\kappa = 2\pi f/U$) assuming the Taylor hypothesis.

From (2.21), the three-dimensional spectrum can be estimated from the one-

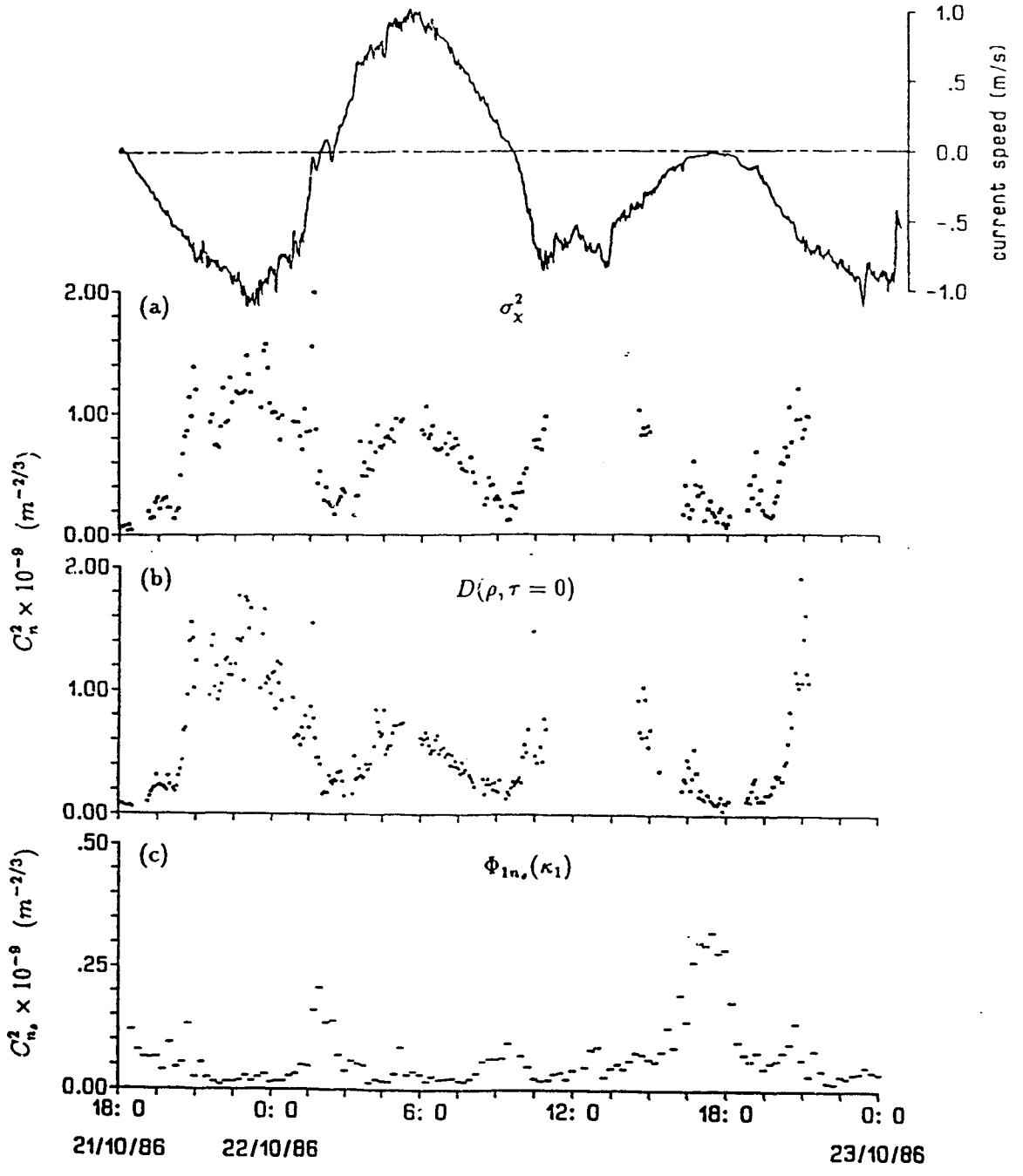

Figure 5.22: (top) Current speed for 30 hours of data. (bottom) Structure parameter C_n^2 (•) calculated from (a) the acoustic log-amplitude variance, σ_χ^2 (5.33) and (b) the wave structure function, $D(\rho, \tau = 0)$ (5.34). (c) Structure parameter $C_{n_s}^2$ (-) calculated from the level of the one-dimensional spectrum of the refractive index fluctuations based on CTD and current meter measurements, $\Phi_{1n_s}(\kappa_1)$ (5.36).

dimensional spectrum assuming isotropy (see Hinze [31]) by,

$$\Phi_{n_s}(\kappa_1) = \frac{-1}{2\pi\kappa_1}\frac{\partial\Phi_{1n_s}}{\partial\kappa_1} = .033C_{n_s}^2\kappa_1^{-11/3}, \tag{5.35}$$

giving,

$$\Phi_{1n_s}(\kappa_1) = a_5 C_{n_s}^2 \kappa_1^{-5/3}, \tag{5.36}$$

where the coefficient $a_5 = 2\pi(0.033)(3/5) = 0.124$ and C_{n_s} is the level of the refractive index fluctuations due to scalar fluctuations (temperature and salinity). The corresponding frequency spectrum is,

$$W_{n_s}(f) = a_5\left(\frac{U}{2\pi}\right)^{2/3} C_{n_s}^2 f^{-5/3}. \tag{5.37}$$

Figure 5.23 shows the one-dimensional spectrum for refractive index fluctuations from scalars as a function of wavenumber (κ_1). This spectrum corresponds to the 21/10/86 2017h time series in Figure 5.3(b) and corresponds to the time A_s in Figure 5.3(a). The outer scale from Figure 5.18 during this time is estimated to be approximately 16 m ($\kappa_o = 0.39\ rad\ m^{-1}$) (see section 5.4.1). A -5/3 slope is also shown for comparison. Since the time series is short (12 minutes) an attempt was made to compute the low wavenumber region using 2 segments of 2048 data points. However, intermittency of the temperature fluctuations introduces some uncertainty into the low wavenumber part of the spectrum.

Based on an outer scale limit, $C_{n_s}^2$ due to scalar fluctuations can be calculated by averaging $\Phi_{1n_s}\kappa_1^{5/3}/a_5$, derived from the CTD time series, over wavenumbers $\kappa_1 > 2\pi/L_o$ where $L_o = 32\ m$ is determined from the phase difference spectrum (see section 5.4.1) and is an upper bound for the inertial subrange. Choosing this large outer scale makes very little difference to the measurement of the scalar refractive index fluctuations since the -5/3 slope applies at these wavenumbers.

Point measurements of $C_{n_s}^2$ in this way can then be compared to the path averaged acoustically derived values of the structure constant C_n^2, which include the effect of both scalar variability and velocity contributions. The refractive index structure parameter determined from the CTD data (Figure 5.22(c)) is compared with the

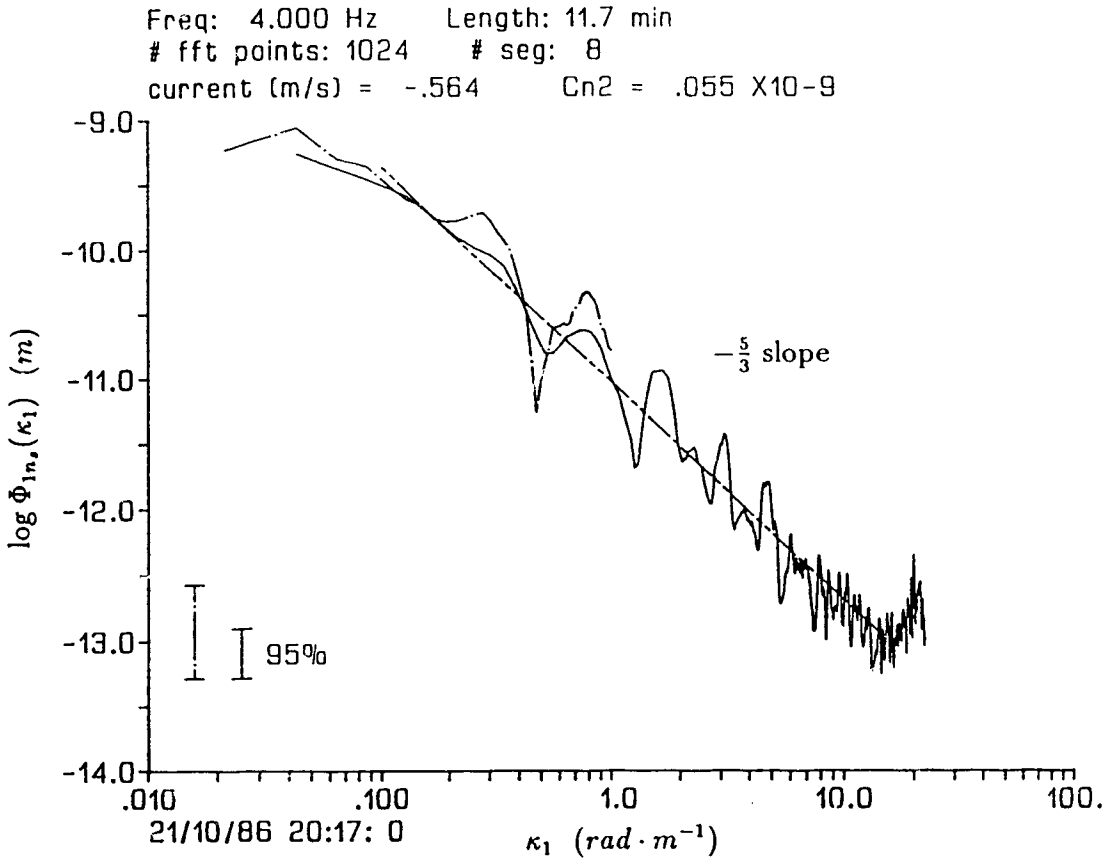

Figure 5.23: The one-dimensional spectral density (two-sided) of the scalar refractive index fluctuations from CTD data when an outer scale of 16 m could be inferred (see A_s in Figure 5.3(a)). Solid curve is based on 1024 point FFT and broken curve is based on 2048 point FFT. A -5/3 slope is shown for comparison.

acoustically derived values in Figure 5.22(a) and (b). Two features stands out. First, the CTD derived values of $C_{n_s}^2$ exhibit peaks close to slack water, presumably associated with advection of imperfectly mixed water. These peaks occur at the same time as the *acoustically* derived C_n^2 time series exhibit minima. Thus the peaks in $C_{n_s}^2$ are quite unrelated to the peaks in C_n^2. Second, except during peaks in the $C_{n_s}^2$ time series which occur briefly at slack water, the values of $C_{n_s}^2$, are at most one quarter of the values of C_n^2, and generally very much less.

The difference between the *in situ* derived values of $C_{n_s}^2$ and the much greater acoustically derived values of C_n^2 imply that turbulent velocity fluctuations must be

the dominant component of the acoustical scintillation.

Another feature that stands out is during ebb flow C_n^2 is greater than the flood flow measurements whereas C_{n_s} shows no difference between ebb and flood flow. This could be explained in terms of the channel geography (see Figure 5.1). During ebb flow eddies generated by the flow interacting with Saanichton Bay are advected through the measurement area thus increasing the level of turbulent velocity fluctuations. These eddies may be generated because of flow separation (see Schlichting [48]) as a result of flow around Cordova spit (the peninsula forming Saanichton Bay). During flood flow there is relatively smooth flow through the channel.

5.4.4 Turbulent kinetic energy dissipation (ϵ)

In section 5.4.3 we have shown that the velocity fluctuations must dominate the acoustical scintillations in the experimental results. In order to make measurements of velocity fluctuations we first define the statistical quantities for vector random fields. First, the velocity correlation tensor is defined as,

$$B_{jk}(\boldsymbol{\rho}) =< u_j(\mathbf{r})u_k(\mathbf{r}+\boldsymbol{\rho}) > \tag{5.38}$$

for homogeneous velocity fluctuations. This correlation matrix has six independent elements, but for isotropic turbulence the number of independent functions reduce to two. Second, the three-dimensional spectral density tensor is defined as,

$$\Phi_{jk}(\mathbf{K}) = \frac{1}{(2\pi)^3}\int\int\int e^{-i\mathbf{K}\cdot\boldsymbol{\rho}}B_{jk}(\boldsymbol{\rho})d\boldsymbol{\rho}, \tag{5.39}$$

with inverse

$$B_{jk}(\boldsymbol{\rho}) = \int\int\int e^{i\mathbf{K}\cdot\boldsymbol{\rho}}\Phi_{jk}(\mathbf{K})d\mathbf{K}. \tag{5.40}$$

Third, for isotropic and homogeneous turbulence the three dimensional spectral density tensor can be written as (see Hinze [31]),

$$\Phi_{jk}(\kappa) = \frac{E(\kappa)}{4\pi\kappa^2}\left(\delta_{jk} - \frac{K_jK_k}{\kappa^2}\right), \tag{5.41}$$

where δ_{jk} is the Kronecker function, and the total turbulent kinetic energy (per unit mass) is defined as

$$\frac{1}{2} < u_ju_j >= \int_0^\infty E(\kappa)d\kappa. \tag{5.42}$$

The wavenumber $\kappa^2 = K_jK_j$ and repeated indices denote summation over all components of the vector.

Tatarskii (personal communication) has pointed out that Ostachev [44] and [43] has recently determined the correct form of the spectral density for refractive index fluctuations from velocity fluctuations. The earlier work of Tatarskii [52] was based on the assumption of zero scattering angle between incident and scattered waves whereas

Ostachev [44] calculates the complete scattering cross section. He thus obtains the spectrum,

$$\Phi_{n_v}(\kappa) = \frac{n_j n_k \Phi}{c_o^2} \frac{\epsilon(\kappa)}{} = \frac{E(\kappa)}{4\pi\kappa^2 c_o^2} = 0.033(\frac{11}{6}C_{n_v}^2)\kappa^{-11/3}, \tag{5.43}$$

where $\hat{\mathbf{n}}$ is the unit vector in the direction of acoustic propagation and

$$E(\kappa) = 1.5\epsilon^{2/3}\kappa^{-5/3} \tag{5.44}$$

is the three-dimensional spectral density for velocity fluctuations (see Hinze [31]) and is the energy associated with a particular scale size $\ell = 2\pi/\kappa$. The turbulent kinetic energy dissipation rate (per unit mass) is expressed as ϵ and $C_{n_v}^2 = C_v^2/c_o$ is the refractive index structure parameter due to vector fluctuations. The total turbulent kinetic energy defined by (5.44) is based on the assumption that there exists a range of wavenumbers, between energy containing $(2\pi/L_o)$ and dissipating $(2\pi/\ell_o)$ wavenumbers, in which the turbulence is locally isotropic. The sound speed c_o in the denominator of (5 43) converts velocity fluctuations to refractive index fluctuations. If we write $\Phi_{n_v}(\kappa)$ in terms of $C_{n_v}^2$ as on the right of (5.43) then we can write

$$\frac{11}{6}C_{n_v}^2 = \frac{\epsilon^{2/3}}{c_o^2 a_6}. \tag{5.45}$$

where the coefficient $a_6 = 4\pi(0.033)/1.5 = 0.276$.

Thus the spectral density for refractive index fluctuations from scalar and velocity fluctuations is defined as,

$$\begin{aligned} \Phi_n(\kappa) &= \Phi_{n_s}(\kappa) + \Phi_{n_v}(\kappa) && (5.46)\\ &= 0.033\left(C_{n_s}^2 + \frac{11}{6}C_{n_v}^2\right)\kappa^{-11/3} && (5.47)\\ &= 0.033C_n^2\kappa^{-11/3}, && (5.48) \end{aligned}$$

where,

$$C_n^2 = C_{n_s}^2 + \frac{11}{6}C_{n_v}^2. \tag{5.49}$$

is the level of the refractive index fluctuations. It should be noted that Ostachev [44] developed his result by working with the square of the refractive index defined as

$n^2 = 1+\xi$. Throughout this thesis we define the squared refractive index as $n^2 = 1+2\eta$ and so our coefficient is 11/6 rather than 22/3 described by Ostachev [44]. Thus by measuring C_n^2 and $C_{n_s}^2$ we can retrieve $11/6C_{n_v}^2$ and thus obtain measurements of the turbulent kinetic energy dissipation from (5.45). The acoustic measurements are path averaged whereas the CTD measurements are an *in situ* measurement. Assuming a uniform distribution for $C_{n_s}^2$, an assumed path average structure parameter for the refractive index fluctuations due to velocity fluctuations can be derived.

The turbulent kinetic energy dissipation rate (per unit mass) calculated from (5.45) is then a path averaged measurement. The results are shown in Figure 5.24 (as +) for 30 hours of data. We calculate $\epsilon = 2.5 \times 10^{-5} m^2\ s^{-3}$ at strong tidal flow and $\epsilon = 3.2 \times 10^{-7} m^2\ s^{-3}$ close to slack water. These values are much higher than found in the open ocean, but are similar to those found by Grant *et.al.* [30] in Seymor Narrows (a tidal channel off Northern Vancouver Island). Their point measurements range from 1.5×10^{-7} to $1.02 \times 10^{-4}\ m^2\ s^{-3}$. Since C_n^2, calculated from the log-amplitude variance, is sensitive to the Fresnel scale, our dissipation measurement is calculated at that scale size. Hence, the dissipation together with the wavenumber corresponding to the Fresnel scale gives the energy associated with Fresnel scale eddies.

These measurements can be checked by using standard estimates for the turbulent kinetic energy dissipation. Within many well-mixed turbulent boundary layers there is a balance between the rate of production of turbulent kinetic energy through the Reynolds stress working on the mean shear and the rate of dissipation of that energy (see Dewey and Crawford [17]). In our channel flow we can use this similar balance to estimate the level to turbulent kinetic energy dissipation. Within a constant stress layer the Reynolds stress is equal to the bottom stress,

$$\tau_0 = \rho u_{*_0}^2, \tag{5.50}$$

and the mean shear follows the law of the wall,

$$\frac{\partial U}{\partial z} = \frac{u_{*_0}}{\mathcal{K} z}, \tag{5.51}$$

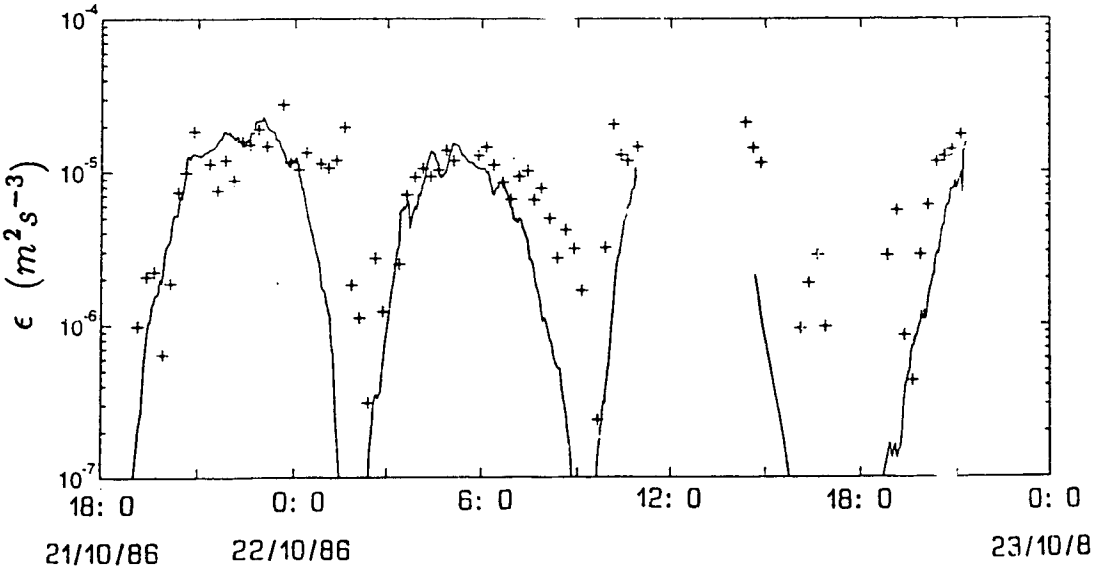

Figure 5.24: Path averaged turbulent energy dissipation (per unit mass) ϵ calculated through the tidal cycle (+) superimposed with theoretical estimates (solid curve) based on a balance between production and dissipation of turbulent energy.

where u_{*0} is the friction velocity measured in the constant stress layer, ρ is the density, $\mathcal{K} = 0.4$ is von Karman's constant and z is the distance from the boundary to the measurement depth within the constant stress layer. Therefore, for neutral stratification the turbulent energy dissipation rate ϵ (per unit mass) is,

$$\epsilon = \frac{\tau_0}{\rho}\frac{\partial U}{\partial z} = \frac{u_{*0}^3}{\mathcal{K}z}. \tag{5.52}$$

Since our acoustic paths are at mid depth of the channel we cannot assume that we are in a constant stress layer. However, it is justified to say that the stress measured at the depth of the acoustic paths is approximately half that in a constant stress layer region. This result arises because the pressure gradient $\frac{\partial P}{\partial x}$ in a channel flow is balanced by the stress gradient $\frac{\partial \tau}{\partial z}$ for zero change in momentum. Assuming that the pressure gradient is constant then the resulting stress τ varies linearly with depth having boundary conditions: $\tau = 0$ at the surface $z = D$, and $\tau = \tau_0$ near the bottom $z = 0$.

The friction velocity measured outside the constant stress layer can be related to

the mean current $U(z)$ through,

$$u_*^2 = C_D U^2, \tag{5.53}$$

where $u_*^2 \sim u_{*_0}^2/2$ for measurements outside the constant stress layer, C_D is the drag coefficient for U measured at some distance z from the boundary . For current speeds measured 1 $m = 100$ cm from the boundary (defined as U_{100}), Sternberg [49] measured a range of drag coefficients ($C_{D_{100}}$) from about 3×10^{-4} to 3×10^{-2} in tidal channels in Puget Sound and the Strait of Juan de Fuca.

The dissipation at mid depth when balance with the production is defined as,

$$\epsilon = \frac{\tau}{\rho_o}\frac{\partial U}{\partial z} = \frac{u_*^3}{\mathcal{K}z}. \tag{5.54}$$

In order to obtain a path averaged measurement of the dissipation we must integrate along the path giving,

$$\overline{\epsilon} = \frac{1}{L}\int_0^L \frac{C_D^{3/2}U^3(y)}{\mathcal{K}z(y)}dy. \tag{5.55}$$

In order to carry out the proper integration, some knowledge of the distribution of $U(y)$ and $z(y)$ is needed. We can use our path averaged current speeds ($\overline{U}$) determined by the slope of the log-amplitude cross covariance function for parallel paths during the linear array deployment (see section 5.4.2). The distance from the boundary to the measurement depth as a function of range ($z(y)$) is well approximated by a fourth order polynomial. We can use a path averaged distance from the boundary ($\overline{z}$) computed by either,

$$\overline{z} = \frac{1}{L}\int_0^L z(y)\, dy \qquad \text{or} \tag{5.56}$$

$$= \left[\frac{1}{L}\int_0^L \frac{1}{z(y)}\, dy\right]^{-1}. \tag{5.57}$$

The results are 13.76 m and 9.62 m respectively and introduce a factor of 1.5 difference. Therefore,

$$\overline{\epsilon} = \frac{C_D^{3/2}\overline{U}^3}{\mathcal{K}\overline{z}}, \tag{5.58}$$

where C_D is the drag coefficient for $\overline{U}$ measured along the acoustic path which is $\overline{z}$ from the boundary.

Estimates of the dissipation in this way for a drag coefficient of $C_D = 3 \times 10^{-3}$ and for $\overline{z} = 13.76\ m$ are shown in Figure 5.24 as a solid curve. The agreement with the acoustically observed dissipation is quite good as the tidal flow increases to its maximum. However, the dissipation exceeds the prediction based on a steady state balance as the current decelerates. For a uniform flow we anticipate a time delay in the turbulent response to a change in tidal forcing associated with the overturning time scale of the energy producing scales. Tennekes and Lumley [55] describe large eddies as losing a significant fraction of their kinetic energy within one turnover time. For vertical eddy scales (30 m diameter) one turnover time is approximately 16 minutes whereas for horizontal eddy scales (335 m diameter) one turnover time is approximately 2.9 hours. Measurements show that in two hours half the energy is lost whereas the steady state solution predicts 17 minutes.

These results illustrate the potential value of acoustical scintillation measurements for the detection of turbulent dissipation, which is a dynamically important but relatively inaccessible variable.

5.5 Γ and X Parameters - Comparison With Other Acoustic Experiments

We are now in a position to make estimates of the scattering strength Γ (3.10) and the normalized propagation range X (3.11) in order to locate them on the Γ, X plane defined by Uscinski *et.al.* [59]. This gives a direct comparison with other acoustic experiments.

Given the acoustic wavenumber k, path length L, refractive index variance $< \eta^2 >$ and the observed acoustical phase variance $< \phi^2 >$, the integral correlation length, L_r is evaluated from (3.13). In the present example, where fully developed turbulence dominates the fine scale properties of the flow, it is appropriate to evaluate both $< \eta^2 >$ and $< \phi^2 >$ over the inertial subrange, that is, for frequencies f lying within the range,

$$\frac{U}{L_o} < f < \frac{U}{\ell_o}. \tag{5.59}$$

The refractive index fluctuations are caused by temperature, salinity and current velocity fluctuations. We obtain $< \eta_s^2 >$ for scalar fluctuations from the integral of the one-dimensional refractive index spectrum defined by (5.36) for wavenumbers $2\pi/L_o < \kappa < 2\pi/\ell_o$. The variance is then defined as,

$$< \eta_s^2 >= 2 \int_{\kappa_o}^{\infty} \Phi_{1n_s}(\kappa_1) d\kappa_1, \tag{5.60}$$

for $\kappa_o = 2\pi/L_o = 0.2$. The measured inner scale is limited by the 4 Hz sampling rate of the CTD to 50 cm during strong tidal flow (1 $m\ s^{-1}$) and to 12.5 cm during weaker flow (0.25 $m\ s^{-1}$). Estimates of the dissipation scale based on the kinematic viscosity ($\nu = 1 \times 10^{-6}$) and calculations of the turbulent energy dissipation (ϵ) indicates $\ell_o = (\nu^3/\epsilon)^{1/4} \approx 0.05\ cm$ for strong flow and $\ell_o \approx 0.13\ cm$ for weak flow, which is in all cases significantly less than the smallest scale detected in our acoustical measurement. The contribution to the variance at these scales is negligible and hence we let the integral limit go to ∞. The outer scale L_o must be bounded by the channel depth of 32 m. However, as discussed above, analysis of the acoustical data imply

$U\ (m\ s^{-1})$	$<\phi^2>\ (rad^2)$	$<\eta^2>$	$L_p\ (m)$	Γ	X
-0.96	0.19	2.56×10^{-9}	1.36	83.3	2.3×10^{-3}
-0.33	0.04	2.51×10^{-10}	2.91	17.5	2.3×10^{-3}

Table 5.3: A summary of the parameters used for measurements of Γ and X for strong and weak ebb flow.

an outer scale of approximately 16 m during a time of slower flow speeds. Most of the time, however, the acoustical spectra are consistent with the 32 m outer scale. Using the maximum bound of 32 m the variances of the refractive index fluctuations due to scalar fluctuations are 1.44×10^{-11} and 1.12×10^{-10} for strong and weak ebb respectively.

We can only estimate the contribution to the variance of the refractive index fluctuations due to vector fluctuations, $<\eta_v^2>$ from the three-dimensional spectrum (5.43). The variance is defined as,

$$\begin{aligned} <\eta_v^2> &= \int_{\kappa_o}^{\infty} 4\pi\kappa^2 \Phi_{n_v}(\kappa) d\kappa &&= \int_{\kappa_o}^{\infty} \frac{E(\kappa)}{c_o^2} d\kappa, \\ &= \frac{1.5\epsilon^{2/3}}{c_o^2} \int_{\kappa_o}^{\infty} \kappa^{-5/3} d\kappa &&= \frac{1}{2} \frac{<u^2+v^2+w^2>}{c_o^2}, \\ &= 2.25 \frac{\epsilon^{2/3}}{c_o^2} \kappa_o^{-2/3} &&= \frac{3}{2} \frac{\sigma_u^2}{c_o^2}. \end{aligned} \tag{5.61}$$

Since the inner scale based on the dissipation measurements is small, we let the integral limit go to ∞. Based on our measurements of ϵ during strong and weak flow the variances of the refractive index fluctuations due to velocity fluctuations are 2.55×10^{-9} and 1.39×10^{-10} respectively. This corresponds to rms velocity fluctuations of 0.06 $m\ s^{-1}$ and 0.01 $m\ s^{-1}$ respectively which are approximately 10% the mean flow.

Measurements of the total refractive index variance $<\eta^2> = <\eta_s^2> + <\eta_v^2>$ using this method, are shown in Table 5.3. Our assumption of a large outer scale implies that the estimated variance for the refractive index fluctuations should be considered an outer limit.

We obtain the phase variance from the integral of the phase spectrum for frequencies $U/L_o < f < U/\ell_o$. The variance is defined as,

$$< \phi^2 >= 2 \int_{U/L_o}^{\infty} W_\phi(f) df. \tag{5.62}$$

Because of measurement related noise at the highest frequencies, the smallest scale size that can be measured using the phase is 22 cm during strong flow and 6 cm during weak flow. Contribution to the phase variance from scales smaller than this is negligible and so we let the integral limit go to ∞. Measurements of $< \phi^2 >$ in this way are shown in Table 5.3 for a time during strong and weak ebb flow.

The corresponding measurements for L_p are also shown. Measurements for L_p are made in this way since the oceanographic data required to calculate the integral correlation length were not obtained. This parameter remains of the same order of magnitude for both flow speeds. The vertical correlation length scale of the refractive index fluctuations, L_V must also be estimated. Since the phase difference measurements are consistent with an outer scale of 32 m, we assume a maximum vertical correlation length scale of 32 m.

Finally, the parameters Γ and X can be estimated and are tabulated in Table 5.3 and are also plotted in Figure 5.25 for comparison with other acoustic propagation experiments. The measurements of refractive index variability is not adequate to allow a precise evaluation of these parameters. Nevertheless, the results clearly indicate that the acoustic experiment is in the weak scattering regime since $\Gamma X < 1$ (Uscinski *et.al.* [59]).

These results serve to place this acoustical environment in the context of other acoustic experiments using the Γ,X plane defined by Uscinski *et.al.* [59]. Figure 5.25 shows values of Γ and X taken from: Ewart and Reynolds [22] Cobb71-MATE77 experiment, Reynolds *et.al.* [47] AFAR experiment, Uscinski *et.al.* [60] Napoli85 experiment. The Cobb71-MATE77 and AFAR experiments made use of the Garrett and Munk [27] and [28] internal wave model for describing the refractive index fluctuations; Napoli85 experiment describes the refractive index fluctuations due to

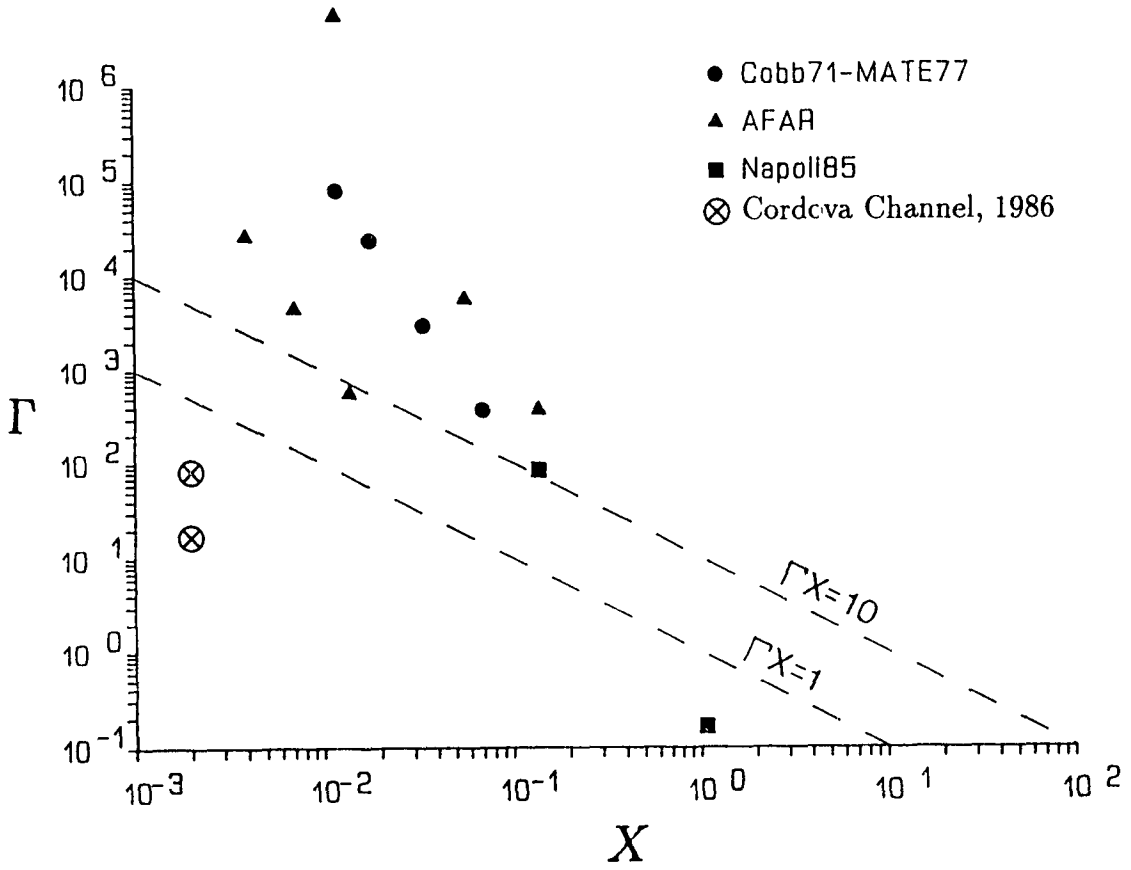

Figure 5.25: The Γ, X parameter plane. Data are taken from: Ewart and Reynolds [22] Cobb71-MATE77 experiment, Reynold's *et.al.* [47] AFAR experiment, Uscinski *et.al.* [60] Napoli85 experiment and Di Iorio and Farmer's [18] present measurements in Cordova Channel.

mixing intrusions. We add to this figure our parameters for high frequency acoustic propagation over short ranges through Kolmogorov turbulence.

5.6 Two-Dimensional Angle of Arrival Distribution

As noted previously the rms phase noise is approximately ±3.2 deg based on a signal to noise ratio of 25 dB in our acoustical scintillation system. What is more interesting, however, is the phase difference, and hence the measurement resolution of the angle of arrival fluctuations (resolution of ±0.02 deg). Since the acoustic signal is detected with a two-dimensional array, we can determine the horizontal and vertical components of the arrival angle.

Figure 5.26 is a schematic diagram showing the horizontal advection of the acoustic waveform due to current flow, and the vertical refraction of the acoustic waveform due to stratification. Positive and negative values of the arrival angle correspond to the directions shown in the schematic. Even though spherical wave acoustic propagation is used, it is assumed that in the vicinity of the receivers the waves are plane. The acoustic arrival angles, relative to the line perpendicular to the receiver axis, θ_{a_x} and θ_{a_z} are obtained by,

$$\sin\theta_{a_x} = \frac{(\phi_l - \phi_r)c_o}{\omega_a \rho_x} = \frac{\delta\phi_x}{k\rho_x} = \frac{\delta\phi_x}{2\pi}\frac{\lambda}{\rho_x}, \tag{5 63}$$

$$\sin\theta_{a_z} = \frac{(\phi_b - \phi_t)c_o}{\omega_a \rho_z} = \frac{\delta\phi_z}{k\rho_z} = \frac{\delta\phi_z}{2\pi}\frac{\lambda}{\rho_z}, \tag{5.64}$$

where subscripts l, r, b and t correspond to the left, right, bottom, and top receivers when viewing the array from the center of the channel (see Figure 5.27), ϕ is the phase in radians, c_o is the average sound speed at 15 metres depth ($\sim 1485\ m\ s^{-1}$), $\omega_a = 2\pi f_a$ is the angular acoustic frequency, $k = 2\pi/\lambda$ is the acoustic wavenumber and ρ is the receiver spacing for the horizontal (x) and the vertical (z) direction. The phase difference $\delta\phi$ is taken using diverging acoustic paths (one transmitter and two receivers).

The sensitivity in the angle of arrival variability relies on two factors: a receiver spacing large enough to accommodate many wavelengths (i.e. $\lambda/\rho \ll 1$) and the

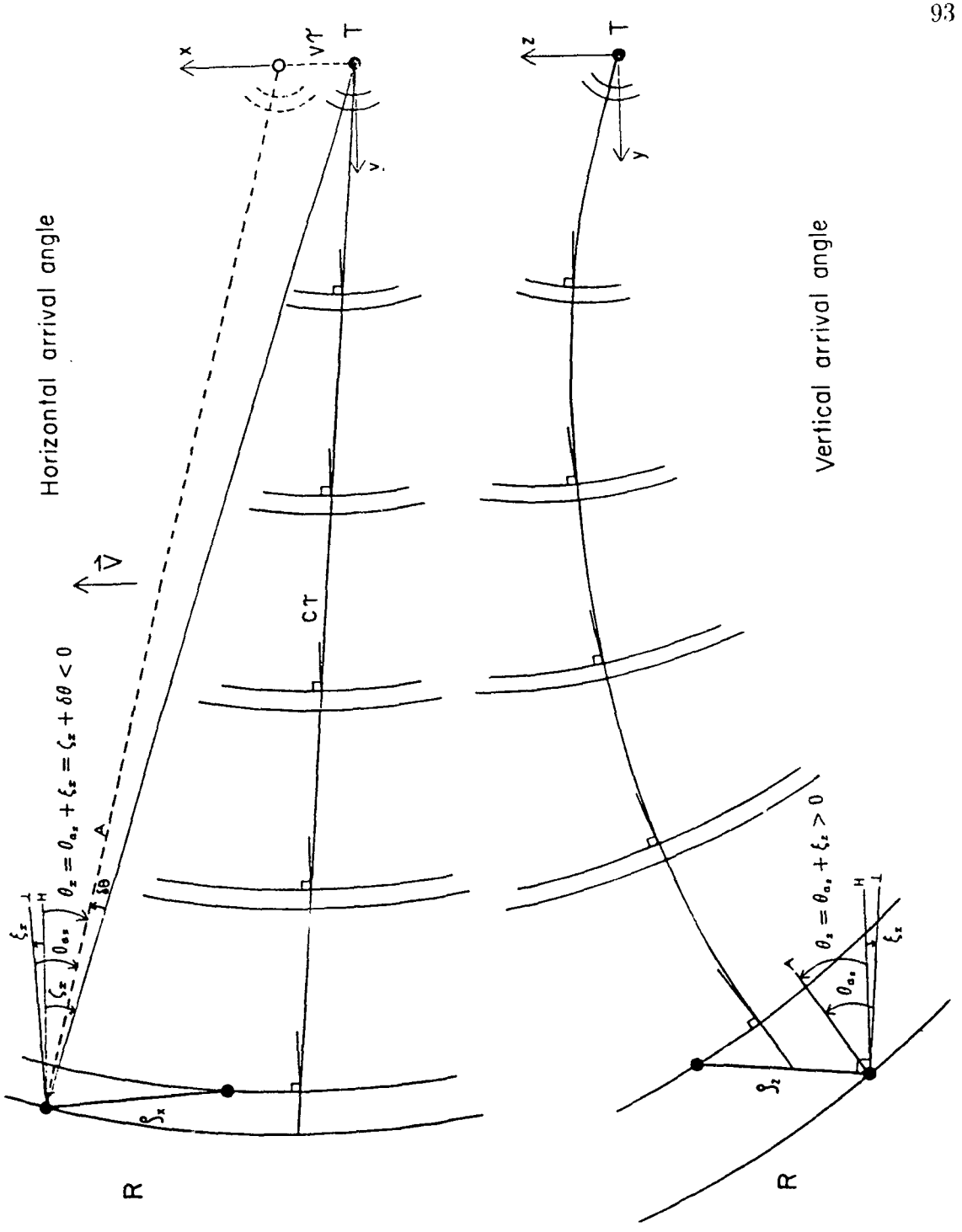

Figure 5.26: Schematic showing the horizontal arrival angle as it is advected by the current (left) and the vertical arrival angle (right) as it is refracted by stratification. Indicated angles are: θ_a = measured acoustic arrival angle relative to the line perpendicular to the receiver separation ($\perp$), $\theta_{x,z}$ = arrival angle relative to the y-axis (H), ξ = angle of the receiver separation relative to H, ζ = angle of receiver array relative to the transmitter array in the x-direction.

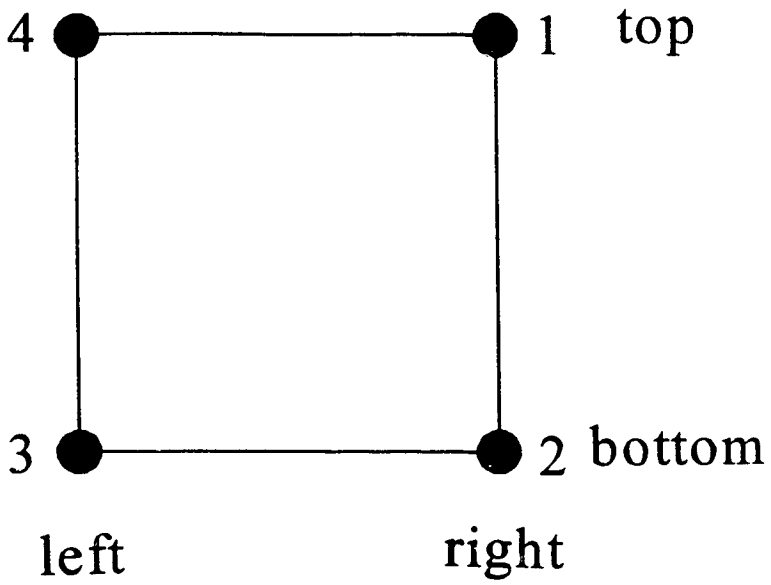

Figure 5.27: Schematic showing the receiver array viewed from the center of the channel. Transducers are labelled 1 to 4. Horizontal directions make use of the top and bottom receivers; vertical directions make use of the left and right receivers.

ability to detect phase differences within a fraction of a cycle. Both these factors are satisfied in our experiment and hence we can measure the angle of arrival with resolution of 0.02 degrees.

The arrival angle calculations are carried out both to examine the slow variations associated with 'deterministic' deflections of the acoustical path, and also to examine the pattern of rapid fluctuations.

5.6.1 Low frequency fluctuations

Sound travelling across the channel can be modified in various ways by the intervening water. Changes in the path averaged refractive index over time scales of minutes to hours exist because of the gross changes in the mean sound speed over the path during the tidal cycle. The amplitude or log-amplitude remains essentially unchanged at these time scales, but significant changes occur in the phase. This is because of changes in the mean sound speed as mixing proceeds and because of the deflections of the acoustical path during the tidal cycle. Horizontal gradients in the sound speed

tend to be small over longer time scales ($> 100s$) and so horizontal refraction can be assumed to be negligible.

Horizontal arrival angle

Figure 5.26 shows the horizontal arrival angle relative to the y-axis as $\theta_x = \theta_{a_x} + \xi_x = \zeta_x + \delta\theta_x$ where θ_{a_x} is the measured acoustic arrival angle defined by (5.63), ξ_x is the geometric angle between the x-axis and the receiver axis, ζ_x is the geometric angle between the transmitter and receiver array, and $\delta\theta_x$ is the deflection caused by the current flow (U). To visualize the effect of the current, consider a spherical wave originating at the transmitter. During the time τ that the wave takes to cross the channel, travelling a total distance $c_o\tau = L$, the apparent source (o), as seen by the receivers, is downstream from the transmitter a distance,

$$D = \int_0^\tau U(t)dt = \int_0^L \frac{U(y)}{c_o}dy \approx U\tau. \tag{5.65}$$

In the final approximation it is assumed that the current speed is uniform across the channel.

Based on the geometry shown in Figure 5.26, it can be shown that the incremental angle due to current flow is given as,

$$\sin\delta\theta_x = \frac{U}{c_o}\left(1 - \frac{U^2}{c_o^2}\right)^{-1/2}\cos\zeta_x. \tag{5.66}$$

Since $U \ll c_o$ and $\cos\zeta_x \sim 1$ for transmitters and receivers directly opposite each other, the above equation reduces to the Mach number of the flow,

$$\sin\delta\theta_x = \frac{U}{c_o}. \tag{5.67}$$

This derivation is based on the advection of acoustic rays and is described as the ray approach since it does not take into account scattering from the turbulence.

Figure 5.28(a) shows measurements of the horizontal arrival angle, based on four minute averages of low passed filtered data, as measured by (5.63) for receivers 4-1. Superimposed on this plot is the arrival angle θ_{a_x} determined by the equation $\zeta_x -$

$\xi_x + \delta\theta_x$. At zero current speed the acoustic arrival angle defines $\zeta_x - \xi_x = -4.35 deg$. The current speed U is shown on the right hand axis for comparison. Clearly equation (5.67) explains the gross features of the horizontal deflections, but not the details. Departure of the flow from a horizontally uniform current together with transverse sound speed gradients results in differences between the angle measured by the current meter and that measured by the acoustic phase.

Detection of the slowly varying horizontal arrival angle due to current advection is a novel measurement which has not previously been reported. This approach to the measurement of path averaged current speed has some unique advantages because, in contrast to the methods described previously, it does not require any assumption regarding the random medium or the sound scattering models; the only assumptions are that horizontal refraction is negligible and that the current remain uniform. (Departure from uniform flow can be considered by applying the appropriate path integration). Another advantage is that the arrival angle method does not invoke the Taylor hypothesis of frozen turbulence, which must be made in estimates using the slope and delay technique. This advantage is particularly valuable where the refractive index variability is due to internal waves.

Vertical arrival angle

Figure 5.26 also shows the vertical arrival angle relative to the y-axis as $\theta_z = \theta_{a_z} + \xi_z$ where θ_{a_z} is the measured acoustic arrival angle defined by (5.64) and ξ_z is the geometric angle between the z-axis and the receiver axis. For low frequency variability the vertical arrival angle, θ_z is dependent on the vertical stratification. Sound speed gradients can result in significant deflections in the vertical. For a constant vertical sound speed gradient $\frac{dc}{dz}$, ray paths are arcs of a circle. For a horizontal range of $L = 670\ m$, the vertical deflection determined by acoustic ray tracing (see Brekhovskikh and Lysanov [4]) is,

$$\tan\theta_z = \frac{L}{2c_o}\frac{dc}{dz} = \frac{L}{2c_o}\frac{\Delta c}{\Delta z}. \tag{5.68}$$

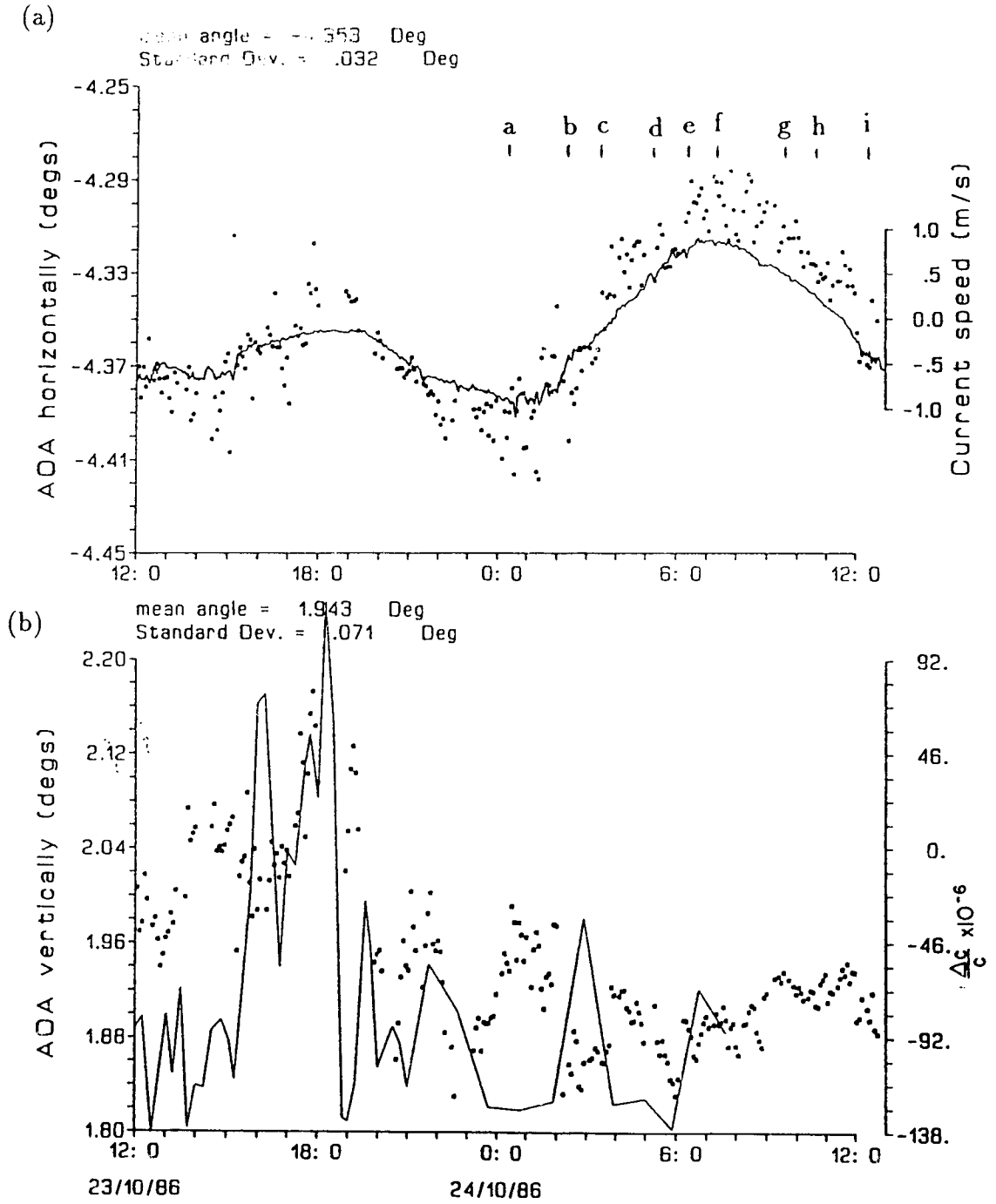

Figure 5.28: (a) Horizontal angle of arrival determined acoustically (dots) by (5.63) together with the angle measured by the Mach number (equation (5.67)) (solid curve). (b) Vertical arrival angle determined acoustically (dots) by (5.64), together with the angle measured by the sound speed gradient (equation (5.68)) (solid curve).

The sound speed gradient $\frac{\Delta c}{\Delta z}$ is obtained from CTD (conductivity, temperature, and depth) profiles.

Figure 5.28(b) shows measurements of the vertical acoustic arrival angle measured by (5.64) for receivers 2-1 in Figure 5.27. Superimposed on this plot is the arrival angle θ_{a_z} determined by the equation $\theta_z - \xi_z$. For a mean sound speed gradient of 0.016 s^{-1}, based only on pressure differences ($\Delta c/c_o = 10.8 \times 10^{-6}$, $\theta_z = 0.2deg$), the acoustic arrival angle estimates $\xi_z = -1.86deg$. Values of $\Delta c/c_o$ using a least squares fit over $\Delta z = 10\ m$ are shown for comparison on the right hand axis of Figure 5.28(b). Differences between acoustical measurements and predictions based on sound speed profiles are to be expected, given that the CTD data are taken at a point approximately 300 m north of the acoustic path, whereas the acoustic information is integrated across the channel. Also, the prediction is based on the assumption that the sound speed profiles are constant across the channel. The decrease in arrival angle at 1900h is, however, consistent with the CTD predictions.

Thus, our acoustic system can detect the slowly varying vertical arrival angle due to changes in stratification. This kind of measurement can be ideal for measuring the path averaged sound speed and hence density gradients. From the measured sound speed gradient the resulting temperature gradient can be found since the effect of salinity on the sound speed can be ignored. The temperature - salinity relation defined in (5.3) then gives the resulting salinity gradient. The density gradient computed from the temperature and salinity gradients can then, in theory, be found.

The change in the vertical arrival angle is twice that of the horizontal arrival angle. The current does not cause large deflections, but changes in stratification cause significant deflections in the vertical angle.

5.6.2 High frequency fluctuations

In order to understand the fluctuations in the arrival angles an understanding of the phase difference fluctuations is needed. Figure 5.29(a) and (b) shows a variance

preserving plot of the phase difference spectra for horizontally and vertically spaced receivers respectively. Superimposed are the theoretical curves computed by evaluating the integrals in (5.23) and (5.24) numerically. As can be seen both theory and experiment agree quite well for each direction.

The peak for the phase difference spectrum using horizontally spaced receivers occurs at frequencies $f \approx 0.22 f_{1_x}$ (corresponding scale size is $\ell = 4.5\rho$) which is consistent with the prediction of Tatarskii [52]. The peak for the phase difference spectrum using vertically spaced receivers, however, is shifted towards lower frequencies so that the spectrum is maximal at $f \approx 0.06 f_{1_z}$ (corresponding scale size is $\ell = 16.5\rho$). Thus, the vertical phase difference fluctuations are sensitive to scales larger than the horizontal phase difference.

The high frequency fluctuations in the arrival angle are analyzed by applying a high pass, third order Butterworth filter with cutoff frequency $f_c = \frac{U}{32m}\ Hz$ to the low passed filtered phase. We choose this cutoff because $32m$ is a maximum bound on the vertical eddy scale and hence the outer scale for isotropic and homogeneous turbulence. The data are filtered both forward and backwards so as to eliminate any phase shifts inherent in the filter. Thus phase fluctuations from scale lengths less than 32 m are analyzed. These structures are advected through the acoustical path generating small scale variability in the phase time series.

The filtered phase difference is now shown in Figure 5.30(a) and (b) for horizontally and vertically spaced receivers respectively. Theoretical predictions are the solid curves, experimental results averaged over the tidal cycle are the dashed curves and filtered results are the dotted curves. The level of the band passed filtered spectrum is higher since the structure function (used to normalize the spectrum) is reduced. The structure function is dominated by the phase difference variance which is the integral of the phase difference spectrum. Since the peak of the phase difference spectrum is broad, measurement of C_n^2 using the structure function will be very sensitive to the high pass filter cutoff frequency. Another reason for choosing this frequency cutoff is because it is the point where the averaged experimental spectrum deviates from the

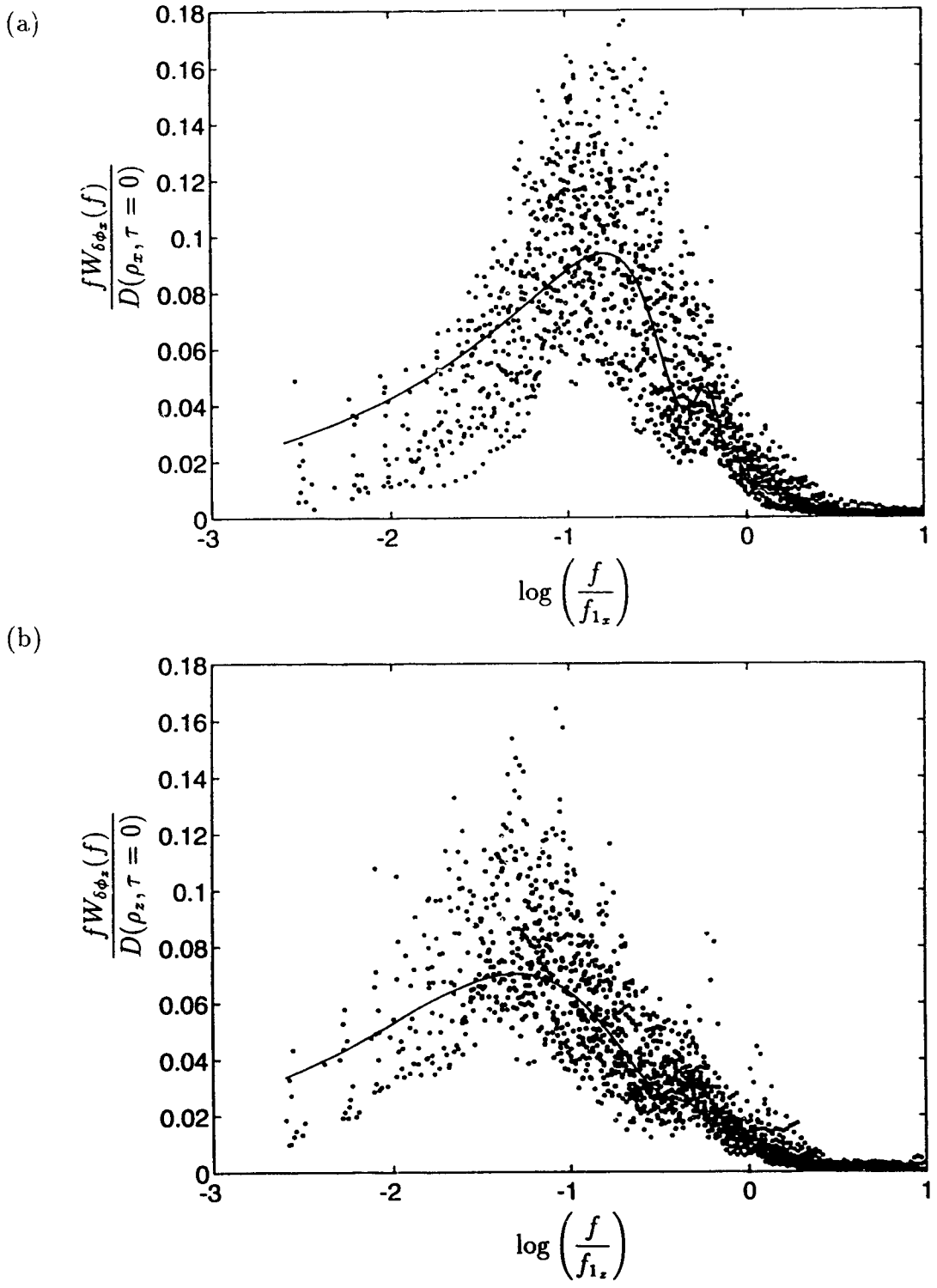

Figure 5.29: Variance preserving plot of the theoretical (solid curve) and experimental (dots) phase difference spectra for (a) horizontally and (b) vertically spaced receivers. Experimental spectra are taken through a tidal cycle. Normalizing frequency is defined as $f_{1_x} = U/\rho_x$ and $f_{1_z} = U/\rho_z$ for $\rho_x = 1.18m$ and $\rho_z = 1.03m$.

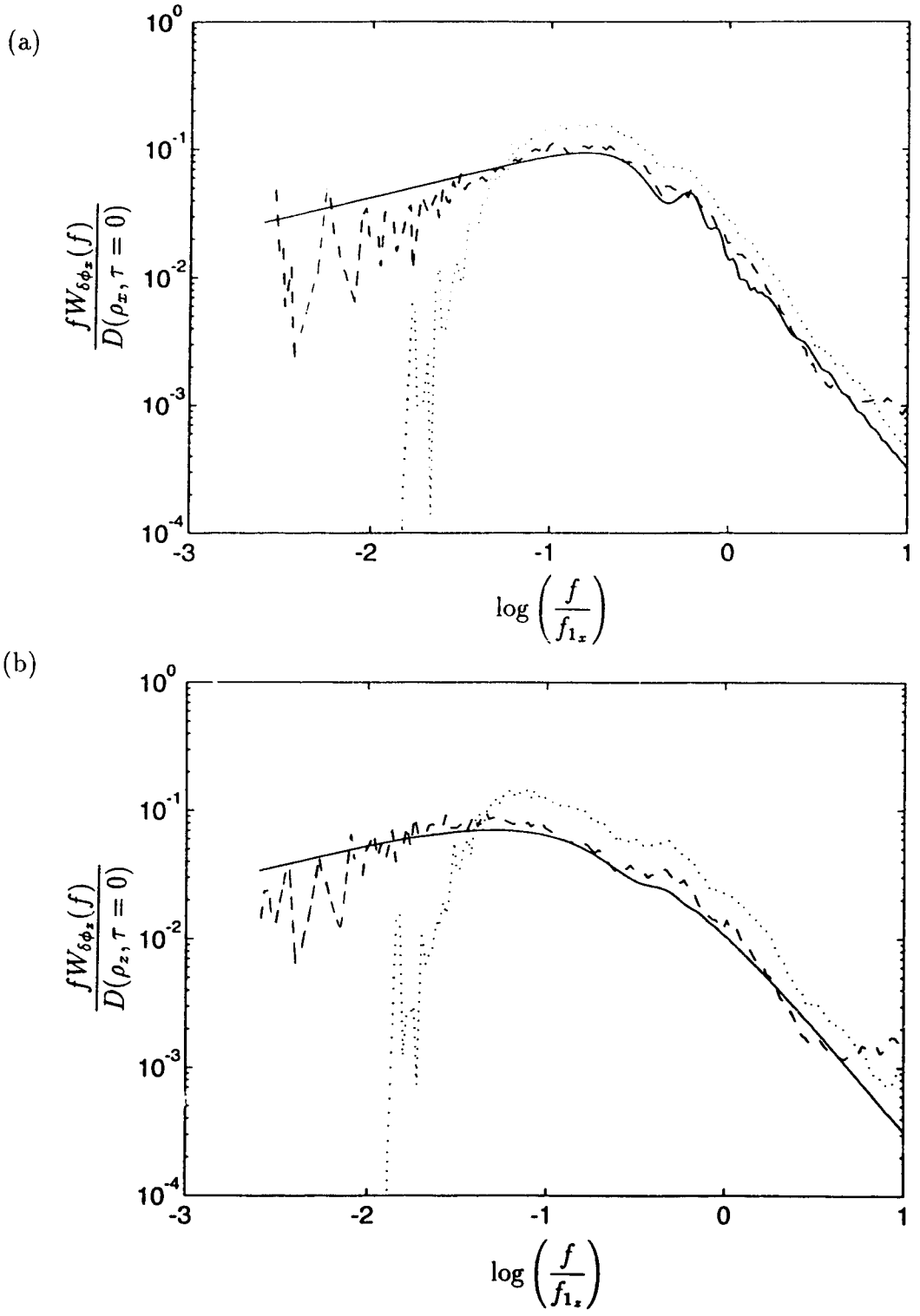

Figure 5.30: Normalized phase difference spectra for (a) horizontally spaced receivers ($f_{1_x} = U/\rho_x$, $\rho_x = 1.18m$) and (b) vertically spaced receivers ($f_{1_z} = U/\rho_z$, $\rho_z = 1.03m$). Theoretical spectra are shown as a solid curve, data with no filtering are shown as a dashed curve and filtered data are shown as a dotted curve.

theoretical curve in the low frequency part of the spectra.

Horizontal and vertical arrival angle correlations

Since we are dealing with high passed filtered data which are zero mean random variables the covariance is the correlation and hence we will use this term throughout. The cross correlation between horizontal and vertical acoustic arrival angles is defined as,

$$< \theta_{x_i}\theta_{z_j}(\tau) >= \frac{1}{k^2\rho_x\rho_z}[C_\phi(0,\tau) - C_\phi(\pm\rho_x,\tau) - C_\phi(\rho_z,\tau) + C_\phi(\pm\rho_d,\tau)], \quad (5.69)$$

where θ_{x_i} and θ_{z_j} denote acoustic arrival angle fluctuations for the i^{th} horizontal (top or bottom) and the j^{th} vertical (left or right) direction respectively and $\pm\rho_d = ((\pm\rho_x - U\tau)^2 + \rho_z^2)^{1/2}$ is the spacing between diagonal receivers. Depending on which receivers are used, the direction of ρ_x must be taken into account because of the mean flow. We can write the arrival angle correlation in terms of the phase cross correlation since we are dealing with high passed filtered data where an outer scale is defined as $L_o = 32\ m$.

This cross correlation function is asymmetric and has a peak at zero time lag. Figure 5.31(a) shows the normalized cross correlation of horizontal and vertical arrival angles. The solid curve is for the horizontal arrival angle determined by receivers 4-1 and the vertical arrival angle determined by receivers 2-1; the dashed curve is for the horizontal arrival angle determined by receivers 3-2 and vertical receivers 2-1. The normalized cross correlations for ebb are shown on the left and for flood they are shown on the right.

At zero time lag, direction of current flow is not important and so,

$$< \theta_{x_i}\theta_{z_j} >= \frac{1}{k^2\rho_x\rho_z}[C_\phi(0,0) - C_\phi(\rho_x,0) - C_\phi(\rho_z,0) + C_\phi(\rho_d,0)]. \quad (5.70)$$

At zero time lag the normalized cross correlation is the correlation coefficient. For ebb flow the correlation coefficients are similar but during flood flow there is more correlation for the $(\theta_{x_{4-1}}, \theta_{z_{2-1}})$ pair.

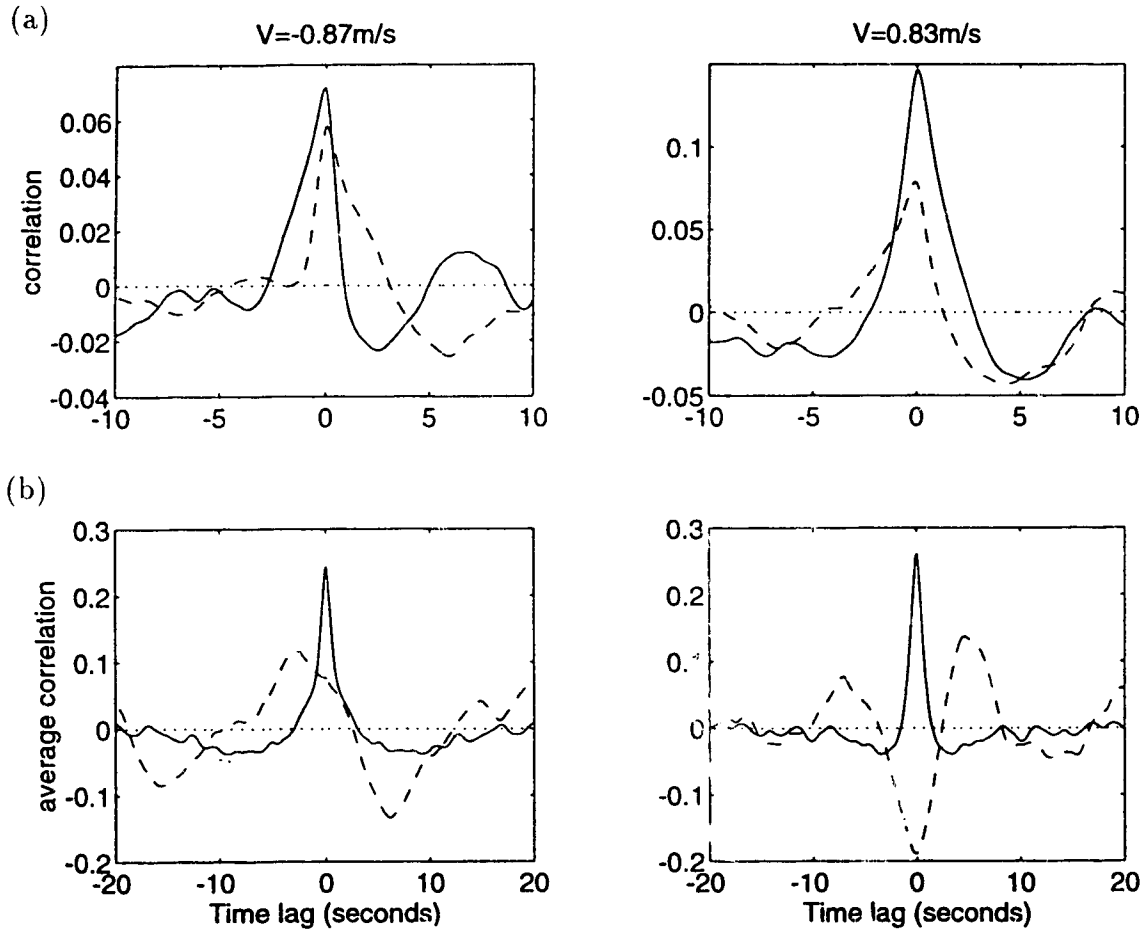

Figure 5.31: Normalized angle of arrival correlations during ebb (left) and flood (right) flow. (a) Correlations from specific horizontally and vertically spaced receivers. Solid curve is $< \theta_{x_{4-1}} \theta_{z_{2-1}}(\tau) >$ and dashed curve is $< \theta_{x_{3-2}} \theta_{z_{2-1}}(\tau) >$. (b) Correlations averaged over the square array. Solid curve is $< \theta_x \theta_z(\tau) >_A$ and dashed curve is $< \theta_x \theta_z(\tau) >_{A_0}$.

In order to remove the asymmetry due to the flow direction, we use the square array (one transmitter and four receivers) to obtain four measurements of (θ_x, θ_z) pairs. This results in an average cross correlation function,

$$< \theta_x\theta_z(\tau) >_A = \frac{1}{4k^2\rho_x\rho_z}[4C_\phi(0,\tau) - 2C_\phi(\rho_x,\tau) - 2C_\phi(-\rho_x,\tau) - 4C_\phi(\rho_z,\tau) + C_\phi(\rho_{42},\tau) + C_\phi(\rho_{24},\tau) + C_\phi(\rho_{31},\tau) + C_\phi(\rho_{13},\tau)], \quad (5.71)$$

where the subscript A denotes average over the array and the labels 1, 2, 3 and 4 correspond to the receiver labels in Figure 5.27. The diagonal spacing $\rho_{42} = \sqrt{(\rho_x - U\tau)^2 + \rho_z^2}$ whereas $\rho_{24} = \sqrt{(\rho_x + U\tau)^2 + \rho_z^2}$. This function normalized by the variances is shown in Figure 5.31(b) as a solid curve during ebb and flood flow. It is symmetric and has a maximum at zero time lag corresponding to,

$$< \theta_x\theta_z >_A = \frac{1}{4k^2\rho_x\rho_z}[4C_\phi(0,0) - 4C_\phi(\rho_x,0) - 4C_\phi(\rho_z,0) + 2C_\phi(\rho_{42},0) + 2C_\phi(\rho_{31},0)], \quad (5.72)$$

$$= \frac{1}{4k^2\rho_x\rho_z}[2D_\phi(\rho_x,0) + 2D_\phi(\rho_z,0) - D_\phi(\rho_{42},0) - D_\phi(\rho_{31},0)] \quad (5.73)$$

The last equality arises by the assumption of stationarity. At zero time lag the normalized cross correlation gives the correlation coefficient. The correlation coefficient is positive throughout the tidal cycle and is consistent with the shape of C_n^2.

In order to remove the positive correlation associated with the spatial lags we compute an average correlation function such that the horizontal and vertical phase correlations are removed. This gives,

$$< \theta_x\theta_z(\tau) >_{A_0} = \frac{1}{4k^2\rho_x\rho_z}[C_\phi(\rho_{42},\tau) + C_\phi(\rho_{24},\tau) - C_\phi(\rho_{13},\tau) - C_\phi(\rho_{31},\tau)] \quad (5.74)$$

where the subscript A_0 denotes an average over the array so as to give zero. This function should theoretically be zero for isotropic and homogeneous turbulence since $\rho_{42} \sim \rho_{31}$ and $\rho_{24} \sim \rho_{13}$. Figure 5.31(b) is a plot of this function normalized by the variances (dashed curve) during ebb and flood flow.

At zero time lag,

$$< \theta_x\theta_z >_{A_0} = \frac{1}{4k^2\rho_x\rho_z}[2C_\phi(\rho_{42},0) - 2C_\phi(\rho_{31},0)], \quad (5.75)$$

$$= \frac{1}{4k^2\rho_x\rho_z}[D_\phi(\rho_{31},0) - D_\phi(\rho_{42},0)], \tag{5.76}$$

where stationarity is assumed for the last equality. This correlation should be zero theoretically, but this is not observed in the data. During ebb flow the correlation coefficient at zero time lag is less than the correlation at other time lags. This implies that the measured correlation may not be significant and that it occurs purely by chance. At flood flow however, there is a strong correlation at zero time lag. At any other time lag the correlation is less suggesting that the observed correlation during flood is significant.

The correlation between horizontal and vertical arrival angles, averaged so as to give zero theoretically at zero time lag, is the difference between the phase structure function evaluated along two perpendicular diagonal directions at zero time lag. This function will show changes in the direction of correlation through the tidal cycle. Since the diagonal spacings are virtually the same it is the difference in the structure parameter C_n^2 measured along the two diagonal directions that gives the arrival angle correlations. For diverging paths the structure parameter measured by the wave structure function is weighted towards the receiver (see Appendix C.2) hence this angle of arrival correlation is also weighted towards the receiver.

Two-dimensional distribution

A two-dimensional angle of arrival distribution can be analyzed by plotting a scatter diagram of vertical versus horizontal arrival angle averaged over the array according to (5.76). Figure 5.32 shows these scatter diagrams for 20 minutes of high passed filtered data taken through the tidal period shown in Figure 5.28(a). Colour is used to tabulate the number of times the acoustic signal comes from a specific direction (that is having a specific vertical and horizontal angle). In effect, these plots are source probability distributions. Facing the receiver array from the center of the channel, a positive horizontal (vertical) angle indicates signals coming from the North (surface). Superimposed on the diagrams are the major and minor axes of the distribution

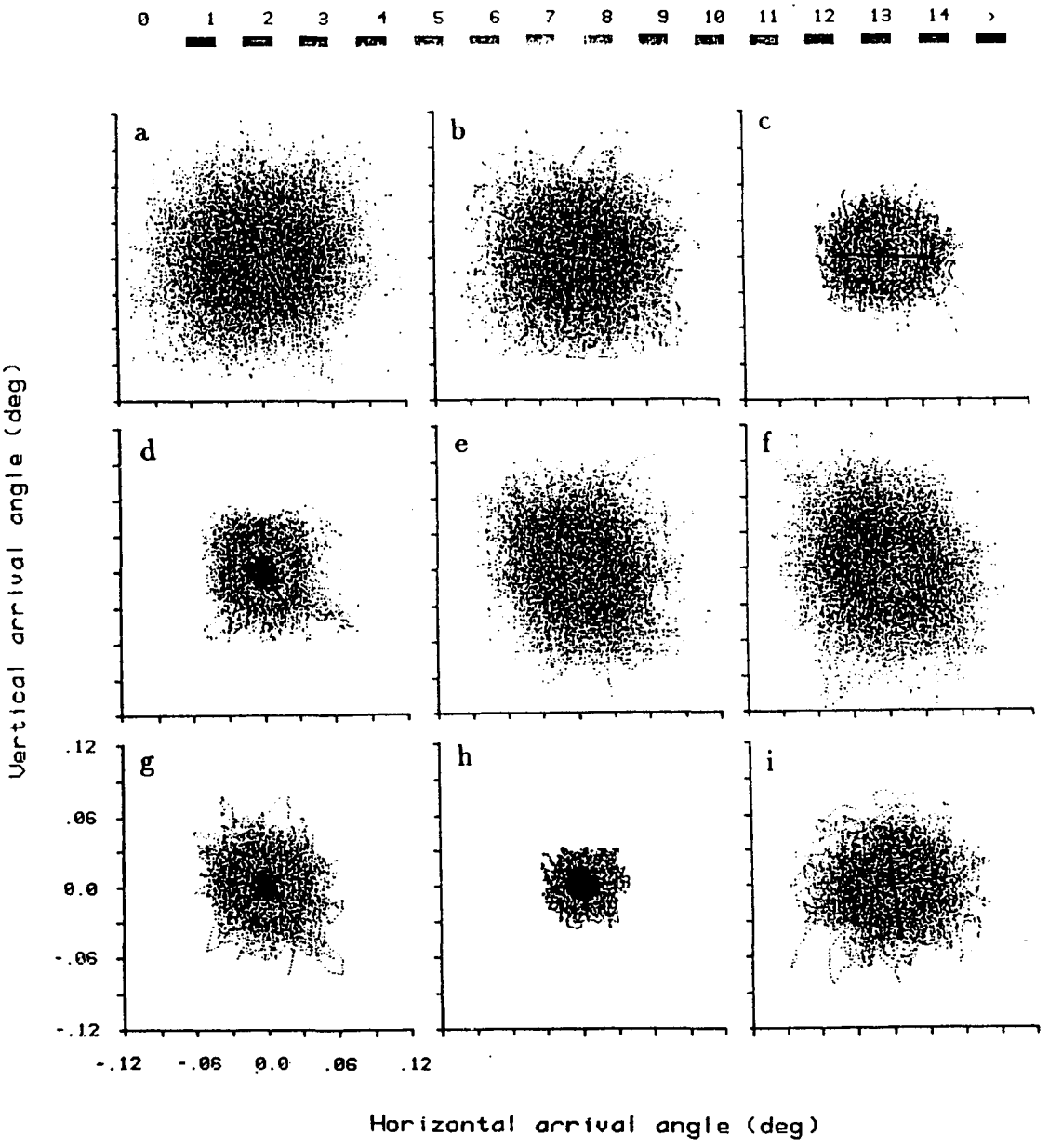

Figure 5.32: Two dimensional angle of arrival distribution through the tidal cycle shown in Figure 5.28. Each plot represents 20 minutes of high passed filtered data and the colour tabulates the number of times the acoustic signal comes from a specific direction.

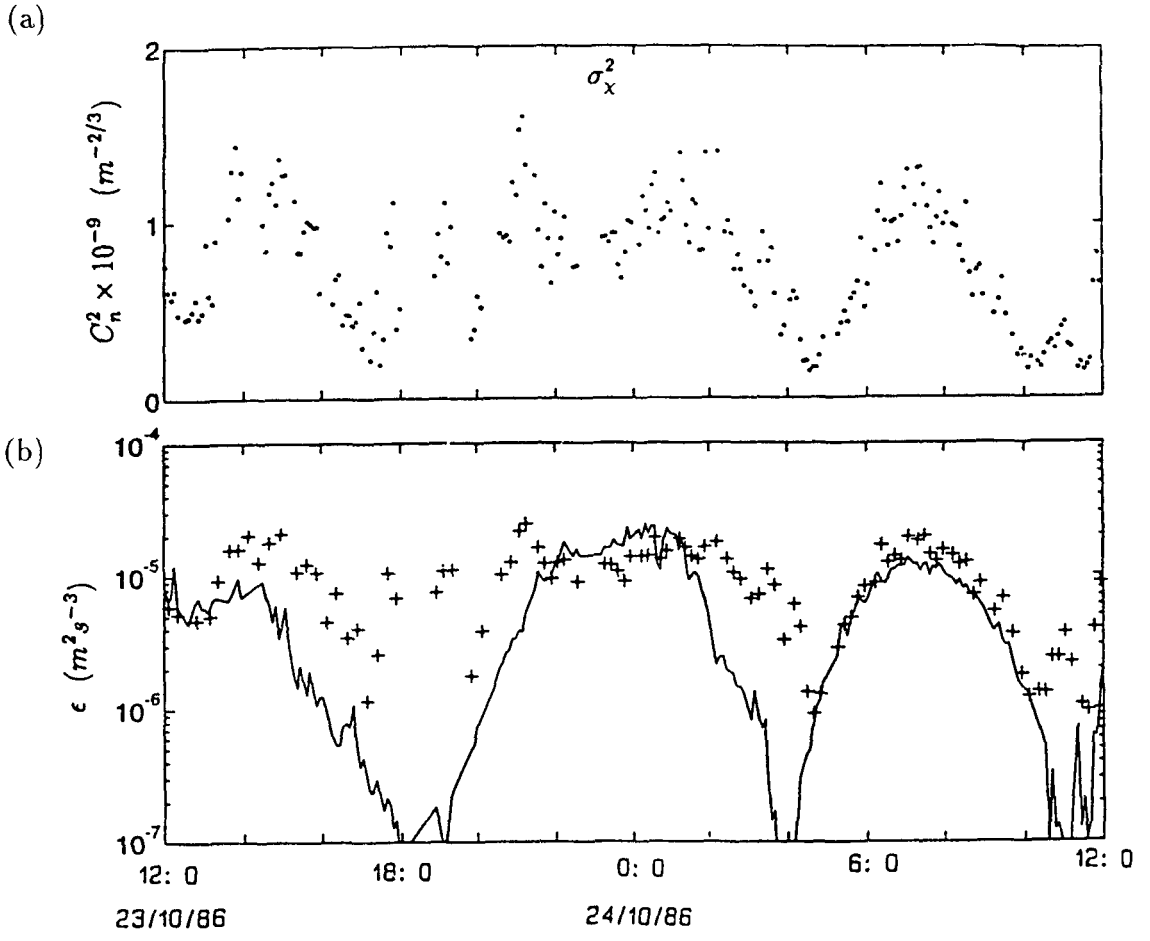

Figure 5.33: (a) Structure parameter C_n^2 (•) calculated from the acoustic log - amplitude variance. (b) Measured turbulent kinetic energy dissipation (+) and the estimated dissipation for a drag coefficient of $C_D = 3 \times 10^{-3}$ (solid curve).

determined by evaluating the eigenvectors of the correlation matrix. The axes are scaled by $2\sqrt{\mathcal{T}_i}$ where $\mathcal{T}_i, i = 1, 2$ are the eigenvalues of the matrix and represent the standard deviation of the scatter along the major ($i = 1$) and minor ($i = 2$) axes.

The degree of scatter can be directly related to the refractive index structure parameter, C_n^2 and hence the dissipation ϵ (calculated by the method described in section 5.4.4) which are shown in Figure 5.33. A large amount of scatter corresponds to times when the refractive index fluctuations (turbulence) are strong. That is, when there is enhanced turbulent velocity fluctuations due to strong tidal flow. Little scat-

ter occurs at slack water since the amount of turbulence is small. If the turbulence is isotropic we would expect a circular distribution corresponding to equal phase structure functions along the diagonals. Under isotropic conditions the acoustic arrival angle distribution would represent a two-dimensional random walk, but this is not observed. Moreover, there is a systematic distortion, implying a correlation between vertical and horizontal deflections which is more pronounced during maximum flood (frames e to g in Figure 5.32).

The standard deviation of the scatter along the major and minor axes ($\sqrt{T_i}$), the angle of the major axis and the correlation coefficient using 10 minute data sets are shown in Figure 5.34. The standard deviation which describes the magnitude of scatter is very similar to the refractive index structure parameter C_n^2 shown in Figure 5.33. The correlation coefficient,

$$r = \frac{< \theta_x' \theta_z' >_{A_0}}{\sqrt{< \theta_x'^{\,2} >< \theta_z'^{\,2} >}} \tag{5.77}$$

is positive during ebb flow and then changes to a negative correlation when the tide begins to flood. This can also be seen in the change of the major axis angle. Although, the correlation is small (± 0.25), its variability is small implying a consistent distortion or anisotropic distribution.

We can test hypotheses about the correlation coefficient r and construct a confidence interval, because the arrival angle (which is small) is proportional to the phase difference which is a Gaussian random variable. Following Devore [16] we test $\mathcal{H}_o : r = 0$ versus $\mathcal{H}_a : r > 0$ ($r < 0$) for a level α test and reject the null hypothesis if the test statistic $T = r\sqrt{n-2}/\sqrt{1-r^2} \geq t_{\alpha,n-2}$ ($\leq -t_{\alpha,n-2}$). Terms in brackets are for flood flow tests. The degrees of freedom are $n-2$ where n is the equivalent degrees of freedom (180 transmissions = 10 seconds) determined by the average zero crossing of the auto correlation for the horizontal and vertical arrival angle using 10 minute time series. The sample correlation coefficient is $r = 0.2$ and -0.25 and the test statistic is $T = 2.72$ and -3.44 during ebb and flood flow respectively. The necessary t critical value for a level $\alpha = .01$ test is $t_{.01,178} = 2.34$. Since $2.72 > 2.34$

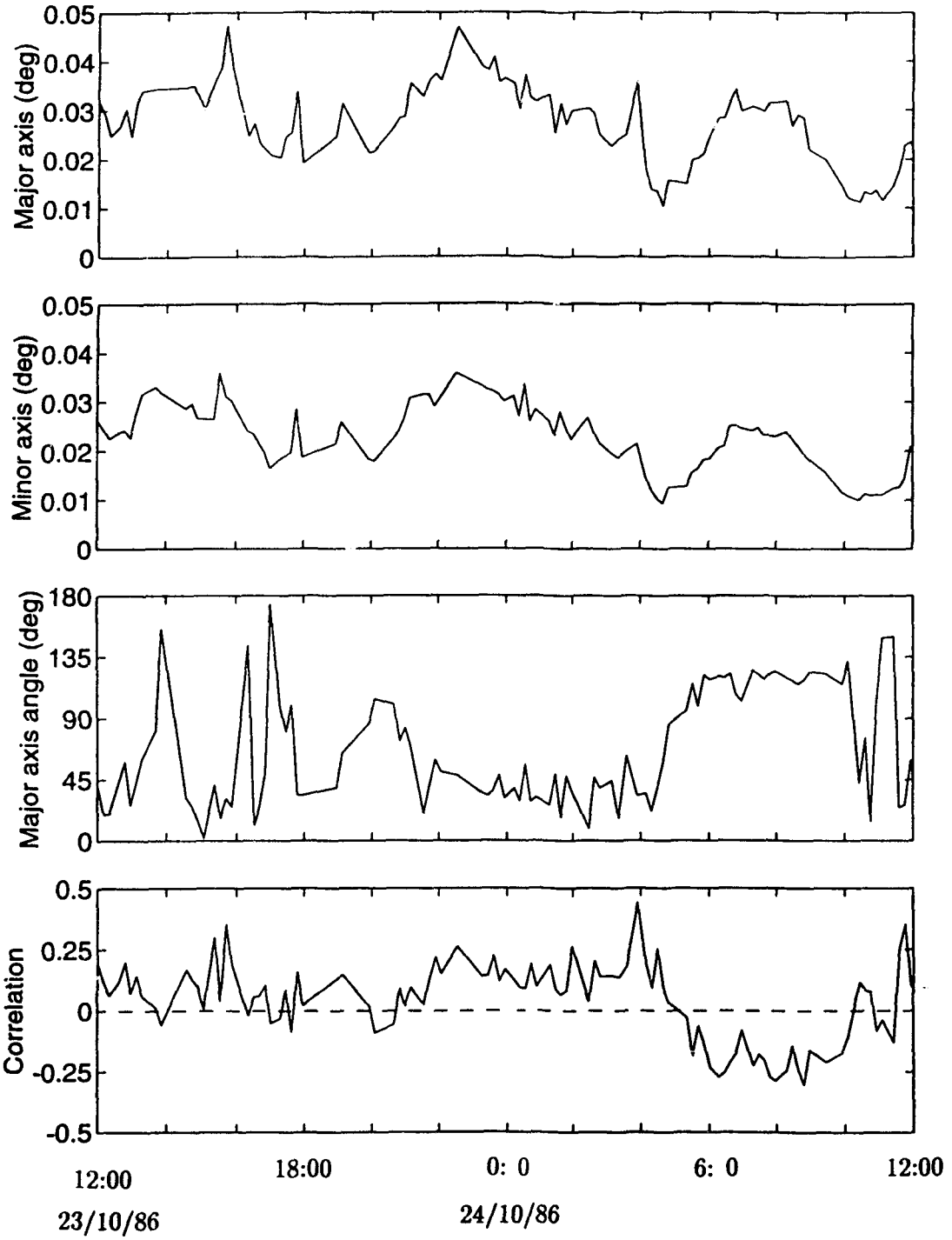

Figure 5.34: Time series showing the standard deviation of the scatter along the major and minor axes, the angle of the major axis relative to the x-axis, and the acoustic arrival angle correlation coefficient averaged over the array.

($-3.44 < -2.33$), we reject $\mathcal{H}_o$ and conclude that the vertical and horizontal arrival angles are positively correlated during ebb flow and negatively correlated during flood flow. A 95% confidence interval for the population correlation coefficient is (0.06,0.34) for ebb flow and $(-0.38, -.11)$ for flood flow. According to the time lag cross correlation functions, correlations during ebb flow seem to occur by chance but the correlations during flood flow seem more significant.

It should be mentioned that the hypothesis test and confidence interval are sensitive to the degrees of freedom. By taking the zero crossing of the auto correlation we are essentially determining the approximate degrees of freedom for the mean angle of arrival ($< \theta >$) and not the degrees of freedom for the correlation ($< \theta_x \theta_z >$). To determine the degrees of freedom for the correlation Davis [13] describes higher level statistical estimators which could be used on this data set. Due to the very large number of data points, the number of degrees of freedom will be large, but much smaller (by a factor of order 100) than the number of samples. Thus the number of degrees of freedom has a negligible effect on the t critical value.

The sign of the correlation coefficient changes at the same time as the mean current shear dU/dz changes which is when the current turns to flood (see Figure 5.21). Since the shear and the arrival angle correlations are obtained by independent methods it confirms that the observed correlation is not noise. During the flood, the correlation coefficient is negative (-0.25) in Figure 5.34 which corresponds to a time when the anisotropic distribution observed in the source probability distributions (Figure 5.32(e) and (f)) is greatest and which also corresponds to a time when the mean shear is significant. Both these results confirm that the turbulence is anisotropic.

Reasons for arrival angle fluctuations and correlations

In order to represent the arrival angle fluctuations in terms of the velocity fluctuations we follow the qualitative arguments of Tatarskii [53]. Suppose two rays separated by ℓ travel through a thickness δy, then the phase difference between the two paths is $\delta\Phi \sim k\delta n \delta y$, where δn is the refractive index difference along the two rays. Since

the phase difference is sensitive to scale sizes ℓ, then we can set $\delta y \sim \ell$ and then the arrival angle for a single inhomogeneity is $\Theta \sim \delta\Phi/k\ell \sim \delta n$. The variances from a single inhomogeneity are then defined as,

$$< \delta\Phi^2 > \sim k^2\ell^2 < \delta n^2 >, \tag{5.78}$$

$$< \Theta^2 > \sim \frac{< \delta\Phi^2 >}{k^2\ell^2} \sim < \delta n^2 > . \tag{5.79}$$

The total mean square phase difference and arrival angle fluctuations due to all $N \sim L/\ell$ inhomogeneities will then be of the order of,

$$< \delta\phi^2 > \sim < \delta\Phi^2 > \frac{L}{\ell} \sim < \delta n^2 > k^2 L\ell, \tag{5.80}$$

$$< \theta^2 > \sim < \Theta^2 > \frac{L}{\ell} \sim < \delta n^2 > \frac{L}{\ell}. \tag{5.81}$$

For scale sizes within the inertial subrange $\ell_o \ll \ell \ll \mathrm{L}_o$, the refractive index structure function follows the two-thirds law $< \delta n^2 > \sim C_n^2 \ell^{2/3}$ (see Tatarskii [52]). Therefore,

$$< \delta\phi^2 > = D_\phi(\ell, 0) \sim C_n^2 \ell^{5/3} k^2 L \tag{5.82}$$

$$< \theta^2 > = \frac{D_\phi(\ell, 0)}{k^2\ell^2} \sim C_n^2 \ell^{-1/3} L \tag{5.83}$$

where the phase structure function defined by (5.21) is used in the equality for each formula. The final approximations derived in this way give the same order of magnitude as that derived by the theory (see equation (C.15)). Experimental measurements define $< \theta_x^2 > \approx < \theta_z^2 > = 2.5 \times 10^{-7}\ rad^2$ during maximum flood which then gives $C_n^2 \sim 0.4 \times 10^{-9}$ for $\ell \sim \rho_x \sim \rho_z$. This is approximately a factor of 3 smaller than the observed C_n^2 measured from the log-amplitude variance and shown in Figure 5.33.

If $< \delta n^2 > \sim \sigma_v^2/c_o^2$ for velocity fluctuations along the ray path, then

$$< \theta^2 > \sim \frac{\sigma_v^2}{c_o^2} \frac{L}{\ell}. \tag{5.84}$$

Experimental measurements for the angle of arrival variance during maximum flood corresponds to a rms cross channel velocity fluctuation of $\sigma_v = 0.03m\ s^{-1}$. This

is the correct order of magnitude for the velocity fluctuations within factors of two or three. As it turns out the cross channel velocity component directly affects the refractive index fluctuations. Cross channel velocity fluctuations can arise because flow through Cordova Channel is a curved flow (see Figure 5.1). This phenomena causes water to pile up on the East side of the channel (towards James Island) thus creating a pressure gradient.

Proceeding in a similar fashion, we can write $< \delta n^2 > \sim < \frac{\partial v}{\partial \ell}^2 > \frac{\ell^2}{c_o^2}$ for velocity gradients between the two rays separated by scale size ℓ. This corresponds to

$$< \theta^2 > \sim < \frac{\partial v}{\partial \ell}^2 > \frac{\ell L}{c_o^2}. \tag{5.85}$$

Experimental measurements predict a rms velocity gradient during maximum flood of $\sqrt{< \frac{\partial v}{\partial \ell}^2 >} \sim 0.03 s^{-1}$ for $\ell \sim \rho_x \sim \rho_z$.

We cannot make estimates of the velocity gradients without making some assumption about the turbulence. If we assume isotropy then $\partial v/\partial x \approx \partial v/\partial z \approx \partial u/\partial x$. The variance in the gradient is then defined as (see Hinze [31]),

$$\left\langle \frac{\partial u}{\partial x}^2 \right\rangle = \int_0^\infty \kappa^2 E(\kappa) d\kappa, \tag{5.86}$$

$$= 1.5\epsilon^{2/3} \int_0^{\kappa_1} \kappa^{1/3} d\kappa, \tag{5.87}$$

where we have used the three dimensional spectrum for velocity fluctuations defined by (5.44) in the last equality and κ_1 corresponds to the spectral limit for variance calculations. Since our angle of arrival fluctuations (high passed filtered phase difference fluctuations) are calculated for $\ell \sim \rho$, it is appropriate to calculate the variance in the velocity gradients at this scale size. The variance in the velocity gradients will be very sensitive to this cutoff. For very small scales, the gradients become very large so that the energy is dissipated by viscosity.

After integration of (5.87), the variance in the velocity gradient is,

$$\left\langle \frac{\partial u}{\partial x}^2 \right\rangle = 1.125\epsilon^{2/3}\kappa_1^{4/3}, \tag{5.88}$$

where $\kappa_1 = 2\pi/\rho = 6.3 rad\ m^{-1}$. From Figure 5.33(b) the dissipation during flood when the mean shear is greatest and when the anisotropy is most pronounced is $2 \times 10^{-5}\ m^2 s^{-3}$. This corresponds to an rms $\partial u/\partial x$ of order $0.09 s^{-1}$ which is a factor of 3 larger than the measured rms gradient from the observed arrival angle variance. This factor of 3 is acceptable since orders of magnitude are correct.

The most interesting angle of arrival correlation is that which changes direction through the tidal cycle. It is related to the difference in the phase structure function evaluated along two perpendicular diagonal directions. From (5.76) it can be shown that,

$$< \theta_x \theta_z >_{A_0} \sim \frac{L\rho_d}{4\rho^2}[< \delta n^2 >_{31} - < \delta n^2 >_{42}], \tag{5.89}$$

$$\sim \frac{L\rho_d}{2c_o^2}\left[\left\langle \frac{\partial v}{\partial \ell_{31}}^2 \right\rangle - \left\langle \frac{\partial v}{\partial \ell_{42}}^2 \right\rangle\right], \tag{5.90}$$

$$\sim -\frac{2L\rho_d}{c_o^2}\left\langle \frac{\partial v}{\partial x}\frac{\partial v}{\partial z} \right\rangle, \tag{5.91}$$

where $\rho \sim \rho_x \sim \rho_z$, $\rho_d^2 = 2\rho^2$ and the cross channel velocity gradient is evaluated along the two perpendicular diagonal directions. Thus the arrival angle correlation averaged over the array is related to the correlation in horizontal and vertical cross channel velocity gradients. Assuming that $\partial v/\partial z > 0$ throughout the tidal cycle, then $\partial v/\partial x$ must change sign. According to the measurements, v increases in the direction of U so that $\partial v/\partial x > 0$ during flood and $\partial v/\partial x < 0$ during ebb.

Thus, we conclude that the magnitude of the arrival angle fluctuations are determined by the cross channel component of the velocity fluctuations. The change in sign in the arrival angle correlations must correspond to the change in correlation between horizontal and vertical cross channel velocity gradients. These results provide motivation for further studies comparing our observations with simultaneous *in situ* measurements of the turbulence parameters.

5.7 Anisotropy Models

In section 5.4.3 we have shown that the main contribution to the observed acoustical scintillations are the velocity fluctuations. In section 5.6.2 we have shown that the cross channel velocity gradients are responsible for the observed angle of arrival correlations. In this section we will attempt to model the anisotropy and also the flattening of the structure function in terms of the spectral density for refractive index fluctuations and also in terms of the horizontal and vertical velocity correlations.

5.7.1 Separable refractivity spectrum

The correlation between horizontal and vertical arrival angles implies an anisotropic distribution in the turbulence. Theories have been developed for sound scattering from anisotropic turbulence under the assumption that the refractivity spectrum $\Phi_n(\mathbf{K})$ is separable in wavenumber $\phi_n(\kappa)$ and orientation $f(\psi)$, in the plane perpendicular to the direction of acoustic propagation (Lee and Harp [36], Gorelov and Dotsenko [29]). We can represent the spectral density as a Fourier series since $f(\psi)$ is periodic with period 2π. This leads to,

$$\Phi_n(\mathbf{K}) = \sum_{m=0}^{\infty} F_m(\kappa)\cos(m\psi - \theta_m), \tag{5.92}$$

where F_m and θ_m are the Fourier amplitude and phase of the m^{th} harmonic respectively.

We apply this anisotropic model to the wave structure function for diverging paths defined by,

$$D(\boldsymbol{\rho}_d, \tau) = 4\pi k^2 \int_0^L dy \int d\mathbf{K}\Phi_n(\mathbf{K})(1 - e^{i\mathbf{K}\cdot(\boldsymbol{\rho}_d y/L - \mathbf{U}(y)\tau)}), \tag{5.93}$$

using diagonal receivers ($\boldsymbol{\rho}_d = \boldsymbol{\rho}_x + \boldsymbol{\rho}_z$). The structure function is chosen since it is the phase difference measurements that show anisotropy. For completeness, the log-amplitude anisotropy is also taken into account. Diagonal receivers are used for two reasons. First, the average correlation between horizontal and vertical arrival angles is

given as the difference between the phase structure function evaluated along two perpendicular diagonal directions (see equation (5.76)). Second, diagonal measurements are more sensitive to simultaneous horizontal and vertical processes.

The vector dot product $\mathbf{K} \cdot (\boldsymbol{\rho}_d y/L - \mathbf{U}(y)\tau)$ can be simplified as $\kappa A \cos(\psi - \beta)$ where A is defined in (3.25) as $\sqrt{(\rho_x y/L - U\tau)^2 + (\rho_z y/L)^2}$, ψ is the angle the refractive index wave vector (κ) makes with the x-axis, and β is the angle that $|\boldsymbol{\rho}_d y/L - \mathbf{U}\tau|$ makes with the x-axis and is defined as,

$$\beta = \begin{cases} \arctan(\frac{\rho_z y/L}{(\rho_x y/L - U\tau)}) & \text{diagonal (3-1) receivers} \\ \arctan(\frac{-\rho_z y/L}{(\rho_x y/L - U\tau)}) & \text{diagonal (4-2) receivers} \end{cases} . \tag{5.94}$$

Inserting the anisotropic turbulence model (5.92) into (5.93) and integrating over the 2-dimensional wave vector space gives (see Gorelov and Dotsenko [29]),

$$\begin{aligned} D(\boldsymbol{\rho}_d, \tau) &= 4\pi k^2 \int_0^L dy \int_{\kappa=0}^{\infty} d\kappa\kappa \sum_{m=0}^{\infty} F_m(\kappa) \\ &\qquad \int_{\psi=0}^{2\pi} d\psi \cos(m\psi - \theta_m)(1 - e^{i\kappa A \cos(\psi-\beta)}), \qquad (5.95) \\ &= 8\pi^2 k^2 \int_0^L dy \int_{\kappa=0}^{\infty} d\kappa\kappa \left[F_0(\kappa) \cos\theta_0 (1 - J_0(\kappa A)) \right. \\ &\qquad \left. - \sum_{m=1}^{\infty} i^m F_m(\kappa) \cos(\theta_m - m\beta) J_m(\kappa A) \right] . \qquad (5.96) \end{aligned}$$

When m is odd, imaginary terms exist. Since it is the real part that we are interested in, without loss of generality we can set $F_m = 0$ for m odd.

Following Lee and Harp [36] we assume elliptical anisotropy since the anisotropy is considered weak and hence higher perturbation terms can be neglected. Therefore, we can set,

$$F_0(\kappa)\cos\theta_0 = a_0 \phi_n(\kappa), \tag{5.97}$$

$$F_2(\kappa) = a_2 \phi_n(\kappa), \tag{5.98}$$

$$F_{2m}(\kappa) = 0 \qquad m \geq 2, \tag{5.99}$$

where $\phi_n(\kappa)$ is the three dimensional spectral density for the refractive index fluctuations defined by (3.7). For isotropic conditions $a_0 = 1$ and $a_2 = 0$. Only the magnitude

of the spectrum changes with direction, not the slope. (For general anisotropy the coefficients $a_0(\kappa)$ and $a_2(\kappa)$ could depend on the wavenumber magnitude κ). The elliptical anisotropy simplification leads to,

$$\begin{aligned} D(\boldsymbol{\rho}_d,\tau) &= 8\pi^2 k^2 \int_0^L dy \int_0^\infty d\kappa\kappa\phi_n(\kappa)[a_0(1-J_0(\kappa A)) \\ &\qquad +a_2\cos(\theta_2-2\beta)J_2(\kappa A)], \qquad (5.100) \\ &= 8\pi^2 k^2 \int_0^L dy \int_{\kappa=0}^\infty d\kappa\kappa\phi_n(\kappa)[a_0(1-J_0(\kappa A)) \\ &\qquad +a_{2_1}\cos 2\beta J_2(\kappa A)+a_{2_2}\sin 2\beta J_2(\kappa A)], \qquad (5.101) \\ &= a_0 D_0(\boldsymbol{\rho},\tau)+a_{2_1}D_{2_1}(\boldsymbol{\rho},\tau)+a_{2_2}D_{2_2}(\boldsymbol{\rho},\tau), \qquad (5.102) \end{aligned}$$

where $a_2=\sqrt{a_{2_1}^2+a_{2_2}^2}$ and $\theta_2=\arctan(a_{2_2}/a_{2_1})$. If we let $a_0=1$ then the structure function is represented in terms of an isotropic term and an anisotropic component. The anisotropic parameters are determined from the experimental data.

In order to remove the effects of C_n^2, (5.102) is normalized by the log-amplitude variance $\sigma_\chi^2=C_\chi(0,0)$ giving,

$$D_N(\boldsymbol{\rho}_d,\tau)=D_{N0}(\boldsymbol{\rho}_d,\tau)+a_{2_1}D_{N2_1}(\boldsymbol{\rho}_d,\tau)+a_{2_2}D_{N2_2}(\boldsymbol{\rho}_d,\tau), \qquad (5.103)$$

where

$$\begin{aligned} D_{N0}(\boldsymbol{\rho}_d,\tau) &= \frac{8\pi^2(.033)}{.124}\left(\frac{k}{L}\right)^{5/6}\int_0^1 ds\int_{\kappa=0}^\infty d\kappa\kappa\kappa^{-11/3}(1-J_0(\kappa A)), \qquad (5.104) \\ D_{N2_1}(\boldsymbol{\rho}_d,\tau) &= \frac{8\pi^2(.033)}{.124}\left(\frac{k}{L}\right)^{5/6}\int_0^1 ds\int_{\kappa=0}^\infty d\kappa\kappa\kappa^{-11/3}\cos 2\beta J_2(\kappa A)), \qquad (5.105) \\ D_{N2_2}(\boldsymbol{\rho}_d,\tau) &= \frac{8\pi^2(.033)}{.124}\left(\frac{k}{L}\right)^{5/6}\int_0^1 ds\int_{\kappa=0}^\infty d\kappa\kappa\kappa^{-11/3}\sin 2\beta J_2(\kappa A)). \qquad (5.106) \end{aligned}$$

Equation (5.103) is linear in the coefficients and so a least squares fit over τ is carried out in order to fit theory with experiment. One condition that is imposed is that the measured structure function at zero time lag must equal the theoretical structure function at zero time lag. To satisfy this condition a least squares fit through a base point is carried out (see Edgar and Himmelblau [19]). This base point will generate an offset corresponding to,

$$D_{\text{off}}=D_N(\boldsymbol{\rho}_d,0)-D_{N0}(\boldsymbol{\rho}_d,0)-a_{2_1}D_{N2_1}(\boldsymbol{\rho}_d,0)-a_{2_2}D_{N2_2}(\boldsymbol{\rho}_d,0). \qquad (5.107)$$

Also, one key parameter that affects the shape of the functions is the current speed, U. It defines the location of the minima and also the slope at zero time lag. We use the path averaged current speed obtained by the delay to peak method described in section 5.4.2 and A.3.

Figure 5.35 shows the theoretical functions for D_{N0}, D_{N2_1} and D_{N2_2} as a function of time lag. Also shown is the experimental wave structure function $\hat{D}_N$ (dotted line) fitted to the theoretical structure function D_N (solid curve). Comparing the experimental structure function to the isotropic structure function (D_{N0}) shows that the anisotropy flattens the experimental curve thus reducing the slope at zero time lag. This may explain why the structure function method underestimates the current speed in our observations (see equation (5.29)).

The anisotropy parameters a_2 and θ_2 are plotted in Figure 5.36(a) and (b) respectively for diagonal 3-1 pairs. (Similar results are obtained for the diagonal 4-2 pair). This time series is taken through the tidal cycle shown in Figure 5.28(a). The fact that $a_2 > 1$ suggests a problem with this model. Convergence in the series for the refractive index spectral density (5.92) occurs slowly even though the fit between the experimental structure function and the model (5.103) is good (see Figure 5.35).

The direction of anisotropy is obtained by maximizing the spectral density,

$$\Phi_n(\mathbf{K}) = \phi_n(\kappa)(1 + a_2 \cos(2\psi - \theta_2)), \tag{5.108}$$

over the direction, ψ. Therefore, the direction of anisotropy is defined as $\psi_a = \theta_2/2$ and is on average ~ 0 degrees during flood flow and ~ -5 degrees during ebb flow. This implies that the anisotropy occurs predominantly in the horizontal direction. That is, the spectral level is higher when measured along the horizontal than it is along the vertical as expected. This is consistent with the phase difference spectral measurements shown in section 5.6.2 for high passed filtered data. Because a_2 is greater than one for most of the tidal cycle, the spectral density (5.108) becomes negative for some angles ψ. For this reason the results from this model are questionable.

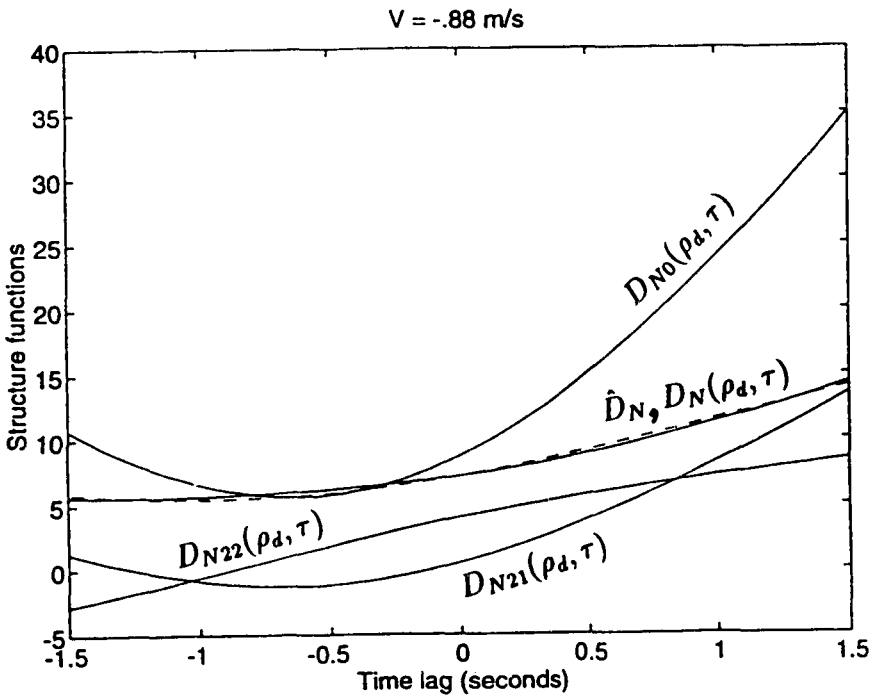

Figure 5.35: Theoretical functions D_{N0}, D_{N2_1}, and D_{N2_2} plotted against time lag. The experimental wave structure function $\hat{D}_N$ is shown as a dashed curve and the best fit $D_N = -2.057 + D_{N0} - 1.593 D_{N2_1} + 0.351 D_{N2_2}$ is shown as a solid curve.

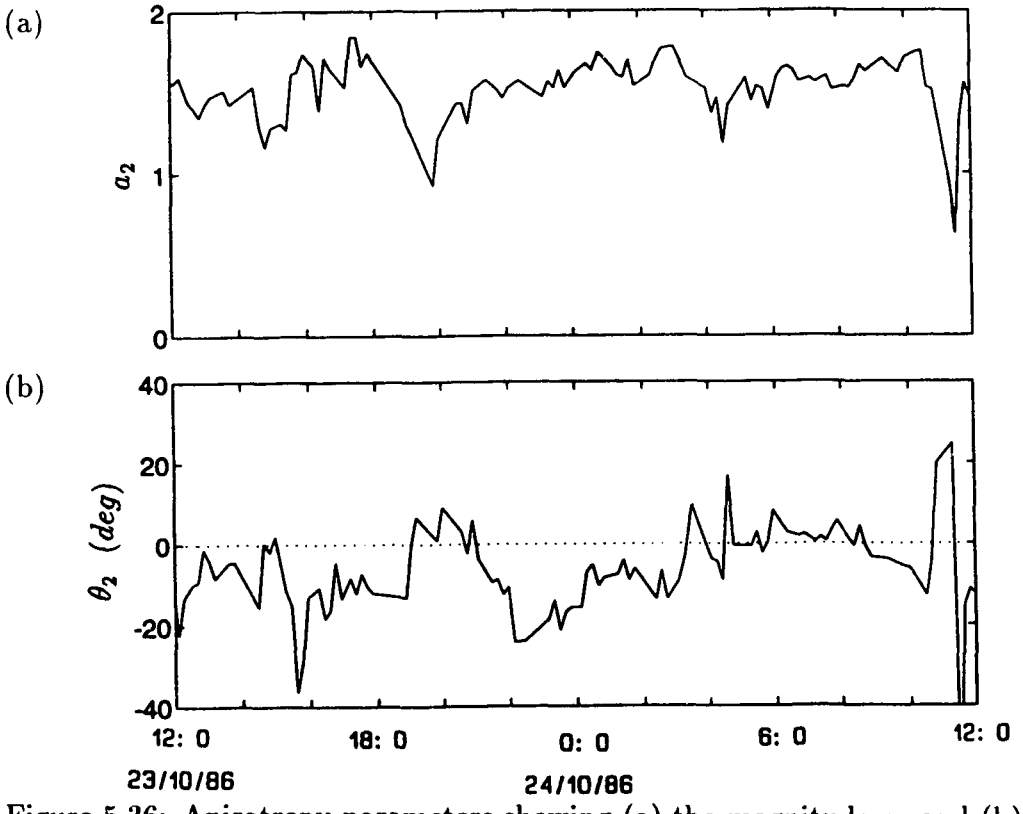

Figure 5.36: Anisotropy parameters showing (a) the magnitude a_2 and (b) direction θ_2 as a function of time. True isotropy occurs for $a_2 = 0$.

5.7.2 Turbulent velocity correlations

In this section we try to use the wave structure function to see if the correlation of horizontal and vertical velocity fluctuations causes the observed anisotropy and also to see if it causes the flattening of the wave structure. The one common term that exists in all the acoustic covariance and structure functions is the exponential term, $\exp(i\mathbf{K}\cdot(\boldsymbol{\varrho}-\mathbf{U}\tau))$ which relates the perturbations present at one point in the receiving plane to those present at another point. If we separate the current velocity $\mathbf{U}=\mathbf{U}_o+\mathbf{u}$ into a mean $\mathbf{U}_o=(U_o,0,0)$ and a fluctuating $\mathbf{u}=(u,v,w)$ component, then the exponential term becomes,

$$\exp(i\mathbf{K}\cdot(\boldsymbol{\varrho}-\mathbf{U}\tau))=\exp(i\mathbf{K}\cdot(\boldsymbol{\varrho}-\mathbf{U}_o\tau))\exp(-i\mathbf{K}\cdot\mathbf{u}\tau). \tag{5.109}$$

Averaging over the fluctuations ($<>_u$), taking into account that the wavenumber integration is over the two-dimensional plane perpendicular to the acoustic path gives,

$$\begin{aligned} <\exp(-i\mathbf{K}\cdot\mathbf{u}\tau)>_u &= <\exp(-iK_xu\tau)\exp(-iK_zw\tau)>_u, & (5.110)\\ &= \exp\left(-\frac{K_x^2\sigma_u^2\tau^2}{2}-K_xK_z<uw>\tau^2-\frac{K_z^2\sigma_w^2\tau^2}{2}\right) & (5.111)\end{aligned}$$

where $\sigma_u^2=<u^2>$ and $\sigma_w^2=<w^2>$ are the variances in the horizontal and vertical velocity fluctuations respectively, and $<uw>$ is the cross covariance of horizontal and vertical velocity fluctuations. Equation (5.111) is obtained by assuming that the velocity fluctuations are Gaussian with a joint probability density,

$$f(u,w)=\frac{1}{2\pi\sigma_u\sigma_w\sqrt{1-r^2}}\exp\left[\frac{-1}{2(1-r^2)}\left(\frac{u^2}{\sigma_u^2}-\frac{-2ruw}{\sigma_u\sigma_w}+\frac{w^2}{\sigma_w^2}\right)\right], \tag{5.112}$$

where $r=<uw>/\sigma_u\sigma_w$ is the correlation coefficient.

Equation (5.111) can be further simplified if we make the assumption that $\sigma_u=\sigma_w$, and if we transform into polar coordinates ($K_x=\kappa\cos\psi$ and $K_z=\kappa\sin\psi$). Therefore,

$$<\exp(-i\mathbf{K}\cdot\mathbf{u}\tau)>_u=\exp\left(-\frac{\kappa^2\sigma_u^2\tau^2}{2}\right)\exp\left(-\frac{\kappa^2\sin 2\psi<uw>\tau^2}{2}\right). \tag{5.113}$$

If u and w are independent ($< uw >= 0$) then (5.113) reduces to an exponential term obtained by Wernik *et.al.* [62]. They incorporate this term in the scintillation theory since it violates the "frozen-in" assumption. They show that the velocity fluctuations reduce the oscillatory character and introduce positive skewness in the log-amplitude cross covariance function. The slope of the log-amplitude cross covariance at zero time lag is, however, independent of σ_u^2. The frozen field result is obtained if $\sigma_u^2 << 2U/\kappa\tau$. Thus, it is the high frequency part (corresponding to the small scale structures) of the scintillation spectrum that will be more susceptible to nonfrozen flow effects.

Measurements of σ_u^2 can be obtained from the dissipation measurement using (5.61). Representative values indicate that $\sigma_u \approx 0.1U$. That is, the rms velocity fluctuations are approximately 10% the mean flow. Measurement of $< uw >$ using (5.113) is not simple because of the dependence on the direction ψ which is a variable of integration. Also, at zero time lag the exponential terms reduce to one and so the velocity correlations affect only the shape of the time-lagged structure functions.

Numerical integration of the wave structure function for diagonal paths,

$$D(\boldsymbol{\rho}_d, \tau) = 4\pi k^2 \int_0^L dy \int_0^\infty d\kappa\kappa\phi_n(\kappa) \int_0^{2\pi} d\psi$$
$$\left[1 - \exp(i\kappa A\cos(\psi - \beta)) \exp\left(-\frac{\kappa^2\sigma_u^2\tau^2}{2}\right) \exp\left(-\frac{\kappa^2 < uw > \tau^2 \sin 2\psi}{2}\right)\right], \quad (5.114)$$

for correlations ranging from $-0.01m^2s^{-2} < < uw > < .01m^2s^{-2}$ with increment $0.001m^2s^{-2}$ were evaluated during strong ebb and flood flow. It was found that the shape of the structure function followed the isotropic form D_{N0} in Figure 5.35. Hence, reasonable values of $< uw >$ do not explain the flattening of the time lagged structure function observed by our measurements.

In the above analysis it was assumed that the correlation $< uw >$ is independent of path position. One of the outstanding difficulties in analysing the correlations is that the acoustical scintillation techniques cannot distinguish between u and w at different points along the path. Thus, $< uw >$ may be quite uncorrelated at a point location and a resulting path average may give spurious results. To avoid this problem, we could assume some distribution for u and w along the path. Thus, the

correlation $< u(y)w(y) >$ is now path dependent. Assuming a distribution other than uniform will ultimately reduce the numbers even more and so we conclude that the flattening of the wave structure function and the arrival angle correlations are not explained by the Reynolds stress.

5.8 Summary and Conclusions

We have measured the temporal frequency spectra for log-amplitude, phase and phase difference and compared it to the Tatarskii weak scattering model (appropriately modified for spherical spreading and aperture averaging effects). Our measurements are consistent with a Kolmogorov turbulence model for the random medium. Aperture averaging over the finite dimensions of the transducers is significant at higher wavenumbers. That is, scales sizes smaller than the diameter of the transducer are effectively averaged out hence suppressing the higher frequencies.

The phase difference spectrum provides an indication of the outer scale of turbulence L_o. We use the phase difference instead of the phase because it is less sensitive to the large scale features. Most of the time the data are described by a von Karman spectrum where $L_o = 32\ m$. There is some evidence that the turbulence power law extends beyond the outer scale leading to overestimates of L_o. The spectral level decreases with decreasing L_o because the wave structure function used as a normalization is determined at $L_o = \infty$. In order to keep the same spectral level for varying outer scales the wave structure function should decrease with decreasing outer scale. It was found that the wave structure function for an outer scale of $16m$ is approximately half that of the wave structure function determined for $L_o = \infty$.

We have measured the path averaged current speed using a variety of techniques for parallel paths. The delay to peak method works very well during currents greater than $0.12m\ s^{-1}$ and is insensitive to the receiver spacing; the slope of the log-amplitude cross covariance function is very sensitive to the receiver spacing. The structure function is flattened, presumably due to anisotropic turbulence conditions, such that the slope at zero time lag is reduced compared to the theoretical slope. There seems to be a factor of 1.5 difference between the current meter and acoustic observations for both parallel and diverging paths using the structure function. In addition, we have used the square array to obtain path averaged measurements of the mean current shear which compares very well to the shear determined from two

vertically spaced current meters. The most significant shear exists during flood which corresponds to a time when the turbulence is most anisotropic.

Measurements of C_n^2 by acoustic methods are compared to measurements of $C_{n_s}^2$ by CTD data. The difference between the two measurements indicates that turbulent velocity fluctuations is the dominant component of our acoustical scintillation measurements. Differences in C_n^2 between flood and ebb indicate that eddies generated in Saanichton Bay are carried by the ebb flow past our measurement area thus increasing the level of the refractive index variability.

Estimates of $C_{n_v}^2$ are determined from the acoustic measurement and the CTD measurement. An outer scale limit for these measurements is not very important since it is the level of the refractive index spectral density that determines the results. From these measurements the path averaged turbulent kinetic energy dissipation rate (per unit mass), ϵ is determined. Our measurements are consistent with estimates of dissipation based on a balance between the production and dissipation of energy for well-mixed, steady flows.

Accuracy of the scattering parameters Γ and X estimates are limited by the outer scale measurement. This is because these measurements are derived based on the integral over the inertial scales of the spectrum for refractive index fluctuations and for phase fluctuations. Using reasonable approximations of L_o and L_V based on our measurements, places Γ and X firmly in the weak scattering regime, consistent with our use of the Tatarskii model for weak scattering by turbulence. Also, comparison with other acoustic propagation experiments indicates that our measurements are taken in a very different environment.

The two dimensional angle of arrival appears to be a very sensitive signal for examining the fine scale features in the flow dynamics over a wide range of scales. For low frequency variability the horizontal arrival angle is consistent with the expected Mach number of the flow and the vertical arrival angle is consistent with that expected on the basis of refraction by sound speed gradients. Stratification causes more variability in the vertical arrival angle (and hence the vertical phase difference) than

the horizontal arrival angle. Measurement of the arrival angles in this way can be used to obtain path averaged current speed and sound speed gradients (hence density gradients) without any detailed knowledge of the scattering process.

The high frequency variability shows that the horizontal and vertical arrival angles are correlated over scale sizes less than 32 m. This directly leads to an anisotropic turbulence explanation. Since it is the velocity fluctuations that cause the acoustical scintillations we hypothesize that they are also the reasons for the observed anisotropy. Using qualitative arguments we show that the angle of arrival correlations averaged over the array can be explained in terms of the cross channel velocity gradient. The correlations which change direction with the changing tide are expressed in terms of the correlation of horizontal and vertical cross stream velocity gradients. If $\partial v/\partial z > 0$ throughout the tidal cycle then it is found that $\partial v/\partial x > 0$ during flood and $\partial v/\partial x < 0$ during ebb. This result is not confirmed with independent estimates or measurements.

If the refractive index spectral density is separable in wavenumber and direction then it can be modelled by a Fourier series. However, since it was found that the series converges slowly and that the refractive index spectrum is negative for some directions, this anisotropy model is questionable. Another attempt at studying the anisotropy was to investigate whether or not the correlation of arrival angles is related to the correlation of horizontal and vertical velocity fluctuations. In order for the velocity correlation to explain the flattening of the wave structure function, it would have to be larger than physically plausible.

We have studied both the forward and the inverse problem of acoustic propagation through random media. The forward problem is examined by showing that a turbulent random medium together with the weak scattering theory describes the acoustic fluctuations. In the inverse problem we have used the acoustic fluctuations to obtain measurements of the oceanographic processes in a turbulent channel flow. The most interesting results obtained from this experiment are measurements of the turbulent kinetic energy parameters - in particular the TKE dissipation.

Chapter 6

Multipath Acoustic Propagation Characteristics in Saanich Inlet

6.1 Introduction

The experimental work described thus far involved propagation through a turbulent flow over a relatively short path. In order to gain experience in the application of this concept in a different environment, the instrument was deployed in Saanich Inlet on the west side of Saanich peninsula (see Figure 6.1). Here the water is deep, stratified and only very weakly influenced by tidal currents. Moreover, the path length was over three times as great (2350 m). It was not practicable to acquire a comprehensive oceanographic data set in Saanich Inlet, sufficient to explain all the details of acoustic variability, and the analysis is therefore restricted to a discussion of deterministic effects and some statistical properties. However, the results do provide an opportunity for investigating the problem of multipath separation, which is a prerequisite for propagation analysis in this environment.

In Cordova Channel the cause of the acoustical scintillations was due to the random refractive index fluctuations inherent in a turbulent boundary layer. In Saanich Inlet the causes of the acoustical scintillations may be due to multiple scattering;

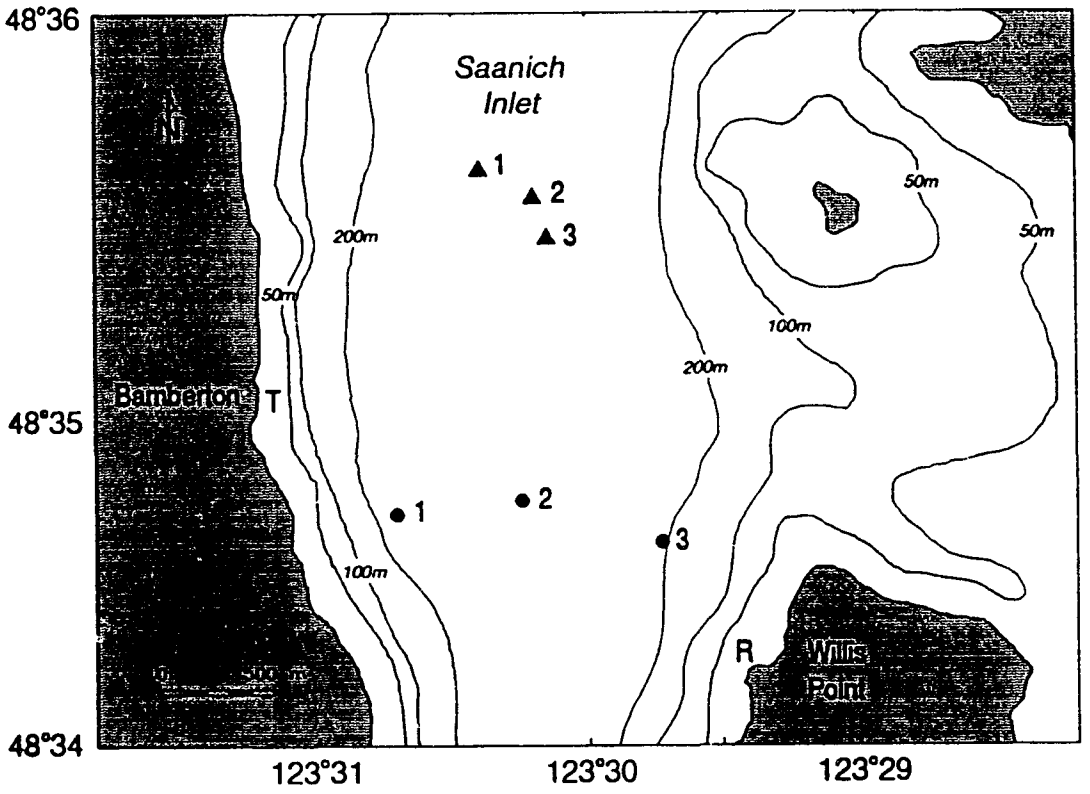

Figure 6.1: Saanich Inlet showing instrument locations, together with the transmitter array (T) and receiver array (R). Recording current meters were moored at stations 1, 2 and 3 (•). Thermistor chains were moored at station 1, 2, and 3 (▲). CTD profiles were done intermittently at station 3▲ and station 2•.

it may be the result of multipaths interfering destructively or constructively, or the scintillations may be due to refractive index variability from internal waves.

This chapter will describe the oceanographic instrumentation used and give an overview of the data collected during the experiment. The technique described in the Cordova Channel experiment for obtaining amplitude and phase will no longer apply because of the multipath conditions. Thus an overview of the acoustic data collected will be shown as well as results from the square array. Some of these results include the development of a multipath separation algorithm for obtaining amplitude

and phase, a correlation analysis between diverging and parallel paths for horizontal and vertical transducers, a probability distribution and finally a spectral analysis of intensity and phase.

6.2 Oceanographic Characteristics

The oceanographic data discussed in this thesis was collected over a three day period and this section describes some of the characteristics observed in Saanich Inlet.

6.2.1 Current meter observations

Each current meter mooring shown in Figure 6.1 has three Aanderaa current meters placed at depths corresponding to the ray path depths: East and West moorings have current meters at 20, 35 and 60 m, the center mooring has current meters at 20, 35 and 110 m. Each instrument records temperature, salinity, current speed and direction at a sampling interval of 5 minutes.

Tidal activity in Saanich Inlet is small. Maximum current observations at 20 metres is of the order 20 $cm\ s^{-1}$. At 60 metres, Figure 6.2 shows practically no current both for the perpendicular and parallel component. Because of this characteristic it is not practicable to calculate the Reynolds number. The temperature and salinity measurements show a periodic cycle corresponding to the internal tide. The horizontal bar ranging in time from April 19, 17:00 to April 20, 02:00 corresponds to simultaneous thermistor profiles and acoustic time series.

6.2.2 CTD observations

Periodic CTD profiles were collected so as to obtain mean sound speed profiles. These profiles are then used for acoustic ray tracing. Also, a temperature - salinity relation from the profiles shows the temperature is a multivalued function of salinity (see Figure 6.3). The water column from the surface to about 50 m can be characterised as a linear T-S relation; the water column from about 80 m to the depth of the Inlet can also be characterised as a linear T-S relation but with opposite direction. From about 50 m to 80 m much variability occurs and no linear relation can be seen. Because of this relation it is difficult to obtain salinity fluctuations from temperature

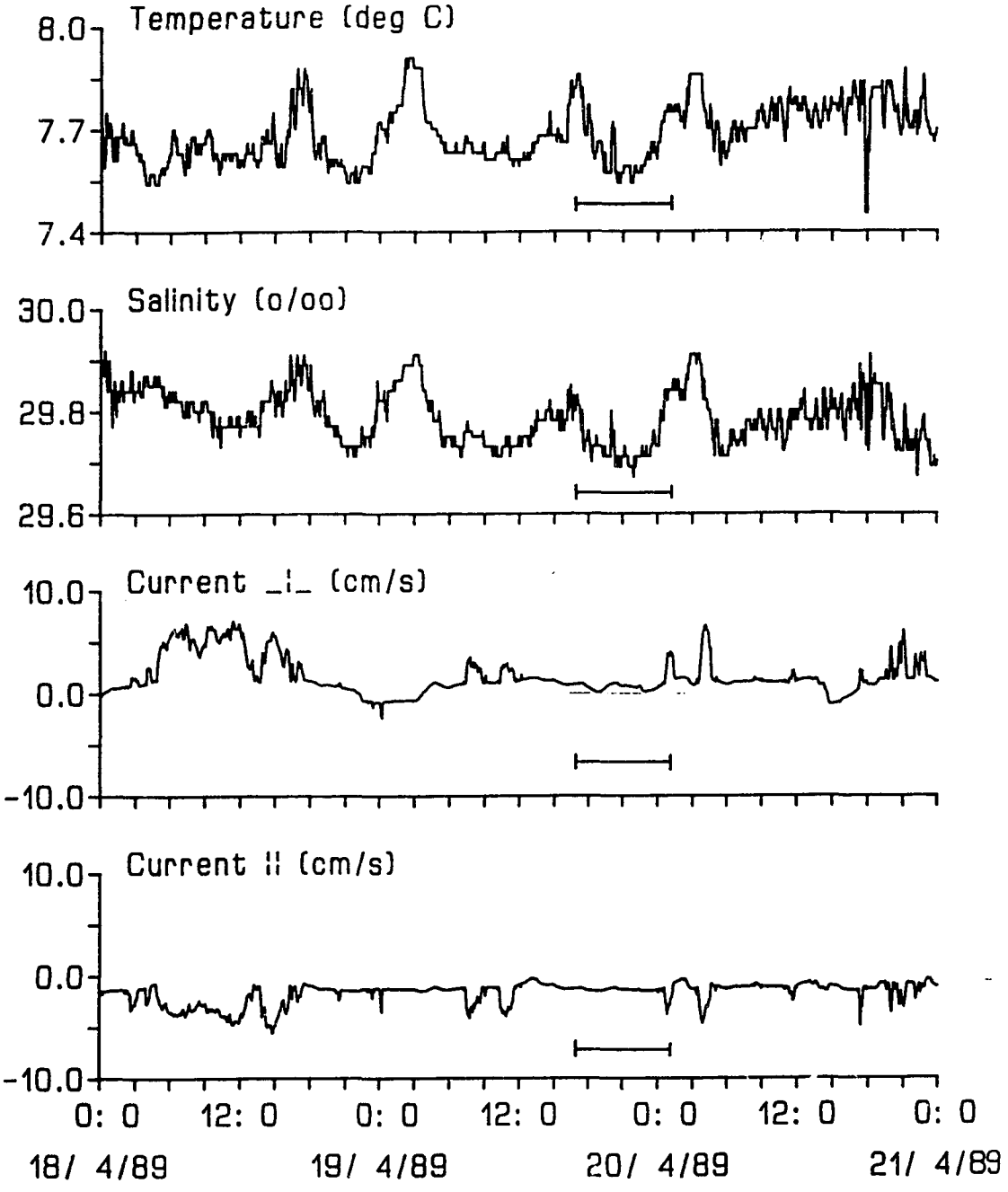

Figure 6.2: Observed current meter data (60 metre) at station 3 (•) for a three day period. Horizontal line coincides with the acoustic and thermistor chain observations described. The $\perp$ component is relative to 120° *True* and the $\parallel$ component is relative to 30° *True*.

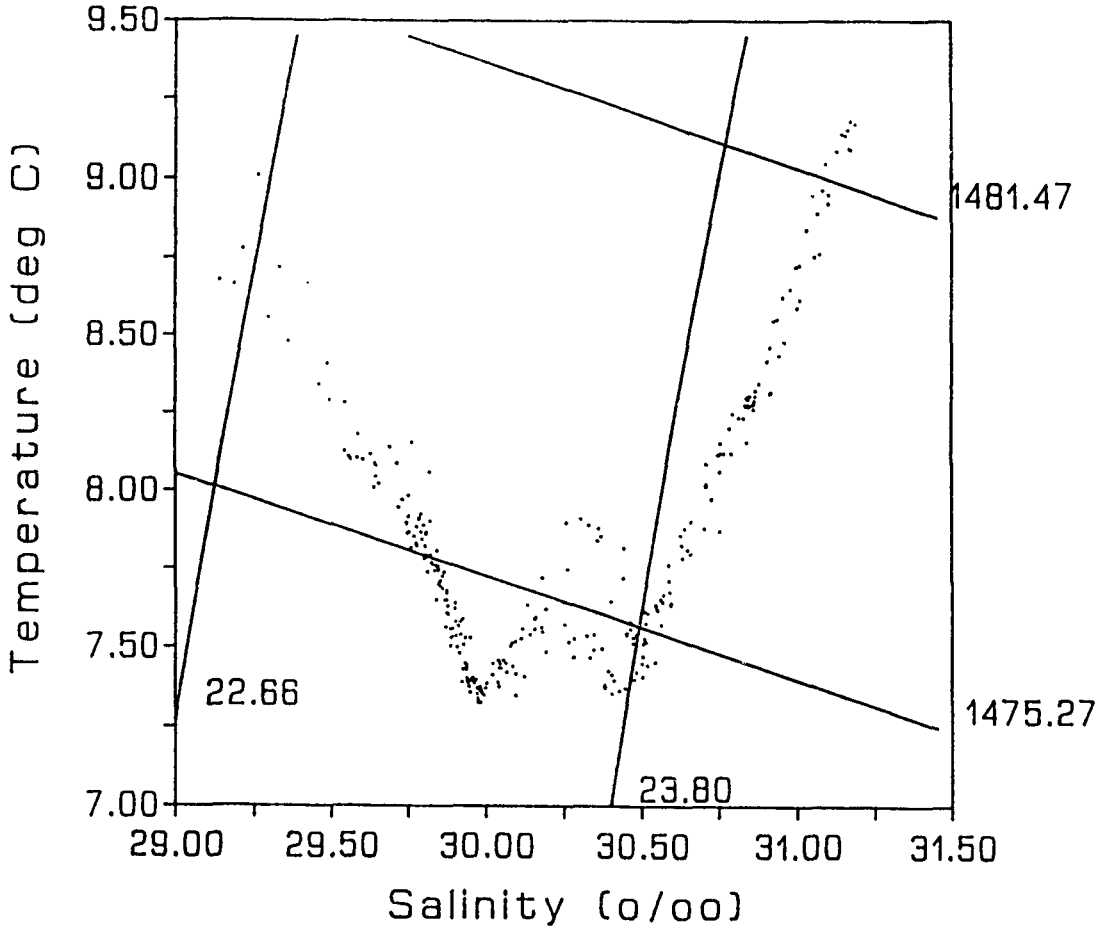

Figure 6.3: Temperature - salinity diagram showing density (σ_t) in $kg\ m^{-3}$ and sound speed in $m\ s^{-1}$ contours.

fluctuations. Since sound speed is dominated by temperature a mean salinity profile together with the temperature measurements from thermistor chains can be used to obtain sound speed.

We can calculate the bulk Richardson number,

$$\mathrm{Ri} = -\frac{g\frac{\Delta\rho}{\rho_o}h}{\Delta U^2}, \tag{6.1}$$

in this environment, as we did for Cordova Channel. Representative values of the current shear, from two current meters separated 40 m vertically, and density shear from CTD profiles, give Ri $\sim$ 8.2, confirming that the turbulence from shear is not strong enough to overcome the stratification. According to Pond and Pickard [45]

when Ri ¿ 1/4, turbulence cannot be generated by the mean shear.

Conductivity, temperature and depth (CTD) profiles were averaged together to obtain the sound speed ($c(z)$) and the Brunt-Vaisala angular frequency ($N(z)$) as a function of depth (see Figure 6.4(a) and (b) respectively). The Brunt-Vaisala angular frequency N in $rad \cdot s^{-1}$ is defined as (see Pond and Pickard [45]),

$$N = \left(-\frac{g}{\rho_o} \frac{d\rho}{dz} \right)^{1/2}, \tag{6.2}$$

where $g = 9.8\ m\ s^{-2}$, $\rho_o = 1023.5\ kg\ m^{-3}$ is the density at 67 m depth and $d\rho/dz$ is the density gradient. The Brunt-Vaisala profile fits the Garrett and Munk [27] exponential profile,

$$N(z) = N_o \exp\left(\frac{z}{B_o}\right) \qquad z < 0, \tag{6.3}$$

where z is the depth, $N_o = 1.91 \times 10^{-2}\ rad\ s^{-1}$ and $B_o = 141.8\ m$ is the maximum depth of the profile. The exponential distribution normally applies to deep open ocean conditions, but it is interesting to see that beyond 20 m depth our data have the same characteristics.

6.2.3 Thermistor chain observations

Three thermistor moorings were placed in a triangular array. Each mooring had sensors ranging from 20 m to 120 m depth with 5 m increment and a sampling rate of 2 minutes. The distances between each of the thermistor moorings are shown in Table 6.1. If these data are used to determined the internal wave field then the minimum length of internal gravity waves that can be sampled is approximately 400 metres using the array. The minimum period that can be sampled is 4 minutes. This would correspond to a phase velocity of 1.7 $m\ s^{-1}$.

The thermistor chains are used to look at the temporal variability in the temperature and sound speed; the temperature measurements together with a mean salinity profile determine the sound speed fluctuations. Temperature time series are shown in Figure 6.5(a) for the three day period shown in Figure 6.2. The horizontal bar

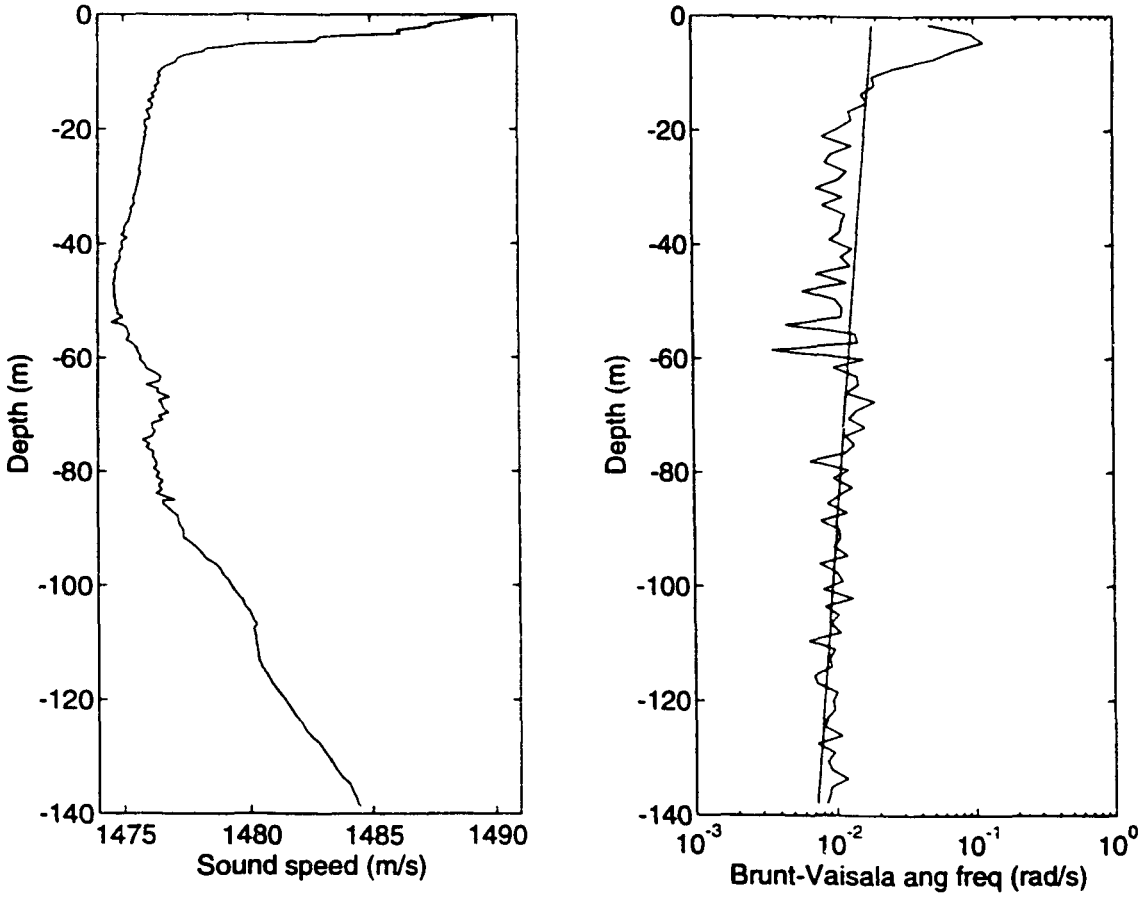

Figure 6.4: Average profiles obtained from 6 CTD casts of (a) sound speed and (b) Brunt-Vaisala angular frequency ($N(z)$) with an exponential least squares fit superimposed.

Instrument	Spacing (m)
THA1-THA2	249m
THA1-THA3	404m
THA2-THA3	181m

Table 6.1: Distance between thermistor moorings.

corresponds to simultaneous acoustic data and expanded temperature profiles and fluctuations shown in Figure 6.5(b) and (c). For depths greater than 80 m the temperature undergoes variations associated with the internal tide. For depths between 60 m and 80 m much variability occurs during the time of the acoustic data possibly due to the passage of internal waves. At $70m$ depth the Brunt-Vaisala frequency is 1.86×10^{-3} Hz corresponding to a minimum period of 9 minutes. Near the surface (20 m) very little variation occurs except for a gradual increase due to surface warming.

Temperature profiles as a function of time for 8 hours of data are shown in Figure 6.5(b). The mean temperature gradient for depths greater than 90 m and less than 40 m remains essentially constant with time. Most of the variability occurs at 60 meters depth which is 25 m below the depth of the transmitting and receiving arrays. The fluctuations in temperature as a function of depth and time are shown in Figure 6.5(c). These profiles were obtained by subtracting the mean temperature profile in (b) from the individual profiles. Maximum temperature fluctuations are of the order 0.15 $deg\ C$.

From the temperature profiles the sound speed profiles can be evaluated using a mean salinity profile from the CTD data. Figure 6.6 shows the mean sound speed for the data shown in Figure 6.5(b). The dashed curve represents the minimum and maximum sound speeds for the eight hour section of data. The data points are shown within these curves. It is clear that most of the variability occurs between 65 and 75 metres. The refractive index variance for this time interval and over this depth range is $< \eta^2 >= 8.11 \times 10^{-6}$.

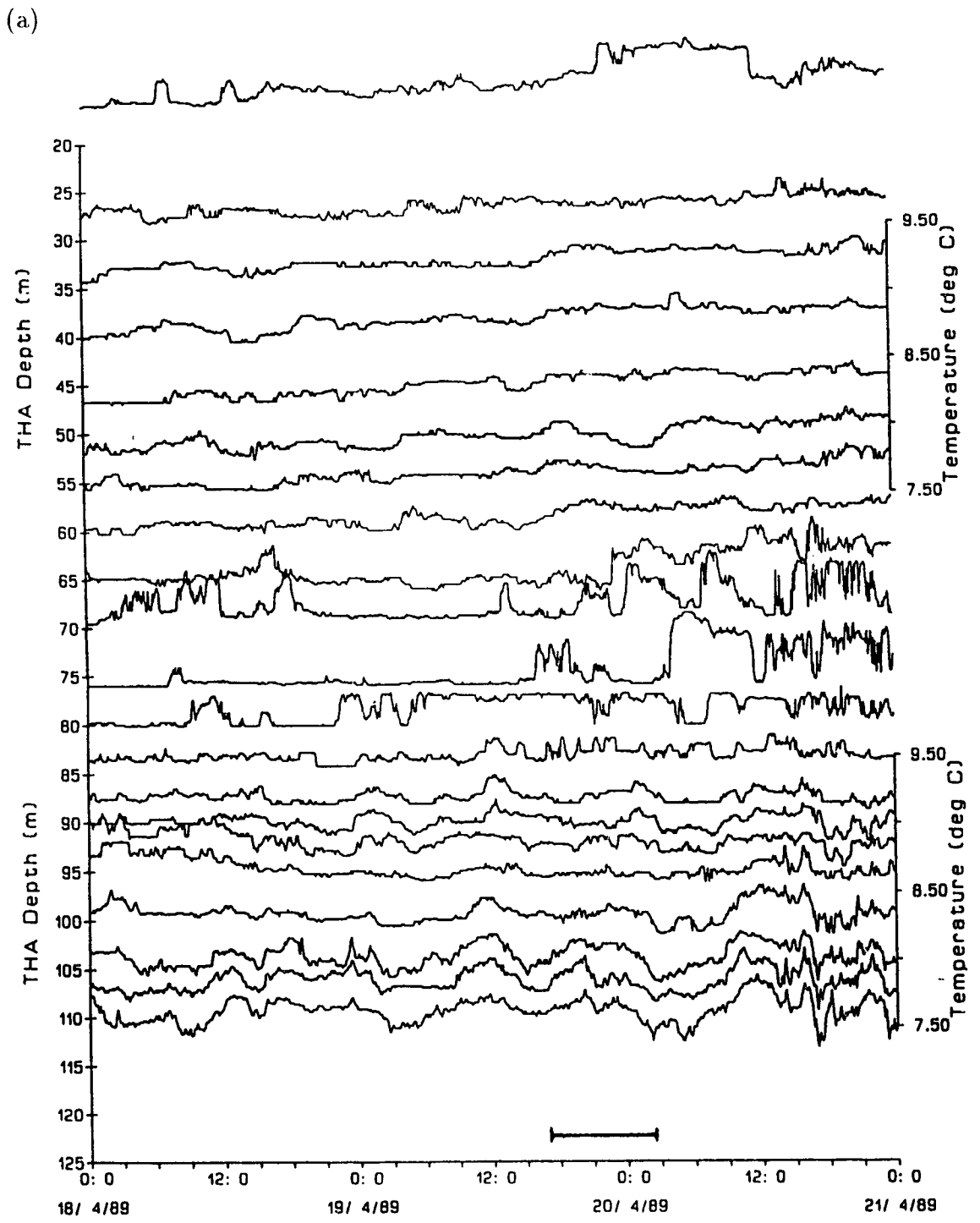

Figure 6.5: (a) Thermistor time series as a function of depth taken at station 3 (▲) for a three day period. (b) Thermistor chain profiles for an 8 hour period on April 4. (c) Temperature fluctuations where the mean temperature profile in (b) is subtracted from each of the profiles.

(b)

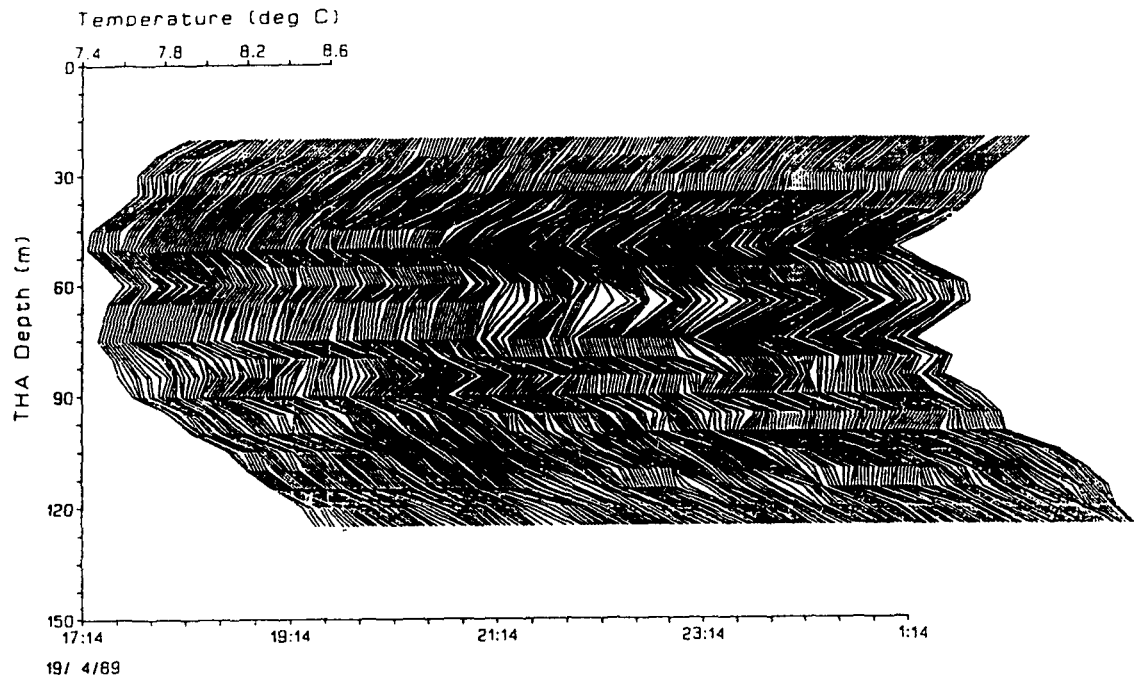

(c)

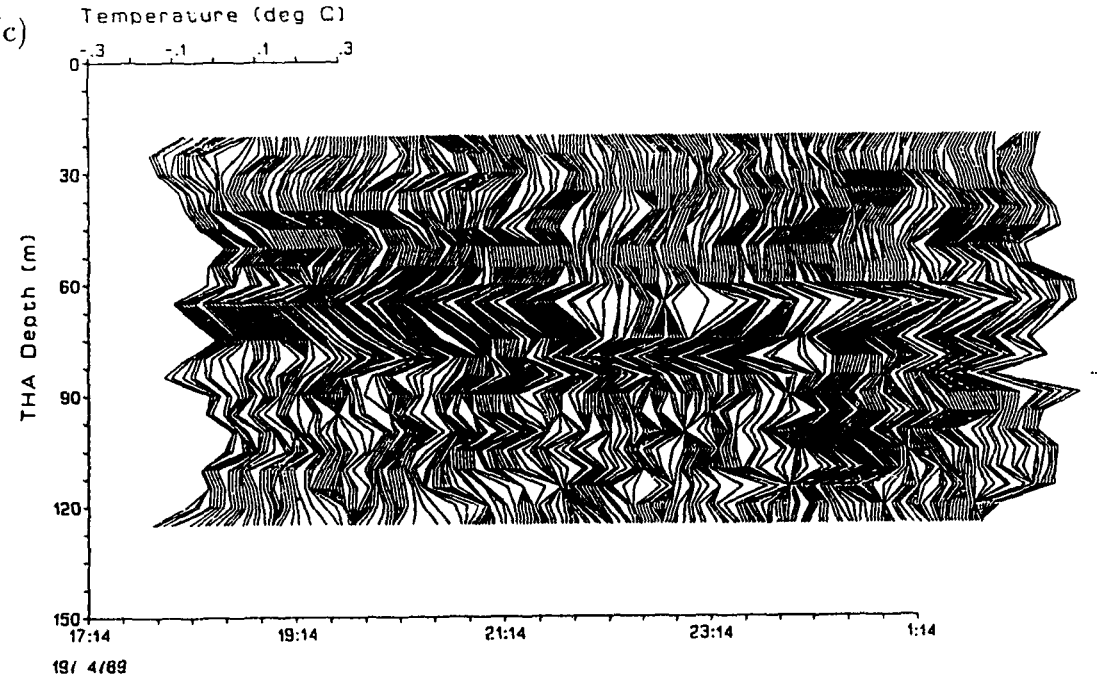

Figure 5.5 continued.

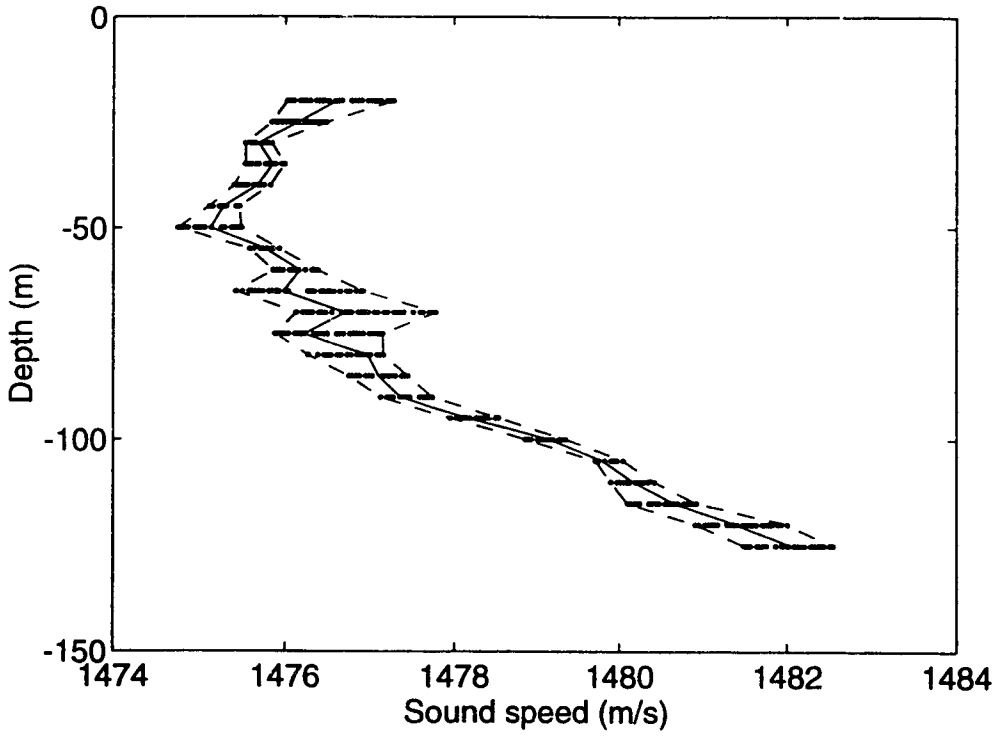

Figure 6.6: Mean sound speed profile (solid curve) from thermistor chains, together with the minimum and maximum profiles (dashed curve). Data are shown as dots.

6.3 Acoustic Characteristics

The acoustic data discussed in this thesis were collected for nine hours and this section describes some its characteristics. Acoustic transmitter and receiver arrays, were deployed as shown in Figure 6.1. Acoustical measurements were made with 4-transmitter and 4-receiver square arrays. The square array was used to shed light on some 2-dimensional features of the acoustic scintillations.

6.3.1 Multipath analysis

The acoustic observations in Saanich Inlet show multipath propagation conditions. Figure 6.7(a) shows the measured amplitude (arbitrary units) which is consistent with Figure 4.4, as a function of relative arrival time (3 ms total) and as a function of elapsed time. The figure represents 9 hours of sub-sampled data (25 second intervals). Comparing the data from all the transmitter and receiver combinations show similar results implying a degree of coherence over the number of multipaths from the 2 metre array.

Using a procedure developed by Booth [3], total travel time and total path length of eigenrays (ray paths that connect the transmitter to the receiver) for a given sound speed profile were calculated. This procedure assumes that the sound speed profile is range independent. Figure 6.7(b) shows that for the given averaged sound speed profile three ray paths are possible for a directional transmitter having beam width $\pm 5 deg$. The time separation between the first and the third arrival is $1.5 ms$. The received acoustic signal shows a time separation of $1.9 ms$. This discrepancy is probably due to the failure of the homogeneity assumption.

The first set of arrivals is refracted upwards into the near surface because of the shallow thermocline. Variations in the refractive index due to mixing at the thermocline may explain the micropath behaviour. The second arrival, although appearing to have a well defined peak, is actually a superposition of three (maximum) closely spaced multipaths. This path will be studied in closer detail because of the

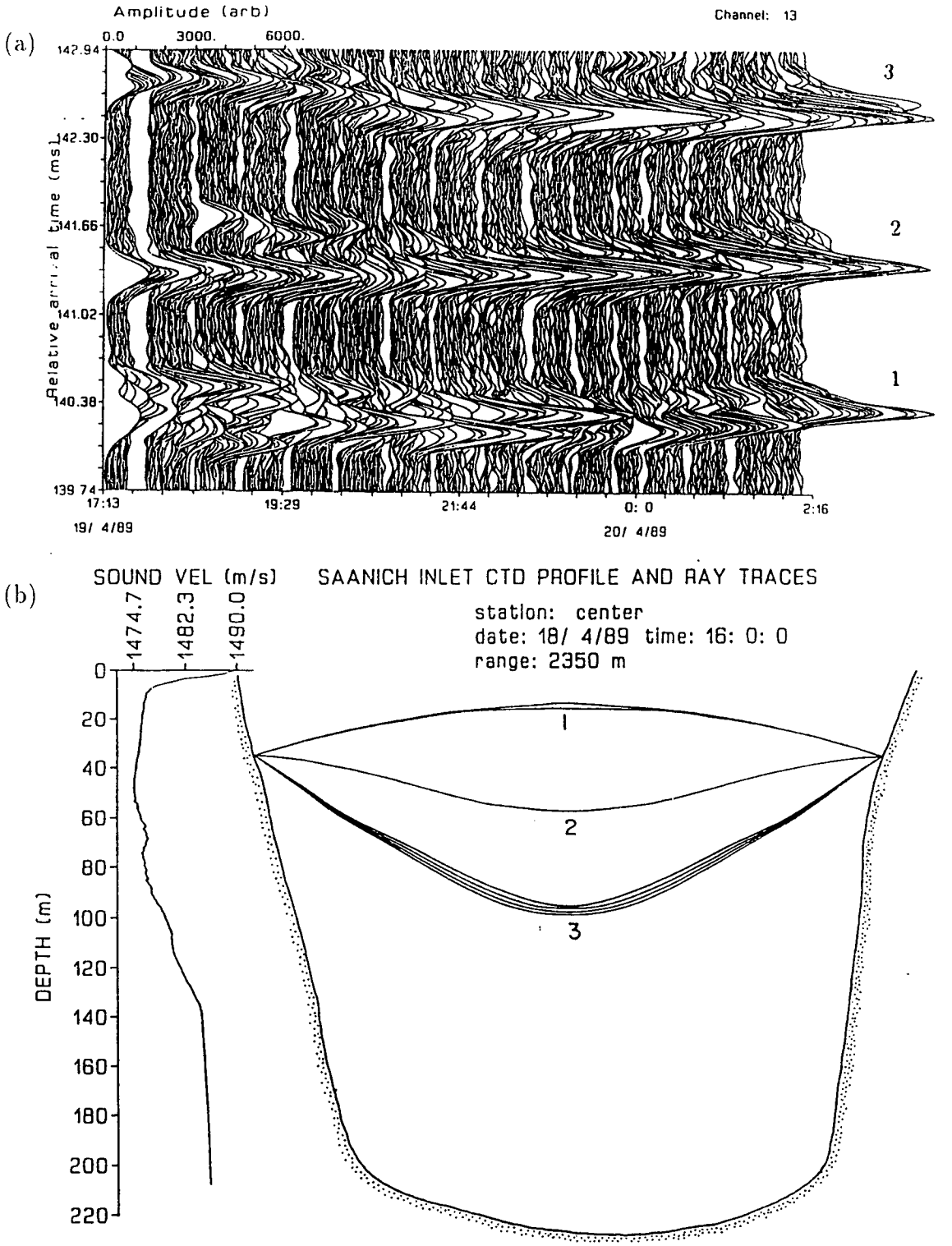

Figure 6.7: (a) Acoustic amplitude measured as a function of relative arrival time and as a function of elapsed time. Measurements are from T4/R4 transducers. (b) Averaged sound speed profile using CTD data and the acoustic eigenrays for a source and receiver at 35 m depth.

interesting temperature variability that occurs at 70 m depth; this depth separates two distinct water types. The third set of arrivals clearly shows phase variations related to the internal tide that exists at 80 m and beyond. The temperature increases during this time resulting in increased sound speed and thus decreased travel time. This is then followed by a decrease in temperature corresponding to an increase in travel time. This arrival also consists of several overlapping multipaths.

There are two factors which determine the travel time and order of arrivals for the eigenrays. One is the length of path travelled between source and receiver and the second is the sound speed and current velocity along the path (see DeFerrari and Nguyen [14]). The first and second arrival of Figure 6.7 have similar path lengths and so it is the difference in the sound speed (and current) along each path that gives the arrival time separation of 1.12 ms. The time separation between the second and third arrival is dominated by both path length differences and sound speed variability.

Reciprocal acoustic transmission measurements in this kind of environment would be ideal for measuring both the temperature and current variability. According to Ko *et.al.* [33] the sum travel times for a reciprocal transmission gives the sound speed (hence temperature) variability along the path; the difference travel times for a reciprocal transmission gives the current speed variability along the path.

6.3.2 Multipath separation algorithm - amplitude and phase calculations

In order to separate closely spaced multipaths, a maximum likelihood estimation algorithm is developed following Ehrenberg *et.al.* [20]. The mathematical model for the received signal $r(t)$ is,

$$r(t) = \sum_{i=1}^{N} A_i s(t - \tau_i) + n(t) \tag{6.4}$$

where A_i and τ_i are the amplitude and arrival times for the i^{th} path, $n(t)$ is the noise and t is the elapsed arrival time. The signal $s(t)$ is known since it is the matched

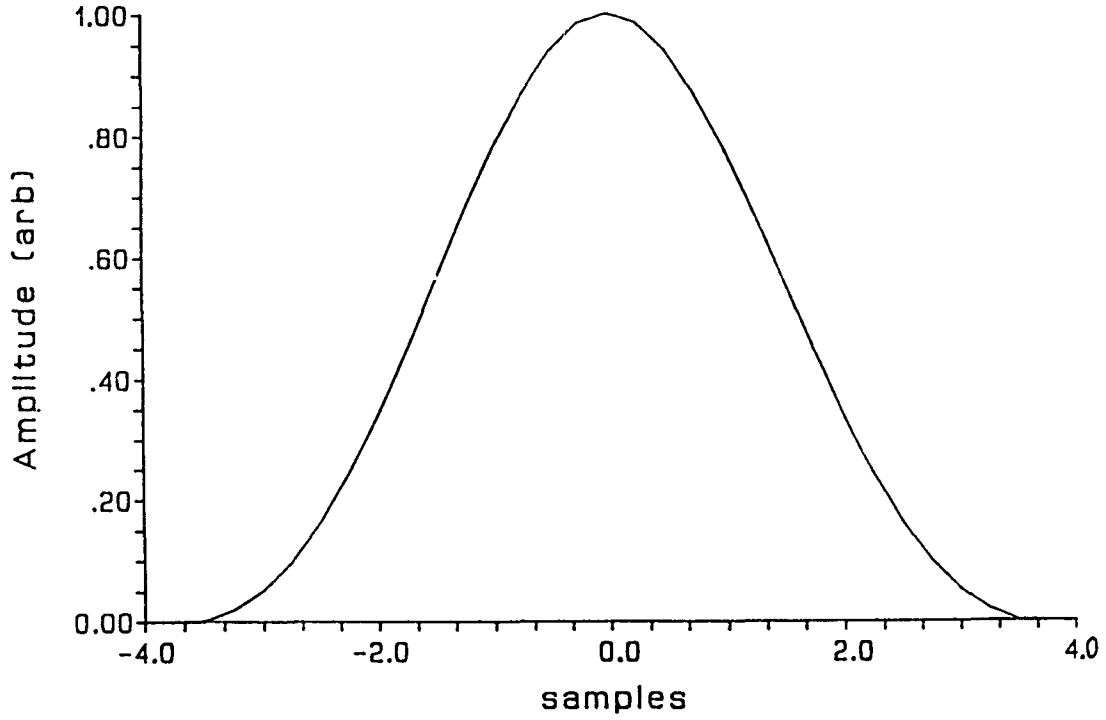

Figure 6.8: Correlation of the received signal with a template of the transmitted pseudo random noise (PRN) code (3 samples = 1 bit = 133 μs).

filter output determined by Menemenlis and Farmer [42],

$$s(t-\tau) = \sum_{n=0}^{9} a_n \left(\frac{t-\tau}{\tau_p}\right)^{2n}, \tag{6.5}$$

where a_n are known coefficients and $\tau_p = 1$ bit is the half-width of the correlation peak. For the Saanich Inlet experiment the bit width was 9 cycles and sampling rate was 3 samples/bit. Therefore, the half-width of the correlation peak is 3 samples. The shape of this correlation function is triangular with a rounded apex and can be seen in Figure 6.8.

The maximum likelihood estimation is derived as follows: minimize,

$$Q = \sum_t \left[r(t) - \sum_{i=1}^{N} A_i s(t-\tau_i) \right]^2, \tag{6.6}$$

$$= \sum_t r(t)^2 - 2\left[\sum_{j=1}^{N} A_j C(\tau_j) - \frac{1}{2} \sum_{j=1}^{N} A_j \sum_{k=1}^{N} A_k B(\tau_j, \tau_k) \right] \tag{6.7}$$

with respect to A_i and τ_i. The function,

$$C(\tau_j) = \sum_t r(t)s(t-\tau_j) \tag{6.8}$$

is the cross correlation between the received and modelled signal and the function,

$$B(\tau_j, \tau_k) = \sum_t s(t-\tau_j)s(t-\tau_k), \tag{6.9}$$

is the auto correlation between the modelled signals. Minimizing Q implies that the second term on the right of (6.7) should be maximized. This maximization problem is written in matrix form as,

$$\text{maximize} \quad \mathcal{C}^T\mathcal{A} - \frac{1}{2}\mathcal{A}^T\mathcal{B}\mathcal{A} \quad \text{w.r.t. } A_i \text{ and } \tau_i, \tag{6.10}$$

where,

$$\mathcal{A}^T = [A_1, A_2, ..., A_N], \tag{6.11}$$

$$\mathcal{C}^T = [C(\tau_1), C(\tau_2), ..., C(\tau_N)], \tag{6.12}$$

$$\mathcal{B} = \begin{bmatrix} B(\tau_1,\tau_1) & B(\tau_1,\tau_2) & ... & B(\tau_1,\tau_N) \\ B(\tau_2,\tau_1) & B(\tau_2,\tau_2) & ... & B(\tau_2,\tau_N) \\ . & . & . & . \\ B(\tau_N,\tau_1) & B(\tau_N,\tau_2) & ... & B(\tau_N,\tau_N) \end{bmatrix}. \tag{6.13}$$

Maximizing (6.10) with respect to each of the A_i yields,

$$\mathcal{A} = \mathcal{B}^{-1}\mathcal{C}. \tag{6.14}$$

Substituting (6.14) into (6.10) gives the following maximization problem,

$$\text{maximize} \quad \frac{1}{2}\mathcal{C}^T\mathcal{B}^{-1}\mathcal{C} \quad \text{w.r.t. } \tau_i. \tag{6.15}$$

Therefore, to determine the maximum likelihood estimate, (6.15) must first be maximized with respect to the arrival time estimates. This equation is a quadratic and is a function of N independent variables and so maximization occurs over an N dimensional space. Powell's quadratically convergent method described in Numerical

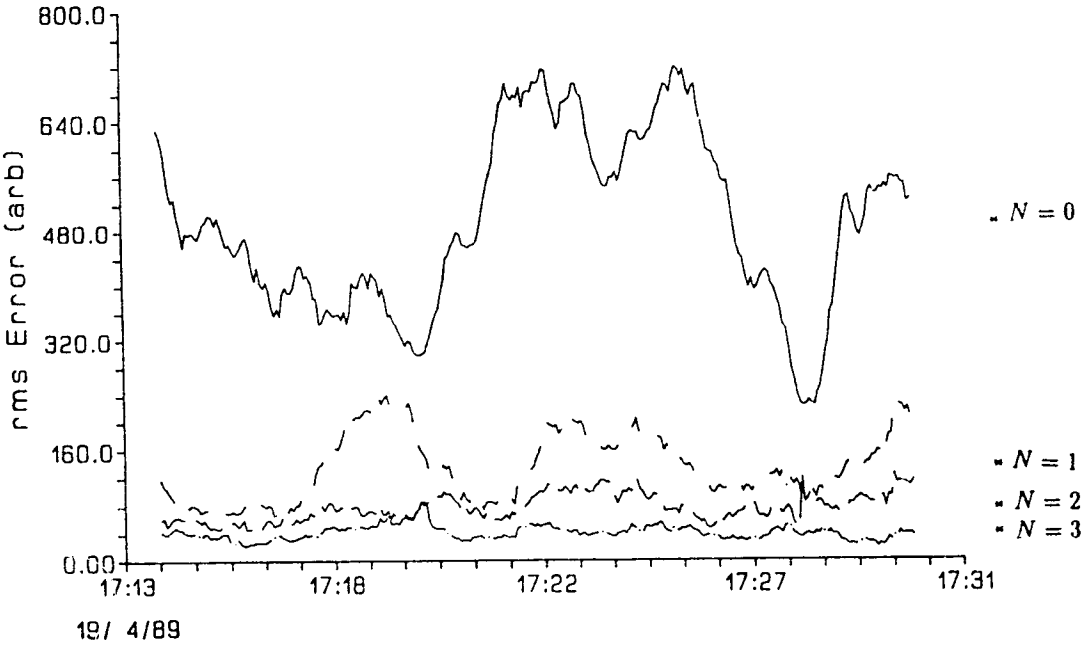

Figure 6.9: Integration of the noise for an assumed number of paths N. The integrated signal level is shown for $N = 0$. Averages are shown as an $*$ on the far right side.

Recipes [46] is used for this procedure. In order to find the arrival times that maximize (6.15) a starting point must be given. For the very first transmission the starting point is determined with a guess; for subsequent transmissions the arrival times for the previous transmission is used as the starting point. Powell's method then converges quickly to the new set of arrival times that maximize (6.15). These values are then used in (6.14) to obtain the amplitude estimates.

In deriving the maximum-likelihood estimate it is assumed that the number of paths N is known and fixed. The number of paths chosen is $N = 3$. This is because the arrival time integration of the noise calculated for $N = 0, 1, 2, 3$ multipaths (see Figure 6.9) gives the correct noise level for $N = 3$. At any given time there can be either no arrivals or a maximum of three arrivals. When there are less than three arrivals the algorithm fits to the noise level. When a single dominant path exists with no interference from other multipaths as in the Cordova Channel experiment, the algorithm described in Appendix D can be used.

Figure 6.10(a) shows a time when the signal level of the main path (A_2) as a function of arrival time is high and Figure 6.10(b) is taken during a time when the signal level (A_2) is low. Superimposed are the three separated paths together with the sum of the three paths. The fit between the model (dashed curve) and the experiment ($*$) is quite good. All paths are resolved. The phase calculated by (5.7) is also shown for comparison ($\times$). The phase is essentially constant over the arrival time of the peak. Because of this characteristic we calculate the phase by linear interpolation at the arrival time estimate.

A number of different parameters have to be adjusted in order to maintain continuous time of arrival and amplitude time series. First, the size of the arrival window has to be adjusted such that the multipaths remain within the window. It was found that a window of size 12 samples was optimal for 30 minute data segments. Second, the noise threshold has to be adjusted such that if a single dominant path exists then the other two paths must fit to the noise. It was found that a threshold of 200 (arbitrary units) in the amplitude was optimal. Third, the time of arrival for each peak is not allowed to jump by more than 1.5 cycles compared to the previous transmission. If they do, then the time of arrival for the previous transmission is used. If the time of arrival still jumps after 10 transmissions, then the window and the starting point for the first transmission have to be adjusted.

Because of all this error checking it was found that the multipath separation algorithm had to be run twice on each data segment. First time through was strictly to find the optimal window size, noise threshold and the starting point for the arrival times; the second time through gave continuous time of arrival and amplitude time series.

Figure 6.11 shows an expanded section of the second set of arrivals shown in Figure 6.7(a). The arrival window spans $0.58ms$ and 16 minutes of data are shown. Superimposed on this plot is a trace of three separated paths scaled by the amplitude. The received signal separated into three paths is shown for the first transmission. This plot illustrates the successful path separation. Most of the time the first and third

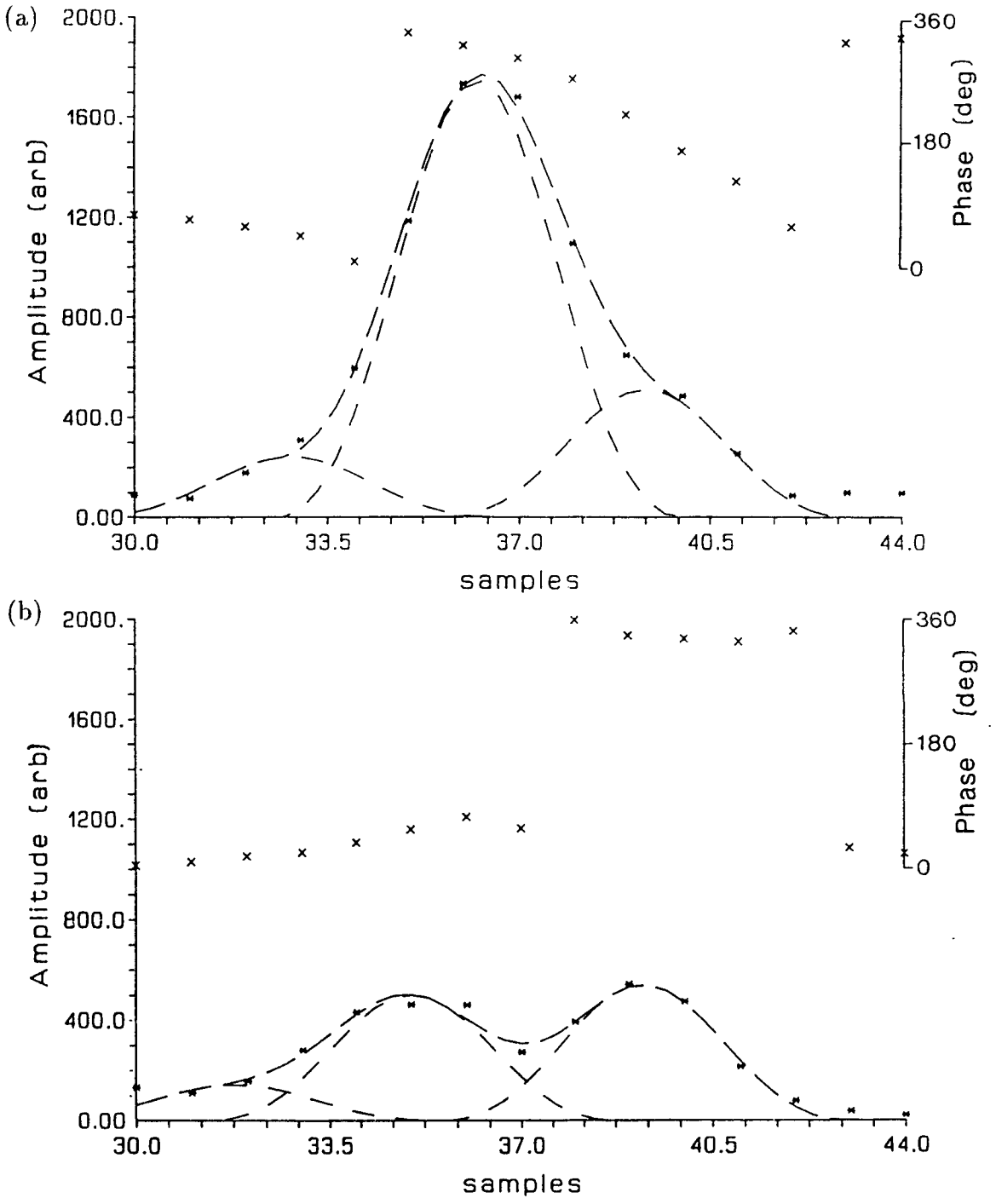

Figure 6.10: Acoustic amplitude (∗) and phase (×) measured as a function of arrival time when (a) the signal level is high and (b) the signal level is low. Superimposed are the resolved paths together with the modelled signal (dashed curve).

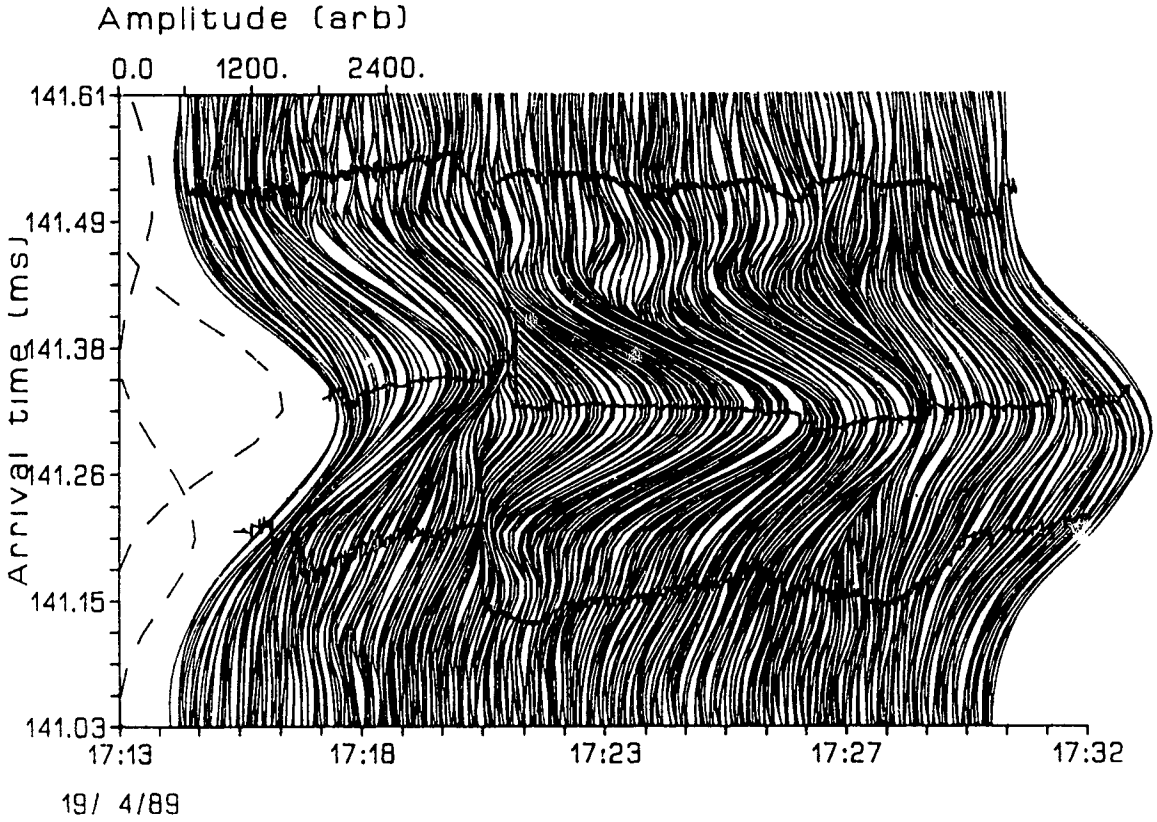

Figure 6.11: Expanded view of the second arrival shown in Figure 6.7(a). Superimposed is a trace of the three separated paths.

path fits to the noise and the second path follows the main arrival. One disadvantage with this algorithm is that the paths can only be separated when the arrival times differ by more than 3 cycles (since our sampling rate is 1 sample every 3 cycles) and so crossing paths are not detected. Interpolation was done so as to increase the sampling rate to 1 sample every cycle in order to improve the fit.

Since the phase is a sensitive measurement of the arrival time relative to the receiver ping timing mark (RPTM) it is used instead of the calculated time of arrival. The calculated arrival time is only used to determine the 360^o phase ambiguity. Figure 6.12 is a short time series (15 minutes) of phase and time of arrival for the second resolved path in Figure 6.11. The phase is determined by linear interpolation at the arrival time estimate (see Figure 6.10) and the time of arrival is determined by (6.15). These time series are plotted to the same scale. Ideally, the phase should follow the

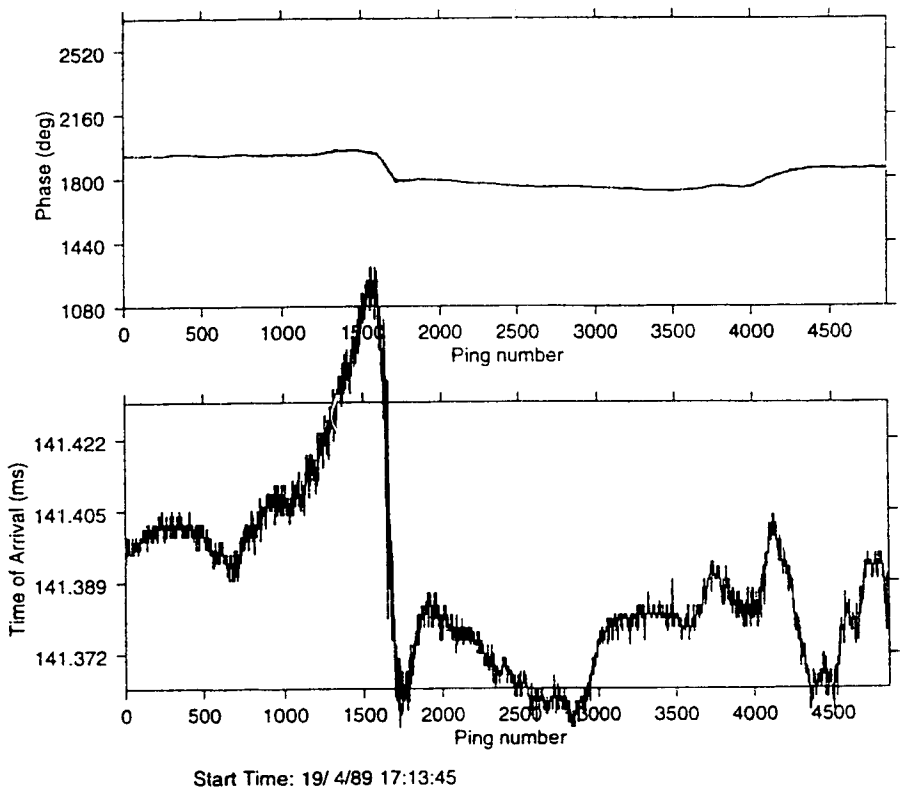

Figure 6.12: The phase and the time of arrival for the second path shown in Figure 6.11 plotted to the same scale.

same trend as the time of arrival, as noted previously in Cordova Channel; but this is not observed. There is more low frequency variability in the arrival time whereas the phase is very stable. This discrepancy could be caused by multipath interference.

Now that we have separated the multipaths, we are in a position to use the amplitude (A) and phase (ϕ) measurements to contribute to our understanding of acoustic propagation in this environment. A time series of the amplitude and phase, for the main path of the second set of arrivals shown in Figure 6.7, is shown in Figure 6.13. Much variability exists in the amplitude - possibly the result of internal waves - whereas the phase undergoes gradual variation associated with the tide. The scintillation index,

$$S_I^2 = \frac{< I^2 > - < I >^2}{< I >^2}, \tag{6.16}$$

where $I = A^2$ is the acoustic intensity, is 1.34 for this 9 hour time series. The weak scattering approximation of Rytov (see Tatarskii [52]) is valid only for $S_I^2 \ll 1.0$. It

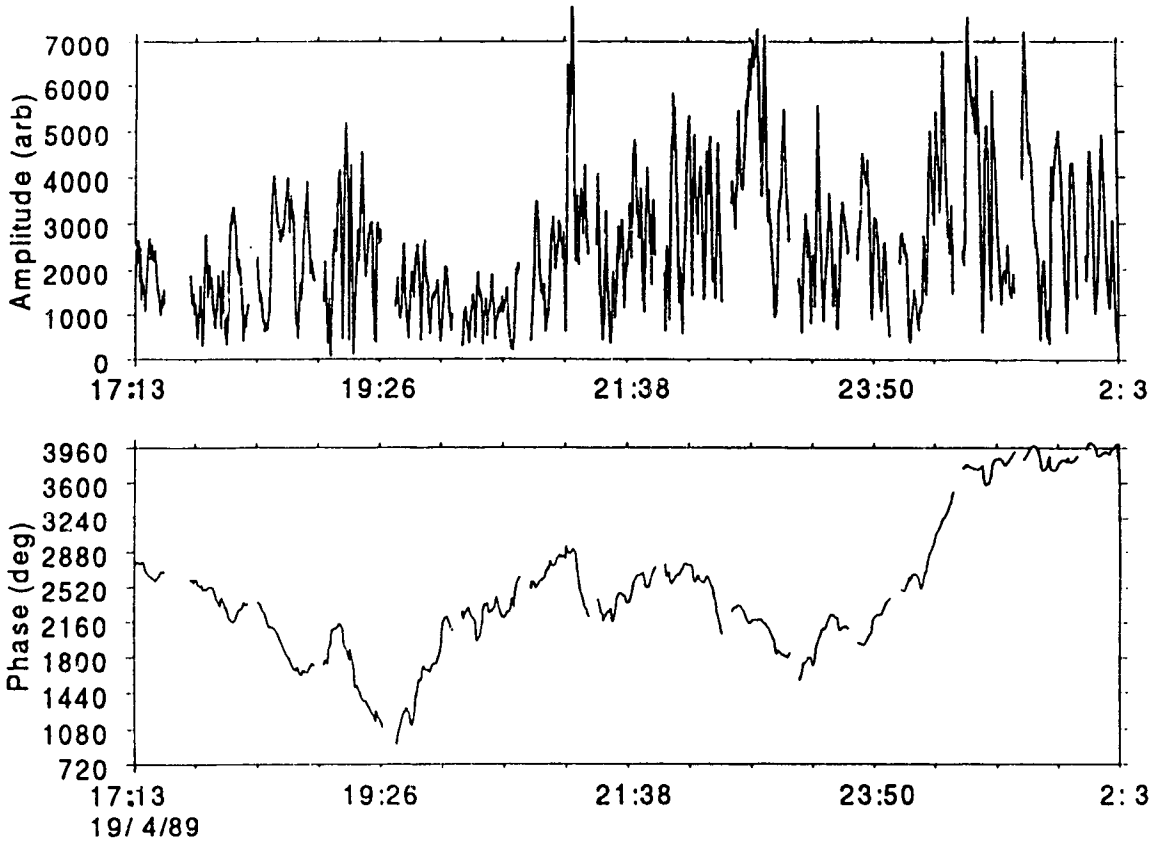

Figure 6.13: Time series of amplitude and phase over a 9 hour period.

is clear that the multiple scatter acoustic propagation model of Uscinski [58] must be used since it is a full range theory.

6.3.3 Correlation analysis

A correlation analysis of the log-amplitude defined as $\chi = \ln\left(\frac{A}{<A>}\right)$ is carried out. Using the square array we can make measurements of the normalized log-amplitude cross-covariance for both diverging and parallel paths using horizontally and vertically spaced transducers. Using a 12 minute data segment, diverging and parallel correlations are shown in Figure 6.14(a) and (b) respectively. For diverging paths (one transmitter and two receivers) both the horizontal and vertical cross covariance show a correlation of 0.8; for parallel paths (two transmitters and two receivers) the

horizontal cross covariance has a high correlation of 0.85 whereas the vertical cross covariance has little correlation. In fact the vertical correlation is negative implying that when a maximum occurs in the amplitude from one transmitter, a minimum occurs in the amplitude from a transmitter displaced 2m vertically.

It is clear that the acoustic signals transmitted from two depths separated by 2 m interact with the random media differently whereas the acoustic signals transmitted at the same depth interact with the media in a similar way. This observation is also supported by the phase measurement leading to the conclusion that the two rays from vertical transmitters with this spacing are statistically independent. This result is unexpected since the Fresnel length is 7.2 m. For the weak scattering regime the correlation length scale for log-amplitude fluctuations is $\sqrt{\lambda L} = 7.2\ m$ and $\sqrt{\lambda L}/3 = 2.4\ m$ for diverging and parallel paths respectively.

6.3.4 Probability distributions

The probability density functions for both the normalized intensity $\frac{I}{<I>}$ and the log intensity $\ln(\frac{I}{<I>})$, where angle brackets denote a temporal average, are considered. For the weak scattering case (the unsaturated regime), the intensity follows a log-normal distribution and the log intensity follows a Gaussian distribution (Tatarskii [52]). Figure 6.15(a) and (b) show that these distributions do not describe the data. Macaskill and Ewart's [39] theory for intensity fluctuations in the saturated regime gives an exponential distribution which seems to provide a good fit to our Saanich Inlet data (see Figure 6.15(a)); the amplitude then follows a Rayleigh distribution (see Dashen *et.al.* [12]). The high acoustic frequency (67 kHz) together with the long range (2.35 km) through stable stratification may put this experiment in the saturated regime. Table 6.2 summarizes the probability distributions for normalized amplitude, intensity, log-amplitude and log-intensity.

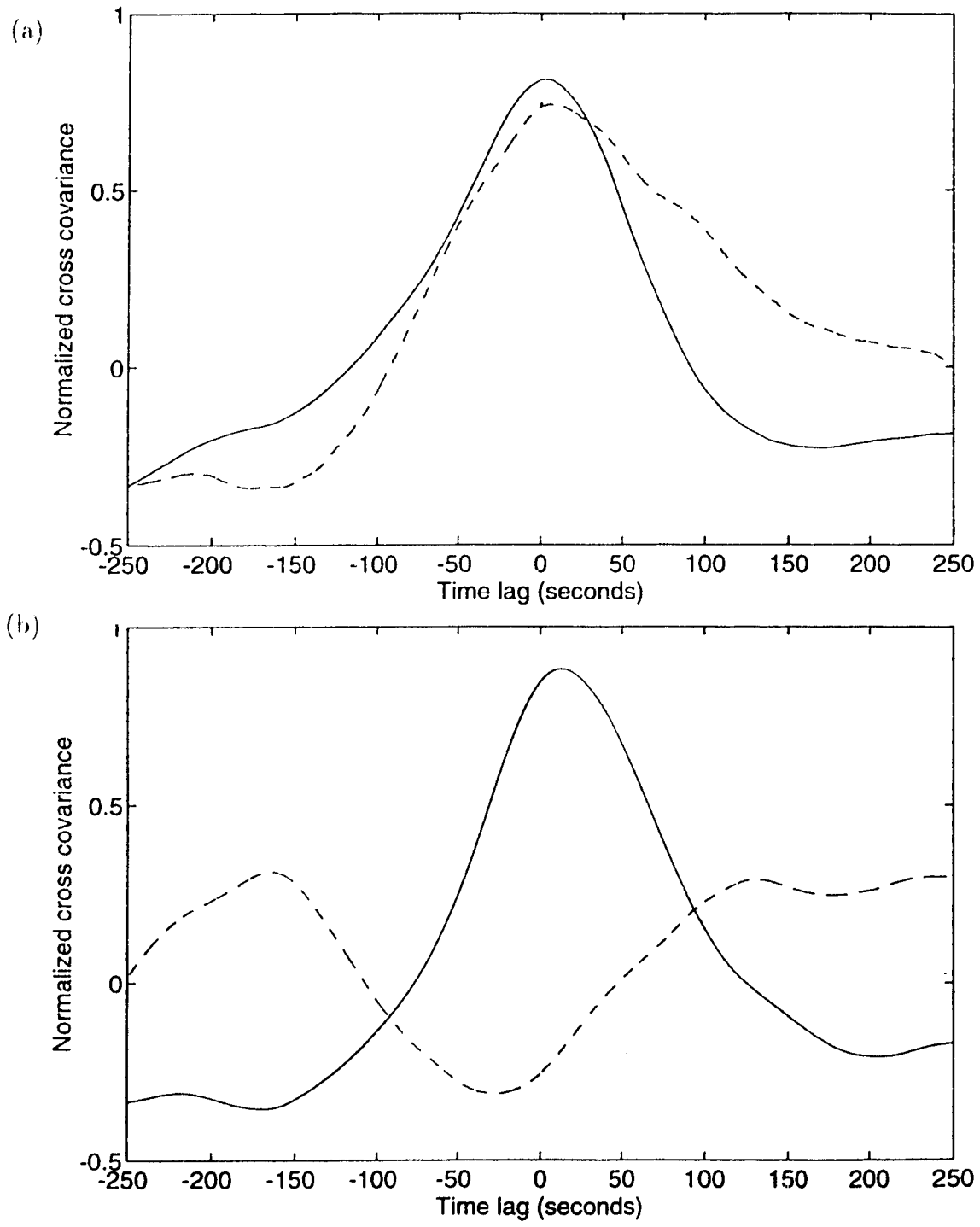

Figure 6.14: The normalized cross covariance of log-amplitude for (a) diverging paths and (b) parallel paths. Solid curve is for horizontally spaced receivers and dashed curve is for vertically spaced receivers.

(a)

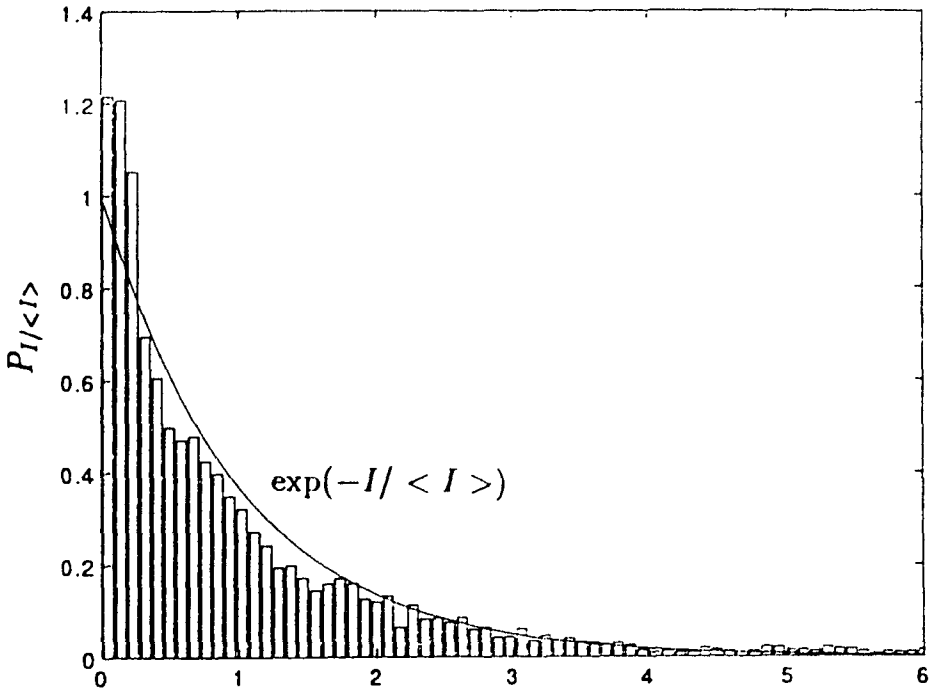

(b)

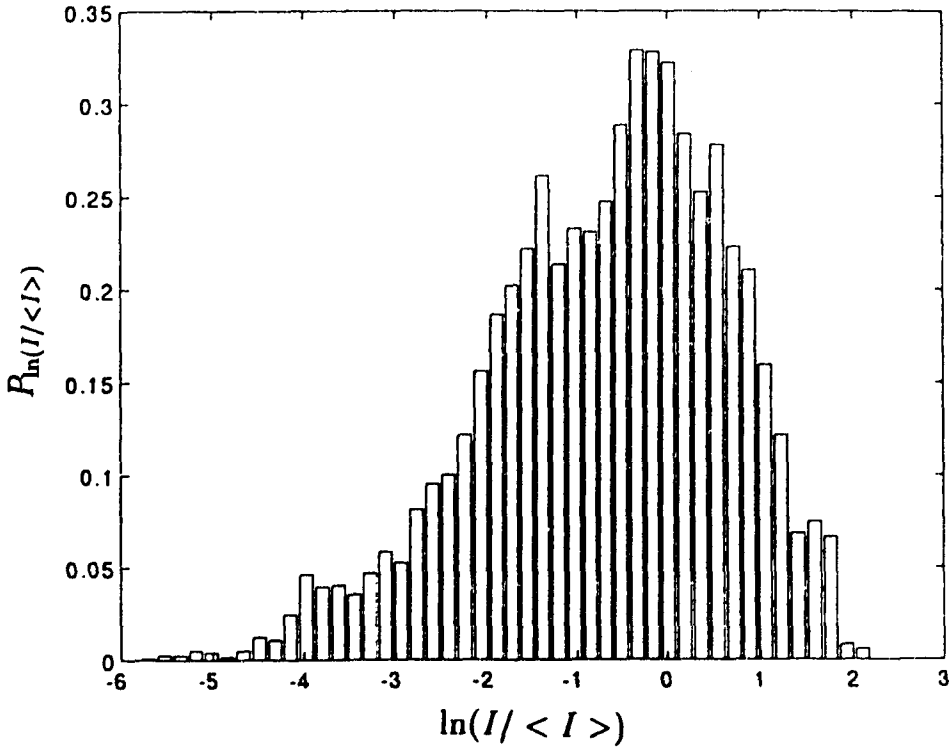

Figure 6.15: Saanich Inlet probability distributions for (a) $\frac{I}{<I>}$ with an exponential distribution superimposed and (b) $\ln\left(\frac{I}{<I>}\right)$.

parameter	unsaturated regime (Cordova Channel)	saturated regime (Saanich Inlet)
$\frac{A}{<A>}$	log-normal	Rayleigh
$\frac{I}{<I>}$	log-normal	exponential
$\ln\left(\frac{A}{<A>}\right)$	Gaussian	–
$\ln\left(\frac{I}{<I>}\right)$	Gaussian	–

Table 6.2: Probability distributions under saturated (Saanich Inlet experiment) and unsaturated conditions (Cordova Channel experiment) for normalized amplitude, intensity, log-amplitude and log-intensity.

6.3.5 Spectral characteristics

The acoustic path that has been analyzed reaches a maximum depth of 67 m and the minimum internal wave period at this depth is $T = 2\pi/N \approx 7$ minutes. The inertial period for Saanich Inlet is 15.9 hours and hence a minimum of 16 hours of acoustical data are required in order to obtain an intensity spectrum for internal wave frequencies. Only 9 hours of data have been processed and so our spectral analysis is restricted to periods less than 4.5 hours.

The power spectral density for the normalized intensity and the phase are shown in Figure 6.16(a) and (b) respectively. The spectra were neither windowed nor averaged. A cosine taper was used where there were gaps in the data. Superimposed on the normalized intensity spectrum is the slope line taken from Ewart *et.al.* [21]. They show that an f^{-3} frequency dependence for frequencies greater than f_N, is consistent with fine structure "frozen" with respect to the internal wave field. Our data fit this frequency dependence quite well.

The power law behaviour for the phase (arrival time) spectrum from the inertial frequency (f_I) to the buoyancy frequency (f_N) is predicted by Desaubies [15], in the weak scattering case, to follow the temporal power law for internal waves. That is, the frequency dependence follows $f^{-2.5}$. This was observed by Ewart and Reynolds

(a)

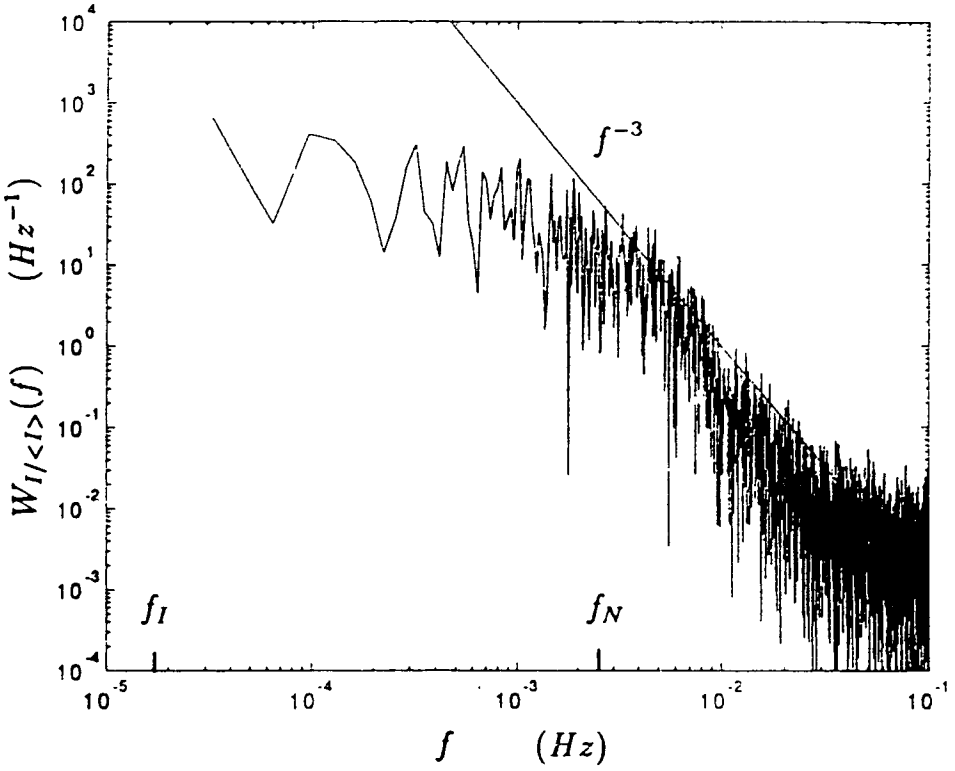

(b)

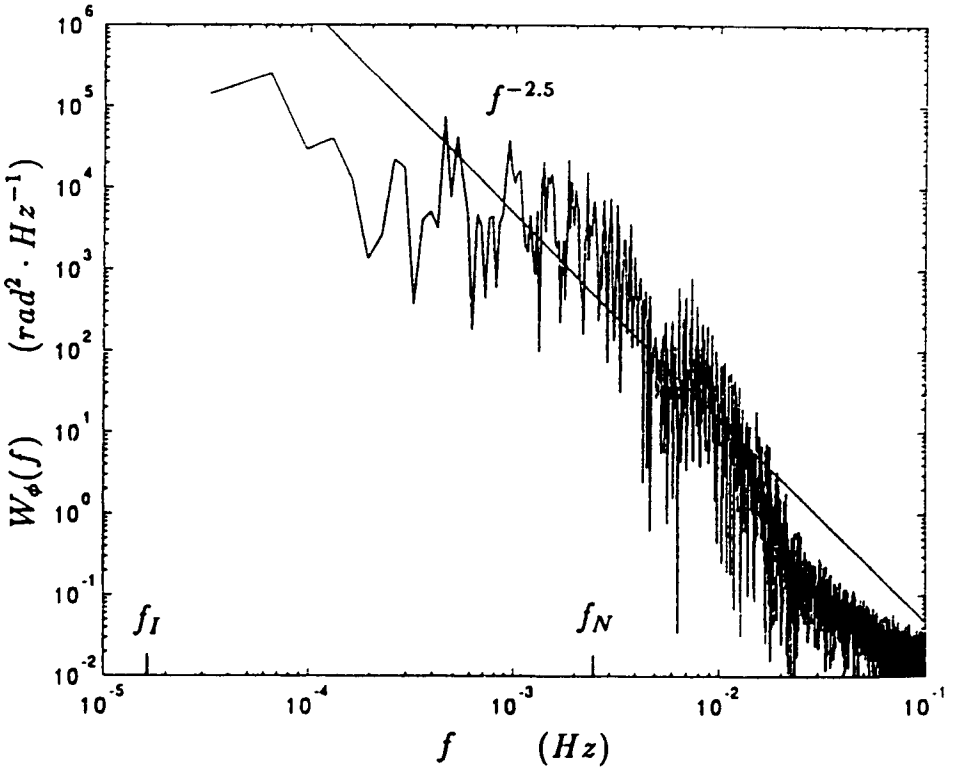

Figure 6.16: (a) Power spectral density for $\frac{I}{<I>}$. f^{-3} dependence is due to fine structure. (b) Power spectral density for ϕ. $f^{-2.5}$ dependence is due to internal waves.

[22] and our data show no $f^{-2.5}$ dependence in the internal wave frequency range. This could be due to multipath interference and some uncertainty inherent in the multipath separation. Also, the model was based on the weak scattering theory where it is assumed to be valid for the phase variability but not the amplitude variability. The intensity fluctuations would be a better way to measure the effects of internal waves once a model for the refractive index fluctuations is established.

6.4 Summary and Conclusions

The oceanographic characteristics in Saanich Inlet seem to suggest that internal waves play a dominant role in producing refractive index variations, particularly at the depth of the second multipath (70 m). Temperature variations at this depth obtained concurrently with the acoustic data show sudden bursts of variability possibly associated with the passage of internal waves. The concept of "frozen" fine structure seems to be consistent with the acoustic observations for frequencies higher than the Brunt-Vaisala frequency.

One of the most interesting results obtained from this data set, is the deterministic variability of the acoustic multipaths. Our relatively simple ray tracing algorithm predicts the number of multipaths and closely approximates the arrival time separation of each path. In theory, our acoustic observations, together with a robust ray tracing algorithm used to separate the path length and sound speed contribution, could be used as an acoustic tomographic instrument to detect mean temperature variability since the currents are small. This would be valuable in this kind of environment.

One of the outstanding difficulties in trying to use wave propagation through Saanich Inlet for the purpose of oceanographic measurements is computing the amplitude and phase for a particular path. In addition to the observed deterministic multipaths there are also micro-multipaths for each path. In studying the second deterministic path, we have separated it into a superposition of three closely spaced micro-multipaths and have applied a maximum likelihood estimation algorithm to compute the amplitude and phase for each micro-multipath. The results prove encouraging for measuring the amplitude variability, but the phase variability (calculated by using the in-phase and quadrature components) could be contaminated by the micro-multipath interference. The amplitude shows large fluctuations ($S_I^2 = 1.34$) implying that the multiple scattering theory should be used to model wave propagation. The phase, however, remains quite stable (total variability over 9 hours is 9 cycles).

Vertical parallel paths show little correlation in the amplitude and also in the phase whereas horizontal parallel and diverging paths show strong correlation. The intensity fluctuations have an approximately exponential probability distribution suggesting that the experimental conditions are nearly saturated. The phase spectrum should show a frequency dependence of $f^{-2.5}$ in the internal wave frequency range but this is not seen, possibly due to multipath interference. The intensity spectrum for $f > f_N$ shows a good fit with the "frozen" fine structure model of Ewart *et.al.* [21].

This data set is in general, more complicated to analyse than the Cordova Channel data set. There are many features that contrast this data set from the Cordova Channel data set. First, the amplitude, phase and time of arrival, can be computed using the maximum likelihood algorithm for both environments except Cordova Channel will have one path and Saanich Inlet will have up to three paths. Second, the phase time series in Cordova Channel has the same general structure as the time of arrival derived by triangular and quadratic interpolation on the amplitude. Thus in contrast to Saanich Inlet data, the 2π ambiguities can be resolved accurately in Cordova Channel. Third, the amplitude variability in Cordova Channel is small ($S_I^2 \approx 0.1$) whereas in Saanich Inlet it is large ($S_I^2 \approx 1.3$). The amplitude variability implies that the weak scattering theory is valid in Cordova Channel and the multiple scattering theory should be valid in Saanich Inlet. Fourth, the oceanographic and geographic characteristics are very different: Saanich Inlet is a deep, wide, quiescent and stratified fjord and Cordova Channel is a shallow, narrow, and tidally influenced channel flow.

In conclusions, these characteristics imply that the refractive index fluctuations can be approximated by the Kolmogorov, isotropic and homogeneous turbulence model in Cordova Channel and possibly the Garrett-Munk internal wave model in Saanich Inlet. Also, in order to use the acoustical scintillation measurements to probe the intervening medium a model for acoustic propagation is needed. For Saanich Inlet the weak scattering theory of Tatarskii [52] is not valid and so the full solution of Uscinski [57] or Dashen [11] should be used.

Chapter 7

Conclusions of the Thesis

The basic thrust of this research is to contribute to the understanding of acoustic propagation in the coastal ocean. The motivation is to add to that body of knowledge that is essential to the new and rapidly growing field of inferring ocean properties from the forward scattered acoustical signal. Since the coastal oceans are rich in phenomena in which turbulence plays a role, the acoustic techniques developed in this thesis proves to be a valuable remote sensing instrument for obtaining path averaged quantities.

Each of the oceanographic properties we have measured give insight into the way in which turbulence plays a role in coastal oceanography. They allow parameterization of the turbulence for numerical models which describe boundary layer mixing and internal mixing (mixing as a result of turbulence within the water column away from the boundaries). The oceanographic measurements that can be achieved with a relatively simple array (vertical and horizontal (square), and linear), as a result of this work, are:

- $\overline{U}$ path averaged current speed perpendicular to the acoustic propagation direction using WPRM models and using the horizontal arrival angle,
- $\frac{dU}{dz}$ the mean current shear from the square array,

C_n^2 path averaged refractive index variability due to both scalar (temperature and salinity) and vector (velocity) fluctuations,

σ_v the rms turbulent cross stream velocity fluctuations,

$\overline{\epsilon}$ path averaged turbulent kinetic energy dissipation if the temperature and salinity variability $C_{n_s}^2$ is known.

$\left\langle \frac{\partial v}{\partial x}\frac{\partial v}{\partial z} \right\rangle$ the correlation of horizontal and vertical cross stream velocity fluctuations,

$\frac{dc}{dz}$ the mean sound speed gradient from the vertical angle of arrival (the density gradient $\frac{d\rho_o}{dz}$ can then be computed),

In addition, spatial aperture filtering techniques allows estimation of the spatial distribution of the following oceanographic parameters along the path: $U(y)$, $C_n^2(y)$ and $\epsilon(y)$. If reciprocal acoustic transmission is used then further parameters can be measured:

$\overline{V}$, v path averaged mean cross stream current speed and fluctuations,

$C_{n_s}^2$ the temperature and salinity contribution to the level of the refractive index fluctuations.

The scientific challenges that still remain are discussed as recommendations for future work.

7.1 Recommendations for future work

For future experiments some recommendations are given. For turbulent environments like Cordova Channel, measurement of the TKE dissipation is of great interest. Further research is needed in order to be able to compare our path averaged acoustical measurement with simultaneous *in situ* measurements of the turbulent kinetic energy dissipation. The dissipation could also be compared with an independent measurement of the turbulent kinetic energy production.

In order to confirm that our angle of arrival correlations are related to the corre-

lation of horizontal and vertical cross stream velocity gradients we need independent *in situ* measurements. This measurement can be obtained with an acoustic doppler current profiler moored at the bottom of the channel.

For mean current flow measurements the horizontal spacing must be optimized for parallel or diverging paths when using the log-amplitude cross covariance technique. The wave structure function technique for calculating current is a peculiar puzzle which should be solved. Further tests with data from future experiments would either show agreement or disagreement with our observations which underestimates the current.

Another scientific challenge that remains is extending the scintillation concept to longer ranges and in less turbulent environments. For oceanographic characteristics similar to Saanich Inlet one important recommendation is to lower the acoustic frequency thus increasing the scale size that can effectively focus the acoustic rays. This may also reduce the multipath acoustic propagation conditions. Also, increasing the Fresnel radius may cause vertically separated parallel paths to show similar trends.

Another important recommendation for this kind of environment is to sample both the spatial and temporal variability of the refractive index. This will then completely define the spectral density of the refractive index fluctuations which can then be used with the appropriate acoustic scattering theory.

Bibliography

[1] G. Arfken. *Mathematical Methods for Physicists.* Academic Press Inc., New York, 1970.

[2] R. Birch and D. D. Lemon. Acoustic flow measurements at the Rocky Reach Dam. In *Proceedings of the International Conference on Hydropower*, Nashville, Tennessee, August 10-13, 1993.

[3] K. H. V. Booth. Conversion of ray tracing package for use on an HP A900 at Institute of Ocean Sciences. Technical report, IOS FP941-8-2515A, 1988.

[4] L. Brekhovskikh and Y. Lysanov. In G. Ecker, W. Engl, and L. B. Felsen, editors, *Fundamentals of Ocean Acoustics*, number 8 in Springer Series in Electrophysics. Springer-Verlag, Berlin, 1982.

[5] L. A. Chernov. *Wave Propagation in a Random Media.* Translated from Russian by R. A. Silverman, McGraw-Hill Inc., 1960.

[6] S. F. Clifford. Temporal-frequency spectra for a spherical wave propagating through atmospheric turbulence. *Journal of the Optical Society of America*, 61(10):1285–1292, 1971.

[7] S. F. Clifford. The classical theory of wave propagation in a turbulent medium. In J. W. Strohbehn, editor, *Laser Beam Propagation in the Atmosphere*, number 25 in Topics in Applied Physics, chapter 3. Springer Verlag, New York, 1978.

[8] S. F. Clifford and D. M. Farmer. Ocean flow measurements using acoustic scintillation. *Journal of the Acoustical Society of America*, 74(6):1826–1832, 1983.

[9] S. F. Clifford, R. J. Hill, J. T. Priestley, B. A. Bohlander, and R. W. McMillan. The spectra of amplitude and phase difference fluctuations of millimeter waves propagating in clear air. In *Proceedings of U. R. S. I.*, Durham, NH, U.S.A., July 28 - August 1, 1986.

[10] G. B. Crawford, R. J. Lataitis, and S. F. Clifford. Remote sensing of ocean flows by spatial filtering of acoustic scintillations: Theory. *Journal of the Acoustical Society of America*, 88(1):442–453, 1990.

[11] R. Dashen. Path integrals for waves in random media. *Journal of Mathematical Physics*, 20(5):894–920, 1979.

[12] R. Dashen, W. H. Munk, K. M. Watson, and F. Zachariasen. In S. M. Flatte, editor, *Sound Transmission Through a Fluctuating Ocean.* Cambridge University Press, 1979.

[13] R. E. Davis. Techniques for statistical analysis and prediction of geopphysical fluid systems. *Geophysical Astrophysical Fluid Dynamics*, 8:245–277, 1977.

[14] H. A. DeFerrari and H. B. Nguyen. Acoustic reciprocal transmission experiments, Florida Straits. *Journal of the Acoustical Society of America*, 79:299–315, 1986.

[15] Y. J. F. Desaubies. On the scattering of sound by internal waves in the ocean. *Journal of the Acoustical Society of America*, 64:1460–1469, 1978.

[16] J. L. Devore. *Probability and Statistics for Engineering and the Sciences.* Brooks/Cole Publishing Co., 1987.

[17] R. K. Dewey and W. R. Crawford. Bottom stress estimates from vertical dissipation profiles on the continental shelf. *Journal of Physical Oceanography*, 18:1167–1177, 1988.

[18] D. DiIorio and D. M. Farmer. Path averaged turbulent dissipation measurements using high frequency acoustical scintillation analysis. *Journal of the Acoustical Society of America*, 96:1056–1069, 1994.

[19] T. F. Edgar and D. M. Himmelblau. *Optimization of Chemical Processes.* McGraw-Hill Chemical Engineering Series, 1988.

[20] J. E. Ehrenberg, T. E. Ewart, and R. D. Morris. Signal processing techniques for resolving individual pulses in a multipath signal. *Journal of the Acoustical Society of America*, 63(6):1861–1865, 1978.

[21] T. E. Ewart, C. Macaskill, and B. J. Uscinski. Intensity fluctuations. Part II: Comparison with the Cobb experiment. *Journal of the Acoustical Society of America*, 74(5):1484–1499, 1983.

[22] T. E. Ewart and S. A. Reynolds. The mid-ocean acoustic transmission experiment, MATE. *Journal of the Acoustical Society of America*, 74(3):785–802, 1984.

[23] D. M. Farmer and S. F. Clifford. Space-time acoustic scintillation analysis: A new technique for probing ocean flows. *IEEE Journal of Oceanic Engineering*, OE-11(1):42–50, 1986.

[24] D. M. Farmer, S. F. Clifford, and J. A. Verrall. Scintillation structure of a turbulent tidal flow. *Journal of Geophysical Research*, 92(C5):5369–5382, 1985.

[25] D. M. Farmer and G. B. Crawford. Remote sensing of ocean flows by spatial filtering of acoustic scintillations: Observations. *Journal of the Acoustical Society of America*, 90(3):1582–1592, 1991.

[26] A. E. Gargett, T. R. Osborn, and P. W. Nasmyth. Local isotropy and the decay of turbulence in a stratified fluid. *Journal of Fluid Mechanics*, 144:231–280, 1984.

[27] C. J. R. Garrett and W. Munk. Space-time scales of internal waves. *Geophysical Fluid Dynamics*, 2:225–264, 1972.

[28] C. J. R. Garrett and W. Munk. Space-time scales of internal waves: A progress report. *Journal of Geophysical Research*, 80(3):291–297, 1975.

[29] V. N. Gorelov and S. V. Dotsenko. Correlation description of two-dimensional anisotropic sound fields. *Soviet Physics Acoustics*, 35(3):255–258, 1989.

[30] H. L. Grant, R. W. Stewart, and A. Moillet. Turbulence spectra from a tidal channel. *Journal of Fluid Mechanics*, 12:241–268, 1962.

[31] J. O. Hinze. *Turbulence: An Introduction to its Mechanism and Theory.* McGraw-Hill Series in Mechanical Engineering, 1959.

[32] A. Ishimaru. *Wave Propagation and Scattering in Random Media*, volume 2. Academic Press Inc., 1978.

[33] D. S. Ko, H. A. DeFerrari, and P. Malanotte-Rizzoli. Acoustic tomography in the Florida Strait: temperature, current and vorticity measurements. *Journal of Geophysical Research*, 94(C5):6197–6211, 1989.

[34] R. J. Lataitis, R. J. Hill, J. T. Priestley, S. F. Clifford, R. A. Bohlander, R. W. McMillan, and W. P. Schoenfeld. Millimeter wave temporal frequency spectra for spherical wave propagation through a turbulent absorbing atmosphere. unpublished manuscript, 1985.

[35] R. S. Lawrence, G. R. Ochs, and S. F. Clifford. Use of scintillations to measure average wind across a light beam. *Applied Optics*, 11(2):239–243, 1972.

[36] R. W. Lee and J. C. Harp. Weak scattering in random media, with applications to remote probing. *Proceedings of the IEEE*, 57(4):375–406, 1969.

[37] D. D. Lemon. Flow measurements by acoustic scintillation drift in the Fraser River estuary. In *Oceans 1993 Proceedings, Engineering in Harmony with the Ocean*, Victoria, B.C. Canada, October 18-21, 1993.

[38] D. D. Lemon, D. N. Knight, R. A. J. Chave, and D. M. Farmer. An acoustic system for measuring ocean flows by space-time scintillation analysis. In *Oceans 1987 Proceedings, The Ocean - An International Workplace*, Halifax, Nova Scotia, Canada, September 28 - October 1, 1987.

[39] C. Macaskill and T. E. Ewart. The probability distribution of intensity for acoustic propagation in a randomly varying ocean. *Journal of the Acoustical Society of America*, 76(5):1466–1473, 1984.

[40] D. Menemenlis. *Acoustical Measurement of Velocity, Vorticity and Turbulence in the Arctic Boundary Layer Beneath Ice.* PhD dissertation, University of Victoria, 1993.

[41] D. Menemenlis. Line-averaged measurement of velocity fine structure in the ocean using acoustical reciprocal transmission. *International Journal of Remote Sensing*, 15(2):267–281, 1994.

[42] D. Menemenlis and D. M. Farmer. Acoustical measurements of current and vorticity beneath ice. *Journal of Atmospheric and Oceanic Technology*, 9(6):827–849, 1992.

[43] V. E. Ostachev. *Sound propagation and scattering in media with random inhomogeneities of sound speed, density and medium velocity*, volume 1 of *Waves in Random Media*, pages 1–26. IOP Publishing Ltd., 1994.

[44] V. E. Ostashev. Propagation and scattering of sound waves in the turbulent media (atmosphere or ocean). *Atmospheric Optics*, 4:653–656, 1991.

[45] S. Pond and G. L. Pickard. *Introductory Dynamical Oceanography.* Pergamon Press, 2nd edition, 1983.

[46] W. H. Press, B. P. Flannery, S. A. Teukolsky, and W. T. Vetterling. Minimization or maximization of functions. In *Numerical Recipes - The Art of Scientific Computing*, chapter 10. Cambridge University Press, 2nd edition, 1986.

[47] S. A. Reynolds, S. M. Flatte, R. Dashen, B. Buehler, and P. Maciejewski. AFAR measurements of acoustic mutual coherence function of time and frequency. *Journal of the Acoustical Society of America*, 77(5):1723–1731, 1985.

[48] H. Schlichting. *Boundary-Layer Theory.* McGraw-Hill Series in Mechanical Engineering, 1968.

[49] R. W. Sternberg. Friction factors in tidal channels with differing bed roughness. *Marine Geology*, 6:243–260, 1968.

[50] J. W. Strohbehn. Line-of-sight wave propagation through the turbulent atmosphere. *Proceedings of the IEEE*, 56(8):1301–1318, 1968.

[51] V. I. Tatarskii. *Wave Propagation in a Turbulent Medium.* Translated from Russian by R. A. Silverman, McGraw-Hill Inc., 1961.

[52] V. I. Tatarskii. *The Effects of the Turbulent Atmosphere on Wave Propagation.* Translated from Russian by Israel Program for Scientific Translations, Jerusalem, 1971.

[53] V. I. Tatarskii. Review of scintillation phenomena. In *Wave Propagation in Random Media (Scintillation)*, Seattle, Washington, USA, August 3 - 7, 1992.

[54] V. I. Tatarskii, A. Ishimaru, and V. U. Zavorotny, editors. *Wave Propagation in Random Media (Scintillation)*, Seattle, Washington, U.S.A., August 3-7, 1992. SPIE Press and Institue of Physics Publishing.

[55] H. Tennekes and J. L. Lumley. *A First Course in Turbulence.* MIT Press, 1972.

[56] R. J. Urick. *Principles of Underwater Sound.* McGraw-Hill Inc., 1983.

[57] B. J. Uscinski. *The Elements of Wave Propagation in Random Media.* McGraw-Hill Inc., 1977.

[58] B. J. Uscinski. Intensity fluctuations in a multiple scattering medium. Solution of the fourth moment equation. *Proceedings of the Royal Society of London*, A380:137–169, 1982.

[59] B. J. Uscinski, C. Macaskill, and T. E. Ewart. Intensity fluctuations. Part I: Theory. *Journal of the Acoustical Society of America*, 74(5):1474–1483, 1983.

[60] B. J. Uscinski, J. R. Potter, and T. Akal. Broadband acoustic transmission fluctuations during NAPOLI85, an experiment in the Tyrrhenian Sea: Preliminary results and an arrival-time analysis. *Journal of the Acoustical Society of America*, 86(2):706–715, 1989.

[61] G. N. Watson. *A Treatise on the Theory of Bessel Functions.* Cambridge University Press, 1966.

[62] A. W. Wernik, C. H. Liu, and K. C. Yeh. Modelling of spaced-receiver scintillation measurements. *Radio Science*, 18(5):743–764, 1983.

Appendix A

Bessel Identities for the Phase Difference Spectrum

In this appendix we make use of some Bessel identities taken from Watson [61] so that we can calculate the phase difference spectrum for both horizontally and vertically spaced receivers. Identities exist for the case ϱ_x parallel to U,

$$\begin{aligned} & J_o\left(\kappa|\boldsymbol{\varrho}_x - \mathbf{U}\tau|\right) + J_o\left(\kappa|\boldsymbol{\varrho}_x + \mathbf{U}\tau|\right) \\ &= \sum_{m=-\infty}^{\infty} J_m(\kappa\varrho_x)J_m(\kappa U\tau) + \sum_{m=-\infty}^{\infty}(-1)^m J_m(\kappa\varrho_x)J_m(\kappa U\tau), \qquad \text{(A.1)} \\ &= 2J_o(\kappa\varrho_x)J_o(\kappa U\tau) + 4\sum_{m=1}^{\infty} J_{2m}(\kappa\varrho_x)J_{2m}(\kappa U\tau), \qquad \text{(A.2)} \end{aligned}$$

and for ϱ_z perpendicular to U,

$$\begin{aligned} & 2J_o\left(\kappa\sqrt{\varrho_z^2 + (U\tau)^2}\right) \\ &= 2\sum_{m=-\infty}^{\infty} J_m(\kappa\varrho_z)J_m(\kappa U\tau)e^{im\pi/2}, \qquad \text{(A.3)} \\ &= 2J_o(\kappa\varrho_z)J_o(\kappa U\tau) + 4\sum_{m=1}^{\infty}(-1)^m J_{2m}(\kappa\varrho_z)J_{2m}(\kappa U\tau). \qquad \text{(A.4)} \end{aligned}$$

The Fourier transform of a $2m$ order Bessel function where $m = 0, 1, 2, ...$, is,

$$\begin{aligned} \int_{\tau=-\infty}^{\infty} e^{-i2\pi f\tau} J_{2m}(\kappa U\tau)d\tau &= \frac{2\cos(2m\theta)}{((\kappa U)^2 - (2\pi f)^2)^{1/2}} \quad \text{for} \quad \kappa > \frac{2\pi f}{U} \qquad \text{(A.5)} \\ &= 0 \quad \text{otherwise} \qquad \text{(A.6)} \end{aligned}$$

where $\sin\theta = -2\pi f/\kappa U$.

Other Bessel identities used are,

$$\cos(\kappa\varrho_x \sin\theta) = J_o(\kappa\varrho_x) + 2\sum_{m=1}^{\infty} J_{2m}(\kappa\varrho_x)\cos(2m\theta), \tag{A.7}$$

and

$$\cos(\kappa\varrho_z \cos\theta) = J_o(\kappa\varrho_z) + 2\sum_{m=1}^{\infty}(-1)^m J_{2m}(\kappa\varrho_z)\cos(2m\theta). \tag{A.8}$$

Therefore, for $\kappa > 2\pi f/U$ and horizontally spaced receivers

$$\begin{aligned}
&\int_{\tau=-\infty}^{\infty} e^{-i2\pi f\tau}[2J_o(\kappa U\tau) - J_o\ \kappa|\varrho_x - U\tau|) - J_o(\kappa|\varrho_x + U\tau|)]d\tau \\
&= \frac{4}{((\kappa U)^2 - (2\pi f)^2)^{1/2}} - \left[2J_o(\kappa\varrho_x)\frac{2}{((\kappa U)^2 - (2\pi f)^2)^{1/2}}\right. \\
&\qquad \left. +4\sum_{m=1}^{\infty} J_{2m}(\kappa\varrho_x)\frac{2\cos(2m\theta)}{((\kappa U)^2 - (2\pi f)^2)^{1/2}}\right], \qquad \text{(A.9)} \\
&= \frac{4}{((\kappa U)^2 - (2\pi f)^2)^{1/2}}\left[1 - \cos(\kappa\varrho_x \sin\theta)\right], \qquad \text{(A.10)} \\
&= \frac{8}{((\kappa U)^2 - (2\pi f)^2)^{1/2}}\sin^2\left(\frac{\varrho_x}{2U}2\pi f\right), \qquad \text{(A.11)}
\end{aligned}$$

and for vertically spaced receivers,

$$\begin{aligned}
&\int_{\tau=-\infty}^{\infty} e^{-i2\pi f\tau}\left[2J_o(\kappa U\tau) - 2J_o(\kappa\sqrt{\varrho_z^2 + (U\tau)^2})\right]d\tau \\
&= \frac{4}{((\kappa U)^2 - (2\pi f)^2)^{1/2}} - \left[2J_o(\kappa\varrho_z)\frac{2}{((\kappa U)^2 - (2\pi f)^2)^{1/2}}\right. \\
&\qquad \left. +4\sum_{m=1}^{\infty}(-1)^m J_{2m}(\kappa\varrho_z)\frac{2\cos(2m\theta)}{((\kappa U)^2 - (2\pi f)^2)^{1/2}}\right], \qquad \text{(A.12)} \\
&= \frac{4}{((\kappa U)^2 - (2\pi f)^2)^{1/2}}\left[1 - \cos(\kappa\varrho_z \cos\theta)\right], \qquad \text{(A.13)} \\
&= \frac{8}{((\kappa U)^2 - (2\pi f)^2)^{1/2}}\sin^2\left(\frac{\varrho_z}{2U}\sqrt{(\kappa U)^2 - (2\pi f)^2}\right). \qquad \text{(A.14)}
\end{aligned}$$

Appendix B

Acoustical Current Measurements

B.1 Log-amplitude cross correlation technique

From equation (3.24) the log-amplitude (χ) cross covariance assuming spherical waves and horizontal parallel paths is given by,

$$C_\chi(\rho_x,\tau) = 4\pi^2 k^2 \int_0^L dy \int_0^\infty d\kappa\kappa\Phi_n(\kappa) J_o(\kappa|\boldsymbol{\rho}_x - \mathbf{U}(y)\tau|) \sin^2\left(\frac{\kappa^2 y(L-y)}{2kL}\right). \quad \text{(B.1)}$$

Following the technique of Lawrence *et.al.* [35], this equation is normalized by the log-amplitude variance $C_\chi(\rho_x = 0, \tau = 0)$, defined by (C.10), in order to remove the structure parameter C_n^2 which arises from the Kolmogorov spectral density defined by (3.7). This gives,

$$C_{N_\chi}(\rho_x,\tau) = \frac{(.033)4\pi^2 k^2}{.124 k^{7/6} L^{11/6}} \int_0^L dy$$
$$\int_0^\infty d\kappa\kappa^{-8/3} J_o(\kappa|\boldsymbol{\rho}_x - \mathbf{U}(y)\tau|) \sin^2\left(\frac{\kappa^2 y(L-y)}{2kL}\right). \quad \text{(B.2)}$$

Differentiating (B.2) with respect to τ and then evaluating the function at $\tau = 0$ gives,

$$\left.\frac{\partial C_{N_\chi}(\rho_x,\tau)}{\partial\tau}\right|_{\tau=0} = \frac{(.033)4\pi^2 k^{5/6}}{.124 L^{11/6}} \int_0^L dy U(y)$$
$$\int_0^\infty d\kappa\kappa^{-5/3} J_1(\kappa\rho_x) \sin^2\left(\frac{\kappa^2 y(L-y)}{2kL}\right). \quad \text{(B.3)}$$

$f_a(Hz)$	ρ_x (m)	β	R_d^{-1}	R_p^{-1}
67567	0.61	0.1589	0.7872	0.8879
67567	1.22	0.3179	0.7845	0.4863
67567	1.18	0.3075	0.7898	0.5183
69444	1.18	0.3118	0.7987	0.5120

Table B.1: Inverse of the calibrating factor R for current speed determination based on diverging acoustic paths (d) and parallel acoustic paths (p).

If we make the substitutions, $s = y/L$, $\pi\alpha^2 = \kappa^2 L/2k$ and $\beta = \rho_x/\sqrt{\lambda L}$, we get,

$$\left.\frac{\partial C_{N_X}(\rho_x,\tau)}{\partial\tau}\right|_{\tau=0} = \frac{.033}{.124}\frac{4\pi^2}{(2\pi)^{1/3}}\left(\frac{k}{L}\right)^{1/2}\int_0^1 dsU(s) \int_0^\infty d\alpha\alpha^{-5/3}J_1(2\pi\beta\alpha)\sin^2(\pi\alpha^2 s(1-s)), \quad \text{(B.4)}$$

$$= 5.6937\left(\frac{k}{L}\right)^{1/2}\int_0^1 dsU(s)W_{C_1}(s,\beta), \quad \text{(B.5)}$$

where $W_{C_1}(s,\beta)$ is a weighting on the current speed. This weighting function is numerically evaluated for different values of β and the results are shown in Figure B.1(a). The most uniform distribution occurs for $\beta = 0.1$ or 0.2 for parallel paths. The weighting function is such that the current speed is weighted towards the center of the channel. Assuming the current speed is uniform across the channel and integrating this weighting function over s for a constant β gives the following equation,

$$\left.\frac{\partial C_{N_X}(\rho_x,\tau)}{\partial\tau}\right|_{\tau=0} = UR_p^{-1}, \quad \text{(B.6)}$$

where R_p^{-1} is defined as the inverse of the calibrating factor for parallel paths and values are tabulated in Table B.1.

For diverging paths the Bessel function $J_1(2\pi\beta\alpha s)$ becomes a function of s. This is because the separation between acoustic paths is no longer ρ_x but is now $\rho_x y/L$. Lawrence *et.al.* [35] evaluate this weighting function numerically for different values of β and the results are shown in Figure B.1(b). The most uniform distribution is

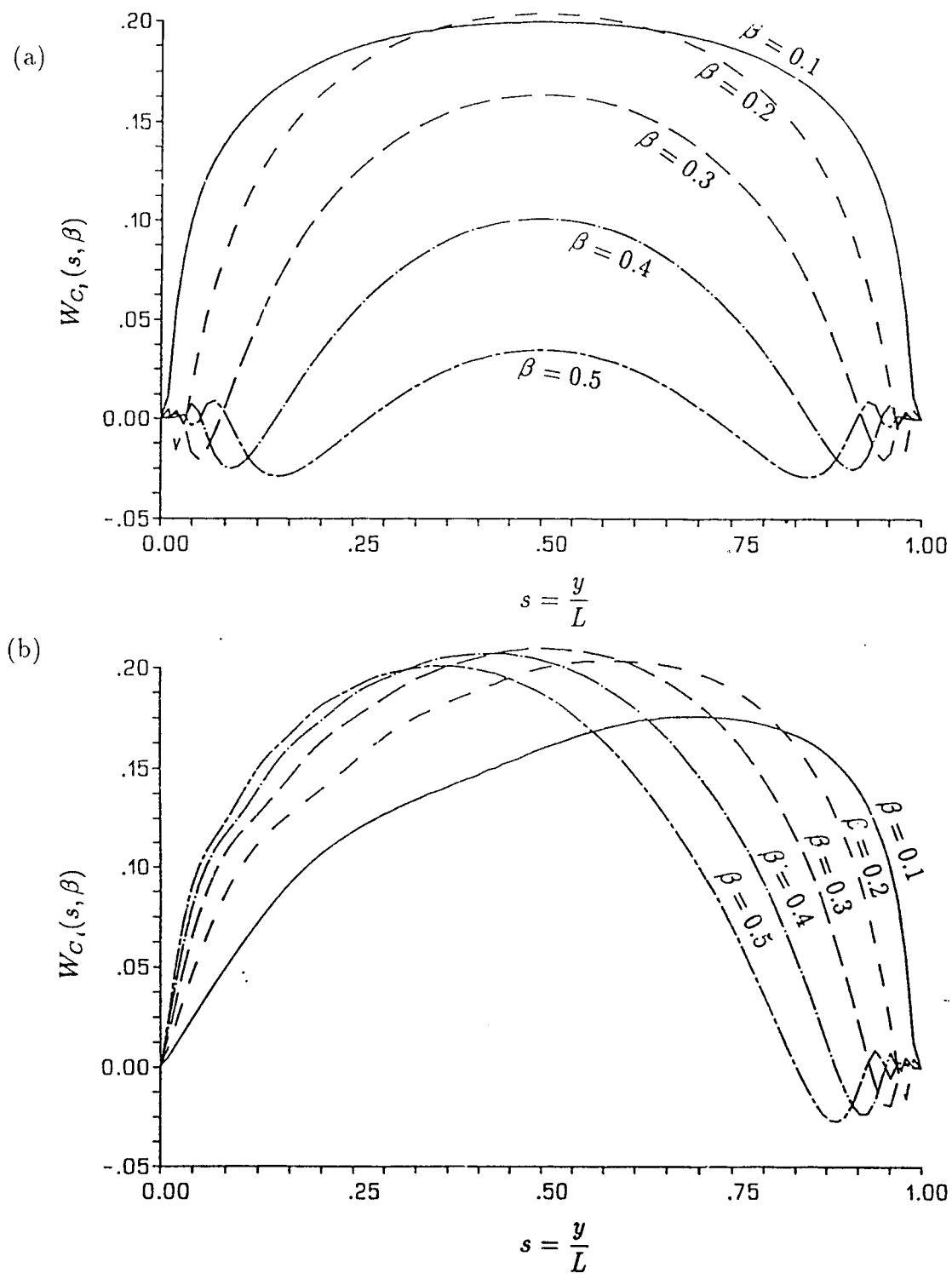

Figure B.1: Weighting function $W_{C_1}(s, \beta)$ for different values of β showing the relative contribution from different parts of the acoustic path to the current speed measurement. (a) Parallel paths. (b) Diverging paths.

for $\beta = 0.3$. This weighting function is such that the maximum sensitivity in current measurement is at the center of the channel. However, for $\beta = 0.15$ more weight is given to the current on the receiver side. Assuming the current is uniform across the channel and integrating this weighting function over s for a constant β gives the following equation for current speed,

$$\left.\frac{\partial C_{N_\chi}(\rho_x,\tau)}{\partial \tau}\right|_{\tau=0} = U R_d^{-1}, \tag{B.7}$$

where R_d^{-1} is defined as the inverse of the calibrating factor for diverging paths and values are also tabulated in Table B.1.

To compute the normalized log-amplitude cross covariance function using the acoustic data the following formula is used,

$$C_{N_\chi}(\rho_x,\tau) = \frac{<\chi'(r,t)\chi'(r+\rho_x,t+\tau)>}{\sqrt{<\chi'(r,t)^2><\chi'(r+\rho_x,t+\tau)^2>}}, \tag{B.8}$$

where $<\ >$ represents an ensemble average over time and
$\chi'(r,t) = \chi(r,t) - <\chi(r,t)>$ is a zero mean process. The slope is then determined by $[C_{N_\chi}(\rho_x,\tau = .1s) - C_{N_\chi}(\rho_x,\tau = -.1s)]/.2$.

B.2 Wave structure function technique

The governing equation for the wave structure function assuming spherical waves and parallel paths is given by (3.31),

$$\begin{aligned} D(\rho_x,\tau) &= D_\chi(\rho_x,\tau)+D_\phi(\rho_x,\tau) \\ &= 8\pi^2k^2\int_0^L dy\int_0^\infty d\kappa\kappa\Phi_n(\kappa)[1-J_o(\kappa|\boldsymbol{\rho}_x-\mathbf{U}(y)\tau|)]. \end{aligned} \tag{B.9}$$

Normalizing this equation by $D(\rho_x,\tau=0)$, differentiating with respect to τ and then evaluating the results at $\tau=0$ gives,

$$\left.\frac{\partial D_N(\rho_x,\tau)}{\partial\tau}\right|_{\tau=0} = -\frac{\int_0^L dyU(y)\int_0^\infty d\kappa\kappa^2\Phi_n(\kappa)J_1(\kappa\rho_x)}{\int_0^L dy\int_0^\infty d\kappa\kappa\Phi_n(\kappa)[1-J_o(\kappa\rho_x)]}. \tag{B.10}$$

Inserting the Kolmogorov spectral density defined by (3.7) and substituting $\alpha=\kappa\rho_x$ and $s=y/L$, gives the following equation,

$$\left.\frac{\partial D_N(\rho_x,\tau)}{\partial\tau}\right|_{\tau=0} = -\frac{\int_0^1 dsU(s)\int_0^\infty d\alpha\alpha^{-5/3}J_1(\alpha)}{\rho_x\int_0^1 ds\int_0^\infty d\alpha\alpha^{-8/3}[1-J_o(\alpha)]}, \tag{B.11}$$

$$= -\frac{\int_0^1 dsU(s)W_{D_1}(s)}{\rho_x\int_0^1 dsW_{D_0}(s)}, \tag{B.12}$$

where $W_{D_1}(s)$ is a weighting function on the current speed. For parallel paths this function is constant and is shown in Figure B.2. This implies that the current speed is uniformly weighted across the channel. Integrating the denominator of (B.12) by parts and making the assumption that the current is uniformly distributed, results in the very simple formula,

$$\left.\frac{\partial D_N(\rho_x,\tau)}{\partial\tau}\right|_{\tau=0} = -\frac{5}{3}\frac{U}{\rho_x}. \tag{B.13}$$

For diverging paths the Bessel functions $J_1(\alpha s)$ and $J_0(\alpha s)$ become functions of the normalized path length s. The weighting function $W_{D_1}(s)$ is now no longer constant but has a distribution shown in Figure B.2 (see Farmer and Clifford [23]). The current speed for diverging paths is thus weighted towards the receiver. Again, integrating the denominator of (B.12) by parts and assuming uniform current results in,

$$\left.\frac{\partial D_N(\rho_x,\tau)}{\partial\tau}\right|_{\tau=0} = -\frac{8}{3}\frac{U}{\rho_x}, \tag{B.14}$$

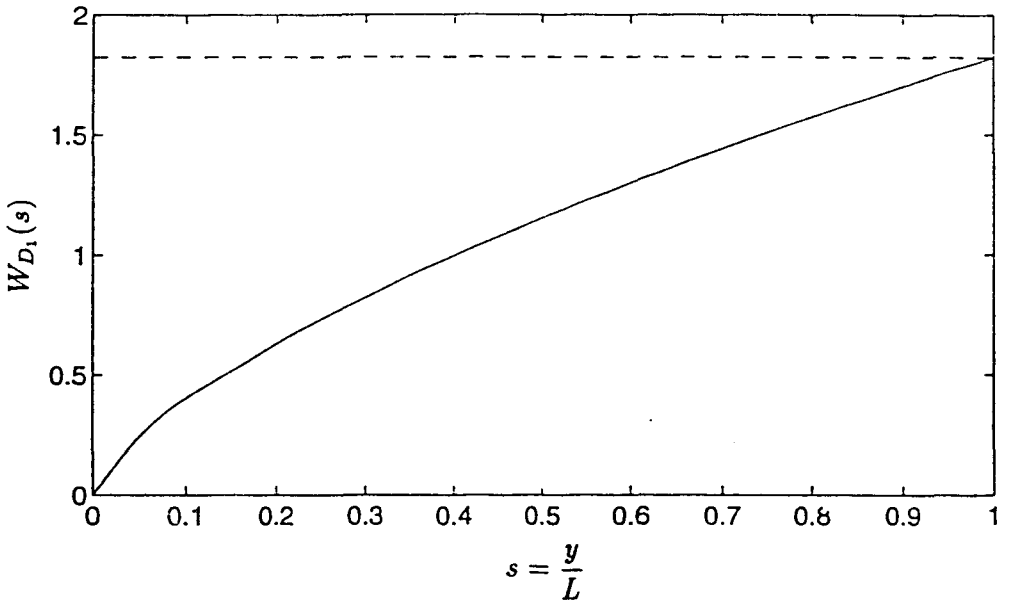

Figure B.2: Weighting function $W_{D_1}(s)$ showing the relative contribution from different parts of the acoustic path to the current speed measurement for parallel paths (dotted curve) and diverging paths (solid curve).

for diverging paths.

The wave structure function can be evaluated from the acoustic data using,

$$\begin{aligned} D(\rho_x,\tau) &= D_\chi(\rho_x,\tau) + D_\phi(\rho_x,\tau), \\ &= <[\chi'(r,t) - \chi'(r+\rho_x, t+\tau)]^2> + \\ &\quad <[\phi'(r,t) - \phi'(r+\rho_x, t+\tau)]^2> . \end{aligned} \tag{B.15}$$

The slope is then determined by, $[D(\rho_x, \tau = .1s) - D(\rho_x, \tau = -.1s)]/.2$.

B.3 Delay to peak

As structures get advected along the channel they leave their signature on the acoustic signal at the time which they cross the acoustic path. The separation between the parallel acoustic paths is known to be ρ_x; the time τ that it takes the structures to pass from one acoustic path to the next is determined by the location of the cross covariance peak. The speed at which structures are advected is therefore,

$$U = \frac{\rho_x}{\tau}, \tag{B.16}$$

for parallel paths.

To obtain a similar equation for diverging acoustic paths we use the average spacing $\rho_x/2$ between the paths. The resulting equation to determine the current speed is therefore,

$$U = \frac{\rho_x}{2\tau}, \tag{B.17}$$

for diverging paths.

Appendix C

Acoustical C_n^2 Measurements

C.1 Log-amplitude variance method

Following the method of Farmer *et.al.* ([24]) the log-amplitude variance σ_χ^2 is by definition $C_\chi(\rho_x = 0, \tau = 0)$. From (3.24) the log-amplitude variance is theoretically,

$$C_\chi(\rho_x = 0, \tau = 0) = 4\pi^2 k^2 \int_0^L dy \int_0^\infty d\kappa \kappa \Phi_n(\kappa) \sin^2\left(\frac{\kappa^2 y(L-y)}{2kL}\right). \qquad \text{(C.1)}$$

Substituting the Kolmogorov spectral density defined by (3.7) and making the substitutions $\pi\alpha^2 = \kappa^2 L/2k$ and $s = y/L$ gives,

$$\begin{aligned} C_\chi(0,0) &= .033(2\pi)^{7/6} k^{7/6} L^{11/6} \int_0^1 ds C_n^2(s) \int_0^\infty d\alpha \alpha^{-8/3} \sin^2\left(\pi\alpha^2 s(1-s)\right) & \text{(C.2)} \\ &= .033(2\pi)^{7/6} k^{7/6} L^{11/6} \int_0^1 ds C_n^2(s) W_{C_0}(s), & \text{(C.3)} \end{aligned}$$

where $W_{C_0}(s)$ is a weighting function on the structure parameter which we have arbitrarily made a function of normalized path length. This weighting function is shown in Figure C.1. The structure parameter using the log-amplitude variance is thus weighted towards the center of the channel.

To evaluate the integrals numerically we follow the technique of Tatarskii [51] and simplify first the integral over the normalized path length. Assuming that the structure parameter is uniform across the channel, substituting $\xi = s - 1/2$ and

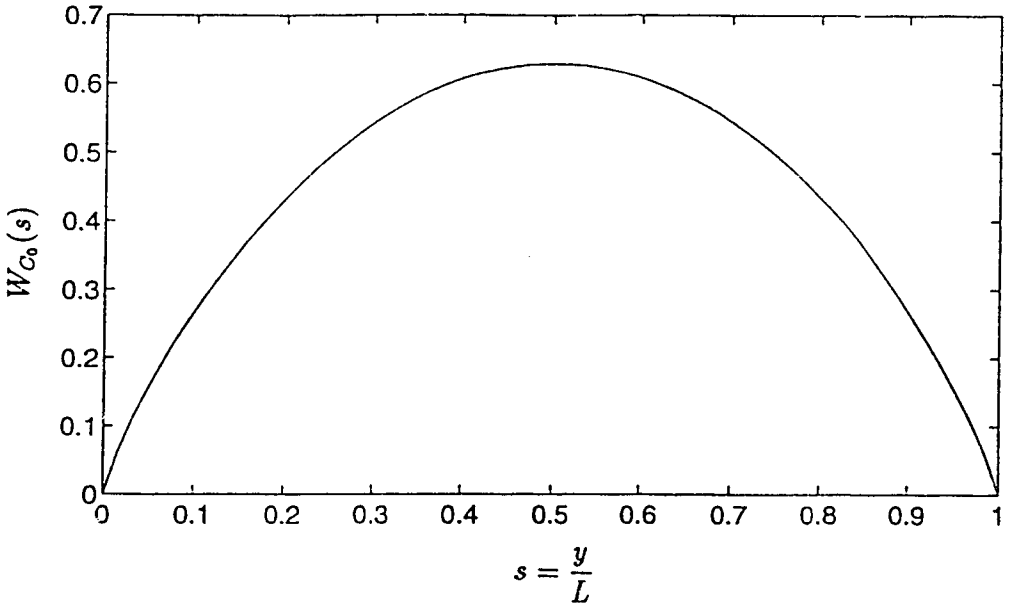

Figure C.1: Weighting function $W_{C_0}(s)$ showing the relative contribution from different parts of the acoustic path to C_n^2.

expanding the $\sin^2$ term in terms of cos, gives the following equation,

$$\int_0^1 \sin^2(\pi\alpha^2 s(1-s))ds = \int_0^{1/2}(1-\cos(2\pi\alpha^2(\xi^2-1/4)))d\xi. \tag{C.4}$$

Expanding the right hand side gives,

$$= \frac{1}{2} - \cos\left(\frac{\pi}{2}\alpha^2\right)\int_0^{1/2}\cos\left(2\pi\alpha^2\xi^2\right)d\xi - \sin\left(\frac{\pi}{2}\alpha^2\right)\int_0^{1/2}\sin\left(2\pi\alpha^2\xi^2\right)d\xi. \tag{C.5}$$

Substituting $2\pi\alpha^2\xi^2 = \frac{\pi}{2}t^2$, then the right hand side becomes,

$$= \frac{1}{2}\left\{1 - \frac{1}{\alpha}\left[\cos\left(\frac{\pi}{2}\alpha^2\right)C(\alpha) + \sin\left(\frac{\pi}{2}\alpha^2\right)S(\alpha)\right]\right\}, \tag{C.6}$$

where the function $C(\alpha)$ and $S(\alpha)$ are called Fresnel integrals (see Tatarskii [52]) and are defined as follows,

$$C(\alpha) = \int_0^{\alpha}\cos\left(\frac{\pi}{2}t^2\right)dt, \tag{C.7}$$

$$S(\alpha) = \int_0^{\alpha}\sin\left(\frac{\pi}{2}t^2\right)dt. \tag{C.8}$$

The log-amplitude variance can then be written as,

$$\sigma_\chi^2 = \frac{.033(2\pi)^{7/6}}{2} C_n^2 L^{11/6} k^{7/6} \int_0^\infty d\alpha \alpha^{-8/3} \left\{ 1 - \frac{1}{\alpha} \left[\cos\left(\frac{\pi}{2}\alpha^2\right) C(\alpha) + \sin\left(\frac{\pi}{2}\alpha^2\right) S(\alpha) \right] \right\}. \quad \text{(C.9)}$$

The integral on the right is a constant and must be evaluated numerically. This constant was found to be 0.87753. Therefore, the log-amplitude variance is defined to be,

$$\sigma_\chi^2 = 0.124 C_n^2 L^{11/6} k^{7/6}. \quad \text{(C.10)}$$

C.2 Wave structure function method

The wave structure function defined by (3.31) for parallel paths and evaluated at $\tau = 0$ is defined as,

$$D(\rho, \tau = 0) = 8\pi^2 k^2 \int_0^L dy \int_0^\infty d\kappa \kappa \Phi_n(\kappa)[1 - J_o(\kappa\rho)], \tag{C.11}$$

where ρ is any spatial separation (horizontal, vertical or diagonal). The resulting C_n^2 measurement would represent refractive index fluctuations along the spatial separation. Making the substitution $\alpha = \kappa\rho$, $s = y/L$ and then inserting the Kolmogorov density gives the following equation,

$$\begin{aligned} D(\rho, \tau = 0) &= 8\pi^2(.033)k^2 L\rho^{5/3} \int_0^1 ds C_n^2(s) \int_0^\infty d\alpha \alpha^{-8/3}[1 - J_o(\alpha)], & \text{(C.12)} \\ &= 8\pi^2(.033)k^2 L\rho^{5/3} \int_0^1 ds C_n^2(s) W_{D_0}(s), & \text{(C.13)} \end{aligned}$$

where $W_{D_0}(s)$ is a weighting function on the structure parameter which we have arbitrarily made a function of normalized path length.

This weighting function is constant for parallel paths and is shown in Figure C.2. Thus, the structure parameter C_n^2 is uniformly weighted across the channel. Assuming that the structure parameter is uniformly distributed across the channel then for parallel paths the wave structure function at zero time lag is,

$$D(\rho, \tau = 0) = 2.91 C_n^2 k^2 L\rho^{5/3}. \tag{C.14}$$

For diverging paths the weighting function $W_{D_0}(s)$ is such that the structure parameter is weighted towards the receiver (see Figure C.2). Proceeding in a similar fashion as described by Farmer *et.al.* [24] the wave structure function at zero time lag for diverging paths is,

$$D(\rho, \tau = 0) = 1.09 C_n^2 k^2 L\rho^{5/3}. \tag{C.15}$$

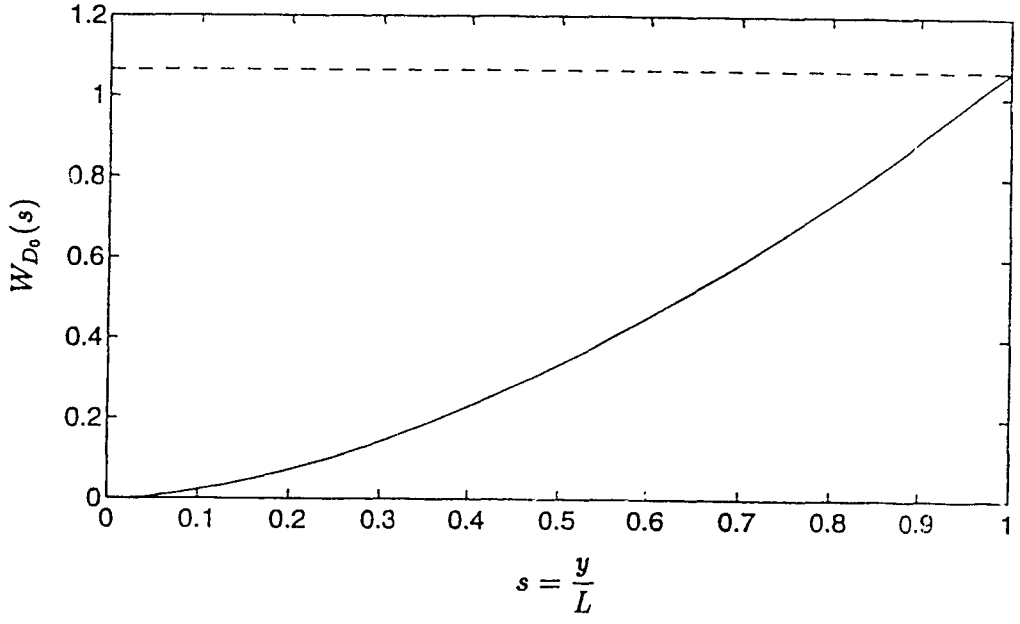

Figure C.2: Weighting function $W_{D_0}(s)$ showing the relative contribution from different parts of the acoustic path to C_n^2 for parallel paths (dashed curve) and diverging paths (solid curve).

Appendix D

Maximum Likelihood Estimation for a Single Path

In order to calculate the amplitude (A), phase (ϕ) and time of arrival (T) for a single acoustic path, a maximum likelihood estimation algorithm is developed following Ehrenberg *et.al.* [20]. The mathematical model for the received signal $r(t)$ is,

$$r(t) = As(t-T) + n(t) \tag{D.1}$$

where t is the elapsed arrival time. The signal $s(t)$ is known since it is the matched filter output determined by Menomenlis and Farmer [42],

$$s(t-T) = \sum_{n=0}^{9} a_n \left(\frac{t-T}{\tau_p}\right)^{2n}, \tag{D.2}$$

where a_n are known coefficients and τ_p is the half-width of the correlation peak. The shape of this function is triangular with a rounded apex and can be seen in Figure 6.8.

The maximum likelihood estimation is derived as follows: minimize,

$$Q = \sum_t [r(t) - As(t-T)]^2, \tag{D.3}$$

$$= \sum_t r(t)^2 - 2\left[AC(T) - \frac{1}{2}A^2B(0)\right], \tag{D.4}$$

with respect to A and T. The function,

$$C(T) = \sum_t r(t)s(t-T) \tag{D.5}$$

is the cross correlation between the received and modelled signal and the function,

$$B(0) = \sum_t s(t-T)s(t-T), \tag{D.6}$$

is the auto correlation of the modelled signal. Minimizing Q implies that the second term on the right of (D.4) should be maximized. That is,

$$\text{maximize} \quad AC(T) - \frac{1}{2}A^2B(0) \quad \text{w.r.t } A \text{ and } T. \tag{D.7}$$

Maximizing (D.7) with respect to A yields,

$$A = \frac{C(T)}{B(0)}. \tag{D.8}$$

Substituting (D.8) into (D.7) gives the following maximization problem,

$$\text{maximize} \quad \frac{1}{2}\frac{C(T)^2}{B(0)} \quad \text{w.r.t. } T. \tag{D.9}$$

Therefore, to determine the maximum likelihood estimate, (D.9) must first be maximized with respect to the arrival time. This equation is quadratic and is a function of one independent variable and so maximization occurs over a one-dimensional space. Powell's quadratically convergent method described in Numerical Recipes [46] is used for this procedure. In order to find the arrival time that maximizes (D.9) a starting point must be given. For the very first transmission the starting point can be determined by peak detection; for subsequent transmissions the arrival time for the previous transmission can be used as a starting point. Powell's method then converges quickly to the new arrival time that maximizes (D.9). These values are then used in (D.8) to obtain the amplitude estimate. The phase can then be calculated by triangular or quadratic interpolation of the in-phase and quadratic components.

Windowing of the data is crucial. Since the peak width is defined by $2\tau_p = 6$ samples say, then it is ideal to do the estimation over only 7 samples. This will

involve adjusting the window with time so that the peak remains centered in the window. Hence a peak tracking routine is required. Some tests were carried out and it was found that a window centered on a running average of the time of arrival was ideal. Taking the center of the window on a specific time of arrival may cause the window to include only part of the peak and thus cause problems. This windowing problem may arise because the time of arrival can be a noisy estimate.

Title of Thesis/Dissertation:

Measurements of Turbulence Parameters and Observations of Multipath Arrivals in Two Contrasting Coastal Environments Using Acoustical Scintillation Analysis.

Author:

DANIELA DI IORIO
June 5,1994